DEVELOPMENT OF NICKEL-BASED CATALYST FOR HIGH-TEMPERATURE WATER-GAS SHIFT REACTION

ANG MING LI

NATIONAL UNIVERSITY OF SINGAPORE

2015

DEVELOPMENT OF NICKEL-BASED CATALYST FOR HIGH-TEMPERATURE WATER-GAS SHIFT REACTION

ANG MING LI

(B.Eng (Hons), National University of Singapore)

A THESIS SUBMITTED

FOR THE DEGREE OF Ph.D. OF ENGINEERING

DEPARTMENT OF CHEMICAL AND

BIOMOLECULAR ENGINEERING

NATIONAL UNIVERSITY OF SINGAPORE

2015

DECLARATION

I hereby declare that the thesis is my original work and it has been written by me in its entirety. I have duly acknowledged all the sources of information which have been used in the thesis.

This thesis has also not been submitted for any degree in any university previously.

_____

ANG MING LI

15 September 2015

Acknowledgements

I would like to express my heartfelt gratitude and sincere appreciation to my supervisor, Prof. Sibudjing Kawi, for his patient guidance, insightful advice and constant encouragement to reach for greater heights during my candidature. As a true educator, he teaches from the heart and not from the book. His strong belief in me has truly inspired me to achieve greater accomplishments for my future endeavors. I would also like to convey my appreciation to Prof. Kus Hidajat for his valuable advice on my research work during group meetings.

Sincere thanks also go to my fellow group members, Dr. Usman Oemar, Dr. Jangam Ashok, Dr. Mo Liuye, Dr. Yasotha Kathiraser, Dr. Saw Eng Toon, Dr. Li Ziwei, Dr. Warintorn Thisartarn, Dr. Thawatchai Maneerung, Mr. Wang Zhigang, Mr. Gao Xingyuan, Mr. Bian Zhoufeng, Ms. Elmira Soghrati and Mr. Parviz Yazdani for their valuable assistance and the many wonderful memories. I am also grateful to the department staff, Mdm. Jamie Siew, Mr. Evan Tan, Mr. Liu Zhi Cheng, Dr. Yuan Ze Liang, Mr. Chia Phai Ann, Mr. Mao Ning, Mr. Qin Zhen and Mr. Ng Kim Poi for their prompt assistance in facilitating my research and in generously sharing their domain knowledge.

Last but not least, I would like to express my deepest gratitude to my family: my parents, brothers, sisters-in-law, nieces and nephews for their continual support and encouragement throughout my life. Not forgetting a heartfelt appreciation to my soul mate, Linus Li, for his love, support and words of motivation throughout my candidature. This thesis is dedicated to them.

Table of Contents

Summary

Hydrogen is envisioned to be the next-generation clean and renewable energy vector. Water-gas shift (WGS) reaction plays a dominant role in promoting the prospect of hydrogen economy by upgrading hydrogen content of syngas. Despite its high activity and low cost, use of nickel-based catalysts in WGS is prohibitive due to its tendency towards methanation which reduces hydrogen yield. In this thesis, several strategies have been applied to suppress methanation. These include: (a) formation of bimetallic Ni-Cu alloy, (b) addition of alkali metals (e.g. Na and K) and (c) formation of core-shell structures. Through techniques such as XAS, in-situ DRIFTS, XPS, H_2/CO-TPR and XRD, causes of WGS activity and selectivity enhancement were elucidated.

Firstly, highly dispersed Ni-Cu nanoparticles supported on SiO_2 were synthesized via an in-situ self-assembly core-shell precursor route using oleic acid (OA). Oleic acid was found to promote the dispersion of both monometallic and bimetallic particles, anchoring small metal particles to the support via enhanced metal-support interactions. 5Ni5Cu/SiO_2 (OA) catalyst exhibits the best WGS activity and lowest methane formation. Methane suppression in the bimetallic catalyst has been attributed to the adsorption of CO on Cu sites in Ni-Cu alloy. Stronger CO adsorption on 5Ni5Cu/SiO_2 (OA) catalyst activates surface terminal hydroxyl groups on silica for enhanced CO conversion. Kinetic measurements demonstrated the promotional effect of OA; 5Ni5Cu/SiO_2 (OA) catalyst obtained a turnover frequency of 0.004 s^{-1} which is double that of 5Ni5Cu/SiO_2 catalyst (0.002 s^{-1}).

Recognizing the importance of hydroxyl groups in enhancing WGS activity, ceria was used as the catalyst support for the nickel-based catalyst. Ceria, which is known for its redox properties, is capable of forming hydroxyl groups upon reduction. These hydroxyl groups serve as vital reaction intermediates in WGS reaction. To further increase the concentration of hydroxyls on the surface of ceria support, alkali metals (e.g. Na and K) were introduced. The role of Na in Ni/CeO_2 was first investigated by varying the loading of Na in the catalysts. Solubility limit of Na^+ in CeO_2 lattice was found to be 2 wt%. At low loadings of Na (0.5 to 2 wt%), Na^+ was incorporated into the CeO_2 lattice, generating a lattice strain and inducing more lattice oxygen anion vacancies, thereby increasing the reducibility of the catalyst. Enhanced catalyst reducibility translated to higher CO conversion at lower reaction temperature of 350 °C. In addition, methanation was found to be inhibited by the interaction between Na and Ni, leading to the absence of subcarbonyl species which are the precursors for methane formation.

Following that, the effect of increasing basicity was studied with the introduction of K in the form of K^+ in the Ni/CeO_2 catalysts by varying the loading of K in the catalysts. An optimum loading of 5 wt% K^+ was found to enhance the WGS activity and selectivity. The role of K^+ in suppressing methane is attributed to the formation of nickel subcarbonyl species through interaction of Ni and K^+, coupled with the strong adsorption of CO on Ni via the formation of bridging carbonyls. In terms of activity enhancement, K^+ served to enhance reduction of CeO_2 and promote water dissociation and formation of hydroxyl

groups on the reduced CeO_2 surface. Kinetic studies on Ni/5K/CeO_2 catalyst suggest that dual-site redox mechanism is the dominant reaction pathway.

Lastly, the importance of metal-support (i.e. Ni-Ce) interface was investigated with novel cubic CeO_2@nickel phyllosilicate@CeO_2 core-shell catalysts which were synthesized by a facile method. Sintering of active Ni was prevented by formation of Ni phyllosilicate (Ni-Phy) which has strong interaction with metal Ni while agglomeration of CeO_2 was eliminated by the encapsulation with Ni-Phy which compartmentalized cubic CeO_2 as separate entities. Secondary CeO_2 shell in dual-coated core-shell catalysts conferred enhanced metal-support interaction and reducibility which is reflected through higher WGS activity and selectivity than single-coated CeO_2@Ni-Phy catalyst.

Keywords: water-gas shift reaction, nickel, ceria, nickel-copper alloy, alkali, core-shell, nickel phyllosilicate

Nomenclature

BET	Brunauer-Emmett-Teller
DRIFTS	Diffuse Reflectance Infrared Fourier Transform Spectroscopy
EDX	Energy Dispersion X-ray
EXAFS	Extended X-ray Absorption Fine Structure
FTIR	Fourier Transform Infra-red
GC	Gas Chromatograph
GHSV	Gas Hourly Space Velocity
HPLC	High Performance Liquid Chromatograph
MS	Mass Spectrometry
TCD	Thermal Conductivity Detector
TEM	Transmission Electron Microscope
TGA	Thermal Gravimetry Analysis
TOF	Turnover Frequency
TPR	Temperature Programmed Reduction
XANES	X-ray Absorption Near Edge Structure
XAS	X-ray Absorption Spectroscopy
XPS	X-ray Photoelectron Spectroscopy
XRD	X-ray Diffraction
WGS	Water-Gas Shift

°C	Degree centigrade
ΔH_i	Heat of adsorption of reaction i (kJ/mol)
ΔS_i	Entropy of adsorption of reaction i (kJ/mol.K)
A_i	Pre-exponential rate constant of reaction i
E_a	Apparent activation energy (kJ/mol)
K_i	Equilibrium constant of reaction i
k_i	Rate constant of reaction i
r_i	Reaction rate of reaction i
T	Temperature (°C/Kelvins)
Wt%	Weight percent
X_{CO}	CO conversion

List of Tables

List of Figures

Chapter 1 Introduction

1.1 Background

Global demand of accelerated energy production and environmental concerns are two of the most cited issues in the 21st century. In order to satisfy the world's ever-growing appetite for energy while preserving the planet, at least 10 terawatt (TW) of carbon-free power is required by mid-century [1]. The erratic fluctuations in petroleum price, limited reserve of fossil fuels, and escalating environmental concerns related to harmful greenhouse gas emissions and its effect on global warming and deterioration of human health have spurred the search for alternative energy sources and development of technologies to reduce the impact of combustion of fossil fuels [2]. At present, the majority of the global energy demand is met by the utilization of fossil fuels. However, this demand is projected to increase by two to three times, and oil and gas supply will not be sufficient to meet this requirement [3]. A promising alternative to fossil fuels is hydrogen. Hydrogen is envisioned to be an ideal, clean energy carrier due to its high energy density, abundance and environmentally benign oxidation product – water.

Industrially, hydrogen is used in a wide array of applications such as ammonia synthesis, hydrodesulphurization, hydrocracking, hydrogenation of hazardous wastes (e.g. polychlorinated biphenyls and dioxins), synthesis of alternative fuels via Fischer-Tropsch (FT) process, food processing, metal refining and electronics manufacturing [4]. There are several reasons which make hydrogen a highly popular candidate for substituting fossil fuels. Firstly, it is a

clean fuel which emits only water upon oxidation. Secondly, it can be produced using any energy sources, with renewable energy being most attractive. Thirdly, it is the most abundant element in the universe and has the highest specific energy content of all conventional fuels. Its energy yield of 122 kJ/g is 2.75 times greater than hydrocarbon fuels [3]. With the numerous advantages that hydrogen offers, it is therefore not surprising that there remains an on-going search for highly efficient and economical hydrogen-producing technologies.

Hydrogen production can be realized through various process technologies such as biomass gasification, coal gasification, pyrolysis, gaseous and aqueous phase reforming, photocatalysis, water splitting, photolysis and others [5-7]. The use of biomass as a feedstock for producing hydrogen is particularly attractive since it is a renewable source. Biomass gasification is based upon partial oxidation of the biomass into a mixture of hydrogen, methane, carbon monoxide, carbon dioxide, and nitrogen known as synthesis gas (syngas). In order to increase the hydrogen to carbon monoxide (H_2:CO) ratio, oxygen or steam are often introduced to the gasification process, resulting in the occurrence of steam reforming reaction in the process. Syngas is then channeled to the water-gas shift (WGS) reactor to further enhance the hydrogen concentration and to tune the H_2:CO ratio to 2:1 for subsequent Fischer-Tropsch synthesis [8]. For hydrogen production, the WGS process is followed by a separation process to produce pure hydrogen.

The WGS reaction [Eq. (1.1)] produces hydrogen while converting carbon monoxide produced from the upstream gasification / reforming reactions, thus

making it a very important intermediate reaction for increased hydrogen production.

$$CO + H_2O \leftrightarrow CO_2 + H_2, \qquad \Delta H = -41.1\ kJ/mol] \tag{1.1}$$

As will be discussed later in the literature review, there are several disadvantages with the existing iron-chromium-based catalyst which is employed industrially for the high temperature WGS reaction; the main reason being the toxicity of Cr which is used in the catalyst formulation. Hence, nickel-based catalyst is selected as a suitable substitute for conducting high temperature WGS in this work. Despite its cheap cost and high catalytic activity in reactions such as CO methanation [9-13] and hydrocarbon reforming [14-21], nickel-based catalysts have not been extensively used in WGS reaction as nickel catalyzes the undesired side reaction, methanation [Eq.(1.2)].

$$CO + H_2 \leftrightarrow CH_4 + H_2O, \quad \Delta H = -206.3\ kJ/mol \tag{1.2}$$

Generally, methanation involves two main stages: CO disproportionation/dissociation and subsequent hydrogenation of deposited C by adsorbed hydrogen. The former was found to be the rate-determining step for nickel-based catalysts in methanation [22]. Thus, it is postulated that by preventing formation of surface carbonaceous species on active nickel sites, methanation during WGSR will be suppressed [23].

In order to circumvent the occurrence of methanation, numerous catalyst designs involving the introduction of promoters or secondary metals and even structural modifications have been proposed. Hence, the key issue to solve

involves engineering the synthesis of a highly active and stable Ni-based catalyst which is capable of suppressing methanation during high temperature WGS reaction for enhanced H_2 production.

1.2 Research Objectives

The main research objective of this thesis is to develop high performance Ni-based catalysts which have excellent activity, selectivity and stability for the high temperature WGS reaction. This will be achieved through modification of the Ni-based catalyst by tuning its structural and chemical properties. The following steps will be carried out:

(i) Investigation on the role of Ni-Cu alloy and its dispersion on WGS activity and selectivity

Methane formation is an undesirable reaction in WGS reaction and addition of secondary metals such as Cu has been shown to suppress methane formation. Bimetallic Ni-Cu/SiO_2 catalysts were developed to study the effect of alloy formation on methane suppression. Besides, the effect of metal dispersion of the Ni-Cu alloy was also studied through the addition of oleic acid in the Ni-Cu/SiO_2 catalysts.

(ii) Investigation of the role of sodium in Ni/CeO_2 catalyst

Alkali metals, such as Na, K, and Ca, have been demonstrated to enhance activity and selectivity of WGS reaction through different routes such as: increased rate in formate decomposition [24] and formation of active hydroxyl groups [25]. The mechanism by which Na increases its selectivity towards WGS reaction was elucidated.

(iii) Investigation of the role of potassium in Ni/CeO_2 catalyst

Following the previous chapter, the effect of potassium on methane suppression and activity enhancement was studied to investigate the effect of increasing basicity. Kinetic study on the most active potassium-doped Ni-CeO_2 catalyst was also conducted to propose a possible reaction mechanism for the catalyst.

(iv) Investigation of cubic CeO_2@Nickel Phyllosilicate@CeO_2 core-shell catalyst

The importance of metal-support interaction is investigated with novel dual-coated core-shell structure with tunable metal-support interfacial area. A facile method to synthesize cubic CeO_2@Nickel Phyllosilicate@CeO_2 core-shell catalysts was developed and the effect of varying nickel phyllosilicate thickness on the strength of metal-support interaction and consequently the WGS activity was investigated.

1.3 Thesis Organization

This thesis consists of eight chapters. In Chapter 1, an overview of the research background, research objectives and thesis outline is provided.

Chapter 2 begins with an overview of the WGS reaction and its thermodynamics, followed by a detailed literature review on the commercial catalysts, recent catalyst development, reaction mechanisms and kinetic models for the WGS reaction.

Chapter 3 presents the experimental methodology for catalyst synthesis, catalytic activity testing and characterization techniques in detail.

Chapter 4 discusses the effect of oleic acid (OA) on monometallic (nickel and copper) and bimetallic (nickel-copper) catalysts. Metal dispersion and metal-support interaction were found to be enhanced by the addition of OA. Characterization techniques such XRD, H_2-TPR, XAS and DRIFTS were employed to confirm the formation of bimetallic Ni-Cu alloy.

Chapter 5 presents the effect of varying Na loading on the WGS activity of Na-doped Ni-CeO_2 (Ni/xNa/CeO_2) catalysts. The methane suppression effect of Na was investigated by examining the surface intermediates formed during CO adsorption. Mode and strength of CO adsorption was found to correlate to methane formation in the catalysts. Besides, the effect of Na on modifying CeO_2 lattice structure and reducibility will be discussed.

Chapter 6 discusses the effect of varying K loading on ceria-supported nickel (Ni/xK/CeO_2) catalysts on the WGS reaction. The effect of K on the mode and strength of CO adsorption on Ni as well as the reducibility of CeO_2 will be elaborated. Furthermore, kinetic studies were also performed to elucidate the possible reaction mechanism for the catalyst with the highest activity and selectivity.

Chapter 7 presents the effect of varying metal-support interaction in cubic-CeO_2@Ni-phyllosilicate@CeO_2 on the WGS reaction. The strength of metal-support interaction was varied by modifying the thickness of the nickel

phyllosilicate layer which was sandwiched between cubic CeO_2 and external layer of CeO_2. The effect of the structure on the activity and selectivity will be discussed.

Chapter 8 presents the main conclusions of this thesis as well as recommendations for future work.

1.4 References

[1] N.Z. Muradov, T.N. Veziroğlu, Int. J. Hydrogen Energ, 33 (2008) 6804.
[2] N. Armaroli, V. Balzani, Angew. Chem. Int. Ed., 46 (2007) 52.
[3] S. Sharma, S.K. Ghoshal, Renewable and Sustainable Energy Reviews, 43 (2015) 1151.
[4] R. Ramachandran, R.K. Menon, Int. J. Hydrogen Energ, 23 (1998) 593.
[5] A.J. Esswein, D.G. Nocera, Chem. Rev., 107 (2007) 4022.
[6] J.D. Holladay, J. Hu, D.L. King, Y. Wang, Catal. Today, 139 (2009) 244.
[7] T.S. Teets, D.G. Nocera, Chemical Communications, 47 (2011) 9268.
[8] M. Asadullah, S.-i. Ito, K. Kunimori, M. Yamada, K. Tomishige, J. Catal., 208 (2002) 255.
[9] M.P. Andersson, F. Abild-Pedersen, I.N. Remediakis, T. Bligaard, G. Jones, J. Engbæk, O. Lytken, S. Horch, J.H. Nielsen, J. Sehested, J.R. Rostrup-Nielsen, J.K. Nørskov, I. Chorkendorff, J. Catal., 255 (2008) 6.
[10] I. Czekaj, F. Loviat, F. Raimondi, J. Wambach, S. Biollaz, A. Wokaun, Appl. Catal. A, 329 (2007) 68.
[11] D. Hu, J. Gao, Y. Ping, L. Jia, P. Gunawan, Z. Zhong, G. Xu, F. Gu, F. Su, Ind. Eng. Chem. Res., 51 (2012) 4875.
[12] M. Krämer, M. Duisberg, K. Stöwe, W.F. Maier, J. Catal., 251 (2007) 410.
[13] Y.S. Mok, H.C. Kang, H.J. Lee, D.J. Koh, D.N. Shin, Plasma Chem. Plasma P., 30 (2010) 437.
[14] J. Ashok, S. Kawi, Int. J. Hydrogen Energ, 38 (2013) 13938.
[15] Z. Li, L. Mo, Y. Kathiraser, S. Kawi, ACS Catal., 4 (2014) 1526.
[16] L. Mo, K.K.M. Leong, S. Kawi, Catal. Sci. Technol., 4 (2014) 2107.
[17] J. Ni, L. Chen, J. Lin, M.K. Schreyer, Z. Wang, S. Kawi, Int. J. Hydrogen Energ, 38 (2013) 13631.
[18] U. Oemar, M.L. Ang, W.F. Hee, K. Hidajat, S. Kawi, Appl. Catal. B, 148–149 (2014) 231.
[19] U. Oemar, P.S. Ang, K. Hidajat, S. Kawi, Int. J. Hydrogen Energ, 38 (2013) 5525.
[20] U. Oemar, K. Hidajat, S. Kawi, Appl. Catal. A, 402 (2011) 176.
[21] K. Sutthiumporn, T. Maneerung, Y. Kathiraser, S. Kawi, Int. J. Hydrogen Energ, 37 (2012) 11195.
[22] J. Sehested, S. Dahl, J. Jacobsen, J.R. Rostrup-Nielsen, J. Phys. Chem. B, 109 (2005) 2432.
[23] H. Yamasaki, Y. Kobori, S. Naito, T. Onishi, K. Tamaru, J. Chem. Soc., Faraday Trans. 77 (1981) 2913.
[24] H.N. Evin, G. Jacobs, J. Ruiz-Martinez, G.A. Thomas, B.H. Davis, Catalysis Letters, 120 (2008) 166.
[25] Q. Fu, H. Saltsburg, M. Flytzani-Stephanopoulos, Science, 301 (2003) 935.

Chapter 2 Literature Review

2.1 Overview of Water-Gas Shift (WGS) reaction

The Water Gas Shift (WGS) reaction is one of the major processes involved in all carbon-based fuel processes. It has a primary purpose of converting most of the carbon monoxide (CO) to carbon dioxide (CO_2) while producing and upgrading hydrogen from synthetic gas produced from upstream processes such as reforming and gasification. Hydrogen generated from the WGS reaction is further utilized for ammonia production via Haber ammonia process in the fertilizer industry and in petrochemical industries for a wide range of applications such as a fuel for power generation and transportation. With the increasing use of gasification for power generation, use of WGS has regained its momentum. The advent of the WGS reaction (Eq. 1.1) can be traced back to 1888 from which it gradually gained importance as a source of hydrogen for the manufacture of ammonia through the Haber process.

The equilibrium reaction, which occurs over a bed of catalyst, converts CO and steam into CO_2 and H_2, and is moderately exothermic. As the reaction is equilibrium limited, the extent of CO conversion is dependent on the reactor temperature. At lower temperatures, CO conversion is thermodynamically favoured, whereas at higher temperatures, reaction is kinetically favoured due to higher catalytic activity. This balance between thermodynamics and kinetics results in the reaction being executed in a series of stages industrially, with inter-reactors cooling, so as to achieve a high extent of CO conversion. Industrially, CO

concentrations can be decreased from 10-50 wt% to 0.3 wt% in a two stage WGS system with interstage cooling [1]. In such system, Fe_2O_3-Cr_2O_3 based catalysts are employed in the high temperature shift (350-450°C) and Cu-ZnO based catalysts are used in the low temperature shift (190-250°C). This section of the thesis provides a review of conventional commercial catalysts, recent catalyst developments, reaction mechanisms, kinetic models and finally rounds up with the limitations of existing catalysts and strategies to tackle these challenges.

2.2 Thermodynamics

Being a reversible and exothermic reaction, the WGS reaction depends on temperature and its equilibrium constant, in the temperature range of 315-480°C, can be expressed by Eq. 2.1.

$$K_{eq} = \frac{y_{CO_2,eq} \cdot y_{H_2,eq}}{y_{CO,eq} \cdot y_{H_2O,eq}} = exp\left(\frac{4577.8}{T} - 4.33\right) \quad (2.1)$$

Later in 1989, Twigg introduced a more complex thermodynamic model which can be applied in a wider temperature range of 200-1199°C, and can be expressed by Eq. 2.2.

$$ln\, K_{eq} = \frac{5693.5}{T} + 1.077lnT + (5.44 \times 10^{-4})T - (1.125 \times 10^{-7})T^2 - \frac{49170}{T^2} - 13.148 \quad (2.2)$$

Where T is in Kelvins.

As shown in both equations, the equilibrium constant K_{eq}, has an inverse relationship with temperature; Keq decreases as temperature increases. Thermodynamically, the reaction is equilibrium-limited. From the perspective of

higher CO conversion and greater H_2 production, it is therefore desirable to operate the reaction at lower temperatures. However, as higher temperatures are more favourable for the kinetics, a two-stage process comprising of a HTS reactor followed by a LTS reactor is often employed.

Furthermore, in order to achieve higher CO conversions, steam to CO ratio, R, used in the reaction is typically greater than the required stoichiometric ratio of 1. Low values of R can lead to catalyst deactivation as a result of coke formation. Though the use of high R drives the equilibrium reaction forward, the use of excess steam is generally not encouraged due to its energy inefficiency. Besides steam to CO ratio, other process parameters such as inlet concentration of CO, CO_2, H_2 and H_2S can also affect the CO conversion due to shifting of the thermodynamic equilibrium and sulfur poisoning of the metal sites in the case of H_2S.

2.3 High temperature shift catalysts

Iron-based catalysts have been utilized for industrial high temperature WGS converters for more than 60 years due to their inherent advantages of excellent poison resistance, thermal stability, and good selectivity [2]. Upon reduction from Fe_2O_3, the partially reduced state of Fe_3O_4 acts as a catalytically active phase for WGS reaction. In order to maintain catalytic activity and stability of iron-based catalysts, chromium is commonly introduced as a structural and textural stabilizer [3, 4]. There have been many postulations on the actual role that Cr_2O_3 plays. As a textural stabilizer, it has been proposed that the Cr_2O_3 prevents sintering of Fe_3O_4 by acting as physical barriers, preventing sintering of

neighbouring Fe_3O_4 particles, and consequent loss of surface area [5-7]. Chinchen et al. proposed that Fe_2O_3-Cr_2O_3 catalysts after reduction consist of Fe_3O_4 crystallites that are in direct contact with each other as well as Fe_3O_4 crystallites which are segregated by partitioning Cr_2O_3 crystallites [6]. At 350°C, Fe_3O_4 crystallites with neighbouring Cr_2O_3 remain comparatively more stable than Fe_3O_4 crystallites which are in direct contact. Another model proposed by Edwards et al. suggest that pure Cr_2O_3 and Fe_3O_4 do not exist as discrete grains, but instead, all Cr^{3+} exists in solid solution within the Fe_3O_4 lattice and chromium exerts its structural stabilizing effect by forming a Cr-rich surface which is more thermodynamically stable than the Fe-rich core, thereby reducing ion diffusion and sintering effect [4]. Besides functioning as a textural promoter, Cr_2O_3 also serves as a structural stabilizer to enhance the intrinsic catalytic activity of Fe_2O_3. Natesakhawat et al. found that two Cr species, namely, Cr^{6+} and Cr^{3+}, exist in the calcined sample[8]. The presence of two oxidation states suggests that Cr species may play a role in the WGS reaction when shuffling through a reduction-oxidation cycle between Cr^{6+} and Cr^{3+}.

Apart from addition of chromium as a textural and structural stabilizer, activity promoters such as Cu are also commonly utilized. Andreev et al. investigated the promotion effect by first-row transition metal oxides on the catalytic activity of Fe-Cr catalysts. Introduction of copper and cobalt oxides displayed the highest promoting effect at 380°C and 340°C, respectively [9]. Kappen et al. studied the state of copper promoter in Fe-Cr-based high temperature shift catalyst by in situ fluorescence XAFS and revealed that Cu

exists in its metallic state under reaction conditions but reoxidises upon exposure to air at room temperature [10]. Not only does metallic Cu serve as additional active sites for catalysis, TPR analysis by Natesakhawat et al. revealed that Cu species also serves as a functional electronic promoter that enhances the reducibility of the iron oxide, thereby increasing the redox rate of the catalysis [8].

Despite the widespread use of Fe-Cr catalysts for high temperature shift (HTS) reactions, there have been concerns about the use of chromium in the HTS catalyst formulation. As a strong carcinogen and toxic, hexavalent chromium, Cr^{6+}, not only poses health hazards, but is also environmentally unfriendly. In contrast, trivalent chromium, Cr^{3+}, has low toxicity and is a nutrient to the body [11]. Even though chromium exists as Cr^{3+} in fresh catalysts, there is a possibility of exposure to Cr^{6+} during catalyst preparation. Thus, there has been ongoing research to replace Cr in the catalyst formulation while maintaining its stability, selectivity and activity. Ozkan et al. [8, 12, 13] have been working extensively on Fe-Al-Cu catalysts and they have found aluminum (Al) to be a potential replacement for Cr as a textural promoter. Furthermore, the preparation method by which the activity promoter, Cu, was introduced was found to decide the extent of activity enhancement. Besides Al, thorium (Th) was also deemed as a suitable candidate to replace Cr. Costa et al. [14] studied the Fe-Th-Cu catalyst system and discovered that the catalyst was more active and selective than commercial Cr- and Cu- doped catalysts when Th and Cu were incorporated into the solid.

2.4 Low temperature shift catalysts

Since the early 1960s, Cu-ZnO-Al_2O_3 based catalysts have been used extensively in industrial low temperature shift (LTS) operations. Copper sintering and the consequent loss of surface area are resolved by the addition of stabilizers such as Al_2O_3, SiO_2, Cr_2O_3, Mn-Cr_2O_3 etc. Many studies have been conducted on the ternary Cu/ZnO/Al_2O_3 and binary Cu/ZnO catalyst systems. Gines et al. [15] studied the activity and structure-sensitivity over Cu-Zn-Al mixed oxide catalysts. Ternary Cu/ZnO/Al_2O_3 was found to be more active than binary Cu/ZnO and it was concluded that although Al was inactive for the WGS reaction, it was essential in enhancing the catalyst performance. Different preparation methods, such as homogenous precipitation, coprecipitation, impregnation and etc., have also been explored to obtain highly dispersed Cu metal species that are highly active and stable.

With the promising outlook in the development of proton exchange membrane fuel cell (PEMFC) technology for stationary and transport applications, there is an increasing demand for pure hydrogen (with low or zero CO). Tremendous effort has been devoted in research on LTS catalysts which are capable of removing high amount of CO. Frequent start-ups and shut-downs occurs during the application of hydrogen production to PEMFCs. Therefore, the catalysts for the shift reaction are sometimes exposed to oxidants such as water and/or oxygen containing atmosphere at low temperatures. The pyrophoric nature of copper-based catalysts thus renders it unsuitable for use with PEMFC applications. It is therefore important to develop highly stable LTS catalysts or

highly active precious metal catalysts. With these requirements in mind, ceria-based noble metal catalysts, such as Au and Pt, have been popular candidates for LTS reaction in PEMFC applications. For instance, Andreeva et al. reported high and stable activity with Au/CeO_2 catalysts for LTS reaction which was attributed to the well dispersion of Au on oxygen-producing CeO_2 [16]. Extensive studies have also been conducted on Pt/CeO_2 catalysts for LTS reaction. Jacobs et al. [17] studied the influence of Pt promoter loading on the partial reduction of ceria. Pt was found to facilitate the surface reduction of active bridging OH groups of ceria, and accelerate decomposition of surface formate – an elementary step proposed to be the rate determining step. In another investigation carried out by Pierre et al. [18], strongly bound $Pt\text{-}CeO_x$ species were found to be responsible for producing finer ceria particles which in turn generated higher amount of surface oxygen

2.5 Sulfur-tolerant shift catalysts

Sulfur-tolerant shift catalysts are necessary when dealing with syngas containing sulfur compounds. These sulfur-containing syngas is usually generated by upstream processes such as gasification and/or partial oxidation of biomass, coal, heavy fuel oil, oil shale and etc. Conventional Cu-based LTS catalysts are sulfur intolerant, while Fe-based HTS catalysts are less active in their sulfided state than in their oxide state. Hence, Co-Mo-alumina catalysts are typically used as sulfur-tolerant, sour gas shift catalysts. These catalysts require a minimum sulfur concentration of 300 ppm in the feed in order to maintain it in its active, sulfided state i.e. Co-Mo sulfide, and failure of which will result in low performance of the catalysts. Besides Co-Mo sulfided catalysts, Ni-Mo sulfided

catalysts are also widely used for the sour gas shift process. Laniecki and Ignacik [19] reported the use of TiO_2-ZrO_2 binary oxide support for Ni-Mo-S catalysts and achieved high activity for the WGS reaction. They attributed the good performance to the choice of support with high surface area and appropriate ratio of acid-base properties. In a bid to cope with higher operating temperatures, high temperature and impurity tolerant WGS catalysts were also developed. Morpeth et al. reported the use of $La_{0.7}Ce_{0.2}FeO_3$ perovskite catalyst which was able to operate in the temperature range of 450-600°C for H_2 production with coal-derived syngas containing H_2S concentration of up to 1100 ppm [20]. High stability and activity lanthanum oxysulfides sulfur tolerant catalysts, e.g. La_2O_2S and Pr_2O_2S, operating in the temperature range of 400-750°C with 700 ppm of H_2S were developed by Valsamakis and Flytzani-Stephanopoulos [21].

2.6 Nickel-based shift catalysts

Nickel-based catalysts have been widely used for reactions such as steam reforming of methane [22, 23], and CO methanation [24-27] owing to its cheap cost and high catalytic performance. However, its application in WGS reaction has been prohibitive due to its high activity towards an undesirable side reaction – methanation – that would consequently reduce the selectivity towards WGS reaction, and thereby decrease H_2 yield. Therefore, much effort has been devoted into developing nickel-based catalysts that suppress methanation reaction (Eq.(1.2 1.2) during WGS reaction.

Generally, methanation involves two main stages: CO disproportionation/dissociation and subsequent hydrogenation of deposited C by

adsorbed hydrogen. The former was found to be the rate-determining step for nickel-based catalysts in methanation [28]. Thus, it is postulated that by preventing formation of surface carbonaceous species on active nickel sites, methanation during WGSR will be suppressed.

2.7 Catalyst designs for enhanced WGS selectivity

In order to circumvent the occurrence of methanation, numerous catalyst designs involving the introduction of secondary metals or promoters has been proposed and the different formulation strategies for suppressing methanation in WGS catalysts are tabulated in **Table 2.1**.

2.7.1 Secondary metals

Secondary metals have been incorporated into catalyst formulations to suppress methane formation. Saw et al. discovered that Ni-Cu alloy phase is the active site for WGS reaction and it can suppress methanation by enhancing CO adsorption, thus preventing CO dissociation during WGS reaction (**Figure 2.1**) [29]. This was further reaffirmed by Lin et al. who reported that the addition of Cu to Ni/CeLaOx catalysts and its subsequent formation of Ni-Cu alloy aided the suppression of methane formation [30]. More recently, Roh et al. showed that NiCu(1:4)-CeO_2 [31] and CuNi/Fe_2O_3 [32] exhibited high WGS activity and selectivity to CO_2 and H_2 at a very high gas hourly space velocity (GHSV) of up to 101000 h^{-1}. The higher selectivity was attributed to the formation of Cu-rich surface that suppressed methanation and higher activity was due to the higher reducibility and mesoporous structure of the catalyst. However, the mechanistic role of Cu-rich surface in inhibiting methanation was not provided in these latter

three systems. In addition, the importance of enhanced CO adsorption on Ni and reducibility of CeO_2 was also reiterated with the addition of Re in Ni/CeO_2 catalyst by Chayakul et al. [33].

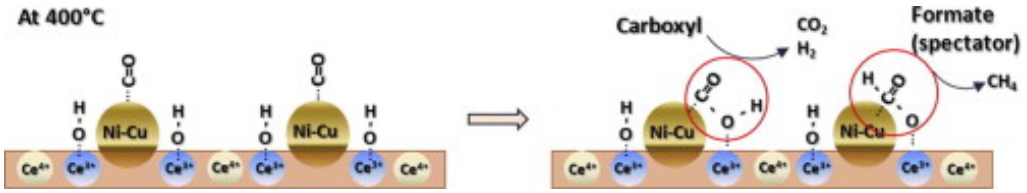

Figure 2-1 Bimetallic $Ni-Cu/CeO_2$ catalyst for methane suppression [29].

Other than Cu, Fe has also been introduced as a secondary metal. In contrast to the observation that enhanced strength of CO adsorption aids in suppression of methanation as in the case of bimetallic Ni-Cu alloy, it was revealed by Watanabe et al. that formation Ni-Fe alloy on hollow Ni-Fe-Al oxide nano-composite catalysts and mesoporous ceria-zirconia supported Ni-Fe catalyst weakened the strength of CO adsorption on Ni metal and suppress hydrogen adsorption, thereby suppressing CO dissociation and subsequent hydrogenation to form methane, thereby allowing WGS reaction to proceed predominantly [34, 35].

In addition, noble metals have also been considered in the bimetallic catalyst formulations. For instance, Chen et al. have investigated the effect of oxide supports (i.e. γ-Al_2O_3, SiO_2, TiO_2, CeO_2 and ZrO_2) over Pt-Ni bimetallic catalysts [36]. Higher activity was attained by the bimetallic Pt-Ni catalyst than monometallic (Pt or Ni) catalyst due to the change in binding energy of CO on the Pt-Ni bimetallic catalyst. Additionally, methane formation was found to be strongly dependent on the nature of the support and followed the trend of

CeO_2>SiO_2~γ-Al_2O_3>ZrO_2~TiO_2. The extent of methanation inhibition was attributed to the difference in densities of hydroxyl groups on the various supports that participate in the WGS reaction to form intermediates. Furthermore, intimate metal-support interaction has also been an attribute postulated for lower methanation observed in Rh-doped ZrO_2 supported Fe_2O_3 catalyst [37].

2.7.2 Alkali and alkaline metals

Extensive studies have been conducted for the promotion by alkali metals for metal or noble metals, and significant improvements have been observed when alkali such as Na, Li and K are doped on Pt-based catalyst supported on oxide supports. Flytzani-Stephanopoulos and co-workers have proposed that sodium (or potassium) atoms provide oxygen in the form of hydroxyls to active Pt metal site forming clusters on which water dissociation occurs [38-40]. On the other hand, it has been postulated by Davis and co-workers that alkali promotes the WGS reaction by weaking the formate C-H bond; decomposition of this bond has been proposed to be the rate-determining step for the low-temperature WGS reaction [41-44]. Specifically, for Ni-based catalysts, the role of alkali and alkaline metals on methane suppression has been attributed to several postulations that are in agreement with that of the above-mentioned noble metal catalysts. Hwang et al. reported that K-modified Ni metal suppressed methanation due to increased density of active hydroxyl group that reacts with CO adsorbed on Ni metal to form the surface intermediate via surface formate mechanism [45]. The increase in hydroxyl groups was likewise observed with K-doped Ru/C catalyst [46]. Similarly, Lee et al. proposed that promotion with Cs in Ni/Fe catalyst increased

the amount of basic sites which enhanced high-temperature WGS reaction through formation of formate intermediate and increased its selectivity of WGSR against methanation [47]. In addition, Meshkani and Rezaei also attributed the suppression of methanation by Ba on mesoporous Fe_2O_3-Al_2O_3-NiO catalyst to the creation of more basic sites [48].

2.7.3 Core-shell

The strategies to suppress methanation in Ni-based catalysts for high-temperature WGS reaction are not just limited to doping of metals. Unique structural configurations have been devised in a bid to increase the selectivity, activity and thermal stability of WGS reaction. Recently, Saw et al. have synthesized highly dispersed bimetallic Ni-Cu@CeO_2 core-shell catalyst (**Figure 2.2**) [49]. The core-shell structure offered advantages in terms of high metal-support interaction, small bimetallic Ni-Cu particle size, and high concentration of surface lattice oxygen for enhancing WGS reaction. Lin and Guliants have developed novel alumina-supported Cu@Ni and Ni@Cu core-shell catalysts and have found that Cu tends to segregate the surface in Cu@Ni catalyst at elevated temperatures due to lower surface tension energy, thereby suppressing the methanation reaction [50].

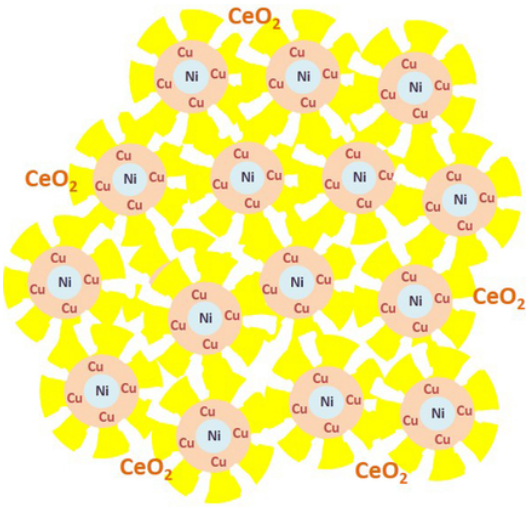

Figure 2-2 Bimetallic Ni-Cu@CeO_2 core-shell catalyst for high-temperature WGS reaction [49].

Noble metal-based core-shell catalysts have also been developed for the low-temperature WGS reaction. When compared to impregnated catalysts, it had been revealed that Pt@$Ce_{0.67}Zr_{0.33}O_2$ catalyst could suppress methanation even at 500 °C [51]. Even though a clear reasoning had not been provided, stronger metal-support interaction through embedment could have been the reason for methane suppression. In fact, Tsang et al. have proposed that the absence of methanation observed in PtAu@CeO_2 was due to the coverage of surface metal sites by thin layer of CeO_2 [52-54]. Similarly, good stability was also exhibited by Pd@CeO_2 catalyst which was developed by Cargnello et al. via a microemulsion procedure [55]. Subsequently, the same group also used the self-assembly method to prepare Pd@CeO_2 catalyst and dispersed it on alumina support. However, the synthesized Pd@CeO_2/Al_2O_3 catalyst exhibited severe deactivation within one hour of WGS reaction and it was attributed to the reduction of the ceria shell which decreased the accessibility of CO to the Pd core [56]. Contrastingly, Pt and

Pd were also dispersed on Si-Al_2O_3 support and Pd@CeO_2/Si-Al_2O_3 showed greater stability due to stronger interaction between Pd and CeO_2 [57]. Recently, these core-shell catalysts were dispersed on multiwalled carbon nanotubes (MWCNT) which were embedded inside mesoporous oxide (i.e. TiO_2, ZrO_2 or CeO_2) layers. It was found that encapsulating Pd or Pt cores within thin layer of CeO_2 helps to prevent metal sintering while MWCNT support provides accessible nanostructure for the core-shell catalysts [58]. From the above studies on core-shell systems, it is evident that they possess unique properties such as enhanced metal-support interaction which can increase the activity and selectivity towards WGS reaction.

2.7.4 Mixed-metal oxide

Besides core-shell configuration, mixed metal oxides have also been developed [59]. Rodriguez et al. revealed that the unique structural configuration of Ni embedded within the $Ce_{1-x}Ni_xO_y$ mixed metal oxide leads to high WGS activity and a simultaneous decrease in methanation [60]. Strong Ni-Ce interaction prevents the formation of bulk-like NiO species, thereby inhibiting the formation of carbonaceous deposits that would block the active sites. The same group by Rodriguez et al. also conducted a related theoretical study on the effect of Ni coverage in CO methanation reaction. It was discovered through density functional theory (DFT) calculations that carbon species are strongly bound on Ni(111), but with Ni/CeO_2(111), oxidative adsorption ($C+CeO_2 \rightarrow CO+CeO_{2-x}$) is preferred, leading to a Mars-van Krevelen mechanism to prevent coke formation and subsequent methanation [61]. Cu incorporated within Al_2O_3 was also shown

to exhibit complete selectivity to CO_2 without methanation due to in-situ formation of boehmite which prevents Cu aggregation [62]. Furthermore, methane suppression in perovskites was also observed and was linked to the changes in chemical nature with B site ion substitution [63].

Table 2.1 Different formulation strategies for suppressing methanation in WGS catalysts

Catalyst	Active metal (wt%)	Promoter metal (wt%)	Metal size (nm)	T (°C)	GHSV (/h) or WHSV (ml/gcat.h)	TOF (s^{-1})	Rate (µmol/ gcat.s)	Reactant Composition (vol%)	Key Contributions	Ref.
Bimetallic										
Ni-Cu/CeO_2	Ni (0-10 wt%)	Cu (0-10 wt%)	12.0 - 16.3	300-500	GHSV = 68000 h^{-1}	0.007 - 0.014	At 350°C: 0.11 - 0.37 (µmol/ m2.s)	5% CO, 25% H2O, balance He	Ni-Cu alloy phase found to be active site and it can suppress methanation by enhancing CO adsorption, thus preventing CO dissociation.	[29]
Ni-Cu/$CeLaO_x$	Ni (4-20 wt%)	Cu (4-20 wt%)	14.0 - 37.0	150-400	WHSV = 60000 ml/gcat.h	-	At 275°C: 9.6 - 27.4	10% CO, 20% H_2O, balance He	Cu_4Ni_{16}/$CeLaO_x$ catalyst showed high activity and strongly inhibited methanation.	[30]
Ni-Cu/CeO_2	Ni (6-15 wt%)	Cu (15-24 wt%)	-	350-550	GHSV = 83665 h^{-1}	-	-	17.02% CO, 9.55% CO_2, 1.03% CH_4, 13.14% H_2, 55.20% H_2O, and 4.06 % N_2	NiCu(1: 4)-CeO_2 exhibited highest selectivity to CO_2 and H_2. Role of mesoporosity and bimetallic compositions in enhancing activity was proposed.	[31]
CuNi/Fe_2O_3	Ni (10 wt%)	Cu (10 wt%)	15-18	350-550	GHSV = 101000 h^{-1}	-	-	38% CO, 21.33% CO_2, 2.3% CH_4, 29.3% H_2, and 9.07% N_2, $H_2O/(CH_4 + CO + CO_2)$ ratio=2	Suppression of methanation attributed to the formation of surface CuNi alloy while high activity is due to increase in lattice strain and decrease in oxygen binding energy.	[32]
Re-Ni/CeO_2	Ni (1-10 wt%)	Re (1 wt%)	19.1 - 27.0	150-600	WHSV = 300000 ml/gcat.h	-	At 300°C: 2.80 - 30.0	5% CO, 10% H_2O, balance He	Re enhances dispersion of Ni oxide, promotes CO adsorption on Ni active sites and reduction of surface CeO_2, facilitating surface redox process, leading to	[33]

									enhanced WGSR rates with high selectivity.	
Ni-Fe/CeO_2-ZrO_2	Ni (0-5 wt%)	Fe (0-5 wt%)	10.3	200-450	GHSV = 10000 h^{-1}	-	-	9.65% CO, 35.7% H_2O, 6.43% CO_2, 38.6% H_2, balance N_2	Ni-Fe alloy weakens the strength of CO adsorption on Ni metal, thereby suppressing CO dissociation and subsequent methanation.	[34]
Ni-Fe-Al_2O_3	Ni (44 wt%)	Fe (42 wt%)	-	200-450	GHSV = 10000 h^{-1}	-	-	9.65% CO, 35.7% H_2O, 6.43% CO_2, 38.6% H_2, balance N_2	Ni-Fe alloy suppresses hydrogen adsorption, allowing WGS to proceed predominantly and suppressing methanation.	[35]
Pt-Ni/X , X= γ-Al_2O_3, SiO_2, TiO_2, CeO_2, ZrO_2	Pt (1.7 wt%)	Ni (1.5 wt%)	1.8 - 2.1	230-350	-	-	-	P_{H2O}=15 Torr, P_{CO}=10 Torr or P_{H2O}=10 Torr, P_{CO}=5 Torr	Higher activity in Pt-Ni catalyst due to change in CO binding energy on the Pt-Ni bimetallic catalyst. Extent of methanation inhibition on different supports (CeO_2<SiO_2~γ-Al_2O_3<HSA-ZrO_2~TiO_2) attributed to difference in densities of active hydroxyls.	[36]
Rh/Fe_2O3/ZrO_2	Rh (0.5 wt%)	Fe_2O_3 (3.57 wt%)	1.8-5.9	350-500	WHSV = 60000 ml/gcat.h (1 bar), 240000 ml/gcat.h (21 bar)	-	-	10% CO, 20% H_2O, 5% H_2, 5% CO_2, and balance N_2.	Methanation was relatively lower over Rh/Fe_2O_3/ZrO_2 compared to Rh/ZrO_2 and was attributed to the close contact between Rh and Fe_2O_3. Two mechanisms (i.e. redox on Fe_2O_3 and associative on Rh). Dominant pathway on Rh/Fe_2O_3/ZrO_2 was not proposed.	[37]

Alkali										
$Ni/xNa/CeO_2$	Ni (10 wt%)	Na = 0.5-10 wt%	4.9 - 26.5	300-600	GHSV = 68000 h^{-1}	0.46	-	5% CO, 25% H_2O, balance He	Methanation was inhibited by interaction between Na and Ni, leading to the absence of subcarbonyl species which are precursors of methanation.	This work
$Ni/xK/CeO_2$	Ni (10 wt%)	K = 0.5-10 wt%	9.0-23	300-600	GHSV = 68000 h^{-1}	-	34.3-36.0	5% CO, 25% H_2O, balance He	Addition of 5 wt% K was found to enhance reducibility of ceria and CO adsorption on Ni via formation of bridging carbonyls, thereby suppressing methanation.	This work
K/Ni	Ni (95 wt%)	K (5 wt%)	-	350	GHSV = 80000 h^{-1}	-	-	7.0% CO, 8.5% CO_2 , 22.0% H_2O, 37% H_2 and N_2 balance	K-modified Ni metal suppressed methanation through increased density of active hydroxyl group that reacts with CO adsorbed on the Ni metal to form the surface formates.	[45]
Ru/C	Ru (2 wt%)	K_2CO_3 = 0 - 10 wt%	3.8	200-325	WHSV = 12000 ml/gcat.h	-	-	20% H_2O, 10% CO, 70% N_2	Hydroscopicity of K_2CO_3 led to more water adsorbed around active sites, balancing the strong CO adsorption on active sites.	[46]
Cs/Ni/Fe	Ni (32-33 wt%)	Cs (3.9-6.0 wt %)	-	400	WHSV = 75000 ml/gcat.h	-	-	56.7% H_2, 10% CO, 26.7% H_2O, and 6.7% CO_2	Cs promotion increased amount of weakly basic sites which would enhance HTS activity through formate formation and selectivity against methanation.	[46]
Fe_2O_3–Al_2O_3–NiO–BaO	Fe/Al = 10, Fe/Ni = 5	3 wt.% Ba	6.8	300-500	WHSV = 30000 ml/gcat.h	-	-	30% CO, 60% H_2, 10% CO_2 (S/G ratio=0.3, 0.6)	Suppression of methanation by Ba addition related to increase in basic sites.	[48]

Core-shell										
$5Ni5Cu@CeO_2$	Ni (5 wt%)	Cu (5 wt%)	2.4-4.0	300-500	GHSV = 68000 h^{-1}	-	-	5% CO, 25% H2O, balance He	Core-shell structure enables high level of metal-support interaction, small bimetallic Ni-Cu particles size and high degree of lattice oxygen. Type I OH and strongly adsorbed CO are active reaction species.	[49]
Cu@Ni/ɣ-Al_2O_3, Ni@Cu/ɣ-Al_2O_3	Ni (5 wt%) Cu (5 wt%)	-	4.7 5.4	125-400	GHSV = 12500 - 25000 h^{-1}	-	-	10 % CO, 20 % H_2O	Cu component tends to segregate to the surface in Cu@Ni catalyst at elevated temperatures due to lower surface energy, thereby suppressing methanation.	[50]
$Pt@CeO_2$ $Pt@Ce_{0.67}Zr_{0.33}O_2$	Pt (5 wt%)	-	4.9 4.3	300-500	GHSV = 30000 h^{-1}	-	-	9.6% CO, 6.0% CO_2, 0.9% CH_4, 35.9% H_2, 38.5% H_2O, and 9.1% N_2	Methanation was suppressed even at 500 °C whereas methanation for impregnated Pt/CeO_2 catalysts. reached 11.3 %.	[51]
$PtAu@CeO_2$	Pt (5 wt%) Au (5wt%)	-	<2	200-500	GHSV=108 000 h^{-1}	-	-	0.77% CH_4, 6.15% CO, 7.68% CO_2, 24.99% H_2, 23.08% H_2O , balance N_2	Absence of methanation attributed to the covering of surface metal sites by thin layer of ceria, which would otherwise catalyze methanation.	[52-54]
Mixed-metal oxide										
$Ce_{1-x}Ni_xO_{2-y}$	Ni (10 wt%)	-	-	-	-	-	-	-	Strong Ni-Ce interaction through embedment prevents the formation of bulk-like Ni^0 particles, thereby inhibiting the formation of carbonaceous deposits that would block active sites. Formate-carbonate mechanism was proposed as main pathway.	[60]

Ni/CeO_2 (111)	Ni	-	-	-	-	-	-	-	Carbon species are strongly bound on Ni(111), however with Ni/CeO2(111), oxidative adsorption is preferred, leading to a Mars-van Krevelen mechanism which prevents coke formation.	[61]
Cu-Al	Cu (10-80 at%)	-	4.7-7.2	200-400	GHSV = 36201 h^{-1}	-	-	6.5% CO, 7.1% CO_2, 0.7% CH_4, 42.4% H_2, 28.7% H_2O, 14.5 % N_2.	Cu-Al exhibited complete selectivity to CO_2 without methanation. In-situ formation of boehmite prevents Cu aggregation and promotes catalyst stability.	[62]
$LaBO_3$ (B = Mn, Fe, Co)	Mn/Fe/Co	Pt (2-6 mol%)	-	250-400	GHSV = 5000 h^{-1}	-	-	37.9% H_2, 13.5% CO, 19.6% CO_2 and balance N2 , steam/CO=4.5	Methanation found to be suppressed in perovskites (e.g. Pt doped Co perovskite) and was linked to the change in chemical nature by B site ions substitution.	[63]

2.8 Reaction mechanisms

The mechanism of WGS reaction has been widely studied over the decades, and in general, they can be broadly classified into two main categories: (a) regenerative (redox) mechanism, and (b) associative (i.e. formate/carboxyl/carbonate) mechanism.

2.8.1 Redox mechanism

The redox mechanism is one in which the rate-determining step (RDS) involves reaction between a gaseous molecule of H_2O or CO with a surface species (surface oxygen atom or oxygen vacancy). It occurs via successive reduction and oxidation of the surface. In this redox mechanism, water dissociates to adsorbed O and adsorbed H completely, and the adsorbed O is then reacted with CO. The well-known two-step redox mechanism proposed by Temkin et al. is shown as follows in Eqs. 2.3 and 2.4:

$$CO + [O] \leftrightarrow CO_2 + [] \tag{2.3}$$

$$H_2O + [] \leftrightarrow H_2 + [O] \quad (RDS) \tag{2.4}$$

where [O] is an oxygen atom on the oxide surface; and [] is an oxygen anion vacant site on the surface caused by the removal of an oxygen atom. CO reduces the surface oxygen atom, and the oxygen vacancy is subsequently filled and oxidized by H_2O. The redox mechanism has been proposed as the dominant reaction pathway for high temperature and low temperature WGS reaction over different catalysts as shown below:

2.8.1.1 Copper-based catalyst

Several mechanistic studies on copper-based catalysts have been conducted on copper single crystal and supported copper catalyst. Beginning with copper single crystal, kinetic studies of atomic Cu (110) surface structure and Cu (111) were conducted by Nakamura et al. via ultra-high vacuum surface analysis techniques. Higher activity was observed with Cu (110) than Cu (111) due to the lower energy barrier required for cleavage of O-H bond in the rate-determining step of the surface redox mechanism [64]. Further studies were conducted on Cu (111) surface by Datta et al. who developed a UBI-QEP (unity bond index-quadratic exponential potential) microkinetic model for energetics prediction of the elementary step in the reaction [65, 66]. From their microkinetic modeling on Cu catalyst, it was revealed that formate and associative reaction mechanisms were dominant at lower temperature, while at higher temperature, modified redox mechanism was dominant.

Besides the two-step redox mechanism proposed by Temkin et al., an eight-step redox mechanism has also been postulated by Ovesen et al. [67] using single crystal studies on copper which was validated with kinetic data for supported Cu-based catalyst, and is illustrated as follows in **Table 2.2**:

:

Table 2.2 Redox mechanism

Step No.	Elementary Step
1.	$H_2O + * \leftrightarrow H_2O^*$
2	$H_2O^* + * \leftrightarrow OH^* + H^*$
3.	$2OH^* \leftrightarrow H_2O^* + O^*$
4.	$OH^* + * \leftrightarrow O^* + H^*$
5.	$H^* + H^* \leftrightarrow H_2 + 2*$
6.	$CO + * \leftrightarrow CO^*$
7.	$CO^* + O^* \leftrightarrow CO_2^* + *$
8.	$CO_2^* \leftrightarrow CO_2 + *$

where "*" refers to an adsorption site which can be located either on the support or the metal oxide and X* denotes an adsorbed X species.

In their study, it was highlighted that the nature of catalyst support can affect the reaction mechanism and that the effect of product inhibition on the mechanism should be taken into consideration. Indeed, it was revealed by Koryabkina et al. that the product gas posed a strong inhibition on the forward WGS reaction rates and the rate-determined step was proposed to be the reduction of surface oxygen by adsorbed CO [68]. In addition, Cu/SiO_2 catalyst prepared via atomic layer epitaxy technique was also found to possess defect site on Cu nanoparticles and followed the redox mechanism [69]. Likewise, density-functional theory (DFT) calculations conducted on Cu/TiO_2(110) catalyst also indicated the dominance of the redox mechanism and that Cu cluster decreased the barrier for CO oxidation [70]. The role of ceria as a support in affecting the mechanism in Cu-based catalysts was also studied. Kinetic analysis was conducted on Cu/Ce/Al catalyst by Quiney et al. and the two-step redox model

suggested that ceria lowered the activation energy for water dissociation [71]. Similarly, a co-operative redox mechanism was proposed by Li et al. for atomic Cu cluster deposited on Ce(La)Ox catalyst wherein CO adsorbed on Cu cluster was oxidized by oxygen from metal interface by ceria followed by rejuvenation of the ceria oxygen vacancy by water [72].

2.8.1.2 Nickel-based catalyst

Nickel supported on ceria has been proven to achieve excellent activity especially at high temperatures. Addition of promoters, such as Re, has been claimed to promote redox mechanism on Ni/CeO_2 catalysts by enhancing CO adsorption on Ni active sites [33]. Mixed metal oxide formed from Ni ionic substitution into ceria has also been reported to follow redox mechanism due to activation and increased mobility of ceria lattice oxygen [46, 73]. Besides experimental studies, DFT calculations conducted on Co-, Fe- and Ni-MoS_2 catalysts also revealed that the redox mechanism was kinetically preferred on Mo, Fe and Co while both redox and carboxyl mechanisms were possible for Ni [74].

2.8.2 Associative mechanism

Generally, there are three main active reaction intermediates proposed in the associative mechanism; namely, formate (HCOO), carboxyl (COOH) and carbonate (CO_3). These mechanisms will be briefly discussed in the following sub-sections.

2.8.2.1 Formate mechanism

The formate mechanism has been largely proposed to be the dominant reaction mechanism for low temperature WGS reaction, particularly on Pt-based, Rh-based and metal oxide catalysts. Important steps involved in the formate mechanism include: (i) dissociation of adsorbed water to form surface hydroxyl groups and hydride species, (ii) reaction between adsorbed CO with surface hydroxyl groups to form surface formate species, (iii) decomposition of surface formates into gaseous CO_2 and surface hydride, and (iv) combination of two surface hydride species to form gaseous H_2. The elementary steps involved in the formate mechanism are outlined in **Table 2.3** [75].

2.8.2.1.1 Metal oxide catalyst

Formate species generated during WGS reaction were first identified with infrared spectroscopy on ZnO and MgO catalysts. Ueno et al. proposed the rate-determining steps on ZnO and MgO to be formate decomposition and dehydrogenation of formates, respectively [76]. Later, Shido et al. further investigated the reaction mechanism on MgO and inferred that in the presence of water, bridge-type formates evolved from unidentate formates, followed by formate decomposition into H_2 and CO_2 via electronic interaction between formate and adsorbed water [77]. Furthermore, Shido et al. also studied the ZnO system and discovered that water not only served as a reactant for formate formation, but also functioned as an activator for decomposition of bidentate formate into H_2 and unidentate carbonate, which later desorbed as CO_2 [78]. However, the promotional effect of reactant on formate decomposition was not

observed on CeO_2 surfaces. Additionally, reaction mechanism on Co-Mn, Co-Cr and Cu-Mn oxide catalysts were also found to proceed via formate mechanism by Hutchings et al. [79, 80].

2.8.2.1.2 Rhodium-based and Platinum-based catalysts

Formate intermediates were first discovered on supported metal catalysts by Shido and Iwasawa [81] who investigated the WGS reaction over Rh/CeO_2 catalyst. A formate mechanism with the schematic as illustrated below in **Figure 2.3** was proposed:

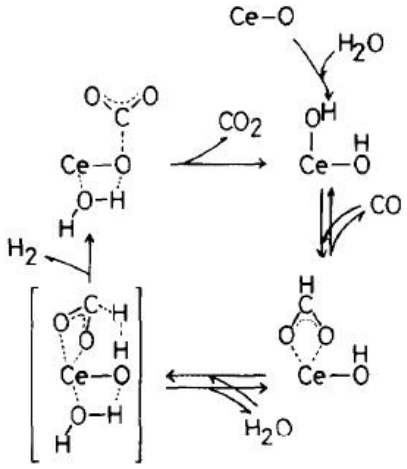

Figure 2-3 Bidentate formate mechanism proposed by Shido and Iwasawa [81].

Their results indicated that the reduction of the ceria surface generated surface geminal hydroxyl (OH) groups, formed by dissociation of H_2O on the oxygen vacancies of partially reduced CeO_2. The adsorbed OH groups then reacts with CO to produce bidentate formates (HCOO), which then decomposed to H_2 and unidentate carbonate, prior to the production of CO_2. Using in-situ DRIFTS studies, Jacob et al. have also shown that formate species are important reaction

intermediates with formation decomposition (i.e. cleavage of C-H) bond as the rate-determining step for Pt-based catalysts supported on CeO_2, Th and ZrO_2 [44, 82-86]. Incorporation of alkali ions such as Na or K in Pt-based catalysts was found to increase catalytic activity by modifying the electronic properties and weakening of C-H bond in formates for easier cleavage of C-H bond [41, 43]. Furthermore, it was discovered that mono-coordinated hydroxyl groups on ZrO_2 support react with CO to form formate intermediates whereas multi-coordinated hydroxyls are responsible for formate decomposition [87].

2.8.2.1.3 Gold-based catalyst

Transient experiments involving CO and H_2O pulse injection revealed that Au/CeO_2 catalyst proceed via formate mechanism over the perimeter interfaces of Au nanoparticles on reduced CeO_2 surface [88]. This was further substantiated by Leppelt et al. who also proposed formate formation on the interface between Au and CeO_2 surface [89, 90]. Furthermore, Jacobs et al. proposed hydrogen spillover from the metal to ceria surface to generate type II bridging OH which reacts with CO in formate formation on Au/CeO_2 catalyst [91]. In addition, a more balanced view was proposed by Burch et al. in his review on Au catalyst, in which the dominant reaction mechanism was suggested to be dependent on the reaction temperature. At low temperature, carbonate or carboxylate and formate mechanisms are prevailing while at high temperature, redox mechanism is dominant [92]. From the above-mentioned studies, it is evident that the rate determining step in formate mechanism is formate decomposition with the aid of co-adsorbed water and this mechanism predominantly occurs at low temperatures.

Table 2.3 Formate mechanism

Step No.	Elementary Step
1.	$CO + * \leftrightarrow CO^*$
2.	$H_2O + * \leftrightarrow H_2O^*$
3.	$H_2O * + \ * \leftrightarrow OH^* + H^*$
4.	$OH^* + * \leftrightarrow \ O^* + H^*$
5.	$CO^* + \ O^* \ \leftrightarrow CO_2^*$
6.	$CO^* + \ OH^* \ \leftrightarrow HCOO^* + *$
7.	$CO^* + \ OH^* \ \leftrightarrow CO_2^* + H^*$
8.	$HCOO^* + * \leftrightarrow CO_2^* + \ H^*$
9.	$HCOO^* + O^* \leftrightarrow CO_2^* + \ OH^*$
10.	$HCOO^* + \ OH^* \ \leftrightarrow CO_2^* + \ H_2O^*$
11.	$HCOO^* + \ H^* \ \leftrightarrow CO_2^* + \ H_2^*$
12.	$H_2O^* + \ O^* \ \leftrightarrow 2OH^*$
13.	$H_2O^* + \ H^* \ \leftrightarrow OH^* + \ H_2^*$
14.	$CO_2^* \leftrightarrow CO_2 + *$
15.	$H^* + H^* \leftrightarrow H_2^*$
16.	$H_2^* \leftrightarrow H_2 + *$

2.8.2.2 Carboxyl mechanism

Lately, carboxyl mechanism is proposed for low-temperature WGS reaction on Cu-, Pt-, and Au-based catalysts. In this mechanism, the formation of carboxyl (COOH) intermediate species from the reaction between adsorbed CO and adsorbed OH is the dominant step. As compared to the formate mechanism discussed earlier, the main difference between these two mechanisms lies in the intermediate species formed during the reaction. In carboxyl mechanism, hydrogen in carboxyl (COOH) species is bonded to oxygen. In contrast, in formate mechanism, hydrogen in formate (HCOO) species is attached to carbon.

The possible elementary steps involved in the carboxyl mechanism are presented in **Table 2.4** [75].

2.8.2.2.1 Copper-based catalyst

Carboxyl, as a new reactive intermediate which plays dominant role in WGS, was first identified by Dumesic and co-workers for low-temperature WGS reaction catalyzed by Cu (111) [93]. The detailed Density Functional Theory (DFT) calculations considered the thermochemistry and activation energy barriers for all the reaction elementary steps in the newly proposed carboxyl mechanism. In the COOH-mediated WGS route, surface OH (rather than atomic O) directly oxidizes CO to form COOH. Formate (HCOO), which is an isomer of COOH, is formed from reaction between CO_2 and H and acts as a spectator species which has a tendency to block active sites. Subsequently, a microkinetic analysis was conducted by the same group and a catalytic cycle comprising of eight elementary reactions was proposed [75]. Through kinetic modeling, it was predicted that formate species formed via hydrogenation of carbon dioxide were the most abundant surface species. However, these species are spectator species which do not participate in the catalytic cycle.

2.8.2.2.2 Gold-based catalyst

Density functional theory (DFT) calculations were conducted by Liu and Rodriguez to investigate WGS reaction on Au_{29} and Cu_{29} nanoparticles using $Au/CeO_2(111)$ and $Cu/CeO_2(111)$ as model catalysts [94]. For comparison purposes, Au(100) and Cu(100) surfaces were also included in the study. Based on DFT calculations, WGS was found to proceed on these catalysts via either

associative carboxyl or redox mechanisms with water dissociation as the common rate-limited step. Redox mechanism was found to be dominant for Cu(100) while associative carboxyl mechanism was dominant for Au(100), Au_{29} and Cu_{29}. In addition, the WGS activity was revealed to decrease in the following order: Cu_{29}>Cu(100)>Cu_{29}>Au(100).

2.8.2.2.3 Platinum-based catalyst

WGS kinetics over μ-structured $Pt/CeO_2/Al_2O_3$ catalysts were investigated by Germani and Schuurman [95], and the reaction rate was found to be zero order with respect to carbon monoxide and strongly inhibited by hydrogen. The kinetic data was best described with a dual-site mechanism, with Pt as the adsorption site for carbon monoxide and ceria as the adsorption site for water. Particularly, it was revealed that the rate-determining step involved the formation of a complex between a carboxyl species and a hydroxyl group which decomposes over active Pt site into carbon dioxide and hydrogen. Besides the investigation on Cu-based catalysts, Dumesic's group also conducted periodic DFT calculations on Pt(111) [96]. Similarly, the derived microkinetic model revealed that the WGS reaction on Pt(111) proceeds via carboxyl mechanism and formate, which was observed experimentally, acts as spectator specie. More recently, the associative carboxyl pathways of the WGS reaction on Pt/CeO_2(111) interface were investigated by Aranifard et al. using periodic DFT calculations [97, 98]. The unique activity of Pt/CeO_2 catalysts were discovered to be best described by the associative carboxyl pathway with redox generation in which oxygen vacancy is created

during the catalytic cycle and the oxygen vacancy serves to stabilize the –COOH and –CO_2 intermediates.

Table 2.4 Carboxyl mechanism

Step No.	Elementary Step
1.	$CO + * \leftrightarrow CO^*$
2	$H^* + H^* \leftrightarrow H_2 + 2*$
3.	$H_2O + * \leftrightarrow H_2O^*$
4.	$CO_2^* \leftrightarrow CO_2 + *$
5.	$H_2O * + \ * \leftrightarrow OH^* + H^*$
6.	$CO^* + OH^* \leftrightarrow COOH_{cis}^* + *$
7.	$COOH_{trans}^* + OH^* \leftrightarrow CO_2^* + H_2O^*$
8.	$COOH_{cis}^* \leftrightarrow COOH_{trans}^*$

2.8.2.3 Carbonate mechanism

The carbonate mechanism was first proposed by Millar et al. based on experimental IR spectroscopy results which showed a band corresponding to "symmetrical" carbonate ion on the Cu/SiO_2 catalyst surface [99]. Through IR spectroscopy, it was suggested that CO was produced after pre-oxidation and the subsequent CO oxidation on Cu proceeded via polydentate carbonates. The carbonate mechanism (as tabulated in **Table 2.5**) was also investigated on the WGS reaction conducted over Fe-Cr catalyst in a catalytic membrane reactor by Lund et al. and the formation of intermediate species was found to temperature dependent [100]. Operando steady-state isotopic transient kinetic analysis (SSITKA) coupled with diffuse reflectance infrared Fourier transform spectroscopy (DRIFTS) were also employed to investigate the mechanism on inverse CeO_2/CuO catalyst [101]. Through isotopic exchange, formates were

excluded as intermediates under the reaction conditions used while carbonates, in particular, bi- or tri-dentate carbonates were suggested as active intermediates on the basis that their rate of formation were similar to that of the corresponding CO_2 products.

Table 2.5 Carbonate mechanism

Step No.	Elementary Step
1.	$CO + 2O^* \leftrightarrow CO_3^{**}$
2	$CO_3^{**} \leftrightarrow CO_3^* + *$
3.	$CO_3^* \leftrightarrow CO_2 + O^*$
4.	$H_2O + * \leftrightarrow H_2O^*$
5.	$H_2O * + O^* \leftrightarrow 2OH^*$
6.	$2OH^* \leftrightarrow 2O^* + H_2$
7.	$H_2O^* + * \leftrightarrow OH^* + H^*$
8.	$2H^* \leftrightarrow H_2 + 2*$

2.8.3 Mechanism of methanation

As emphasized earlier, the key objectives of this research focus on the development of highly selective Ni-based catalyst for the WGS reaction. Methanation, which is a highly undesirable side reaction, decreases the H_2 yield obtained through the WGS reaction. Hence, in this section, the mechanism of methanation will be briefly discussed to shed some light on how this side reaction occurs concurrently with the WGS reaction.

Methanation of CO over Ni ($CO+3H_2 \rightarrow CH_4+H_2O$) can be largely classified into two broad categories [102]: (a) the formyl chain mechanism, and (b) the surface carbide mechanism, as shown in **Figure 2.4** and **Figure 2.5**. In the

formyl chain mechanism, the chemisorbed formyl radicals are formed from chemisorbed CO or H_2, which then undergoes a chain reaction for generating CH_4. On the other hand, the surface carbide mechanism proceeds via a dissociation of CO (on Ni) into chemisorbed C and O species at temperatures above 450K. The adsorbed carbon can then be converted into CH_4 by reacting with H_2.

Figure 2-4 The formyl chain mechanism

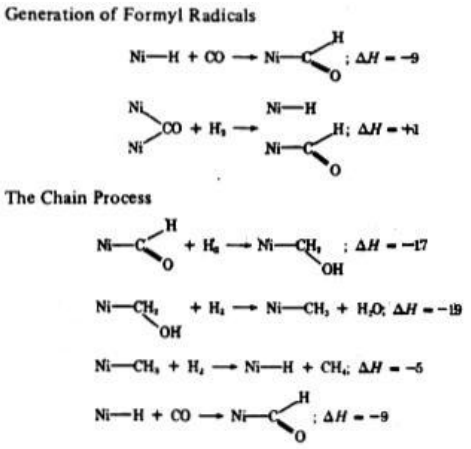

Figure 2-5 The surface carbide mechanism

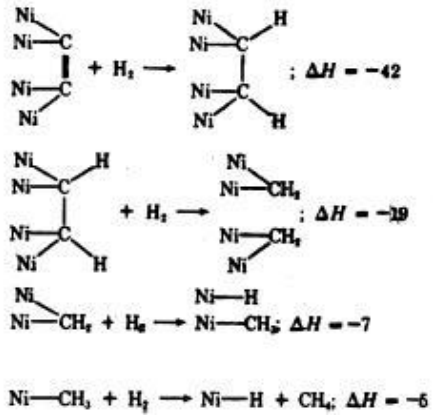

During WGS reaction, both mechanisms are possible at low steam to CO ratios [52]. However, with the utilization of high steam to CO ratios, methanation is likely to occur via the formyl chain mechanism as compared to the surface carbide due to the lower tendency of carbon deposition in the presence of large amount of steam. Therefore, in a bid to suppress methanation, the developed catalyst should present a high energy barrier for CO dissociation – a reaction step that takes place in both pathways – to occur.

2.9 Kinetic models

Kinetic models provide insights to the rate of the reaction and are essential in the design of reactors. Various kinetic models have been proposed for WGS reaction mechanisms. Generally, a simple power law model (Eq. 2.5) in the following form is used to present to kinetic rate of WGS reaction:

$$r = k_f[P_{CO}]^a[P_{H2O}]^b[P_{CO2}]^c[P_{H2}]^d(1-\beta) \quad (2.5)$$

where $\beta = ([P_{CO2}][P_{H2}])/(K[P_{CO}][P_{H2O}])$ is the approach to equilibrium. To ensure that the reaction was conducted away from equilibrium, the values of β are usually maintained below 0.2. Even though the power law model offers a rough estimation of the reaction order of the reactant and products in affecting the on reaction rate, the disadvantage of utilizing such empirical model lies in the lack of information about the reaction mechanism of the catalyst. As discussed in the earlier section on reaction mechanisms, a detailed microkinetic study encompassing elementary steps based on the Eley-Rideal model or Langmuir-Hinshelwood model would have to be performed in order to gain a holistic view of the catalyst reaction mechanism. **Table 2.6** summarizes the power law parameters for various WGS catalysts reported in recent literature.

Table 2.6 Power law parameters for various WGS catalysts

Catalyst	T (°C)	E_a (kJ/mol)	Reaction order				Ref.
			CO	**H_2O**	**CO_2**	**H_2**	
Fe_2O_3-Cr_2O_3-CuO	450	88	0.9	0.3	-0.2	-0.1	[103]
$La_{0.7}Ce_{0.2}FeO_{2.85}$	550	86	0.8	0.0	-0.2	0.0	[104]
10at%Cu-Ce(30at%La)O_x	450	70	0.8	0.2	-0.3	-0.3	[105]
10at%Cu-Ce(8at%La)O_x	300	60	0.8	0.5	-0.5	-0.4	[105]
8%CuO-CeO_2	240	56	0.9	0.4	-0.6	-0.6	[68]
8%CuO-Al_2O_3	200	62	0.9	0.8	-0.7	-0.8	[68]
8%CuO-15%CeO_2-Al_2O_3	200	32	0.7	0.6	-0.6	-0.6	[68]
40%CuO/ZnO/Al_2O_3	190	79	0.8	0.8	-0.9	-0.9	[68]
2%Pd2%Zn/Al_2O_3	280	75	0.3	0.6	-0.1	-0.4	[106]
1%Pd/CeO_2	200	-	0.0	0.5	0.5	-1.0	[107]
2%Pt/CeO_2-ZrO_2	210	71	0.1	0.7	-0.2	-0.6	[108]
2%Pt-1%Re/CeO_2-ZrO_2	210	71	-0.1	0.9	-0.1	-0.3	[108]
1%Pt/Al_2O_3	315	84	0.1	1.1	-0.1	-0.5	[109]
1%Pt/CeO_2	200	75	-0.1	0.5	-0.1	-0.4	[109]
0.5%Pt-0.5%Re/TiO_2	300	30	0.4	0.7	0.0	-0.4	[110]
0.5%Pt/TiO_2	210	11	0.5	1.0	0.0	-0.7	[111]

2.10 References

[1] C. Ratnasamy, J.P. Wagner, Catal. Rev., 51 (2009) 325.
[2] J.R. Ladebeck, J.P. Wagner, in: W. Vielstich, H.A. Gasteiger, A. Lamm, H. Yokokawa (Eds.) Handbook of Fuel Cells – Fundamentals, Technology and Applications., John Wiley & Sons, Ltd., 2010.
[3] J.C. Gonzalez, M.G. Gonzalez, M.A. Laborde, N. Moreno, Applied Catalysis 20 (1986) 3.
[4] M.A. Edwards, D.M. Whittle, C. Rhodes, A.M. Ward, D. Rohan, M.D. Shannon, G.J. Hutchings, C.J. Kiely, PCCP, 4 (2002) 3902.
[5] G.C. Chinchen, R.H. Logan, M.S. Spencer, Applied Catalysis, 12 (1984) 69.
[6] G.C. Chinchen, R.H. Logan, M.S. Spencer, Applied Catalysis, 12 (1984) 89.
[7] G.C. Chinchen, R.H. Logan, M.S. Spencer, Applied Catalysis, 12 (1984) 97.
[8] S. Natesakhawat, X.W.L. Zhang, U.S. Ozkan, Journal of Molecular Catalysis A: Chemical, 260 (2006) 82.
[9] A. Andreev, V. Idakiev, D. Mihajlova, D. Shopov, Applied Catalysis, 22 (1986) 385.
[10] P. Kappen, J.-D. Grunwaldt, B.S. Hammershøi, L. Troger, B.S. Clausen, J. Catal., 198 (2001) 56.
[11] C. Pellerin, S.M. Booker, Environ. Health Perspect., 108 A402.
[12] L. Zhang, X. Wang, J.-M.M. Millet, P.H. Matter, U.S. Ozkan, Appl. Catal. A, 351 (2008) 1.
[13] P. Gawade, B. Mirkelamoglu, B. Tan, U.S. Ozkan, Journal of Molecular Catalysis A: Chemical, 321 (2010) 61.
[14] J.L.R. Costa, G.S. Marchetti, M.d.C. Rangel, Catal. Today, 77 (2002) 205.
[15] M.J.L. Gines, N. Amadeo, M. Laborde, C.R. Apesteguia, Appl. Catal. A, 131 (1995) 283.
[16] D. Andreeva, I. Ivanov, L. Ilieva, M.V. Abrashev, Appl. Catal. A, 302 (2006) 127.
[17] G. Jacobs, U.M. Graham, E. Chenu, P.M. Patterson, A. Dozier, B.H. Davis, Journal of Catalysis, 229 (2005) 499.
[18] D. Pierre, W. Deng, M. Flytzani-Stephanopoulos, Topics in Catalysis, 46 (2007) 363.
[19] M. Laniecki, M. Ignacik, Catal. Today, 116 (2006) 400.
[20] L.D. Morpeth, Y. Sun, S.S. Hla, D. French, G.J. Duffy, J.H. Edwards, Int. J. Hydrogen Energ, 37 (2012) 1475.
[21] I. Valsamakis, M. Flytzani-Stephanopoulos, Appl. Catal. B, 106 (2011) 255.
[22] J. Xu, G.F. Froment, AIChE Journal, 35 (1989) 88.
[23] J.M. García-Vargas, J.L. Valverde, A. de Lucas-Consuegra, B. Gómez-Monedero, P. Sánchez, F. Dorado, Appl. Catal. A, 431-432 (2012) 49.
[24] I. Czekaj, F. Loviat, F. Raimondi, J. Wambach, S. Biollaz, A. Wokaun, Appl. Catal. A, 329 (2007) 68.
[25] D. Hu, J. Gao, Y. Ping, L. Jia, P. Gunawan, Z. Zhong, G. Xu, F. Gu, F. Su, Ind. Eng. Chem. Res., 51 (2012) 4875.
[26] S.H. Kim, S.-W. Nam, T.-H. Lim, H.-I. Lee, Appl. Catal. B, 81 (2008) 97.

[27] Y.S. Mok, H.C. Kang, H.J. Lee, D.J. Koh, D.N. Shin, Plasma Chem. Plasma P., 30 (2010) 437.
[28] J. Sehested, S. Dahl, J. Jacobsen, J.R. Rostrup-Nielsen, J. Phys. Chem. B, 109 (2005) 2432.
[29] E.T. Saw, U. Oemar, X.R. Tan, Y. Du, A. Borgna, K. Hidajat, S. Kawi, J. Catal., 314 (2014) 32.
[30] J.-H. Lin, P. Biswas, V.V. Guliants, S. Misture, Appl. Catal. A, 387 (2010) 87.
[31] A. Jha, D.-W. Jeong, W.-J. Jang, C.V. Rode, H.-S. Roh, RSC Advances, 5 (2015) 1430.
[32] A. Jha, D.-W. Jeong, J.-O. Shim, W.-J. Jang, Y.-L. Lee, C.V. Rode, H.-S. Roh, Catal. Sci. Technol., 5 (2015) 2752.
[33] T.S. Kingkaew Chayakul, Sunantha Hengrasmee, Catal. Today, 175 (2011) 420.
[34] K. Watanabe, T. Miyao, K. Higashiyama, H. Yamashita, M. Watanabe, Catal. Commun., 12 (2011) 976.
[35] K. Watanabe, T. Miyao, K. Higashiyama, H. Yamashita, M. Watanabe, Catal. Commun., 10 (2009) 1952.
[36] T. Wang, M.D. Porosoff, J.G. Chen, Catal. Today, 233 (2014) 61.
[37] A.A. Hakeem, R. S. Vásquez, J. Rajendran, M. Li, R.J. Berger, J.J. Delgado, F. Kapteijn, M. Makkee, J. Catal., 313 (2014) 34.
[38] Y. Wang, Y. Zhai, D. Pierre, M. Flytzani-Stephanopoulos, Appl. Catal. B, 127 (2012) 342.
[39] Y. Zhai, D. Pierre, R. Si, W. Deng, P. Ferrin, A.U. Nilekar, G. Peng, J.A. Herron, D.C. Bell, H. Saltsburg, M. Mavrikakis, M. Flytzani-Stephanopoulos, Science, 329 (2010) 1633.
[40] B. Zugic, D.C. Bell, M. Flytzani-Stephanopoulos, Appl. Catal. B, 144 (2014) 243.
[41] H. Evin, G. Jacobs, J. Ruiz-Martinez, G. Thomas, B. Davis, Catal. Lett., 120 (2008) 166.
[42] G. Jacobs, T.K. Das, Y. Zhang, J. Li, G. Racoillet, B.H. Davis, Appl. Catal. A, 233 (2002) 263.
[43] L.Z. Linganiso, G. Jacobs, K.G. Azzam, U.M. Graham, B.H. Davis, D.C. Cronauer, A.J. Kropf, C.L. Marshall, Appl. Catal. A, 394 (2011) 105.
[44] J.M. Pigos, C.J. Brooks, G. Jacobs, B.H. Davis, Appl. Catal. A, 328 (2007) 14.
[45] K.-R. Hwang, C.-B. Lee, J.-S. Park, J. Power Sources, 196 (2011) 1349.
[46] V.M. Shinde, G. Madras, Appl. Catal. B, 123-124 (2012) 367.
[47] J.Y. Lee, D.-W. Lee, M.S. Lee, K.-Y. Lee, Catal. Commun., 15 (2011) 37.
[48] F. Meshkani, M. Rezaei, Catal. Commun., 58 (2015) 26.
[49] E.T. Saw, U. Oemar, M.L. Ang, K. Hidajat, S. Kawi, ChemCatChem, (2015) n/a.
[50] J.-H. Lin, V.V. Guliants, Appl. Catal. A, 445-446 (2012) 187.
[51] B. Liu, H. Xu, Z. Zhang, Catal. Commun., 26 (2012) 159.
[52] C.M.Y. Yeung, S.C. Tsang, J. Phys. Chem. C, 113 (2009) 6074.
[53] C.M.Y. Yeung, S.C. Tsang, Catal. Lett., 128 (2009) 349.

[54] C.M.Y. Yeung, S.C. Tsang, Journal of Molecular Catalysis A: Chemical, 322 (2010) 17.
[55] M. Cargnello, T. Montini, S. Polizzi, N.L. Wieder, R.J. Gorte, M. Graziani, P. Fornasiero, Dalton Transactions, 39 (2010) 2122.
[56] N.L. Wieder, M. Cargnello, K. Bakhmutsky, T. Montini, P. Fornasiero, R.J. Gorte, J. Phys. Chem. C, 115 (2011) 915.
[57] L. Arroyo-Ramírez, C. Chen, M. Cargnello, C.B. Murray, R.J. Gorte, Catal. Today, 253 (2015) 137.
[58] M. Cargnello, M. Grzelczak, B. Rodríguez-González, Z. Syrgiannis, K. Bakhmutsky, V. La Parola, L.M. Liz-Marzán, R.J. Gorte, M. Prato, P. Fornasiero, J. Am. Chem. Soc., 134 (2012) 11760.
[59] J.-H. Lin, V.V. Guliants, Appl. Catal. A, 445–446 (2012) 187.
[60] L. Barrio, A. Kubacka, G. Zhou, M. Estrella, A. Martínez-Arias, J.C. Hanson, M. Fernández-García, J.A. Rodriguez, J. Phys. Chem. C, 114 (2010) 12689.
[61] J. Carrasco, L. Barrio, P. Liu, J.A. Rodriguez, M.V. Ganduglia-Pirovano, J. Phys. Chem. C, 117 (2013) 8241.
[62] R.B. Mane, D.-W. Jeong, A.V. Malawadkar, H.-S. Roh, C.V. Rode, ChemCatChem, 6 (2014) 1698.
[63] T. Rajesh, A. Upadhyay, A.K. Sinha, S.K. Deb, R.N. Devi, Journal of Molecular Catalysis A: Chemical, 395 (2014) 506.
[64] J. Nakamura, J.M. Campbell, C.T. Campbell, J. Chem. Soc., Faraday Trans., 86 (1990) 2725.
[65] C. Callaghan, I. Fishtik, R. Datta, M. Carpenter, M. Chmielewski, A. Lugo, Surf. Sci., 541 (2003) 21.
[66] I. Fishtik, R. Datta, Surf. Sci., 512 (2002) 229.
[67] C.V. Ovesen, P. Stoltze, J.K. Norskov, C.T. Campbell, J. Catal., 134 (1992) 445.
[68] A.A.P. N.A. Koryabkina, W.F. Ruettinger, R.J. Farrauto, and F.H. Ribeiro, J. Catal., 217 (2003) 233.
[69] C.-S. Chen, T.-W. Lai, C.-C. Chen, J. Catal., 273 (2010) 18.
[70] S.-F. Peng, J.-J. Ho, PCCP, 13 (2011) 20393.
[71] A.S. Quiney, Y. Schuurman, Chem. Eng. Sci., 62 (2007) 5026.
[72] Y. Li, Q. Fu, M. Flytzani-Stephanopoulos, Appl. Catal. B, 27 (2000) 179.
[73] V.M. Shinde, G. Madras, Appl. Catal. B, 132-133 (2013) 28.
[74] Y.-Y. Chen, M. Dong, J. Wang, H. Jiao, J. Phys. Chem. C, 116 (2012) 25368.
[75] R.J. Madon, D. Braden, S. Kandoi, P. Nagel, M. Mavrikakis, J.A. Dumesic, J. Catal., 281 (2011) 1.
[76] A. Ueno, T. Onishi, K. Tamaru, Transactions of the Faraday Society, 66 (1970) 756.
[77] T. Shido, K. Asakura, Y. Iwasawa, J. Catal., 122 (1990) 55.
[78] T. Shido, Y. Iwasawa, J. Catal., 129 (1991) 343.
[79] G.J. Hutchings, R.G. Copperthwaitet, F.M. Gottschalk, R. Hunter, J. Mellor, S.W. Orchard, T. Sangiorgio, J. Catal., 137 (1992) 408.

[80] G.J. Hutchings, F. Gottschalk, R. Hunter, S.W. Orchard, J. Chem. Soc., Faraday Trans., 85 (1989) 363.
[81] T. Shido, Y. Iwasawa, J. Catal., 141 (1993) 71.
[82] G. Jacobs, E. Chenu, P.M. Patterson, L. Williams, D.E. Sparks, G.A. Thomas, B.H. Davis, Appl. Catal. A, 258 (2004) 203.
[83] G. Jacobs, B.H. Davis, Appl. Catal. A, 333 (2007) 192.
[84] G. Jacobs, U.M. Graham, E. Chenu, P.M. Patterson, A. Dozier, B.H. Davis, J. Catal., 229 (2005) 499.
[85] G. Jacobs, P.M. Patterson, U.M. Graham, D.E. Sparks, B.H. Davis, Appl. Catal. A, 269 (2004) 63.
[86] G. Jacobs, P.M. Patterson, L. Williams, E. Chenu, D. Sparks, G. Thomas, B.H. Davis, Appl. Catal. A, 262 (2004) 177.
[87] P.O. Graf, D.J.M. de Vlieger, B.L. Mojet, L. Lefferts, J. Catal., 262 (2009) 181.
[88] H. Sakurai, T. Akita, S. Tsubota, M. Kiuchi, M. Haruta, Appl. Catal. A, 291 (2005) 179.
[89] A. Karpenko, R. Leppelt, V. Plzak, R.J. Behm, J. Catal., 252 (2007) 231.
[90] B.S. R. Leppelt, V. Plzak, M. Kinne, R. Behm, J. Catal., 244 (2006) 137.
[91] G. Jacobs, S. Ricote, P.M. Patterson, U.M. Graham, A. Dozier, S. Khalid, E. Rhodus, B.H. Davis, Appl. Catal. A, 292 (2005) 229.
[92] R. Burch, PCCP, 8 (2006) 5483.
[93] A.A. Gokhale, J.A. Dumesic, M. Mavrikakis, J. Am. Chem. Soc., 130 (2008) 1402.
[94] P. Liu, J.A. Rodriguez, J. Chem. Phys., 126 (2007) 164705.
[95] G. Germani, Y. Schuurman, AIChE Journal, 52 (2006) 1806.
[96] L.C. Grabow, A.A. Gokhale, S.T. Evans, J.A. Dumesic, M. Mavrikakis, J. Phys. Chem. C, 112 (2008) 4608.
[97] S. Aranifard, S.C. Ammal, A. Heyden, J. Phys. Chem. C, 118 (2014) 6314.
[98] S. Aranifard, S.C. Ammal, A. Heyden, J. Catal., 309 (2014) 314.
[99] G.J. Millar, C.H. Rochester, C. Howe, K.C. Waugh, Mol. Phys., 76 (1992) 833.
[100] D. Ma, C.R.F. Lund, Ind. Eng. Chem. Res., 42 (2003) 711.
[101] A.L. Cámara, S. Chansai, C. Hardacre, A. Martínez-Arias, Int. J. Hydrogen Energ, 39 (2014) 4095.
[102] W.A. Goddard, S.P. Walch, A.K. Rappe, T.H. Upton, C.F. Melius, Journal of Vacuum Science & Technology, 14 (1977) 416.
[103] S.S. Hla, D. Park, G.J. Duffy, J.H. Edwards, D.G. Roberts, A. Ilyushechkin, L.D. Morpeth, T. Nguyen, Chem. Eng. J., 146 (2009) 148.
[104] S.S. Hla, Y. Sun, G.J. Duffy, L.D. Morpeth, A. Ilyushechkin, A. Cousins, D.G. Roberts, J.H. Edwards, Int. J. Hydrogen Energ, 36 (2011) 518.
[105] X. Qi, M. Flytzani-Stephanopoulos, Ind. Eng. Chem. Res., 43 (2004) 3055.
[106] L. Bollmann, J.L. Ratts, A.M. Joshi, W.D. Williams, J. Pazmino, Y.V. Joshi, J.T. Miller, A.J. Kropf, W.N. Delgass, F.H. Ribeiro, J. Catal., 257 (2008) 43.
[107] S. Hilaire, X. Wang, T. Luo, R.J. Gorte, J. Wagner, Appl. Catal. A, 258 (2004) 271.

[108] R. Radhakrishnan, R.R. Willigan, Z. Dardas, T.H. Vanderspurt, Appl. Catal. B, 66 (2006) 23.
[109] A.A. Phatak, N. Koryabkina, S. Rai, J.L. Ratts, W. Ruettinger, R.J. Farrauto, G.E. Blau, W.N. Delgass, F.H. Ribeiro, Catal. Today, 123 (2007) 224.
[110] K.G. Azzam, I.V. Babich, K. Seshan, L. Lefferts, Appl. Catal. B, 80 (2008) 129.
[111] C.M. Kalamaras, P. Panagiotopoulou, D.I. Kondarides, A.M. Efstathiou, J. Catal., 264 (2009) 117.

Chapter 3 Experimental Methodology

In this chapter, the reactor system, experimental procedures, catalytic activity measurement, kinetic measurement and common characterization techniques performed in the study will be elaborated. As several catalyst synthesis methods were employed for the preparation of the catalysts, the details of the catalyst preparation methods will be presented in the specific chapters in this thesis.

3.1 Catalytic reactor system

For catalytic testing of WGS reaction, a micro-catalytic reactor system (as illustrated in **Figure 3.1**) in a single pass, steady-state plug flow mode was employed. In each test, 50 mg of catalyst was packed in between two layers of quartz wool in the reactor that was positioned in a Carbolite furnace. The catalyst was reduced under 10 ml/min of purified H_2 at 650 °C (unless otherwise specified) for 1 hour. Prior to introduction of reactant gases, 10 ml/min of purified He was used to purge the remaining H_2 out of the system. Deionized water was used as the steam source and was pumped into pre-heated gas line using a calibrated Shimadzu HPLC pump. The pre-heated gas line which was maintained at 150 °C vaporizes the water into steam, before it was mixed with the other reactant gases. A total feed flow rate of 50 ml/min was used and the reactant gas mixture consisted of: 5 mol% CO, 25 mol% H_2O, and balance He. The reaction studies were conducted in the temperature range of 350 °C – 650 °C at a gas hourly space velocity (GHSV) of about 68,000 h^{-1}. The effluent product from the reactor was passed through a cold trap to condense the water and the non-condensable product

gases were analyzed with an on-line HP-GC equipped with a Hayesep D column. Measurements were collected when the reaction had attained steady-state.

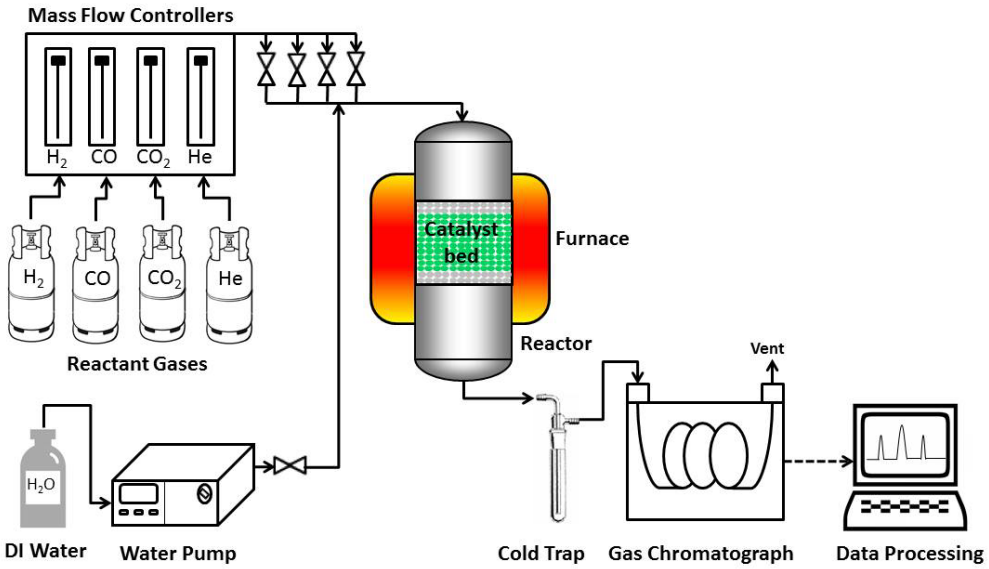

Figure 3-1 Experimental setup for water-gas shift reaction testing

3.2 Catalytic activity measurement

The catalytic performances were evaluated based on the activity and selectivity. The catalyst activity (mol%) was presented as CO conversion to CO_2 (X_{CO}) in Eq. 3.1:

$$X_{CO,WGS} = \frac{[CO_2]_{out}}{[CO]_{out} + [CO_2]_{out}} \tag{3.1}$$

The selectivity was gauged based on the CH_4 and H_2 yields which were calculated according to Eq. 3.2:

$$\%\, CH_4\ (H_2) Yield = \frac{[CH_4]_{out}\ ([H_2]_{out})}{[CO_2]_{out} + [H_2]_{out} + [CH_4]_{out}} \tag{3.2}$$

For turnover frequency (TOF) calculations and derivation of reaction rates, the catalytic activity testing was performed with diluted catalysts (diluted with powder quartz SiO_2) with a total flow rate of 100 ml/min in order to maintain a total CO conversion of below 10%. The TOF was calculated according to the Eq. 3.3:

$$TOF = \frac{mol\ of\ CO\ converted}{mol\ of\ Ni\ metal\ x\ time\ (s)} \tag{3.3}$$

3.3 Kinetic measurement

Kinetic measurement was performed with total CO conversion maintained below 15% by varying the catalyst concentration through dilution with quartz silica. High reactant flow rate was employed to attain low CO conversion in order to eliminate the mass transfer resistance. The internal mass transfer can be neglected since the catalysts used in this study were of nano-size. Kinetic measurements were taken at 25 °C intervals over a temperature range of 325 to 400 °C under atmospheric pressure using the specified catalyst. The gas composition was varied over the range of 2.5% to 10% CO, 10% to 55% H_2O, 5% to 25% CO_2, 5% to 20% H_2 and balance He. The apparent reaction order measurement was also derived at these reaction conditions at 400 °C. All data are collected after the reaction had reached steady-state and the rate of reaction was derived based on Eq. 3.4:

$$Rate\ (r) = \frac{mol\ of\ CO\ converted}{metal\ surface\ area\ (m^2)\ x\ time\ (s)} \tag{3.4}$$

3.4 Characterization techniques

The characterization methods and the equipments used are described in this section.

3.4.1 Brunauer-Emmett-Teller (BET) surface area

The BET surface area of the catalysts was measured using Micromeritics ASAP 2010 analyzer at 77K by the nitrogen adsorption and desorption isotherms. Prior to analysis, about 0.1 g of sample was degassed with He at 300 °C for 12 hours to remove all surface impurities and moisture. The net weight of the sample was obtained by comparing the weight of the sample before and after degassing. The sample cell was then placed into the analysis station with liquid nitrogen at 77K as adsorbate.

3.4.2 N_2O Pulse Titration

Nitrous oxide (N_2O) pulse titration was done using the Thermo Scientific TPDRO-1100 System to calculate the amount of active sites and metal dispersion. The first H_2-TPR was performed using 0.05 g of catalyst up to the required reduction temperature, followed by cooling down to room temperature under N_2. Purified N_2O gas was then introduced to the system by pulse injection until saturation. A second H_2-TPR was carried out for up to 650 °C. The amount of adsorbed N_2O was used to calculate the amount of active sites while the comparison between the first and second H_2-TPR results was used to calculate the metal dispersion.

3.4.3 Inductive-coupled plasma-mass spectrometer (ICP-MS)

ICP-MS was conducted with Agilent ICP-MS HP7500a to measure the metal content in the catalyst. A mixture of 30% hydrogen peroxide and concentrated nitric acid in the volumetric ratio of 1:1 was used to ensure that the sample was completely dissolved. Standard solutions of the target metals (e.g. Ni, Ce and Si) were prepared to determine the actual amount of the metals contained in the samples.

3.4.4 X-ray diffraction (XRD)

XRD analysis has great importance as a “fingerprint” in the identification of materials. Through XRD, vital information on the crystallinity and lattice parameters (i.e. Miller indices) can be derived based on the parallel planes of atoms that intersect the unit cells and define the directions and distances in the crystal. A Shimadzu XRD-6000 powder diffractometer was used for the XRD analysis with Cu target K-α ray as the X-ray source. The measurement conditions were under 40 kV voltage and 30 mA current using the following parameters: divergence slit of 1.0000°, scattering slit of 1.0000° and receiving slit of 0.30000 mm. A scanning speed of 1°/min was used over an angular range of $20° < 2\theta < 80°$. The average crystal sizes were determined from XRD peak broadening using Scherrer’s equation, $t = K\lambda/FWHM\cos\theta$, where t is the average dimension of crystallites along the [hkl] direction, λ is the wavelength of X-ray irradiation (1.543 Å), θ is the position of the (hkl) diffraction peak, K is the Scherrer constant which is typically considered to be 0.9 and FWHM is the line width at half maximum height. The lattice parameter was determined from Bragg’s Law with

the intensity of the most prominent peak (200) and (111) for Ni and Ce, respectively. The mean crystallite size of cerium and nickel oxide was estimated through Scherrer equation by line broadening of (200) and (111) peak, respectively.

3.4.5 H_2-Temperature-programmed reduction (H_2-TPR)

Temperature-programmed reduction (TPR) measurement for the fresh catalyst was performed on Thermo Scientific TPDRO-1100 System, equipped with a thermal conductivity detector (TCD). 0.05 g of catalyst was outgassed in helium (He) for 1 h at 300 °C prior to TPR analysis to remove any impurities and then cooled down to room temperature. 80 ml/min of 5% H_2/N_2 gas was then fed to the catalyst while the temperature of the furnace was ramped up from 50 to 900 °C at a heating rate of 10 °C/min.

3.4.6 High-resolution transmission electron microscopy (HR-TEM)

Particle sizes of the reduced and fresh catalysts were deduced from TEM images which were obtained via JEM 2010F TEM equipment operated at an acceleration voltage of 200 kV. Prior to TEM analysis, the sample is dispersed in ethanol and ultrasonicated for 30 min before introducing one droplet of the diluted sample onto a copper grid and dried at atmospheric conditions.

3.4.7 X-ray photoelectron spectroscopy (XPS)

X-ray photoelectron spectroscopy (XPS) was performed to obtain information on the surface chemical composition and binding energy of the elements. The analysis was conducted using a Kratos AXIS spectrometer

equipped with a monochromatic Al-Kα (hν=1486.71 eV) radiation source operated at 5 mA and 15 kV. The binding energy (BE) was calibrated based on the line position of C 1s (284.50 eV). Prior to XPS analysis, the catalysts were reduced under pure H_2 at the required reduction temperature for 1 hour and cooled down to room temperature of about 30 °C before transferring to the sample stub promptly.

3.4.8 X-ray absorption spectroscopy (XAS)

XAS spectra of xNiyCu/SiO_2 (discussed in Chapter 4) and Ni/xK/CeO_2 catalysts (covered in Chapter 6) were measured at the Argonne National Laboratory, USA, and Singapore Synchrotron Light Source (SSLS), respectively. The procedures undertaken at each facility will be elaborated as follows.

3.4.8.1 XAS procedures for bimetallic xNiyCu/SiO_2 catalysts

For the xNiyCu/SiO_2 catalysts, Cu (8.979 keV) and Ni (8.333 keV) K-edge X-ray absorption measurements were conducted on the bending magnet beamline of the Materials Research Collaborative Access Team (MRCAT, 10-BM) at the Advanced Photon Source (APS) at Argonne National Laboratory. The X-ray ring at APS has a current of 102 mA and the beamline has a flux of 5 x 10^{10} photons/s. Photon energies were selected using a water-cooled, double-crystal Si(111) monochromator, which was detuned by approximately 50% to reduce harmonic reflections. Measurements were made in transmission mode, and data points were acquired in three separate regions: a pre-edge region (-250 to -30 eV, step size = 10 eV, dwell time = 0.25 s), the XANES region (-30 to +30 eV, step size = 0.5 eV, dwell time = 0.25 s), and the EXAFS region (to 13 $Å^{-1}$, step size =

0.07 $Å^{-1}$, dwell time = 1s). The ionization chambers were optimized for the maximum current with linear response (~10^{10} photons detected/sec) with 10% absorption in the incident ion chamber and 70% absorption in the transmission detector. The X-ray beam was 0.5 × 2.5 mm^2 and data were collected in transmission mode. A third detector in series simultaneously collected a foil reference spectrum with each measurement for energy calibration. Catalysts were reduced in a continuous-flow reactor, which consisted of a quartz tube (1 inch OD, 10 inch length) sealed with Kapton windows by two Ultra-Torr fittings. Ball valves were welded to each Ultra-Torr fitting and served as the gas inlet and outlet. An internal K type thermocouple was placed against the catalyst sample holder to monitor temperature. Catalyst samples were pressed into a cylindrical sample holder consisting of six wells, each forming a self-supporting wafer. The catalyst amount was calculated to give an absorbance (μx) of approximately 1.0. The catalysts were reduced in flowing 3.5% H_2 in He (50 cm^3 (STP) min^{-1}) at 723 K, purged with flowing He at 723 K for 10 min and then cooled to room temperature. XAS spectra were collected in He at room temperature for the reduced samples. Traces of oxygen and moisture in the gases were removed by means of a purifier (Matheson PUR-Gas Triple Purifier Cartridge).

XAS spectra were analyzed using WinXAS 3.2 software. The data were obtained from -250 eV below the edge to 850 eV above the edge and normalized with linear and cubic fits of the pre-edge and post edge regions, respectively. The EXAFS was extracted by performing as cubic spline fit with 5 nodes from 2.5 to 13 Å-1. The first shell Cu-Cu, Ni-Ni and Ni-O scattering paths were fit using

experimental phase and amplitude functions from Cu foil (12 at 2.55 Å), Ni foil (12 at 2.49 Å) and NiO (6 at 2.09 Å), respectively.

At the Ni edge, samples with oleic acid were partially oxidized and partially reduced resulting in overlapping peaks from Ni-O, Ni-Ni and the higher shell Ni-O-Ni in NiO. As a result, a direct fit of the metallic Ni peak was not possible. The structure was fit by the following procedure. First, the Ni-Ni coordination number was estimated by assuming the metallic bond distance (2.49 Å) and a typical value of sigma squared. From this coordination number, the Ni-Ni scattering contribution was approximated by taking the EXAFS of Ni foil and multiplying chi by a constant to give the first shell coordination number of the sample. This metallic chi was then subtracted from the sample. The resulting difference chi has nearly no peak due to Ni-Ni allowing for fitting of the Ni-O scattering. In addition, the scattering from the high shell Ni-O-Ni in the sample was isolated by an inverse Fourier transfer. Subtraction of the EXAFS of these higher shell peaks from the sample EXAFS eliminated the overlap of the Ni-Ni with Ni-O-Ni peaks allowing for fitting of the former. For the oxidized Ni samples, the true Ni-Ni coordination number was determine from the fit coordination number divided by the fraction of metallic Ni. The latter was estimated by linear combination fitting of the XANES with Ni foil and NiO, and the Ni-O coordination number in the sample divided by 6, i.e., the coordination number of NiO. These two methods agreed within about 5%. Estimates of the Cu and Ni particles size were made using the experimental correlation of particle size and coordination number determined for FCC metals.

3.4.8.2 XAS procedures for potassium-doped Ni/CeO_2 catalysts

For the Ni/xK/CeO_2 catalysts, Ni K-edge and the Ce LIII-edge XAS were measured in fluorescence and transmission mode at room temperature at the Singapore Synchrotron Light Source (SSLS), XAFCA Facility. A Si (111) double crystal monochromator was used to monochromatize the X-rays from the 0.7 GeV electron storage ring. Appropriate amounts of samples were diluted with boron nitride and pelletized into a 10 mm disk-shaped pellet and then reduced at 650 °C under hydrogen for an hour. The reduced samples were sealed with kapton tape to prevent air exposure and oxidation. Each sample was scanned thrice to improve the signal-to-noise ratio and to ensure reliability of the data. XAS data were examined and fitted using the XAS analysis software, WinXAS. Fourier transform of k^3-weighted EXAFS data were performed over the range of k = 2 – 12$Å^{-1}$.

3.4.9 CO-Temperature-programmed reduction-mass spectroscopy (CO-TPR-MS)

Carbon monoxide temperature-programmed reduction was performed using a fixed bed reactor system coupled with Shimadzu Gas Chromatograph Mass Spectrometer (GCMS-QP2010). 0.05 g of catalyst was first reduced under pure H_2 at the reduction temperature for 1 h and cooled down to room temperature under He. Subsequently, 5% CO in He with a flow rate of 60 ml/min was flowed through the catalyst while the temperature of the furnace was increased to 900 °C at a heating rate of 10 °C/min. The outlet gas stream from the reactor system was

analysed continuously using the MS to measure the consumption and production of CO and CO_2, respectively.

3.4.10 Diffuse reflectance fourier transform infrared spectroscopy (DRIFTS)

In-situ DRIFTS data were collected using a Bruker FTIR spectrometer equipped with a Harrick Praying Mantis DRIFTS cell connected to a gas flow system. The catalyst was reduced at the reduction temperature for 1 h and cooled down to room temperature of about 30 °C. In studies conducted to simulate methanation conditions, H_2 was introduced alongside with CO. Prior to introducing CO and H_2, the reduced catalyst was flushed with He for 10 min to remove residual H_2. Stepwise heating and cooling with an increment of 50 °C up to 600 °C were applied. Temperature was held for 15 min at each step to ensure steady state had been attained before measurement was taken. At each temperature, 100 scans were taken to improve the signal-to-noise ratio and the scans were measured with a resolution of 4 to give a data spacing of 1 cm^{-1}.

Chapter 4 Bimetallic Ni-Cu/SiO_2 for Water-Gas Shift Reaction: Activating Surface Hydroxyls via Enhanced CO Adsorption

In this chapter, highly dispersed Ni-Cu nanoparticles supported on SiO_2 were synthesized via an in-situ self-assembly core-shell precursor route. Monometallic (Ni and Cu) and bimetallic (Ni-Cu) catalysts were synthesized, characterized with XRD, H_2-TPR, XAS, XPS, CO-TPR, DRIFTS and N_2 adsorption analysis and tested for water-gas shift reaction. Formation of highly dispersed Ni-Cu alloy was confirmed via XRD, H_2-TPR, XAS and DRIFTS. Oleic acid was found to promote the dispersion of both monometallic and bimetallic particles, anchoring small metal particles to the support via enhanced metal-support interactions. DRIFTS results suggest that CO adsorbs on Cu sites in Ni-Cu alloy thereby suppressing methanation. Additionally, stronger CO adsorption on 5Ni5Cu/SiO_2 (OA) catalyst activates surface terminal hydroxyl groups on silica for enhanced CO conversion. The promotional effect of OA on WGS activity was evidenced through kinetic measurements; 5Ni5Cu/SiO_2 (OA) catalyst obtained a turnover frequency of 0.004 s^{-1} which is twice that of 5Ni5Cu/SiO_2 catalyst (0.002 s^{-1}).

4.1 Introduction

Hydrogen production via water-gas shift reaction (WGSR) (Eq.1.1) is an important industrial process. Reaction of steam with a chosen carbonaceous source (coal, coke, natural gas, naphtha etc) produces synthesis gas (syngas), which is a mixture of hydrogen (H_2) and carbon monoxide (CO) in varying ratios.

In the WGSR, CO is converted to CO_2 and the produced H_2 is upgraded from the syngas that is generated from upstream processes such as gasification and reforming.

Nickel-based catalysts have been used widely on reactions such as CO methanation [1-5] and reforming of hydrocarbons [6-13] due to its low cost and high reactivity. However, application of monometallic Ni-based catalysts for WGSR has been prohibitive due the occurrence of methanation which reduces its selectivity and hydrogen yield. In order to circumvent the occurrence of methanation, numerous catalyst design strategies have been applied. These strategies include promotion with alkali metals [14-19], introduction of secondary metals [20-25], synthesis of catalysts with unique structural configurations such as core-shell [26] and mixed metal oxides [27]. Copper, on the other hand, has been used in Cu-ZnO based catalysts for commercial low-temperature WGSR. However, stability and safety issues arise with the use of Cu-based catalysts due to its ease in sintering and pyrophoricity. Therefore, several methods such as addition of secondary metals [28-30] and synthesis of nanoscale catalysts using advanced techniques [31, 32] have been applied in a bid to transform it into a non-pyrophoric and durable catalyst. Synergistic effects have been found to exist in bimetallic formulations and in particular, bimetallic Ni-Cu metals has been applied extensively on reactions such as CO methanation [33], ethanol steam reforming [34], methane oxidation and decomposition [35, 36]. However, its application for water-gas shift reaction (WGSR) has not been widely explored. At

present, bimetallic Ni-Cu metals supported on various supports such as SiO_2 [37], Al_2O_3 [38] and CeO_2 [24] have been studied. It has been shown that bimetallic Ni-Cu alloy can present several advantages over monometallic Ni or Cu supported catalysts. For instance, Lin et al. revealed that the formation of Ni-Cu alloy via addition of Cu to $Ni/CeLaO_x$ catalyst suppressed methane formation [23]. This is further affirmed by Saw et al. who discovered that Ni-Cu alloy phase is the active site for WGS reaction and it can suppress methanation by enhancing CO adsorption, thus preventing CO dissociation during WGS reaction [24]. More recently, Roh et al. showed that NiCu(1:4) exhibited the highest selectivity to CO_2 and H_2 with 85% CO conversion at a very high gas hourly space velocity (GHSV) of 83665 h^{-1} [20]. It was proposed that the formation of Cu-rich surface suppressed methanation while the higher reducibility and mesoporous structure of the catalyst led to the enhanced catalytic activity.

Catalyst preparation method plays a vital role in the physical properties and catalytic performance of the catalysts. Our group has previously reported highly dispersed Cu/SiO_2 catalyst (Cu particle size < 2.0 nm) and Ni/SiO_2 (Ni particle size < 3.0 nm) via *in-situ* self-assembled core-shell precursor route [8, 39]. With the addition of a small amount of oleic acid (OA), metal dispersion was found to be drastically enhanced. It was discovered that core-shells with metal oleate as shells and metal nitrate species as cores, were formed *in-situ* by self-assembly. This self-assembly is crucial in preventing the agglomeration of the particles due to the steric hindrance imposed by OA during thermal treatment. As

compared to the catalyst prepared by conventional impregnation method, the highly dispersed Cu/SiO_2 catalyst prepared with addition of OA achieved better catalytic performance for WGS reaction. However, the CO conversion was <50% at 300 ^oC on the highly dispersed Cu/SiO_2 catalyst. Therefore, the catalytic activity of Cu/SiO_2 can be further improved. It is therefore the objective of this work to further improve the catalytic activity of Cu/SiO_2 by addition of Ni and to investigate the extensibility of the reported method to prepare bimetallic catalysts.

4.2 Experimental

4.2.1 Catalyst preparation

The method of catalyst preparation follows the procedures that were reported in our previous paper [8], but with slight modifications for impregnation of bi-metals. The total metal loading is designated to be 10 wt%, with x and y in $xNiyCu/SiO_2$ denoting the number of moles of Ni and Cu, respectively. A series of $xNiyCu/SiO_2$ catalysts were prepared by varying the molar ratio of Ni to Cu while maintaining the molar ratio of oleic acid (OA) to metal to be 0.25. The typical procedures for preparing $5Ni5Cu/SiO_2$ catalysts are briefly described as follows: 1.32 g copper (II) nitrate hexahydrate (Sigma-Aldrich, 99.99%) and 1.10 g nickel (II) nitrate hexahydrate (Sigma-Aldrich, 99.99%) were dissolved in 9.00 mL of de-ionized water. Subsequently, 0.64 g of oleic acid (OA) (Sigma-Aldrich, ≥99%) was added to the solution based on the specified molar ratio of OA/(Ni+Cu)=0.25. Following that, 5.00 g of spherical silica support (Kanto Chemicals Co. Inc., Silica Gel 60 with particle size of 20-50 μm and specific area

of 753 m^2/g) was added into the mixture and stirred homogenously. The impregnated catalysts were dried in the fumehood at room temperature for 12 h and then in the oven at 100 °C for 12 h. To ensure homogeneity, the catalysts were stirred intermittently during the drying process and lastly, the catalysts were calcined at 450 °C for 4 h at a ramping rate of 2 °C/min.

4.3 Catalyst characterization

The xNiyCu/SiO_2 catalysts were characterized by BET, N_2O pulse titration, XRD, H_2-TPR, XPS, XAS, HR-TEM, DRIFTS and CO-TPR-MS. The details of these characterization techniques are described in Section 3.4 and in particular, the details of XAS technique follow the description covered in as Section 3.4.8.1. For analyses which required catalyst reduction, the reduction condition employed for xNiyCu/SiO_2 catalysts was 450 °C for 1 h.

4.4 Catalyst activity and kinetic measurements

The procedures for catalyst activity testing of xNiyCu/SiO_2 catalysts follow the description stated in Section 3.2. Stability test was conducted for 5Ni5Cu/SiO_2 and 5Ni5Cu/SiO_2 (OA) catalysts for 75 h and the results are shown in **Appendix A**. For the kinetic measurements and turnover frequency (TOF) calculations, about 200 mg of catalyst was added to a reactor in a tubular plug flow reactor setup and the procedure for kinetic measurements were similar to those as described elsewhere [40, 41]. The catalysts were reduced in pure H_2 with a flow rate of 10 ml/min at 450 °C for 1 h followed by a pretreatment at the standard WGS conditions (6.8% CO, 21.9% H_2O, 8.5% CO_2, 37.4% H_2, and

balance Ar) with a flow rate of 75.4 ml/min at 360 °C for 20 h. In order to ensure that the conversion was below 10%, the temperature was maintained at 360 °C for 5Ni5Cu/SiO_2 and lowered to 320 °C for 5Ni5Cu/SiO_2 (OA) after the pretreatment. The reaction rates were measured and the apparent activation energies were taken by varying the temperature range over a range of 30 °C while maintaining the standard conditions.

4.5 Results and Discussion

4.5.1 X-ray diffraction (XRD)

The catalysts were analyzed using XRD to identify the crystalline phases and the XRD patterns of the calcined catalysts are presented in **Figure 4.1**. The average crystallite sizes of NiO were calculated by line broadening of (200) line of NiO at about 2θ = 43.3° using Scherrer's equation. Likewise, the average crystallite sizes of CuO were calculated by line broadening of (111) line of CuO at about 2θ = 39°. As illustrated in **Figure 4.1(a)** and **Figure 4.1(b)**, the two diffraction peaks of cubic NiO (JCPDS No. 04-0835) are observed evidently in 10Ni/SiO_2 but as very broad peaks in 10Ni/SiO_2 (OA). This indicates that the addition of OA promoted the dispersion of NiO species and reduced the NiO crystallite size drastically from 11 nm to a size that was non-detectable by XRD (< 2 nm). Moving on to the pure Cu catalysts, both 10Cu/SiO_2 and 10Cu/SiO_2 (OA) exhibit the characteristic diffraction peaks of monoclinic CuO (JCPDS No. 05-0661) at 2θ = 35.7° and 39° as shown in **Figure 4.1(e)** and **Figure 4.1(f)**. However, it is obvious that in the absence of OA, 10Cu/SiO_2 displays sharper

diffraction peaks, indicating the formation of larger crystallites (25 nm) as compared to that of 10Cu/SiO_2 (OA) (10 nm). As in the case of NiO, the addition of OA promoted the dispersion of CuO species and this observation is in line with our previous reports which investigated the effect of OA on the dispersion of NiO and CuO in La-promoted silica-supported catalysts [8, 39]. Similar observation was made with the bimetallic catalysts. As shown in **Figure 4.1(c)** and **Figure 4.1(d)**, the NiO and CuO peaks, which are present in 5Ni5Cu/SiO_2, are absent in 5Ni5Cu/SiO_2 (OA), indicating the presence of highly dispersed NiO and CuO species in the latter. For 5Ni5Cu/SiO_2, the NiO crystallite size is 7.4 nm while the CuO crystallite size is 13 nm.

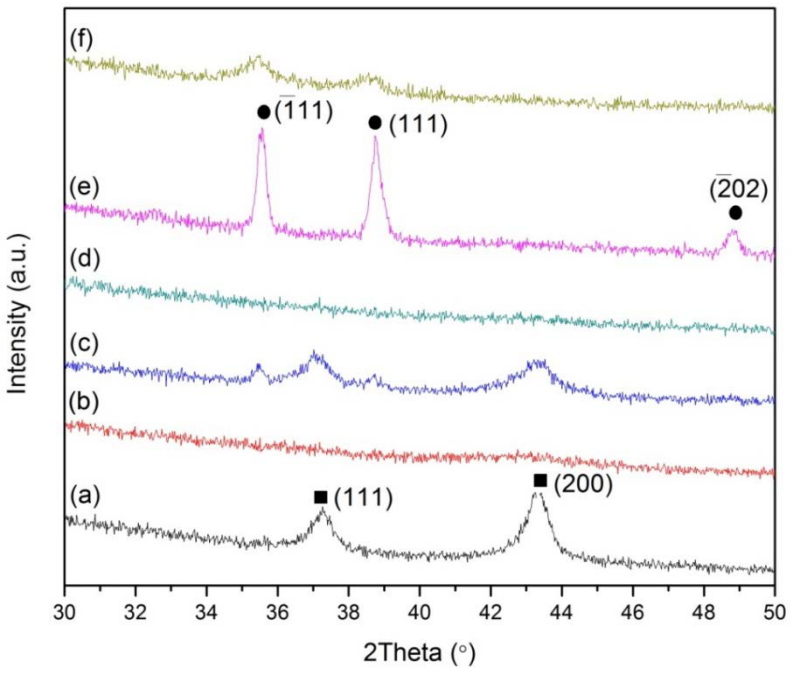

Figure 4-1 XRD patterns of freshly calcined (a) 10Ni/SiO_2, (b) 10Ni/SiO_2 (OA), (c) 5Ni5Cu/SiO_2, (d) 5Ni5Cu/SiO_2 (OA), (e) 10Cu/SiO_2 and (f) 10Cu/SiO_2 (OA) catalysts. Squares denote NiO phase and circles denote CuO phase.

Figure 4.2 shows XRD profiles of the reduced catalysts scanned from 30° to 50°. As presented in **Figure 4.2(a)** and **Figure 4.2(b)**, the reduced 10Ni/SiO_2 catalyst displays the major nickel metal diffraction at 44.6° (JCPDS 04-0850), whereas the nickel metal diffraction peak of 10Ni/SiO_2 (OA) catalysts can hardly be discerned, indicating presence of small metallic nickel in the latter. The crystallite size for 10Ni/SiO_2 catalyst was calculated to be 9.4 nm. For the monometallic Cu catalysts, both 10Cu/SiO_2 and 10Cu/SiO_2 (OA) catalysts exhibit copper metal diffraction peak at 43.4° (JCPDS 04-0836) as illustrated in **Figure 4.2(e)** and **Figure 4.2(f)**, respectively. However, it is evident that 10Cu/SiO_2 (OA) catalyst shows a broader peak than the prior, implying that with the addition of OA, smaller metallic copper crystallite (11 nm) was formed as compared to 10Cu/SiO_2 catalyst (40 nm). The XRD profiles for the reduced bimetallic catalysts are shown in **Figure 4.2(c)** and **Figure 4.2(d)**. A diffraction peak situated at an intermediary position between that of nickel and copper metal can be clearly observed for 5Ni5Cu/SiO_2 catalyst (6.6 nm) while a broad peak centred at this position is found for 5Ni5Cu/SiO_2 (OA) catalysts. The presence of the peak at this intermediary position infers the formation of Ni-Cu alloys in both the bimetallic catalysts.

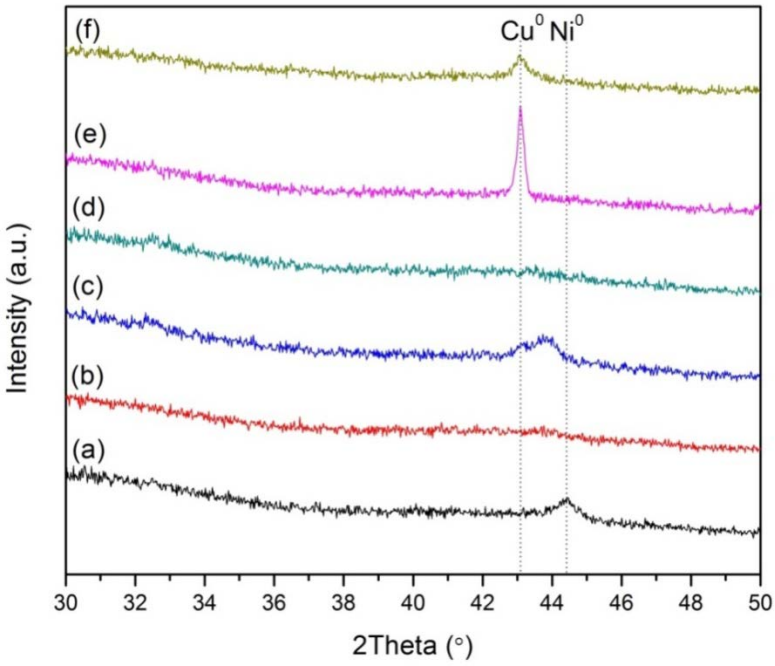

Figure 4-2 XRD patterns of reduced (a) 10Ni/SiO_2, (b) 10Ni/SiO_2 (OA), (c) 5Ni5Cu/SiO_2, (d) 5Ni5Cu/SiO_2 (OA), (e) 10Cu/SiO_2 and (f) 10Cu/SiO_2 (OA) catalysts.

4.5.2 H_2-temperature-programmed-reduction (H_2-TPR)

The H_2-TPR profiles and the H_2 consumptions of xNiyCu/SiO_2 catalysts are presented in **Figure 4.3** and **Table 4.1**, respectively. From **Figure 4.3(a)**, the reduction profile of 10Ni/SiO_2 can be seen to possess three peaks. The main peak at 351 °C together with a subtle peak at 371 °C can be attributed to the reduction of bulk NiO species which has negligible or weak interaction with the silica support [42]. The presence of two peaks instead of one is most likely a result of inhomogeneous distribution of the same species on the silica surface and the dominance of this low temperature peak indicates the presence of a sizeable fraction of large NiO particles. The third shoulder peak which is broad and centered at 500 °C can be assigned to the reduction of NiO species that have

strong interaction with the silica support [43]. In contrast, as shown in **Figure 4.3(b)**, the reduction profile of 10Ni/SiO_2 (OA) consists of one main reduction peak centered at 469 °C, indicating the existence of a large fraction of highly dispersed NiO species with a stronger metal-support interaction than 10Ni/SiO_2 due to the addition of OA. As a result of this strong metal-support interaction, only the surface NiO species were reduced while the NiO species beneath that were strongly interacting with the 10Ni/SiO_2 (OA) catalyst were not fully reduced at 450 °C as shown in XAS results later. This is in agreement with studies conducted by Dumitriu et al. who reported a modified incipient wetness impregnation method which was claimed to anchor and stabilize NiO crystallites via layered 1:1 Ni-PS phases located at the silica surface, leading to higher reduction temperature at 530 °C [44].

Next, the reduction profile of 10Cu/SiO_2 as shown in **Figure 4.3(e)** is composed of three reduction peaks situated at 215 °C, 257 °C and 328 °C. According to literature, the first two peaks at 215 °C and 257 °C can be assigned to the reduction of highly dispersed CuO nanoparticles; specifically, for the reduction of CuO clusters and ionic Cu interacting with the support, while the third peak at 328 °C can be attributed to the reduction of bulk CuO species [24, 39, 45-47]. This is in line with the observation made by Kugai et al. who reported three reduction peaks for Cu/CeO_2 catalysts with Cu loading of 10 wt% and above. The two reduction peaks at around 135 °C and 160 °C were assigned to the reduction of highly dispersed CuO cluster interacting with ceria and/or bulk

copper species while the third reduction peak had been attributed to the reduction of bulk CuO species [48]. In this case, copper which is supported on a non-reducible oxide (silica) has comparatively higher reduction temperatures as those observed for the copper supported on reducible oxide (e.g. ceria). This is supported by the findings of Delk and Vavere who reported higher reduction peaks at 229 °C and 268 °C for 1 and 4 wt% copper supported on silica as compared to their titania-supported counterparts which had reduction peaks at 130 °C and 220 °C for the two respective copper loadings [47]. In contrast, as presented in **Figure 4.3(f)**, the reduction profile of 10Cu/SiO_2 (OA) consists of two reduction peaks at 219 °C and 238 °C, which can be assigned to the reduction of highly dispersed CuO species with close proximity to the support. The absence of the third reduction peak at higher reduction temperature (> 300 °C) indicates that the addition of OA promoted the dispersion of CuO species and increased the reducibility of the 10Cu/SiO_2 (OA) catalyst.

The combination of Ni and Cu lowers the reduction temperature of NiO and CuO in 5Ni5Cu/SiO_2 as illustrated in **Figure 4.3(c)**. The reduction at lower temperature of 206 °C can be attributed to the partial reduction of CuO species while the reduction at higher temperature 241 °C can be attributed to the reduction of residual CuO and NiO. On closer observation, the broad reduction band centered at 454 °C can be assigned to the reduction of residual NiO [49]. On the other hand, as presented in **Figure 4.3(d)**, the reduction profile of 5Ni5Cu/SiO_2 (OA) comprises of two reduction peaks. The main reduction peak at 234 °C can be ascribed to the reduction of CuO and NiO while the broad

reduction peak centered at 448 °C corresponds to the reduction of NiO that is strongly interacting with the silica support. The presence of one single dominant peak that is a result of overlapping of the reduction peaks of CuO and NiO suggest that the CuO and NiO species are in intimate contact with each other in 5Ni5Cu/SiO_2 (OA) since they can be reduced concomitantly [49]. This suggests that in the bimetallic catalysts, there exists synergism between nickel and copper and the resultant alloy increases the reducibility of the bimetallic catalyst. Hence, comparison of the reduction profiles of OA-promoted catalysts with those without OA reveals that the addition of OA is beneficial in the dispersion of the metal oxide species in both monometallic and bimetallic catalysts. In the bimetallic catalysts, the enhanced dispersion of NiO and CuO enabled close proximity between the two species, eventually promoting the formation of highly dispersed Ni-Cu alloy. This result is in agreement with the XRD analysis which showed that OA aided the formation of smaller crystallites of Ni-Cu alloy.

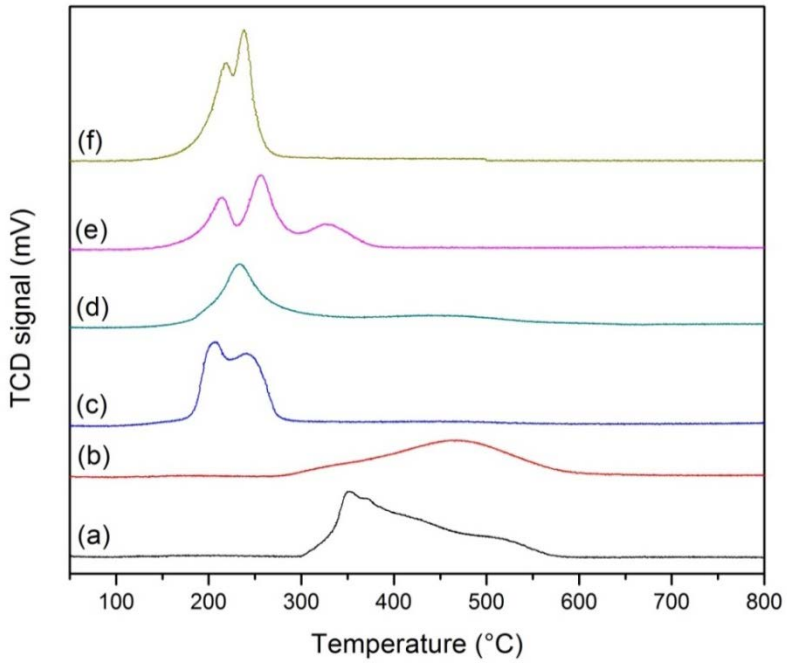

Figure 4-3 H_2-TPR profiles of (a) 10Ni/SiO_2, (b) 10Ni/SiO_2 (OA), (c) 5Ni5Cu/SiO_2, (d) 5Ni5Cu/SiO_2 (OA), (e) 10Cu/SiO_2 and (f) 10Cu/SiO_2 (OA) catalysts.

Table 4.1 Physicochemical parameters for xNiyCu/SiO_2 catalysts

	BET surface area (m^2/g)	**Metal dispersion[a] (%)**	**Metal particle size[b] (nm)**	**Metal particle size[c] (nm)**	**Crystallite size[d] (nm)**				**H_2 consumption[e] (mmol/g)**
					NiO [200]	CuO [111]	Ni [111]	Cu [111]	
10Ni/SiO_2	536.8	32.9	3.1	9.0	11	-	9.4	-	43.7
10Ni/SiO_2 (OA)	585.4	84.7	1.2	3.0	n.d.	-	n.d.	-	33.3
5Ni5Cu/SiO_2	580.6	35.7	2.8	7.0	7.4	13		6.6	36.0
5Ni5Cu/SiO_2 (OA)	448.9	84.9	1.2	3.5	n.d.	n.d.		n.d.	33.9
10Cu/SiO_2	596.4	13.9	3.6	2.5	-	25	-	40	33.2
10Cu/SiO_2 (OA)	579.9	17.4	2.9	4.5	-	11	-	11	33.2

[a] Metal dispersion was calculated by N_2O pulse titration

[b]Metal particle size was determined by the expression, d= 101/metal dispersion(%)

[c] Metal particle size was determined by XAS

[d] Crystallite size was determined by XRD with the Scherrer equation

[e] H_2 consumption below 650 ˚C in TPR profiles shown in **Figure 4.3**

n.d. not detectable

4.5.3 X-ray photoelectron spectroscopy (XPS)

The chemical states of surface Ni and Cu on the reduced catalysts were examined by XPS. **Figure 4.4(a)** displays the Ni $2p_{3/2}$ core level spectra of the reduced Ni-containing catalysts. The binding energies (BEs) of Ni metal and its satellite peaks are 852.6 eV, 858.8 eV and 856.3 eV, respectively, while that of Ni^{2+} in NiO and its satellite peaks are 853.7 eV, 855.4 eV and 860.9 eV, respectively [50]. As evident from **Figure 4.4(a)**, there is a clear shift of the main peak to higher BEs for the catalysts with OA. The main peak situated at about 856.0 eV is higher than the main characteristic peak of NiO at 853.7 eV and it can be assigned to Ni species that have strong interactions with the SiO_2 support [8]. Similar assignment had been made by Ungureanu et al. who had attributed the Ni $2p_{3/2}$ BE values of between 855.4 eV and 856.0 eV to be indicative of strong nickel-support interactions in Ni-Cu/SBA-15 catalysts [44]. Besides, it has been reported that the BE values of Ni in nickel silicates such as 1:1 nickel phyllosilicate, Ni_2SiO_4, and $NiSiO_3$ lie in the range between 855.6 eV and 856.9 eV [7]. The results from XPS are in agreement with that of H_2-TPR which revealed that Ni-containing catalysts with OA had a higher reduction peak, suggesting presence of Ni species which are strongly interacting with SiO_2 support.

The Cu $2p_{3/2}$ core level spectra of the reduced Cu-containing catalysts are illustrated in **Figure 4.4(b)**. In general, the BE values of 932.1 – 932.6 eV can be assigned to Cu^+/Cu^0 species while higher BE values of 933.5 – 933.8 eV can be ascribed to Cu^{2+} species [51]. Comparing $10Cu/SiO_2$ and $10Cu/SiO_2$ (OA)

catalysts, it can be observed that Cu in $10Cu/SiO_2$ was fully reduced and possessed the BE of 932.2 eV while that of $10Cu/SiO_2$ (OA) shifted to higher BE. As shown earlier in H_2-TPR results and subsequently in the XANES results, Cu is fully reduced in all Cu-containing catalysts at the reduction temperature of 450 °C. Hence, the observed shift to higher BE in the $10Cu/SiO_2$ (OA) can be attributed to Cu^0 species which has stronger interaction with SiO_2 support. Moreover, the BE values are shifted even higher upon the incorporation of Ni in the bimetallic catalysts. The main BE values for $5Ni5Cu/SiO_2$ and $5Ni5Cu/SiO_2$ (OA) catalysts are 933.5 eV and 933.8 eV, respectively. The shift to higher BEs can be attributed to the charge transfer from Cu to the unfilled d-band of Ni in Ni-Cu alloy and also possibly to the oxidation of Cu [52, 53].

Furthermore, from the surface compositions tabulated in **Table 4.2**, it appears that there is a slight surface enrichment in Cu for the bimetallic catalysts as indicated by the Ni/Cu atomic ratio that is less than unity. The surface enrichment in Cu was reported in literature for bimetallic Ni-Cu systems and had been attributed to thermodynamic considerations in which Cu segregation to the surface serves to lower the surface free energy of Ni-Cu bimetallic particles [21, 51].

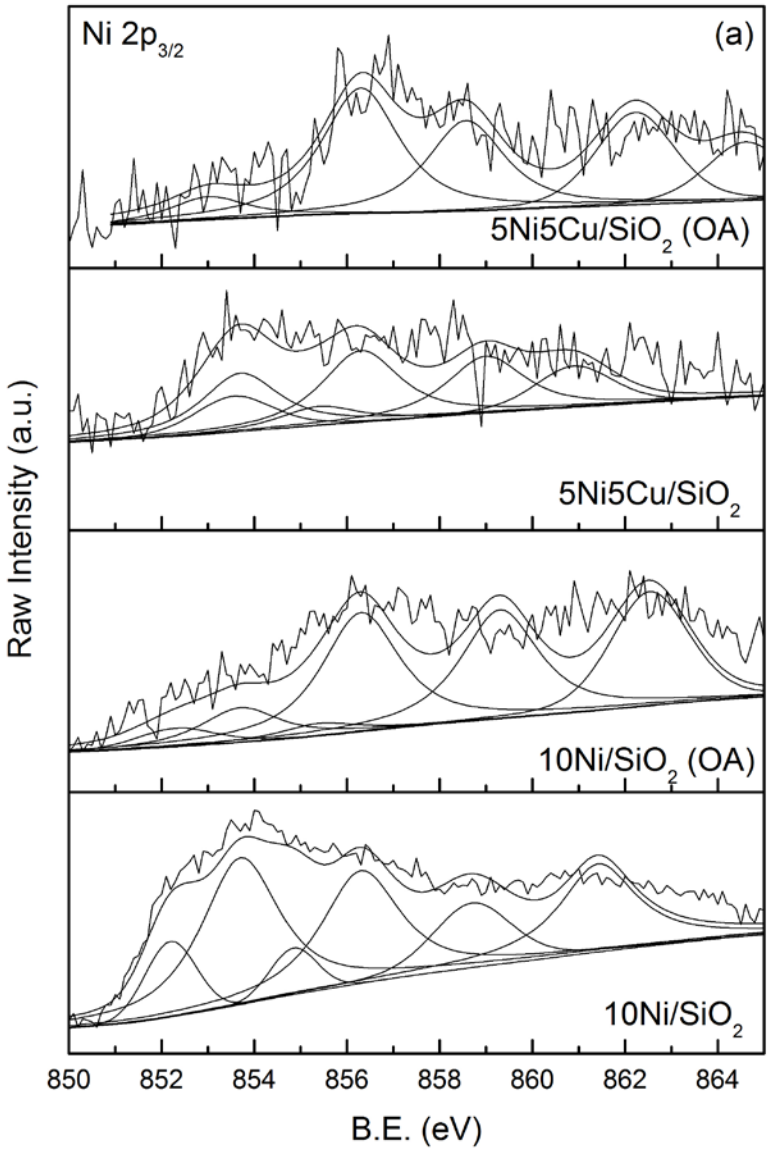
Ni 2p3/2
(a)
5Ni5Cu/SiO2 (OA)
5Ni5Cu/SiO2
10Ni/SiO2 (OA)
10Ni/SiO2
Raw Intensity (a.u.)
850
852
854
856
858
860
862
864
B.E. (eV)

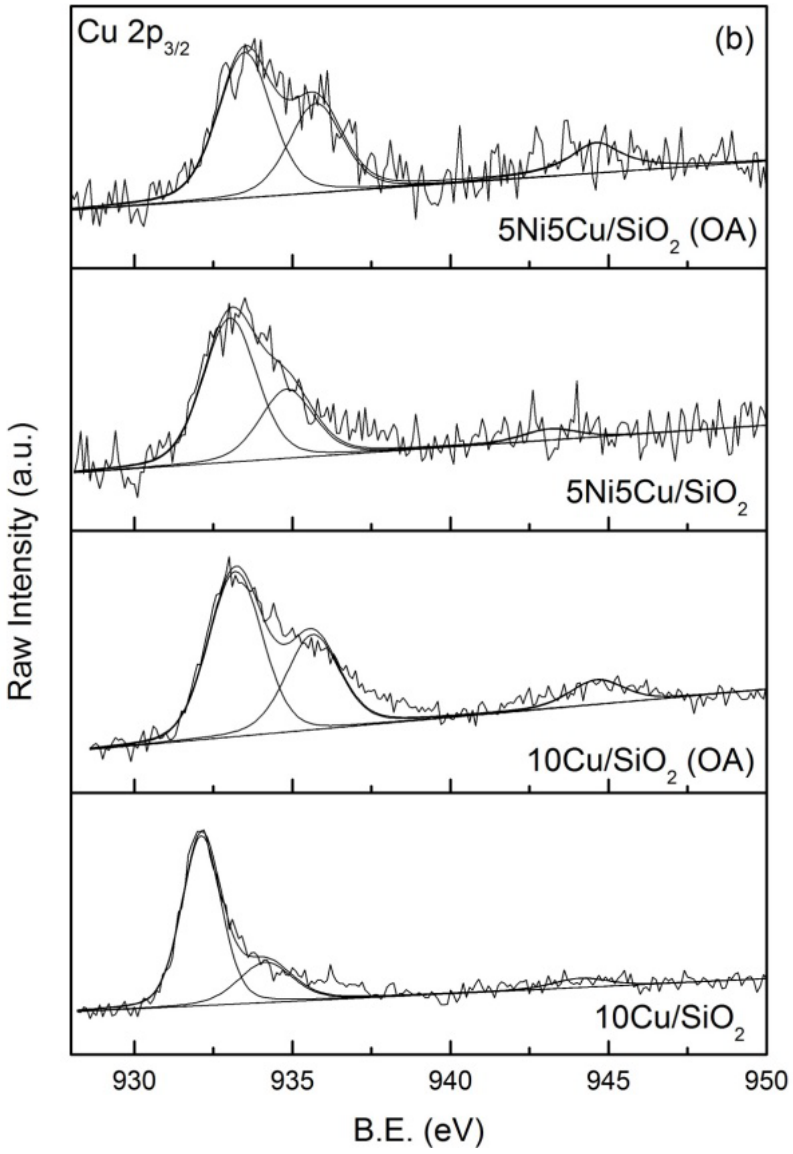

Figure 4-4 XPS Spectra for (a) Ni $2p_{3/2}$ and (b) Cu $2p_{3/2}$ of $xNiyCu/SiO_2$ catalysts.

Table 4.2 Surface composition derived from XPS

Catalyst	Surface composition (at%)				Surface composition (wt%)				Nickel / Copper ratio
	Ni	Cu	O	Si	Ni	Cu	O	Si	[Ni/Cu]
10Ni/SiO_2	5.2	-	71.9	23.0	14.4	-	54.8	30.8	-
10Ni/SiO_2 (OA)	2.9	-	71.9	25.3	8.32	-	56.7	35.0	-
5Ni5Cu/SiO_2	1.54	1.62	70.8	26.1	4.40	5.01	55.0	35.6	0.951
5Ni5Cu/SiO_2 (OA)	1.20	1.26	72.3	25.2	3.97	3.50	57.4	35.2	0.952
10Cu/SiO_2	-	1.41	72.7	25.9	-	4.54	58.8	36.7	-
10Cu/SiO_2 (OA)	-	1.33	74.5	24.1	-	4.31	61.0	34.7	-

4.5.4 X-ray absorption spectroscopy (XAS)

The Cu edge XANES spectra (8.96 to 9.01 keV) of Cu foil with the reduced 10Cu/SiO_2 and 5Ni5Cu/SiO_2 catalysts are shown in **Figure 4.5(a)** while that of 10Cu/SiO_2 (OA) and 5Ni5Cu/SiO_2 (OA) are shown in **Figure 4.5(b)**. The edge energies of the reduced catalysts (with and without OA) are the same as Cu foil, indicating presence of metallic Cu. In addition, the intensities of the white line, ca. 8.995 keV, of the catalysts are the same as that of Cu foil, suggesting that Cu is fully reduced in the catalysts. On a closer scrutiny, the shapes of XANES of 5Ni5Cu/SiO_2 (with and without OA) are different from that of 10Cu/SiO_2 (with and without OA), inferring a change in the coordination environment, i.e., bimetallic Ni-Cu nanoparticle formation.

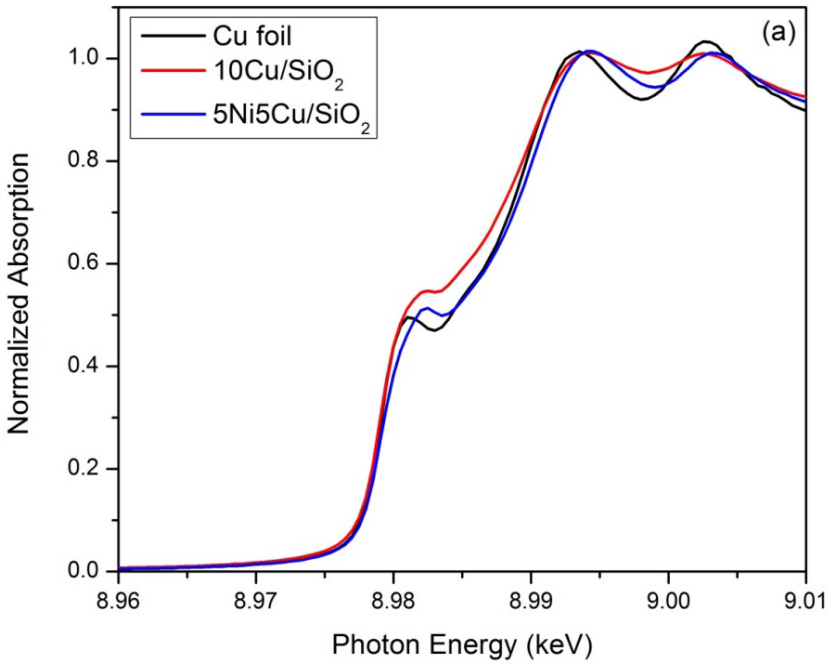

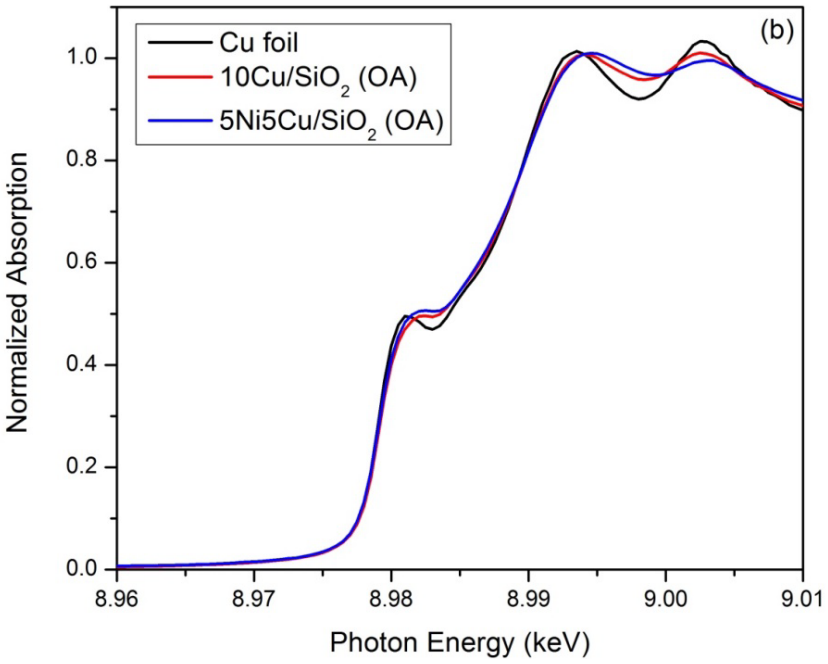

Figure 4-5 Cu edge XANES spectra of Cu foil with reduced (a) 10 Cu/SiO_2 and $5Ni5Cu/SiO_2$, and (b) $10Cu/SiO_2$ (OA) and $5Ni5Cu/SiO_2$ (OA) catalysts.

Ni edge XANES spectra (8.31 to 8.37 keV) of Ni foil and NiO reference with reduced catalysts, $10Ni/SiO_2$ and $5Ni5Cu/SiO_2$, with and without OA, are shown in **Figure 4.6(a)** and **Figure 4.6(b)** respectively. Both figures present the same features for the samples with OA; a large white line, ca. 8.35 keV, of the $10Ni/SiO_2$ (OA) and $5Ni5Cu/SiO_2$ (OA) can be observed and it implies that there is a significant amount of Ni^{2+} in the reduced catalyst, i.e., Ni in $10Ni/SiO_2$ (OA) and $5Ni5Cu/SiO_2$ (OA) was not fully reduced at 450 °C. A XANES fit of the Ni edge XANES spectra of reduced $10Ni/SiO_2$ (OA) and $5Ni5Cu/SiO_2$ (OA) reveals that the catalyst contains about 50% NiO and 50% metallic Ni. This result is consistent with that of H_2-TPR which showed that $10Ni/SiO_2$ (OA) and

5Ni5Cu/SiO_2 (OA) possesses a broad reduction peak centered at about 450 °C which was ascribed to nickel strongly interacting with SiO_2.

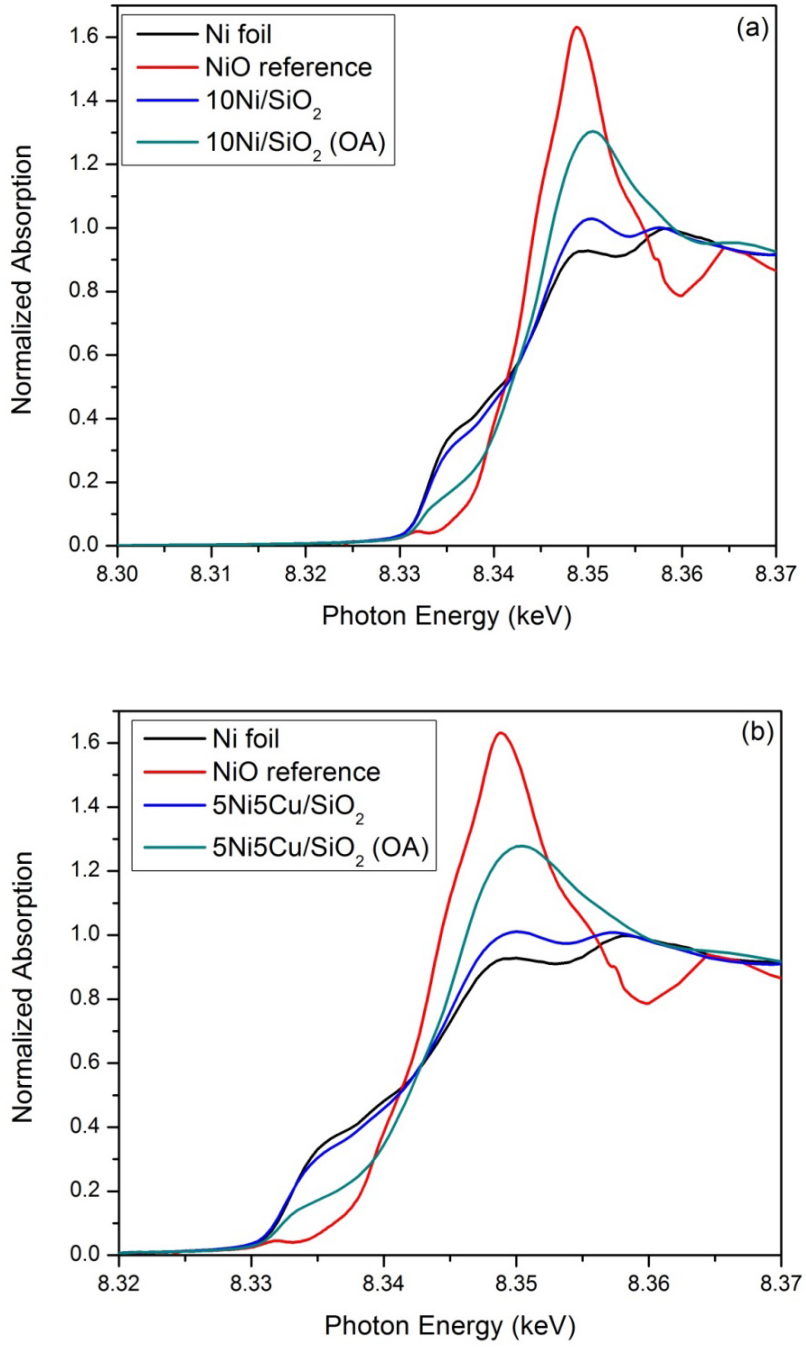

Figure 4-6 Ni edge XANES spectra of Ni foil and NiO reference with reduced (a) 10 Ni/SiO_2 and 10 Ni/SiO_2 (OA), and (b) 5Ni5Cu/SiO_2 and 5Ni5Cu/SiO_2 (OA) catalysts.

The local coordination structures of the catalysts were examined by Cu and Ni edges EXAFS analysis and the fits of the k^2-weighted Fourier Transform (FT) data for the reduced catalysts and the references (NiO, Ni, and Cu) are tabulated in **Table 4.3**. The Cu edge EXAFS spectra of $10Cu/SiO_2$ and $10Cu/SiO_2$ (OA) catalysts are presented in **Figure 4.7(a)**. The lower intensity of the magnitude of the FT of $10Cu/SiO_2$ catalyst indicates a smaller Cu-Cu coordination number and smaller particle size. On the other hand, comparing the Cu edge EXAFS spectra of $5Ni5Cu/SiO_2$ and $5Ni5Cu/SiO_2$ (OA) as illustrated in **Figure 4.7(b)**, it is evident that the magnitude of $5Ni5Cu/SiO_2$ is higher than that of $5Ni5Cu/SiO_2$ (OA), with a higher Cu-Cu coordination number of 10.9 and bigger particle size of 7.0 nm than that of $5Ni5Cu/SiO_2$ (OA) which has a CN of 8.5 and nanoparticle size of 3.5 nm. These observations suggest that in the presence of Ni, OA is effective in promoting dispersion and formation of small Cu nanoparticles in bimetallic $NiCu/SiO_2$ catalyst.

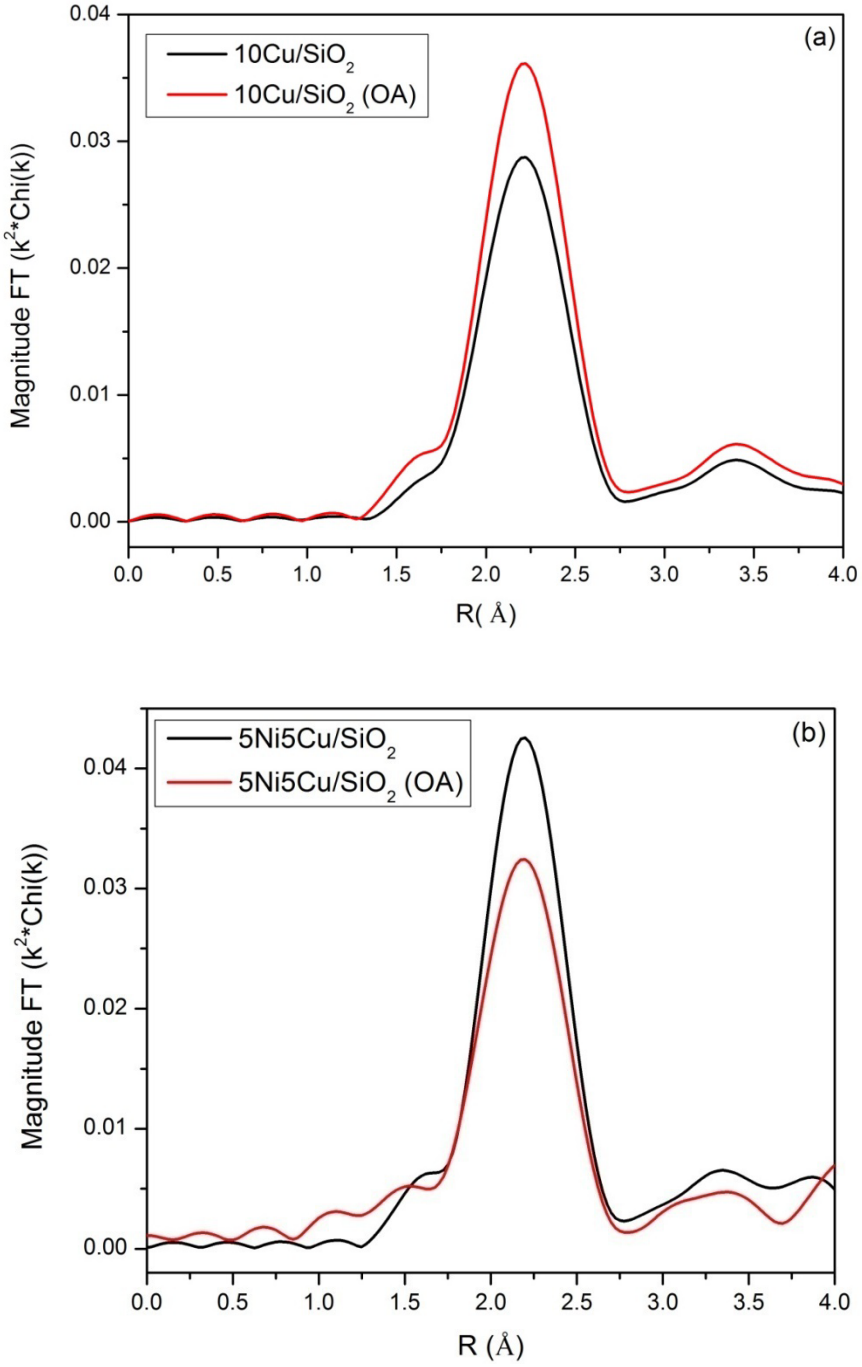

Figure 4-7 Cu edge EXAFS spectra of reduced (a) 10 Cu/SiO_2 and 10 Cu/SiO_2 (OA), and (b) 5Ni5Cu/SiO_2 and 5Ni5Cu/SiO_2 (OA) catalysts.

The Ni edge EXAFS spectra of reduced 10 Ni/SiO_2 and $10Ni/SiO_2$ (OA) catalysts are illustrated in **Figure 4.8(a)**. The FT magnitude of $10Ni/SiO_2$ has been reduced by 50% to better compare with $10Ni/SiO_2$ (OA). As shown in **Figure 4.8(a)**, $10Ni/SiO_2$ catalyst only has metallic Ni-Ni scatters, indicating that it is fully reduced at 450 °C. In contrast, $10Ni/SiO_2$ (OA) has additional scatters of Ni-O and Ni-O-Ni from unreduced NiO. The true Ni-Ni CN for $10Ni/SiO_2$ (OA) was derived using the methods as described earlier in the experimental section and utilizing experimental correlation of particle size and coordination determined for FCC metals, the estimated Ni particle sizes for $10Ni/SiO_2$ and $10Ni/SiO_2$ (OA) are 9.0 nm and 3.0 nm, respectively. Hence, it is evident that OA is effective in suppressing the growth of Ni nanoparticles and in promoting the dispersion of Ni nanoparticles on SiO_2.

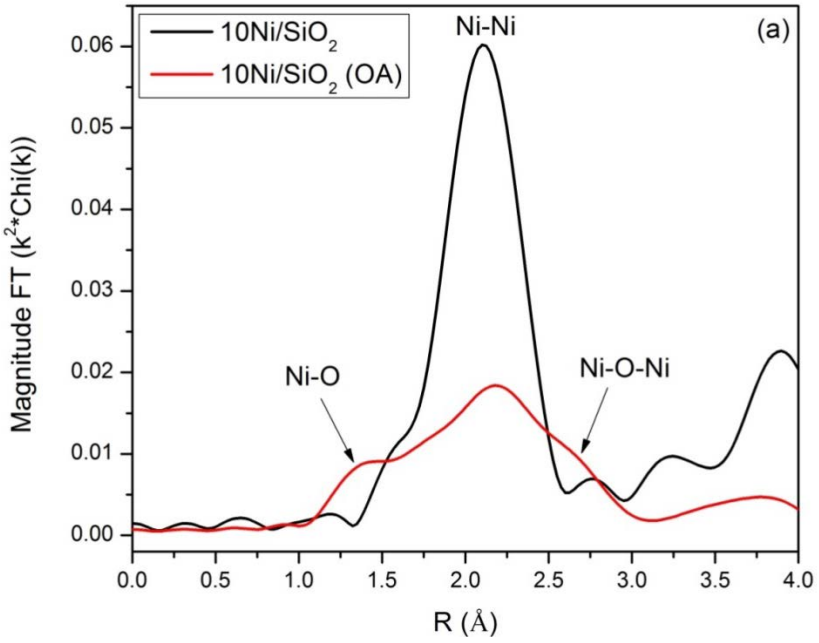

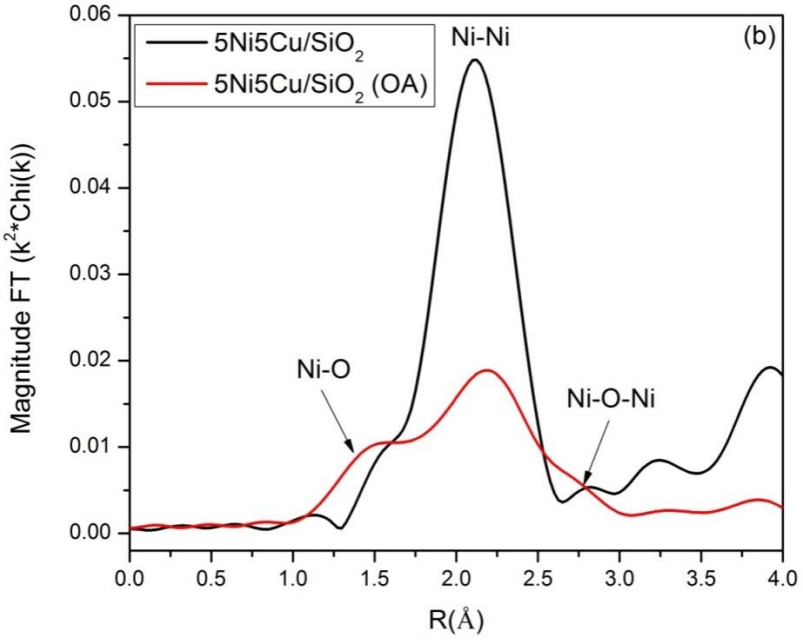

Figure 4-8 Ni edge EXAFS spectra of reduced (a) 10 Ni/SiO_2 and 10 Ni/SiO_2 (OA), and (b) 5Ni5Cu/SiO_2 and 5Ni5Cu/SiO_2 (OA) catalysts.

Likewise, in the Ni EXAFS spectra of 5Ni5Cu/SiO_2 and 5Ni5Cu/SiO_2 (OA) shown in **Figure 4.8(b)**, 5Ni5Cu/SiO_2 catalyst is fully reduced at 450 °C while 5Ni5Cu/SiO_2 (OA) is partially reduced. The true Ni-Ni CN for 5Ni5Cu/SiO_2 and 5Ni5Cu/SiO_2 (OA) are 7 nm and 3 nm, respectively.

The formation of homogenous NiCu alloy can be affirmed from the XAS analysis as summarized in **Table 4.3**. In the absence of OA, the coordination numbers of Cu-Cu(Ni) and Ni-Ni(Cu) are identical, indicating uniform distribution of Ni and Cu. Likewise, in the presence of OA, the coordination numbers of Cu-Cu(Ni) and Ni-Ni(Cu) are very similar, suggesting nearly uniform distribution of Ni and Cu. A point to note is that the errors in fitting the Ni edge are larger due to the overlapping peaks from NiO at about 50% of the sample.

Moreover, in the NiCu samples, the Cu-Cu(Ni) distance is 0.02 Å shorter than Cu-Cu in Cu foil (or monometallic Cu catalysts), while at the Ni edge, the Ni-Ni(Cu) bond distance is 0.01 A longer than in Ni foil. The small shifts in bond distance suggest alloy formation. Furthermore, the sizes of Cu in $10Cu/SiO_2$ is 2.5 nm and Ni in $10Ni/SiO_2$ is 9.0 nm, while Cu-Cu(Ni) and Ni-Ni(Cu) are both 7.0 nm. The same particle size obtained at both the Cu and Ni edges for $5Ni5Cu/SiO_2$ suggests that these are alloys of uniform composition of Ni and Cu. If alloys were not formed and independent Cu and Ni particles existed, one would expect presence of Cu and Ni particles of 2.5 nm and 9.0 nm, respectively, rather than the same size for both. Similarly, for the samples with OA, the sizes of Cu in $10Cu/SiO_2$ (OA) is 4.5 nm and Ni in $10Ni/SiO_2$ (OA) is 3.0 nm, while Cu-Cu(Ni) and Ni-Ni(Cu) have very similar sizes of 3.5 nm and 3.0 nm, respectively. The similarity in the particle size at both the Cu and Ni edge in the $5Ni5Cu/SiO_2$ (OA) catalyst suggests that these are alloys of uniform composition of Ni and Cu.

Table 4.3 EXAFS and XANES fits on xNiyCu/SiO_2 (with and without OA) catalysts pre-reduced at 450 °C

Sample	**Treatment**	**Ni^{2+}**	**Ni^0**	**Scatter**	**N**	**R, Å**	**DWF (x 10^3)**	**Eo, eV**	**Est. Size (nm)**
NiO	Standard	1.0	-	Ni-O	6	2.09	-	-	-
Ni Foil	Standard	-	1.0	N-Ni	12	2.49	-	-	-
10Ni/SiO_2	H_2 450°C			N-Ni	11.6	2.49	1.0	0.4	9.0
10Ni/SiO_2 (OA)	H_2 450°C	0.5	0.5	Ni-O	3.4	2.06	1.0	11.5	0.55 oxidized
				Ni-Ni	3.6	2.49	1.0	1.5	3.0
5Ni5Cu/SiO_2	H_2 450°C	-	1.0	Ni-Ni(Cu)	10.9	2.50	1.0	0.2	7.0
5Ni5Cu/SiO_2 (OA)	H_2 450°C	0.5	0.5	Ni-O	3.4	2.06	1.0	11.9	0.55 oxidized
				Ni-Ni(Cu)	3.7	2.50	1.0	1.4	3.0
Sample	**Treatment**	**Cu^{2+}**	**Cu^0**	**Scatter**	**N**	**R, Å**	**DWF (x 10^3)**	**Eo, eV**	**Est. Size (nm)**
Cu Foil	Standard	-	1.0	Cu-Cu	12	2.56	-	-	-
10Cu/SiO_2	H_2 450°C	-	1.0	Cu-Cu	7.5	2.55	1.0	-0.6	2.5
10Cu/SiO_2 (OA)	H_2 450°C	-	1.0	Cu-Cu	9.4	2.55	1.0	-0.4	4.5
5Ni5Cu/SiO_2	H_2 450°C	-	1.0	Cu-Cu(Ni)	10.9	2.53	1.0	-0.5	7.0
5Ni5Cu/SiO_2 (OA)	H_2 450°C	-	1.0	Cu-Cu(Ni)	8.5	2.52	1.0	-1.1	3.5

4.5.5 Transmission electron microscopy (TEM)

To further reaffirm the promotion of OA on improving the metal dispersion and decreasing the particle size, TEM analysis was conducted on 5Ni5Cu/SiO_2 and 5Ni5Cu/SiO_2 (OA). **Figure 4-9(a)** presents the TEM image of reduced 5Ni5Cu/SiO_2 catalyst. The mean particle size of Ni-Cu alloy was about 8 nm. In contrast, as shown in **Figure 4-9(b)**, Ni-Cu particles with a size of about 3 nm were homogenously dispersed in 5Ni5Cu/SiO_2 (OA) catalyst. Evidently, the TEM results are in line with the results obtained from XAS and XRD, and they further reaffirmed that OA could effective promote metal dispersion as well as reduce the metal particle sizes.

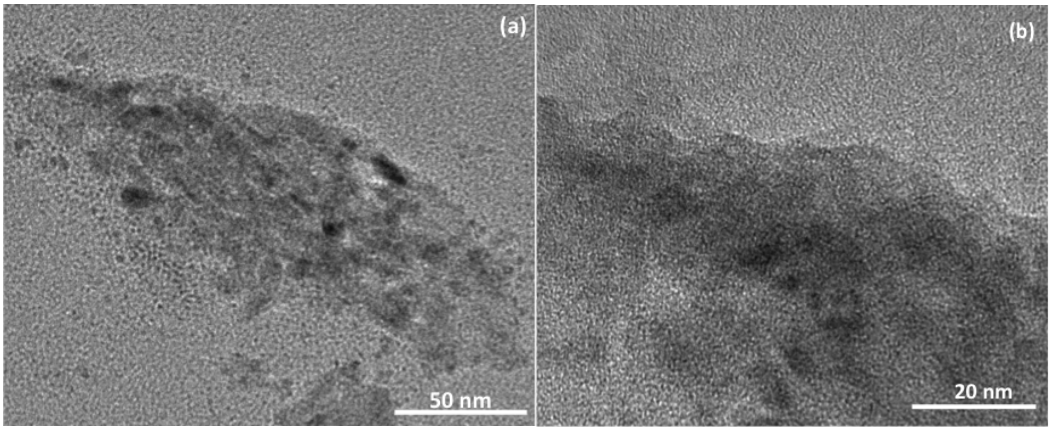

Figure 4-9 TEM images of (a) 5Ni5Cu/SiO_2 and (b) 5Ni5Cu/SiO_2 (OA) catalyst.

4.5.6 Catalytic activity and selectivity

The WGS activities of the catalysts were measured from 250 °C to 450 °C and the results are presented in **Figure 4-10(a)**. Among the catalysts, 5Ni5Cu/SiO_2 (OA) catalyst achieved the best performance; achieving CO conversion of 96.8 % at 400 °C (close to the equilibrium CO conversion of

98.1 %) while maintaining high selectivity towards WGS reaction. In contrast, 5Ni5Cu/SiO_2 catalyst attained lower CO conversion of 78.9 % at 400 °C. In both catalysts, no methane was produced and the explanation for this phenomenon will be provided later in the DRIFTS section. Comparatively, the monometallic catalysts attained less satisfactory performances than the 5Ni5Cu/SiO_2 (OA) catalyst. At 400 °C, the percentages of CO conversion are 87.4 % and 92.3% for 10Ni/SiO_2 and 10Ni/SiO_2 (OA), respectively. As shown in XAS results earlier, despite being only 50% reduced, 10Ni/SiO_2 (OA) catalysts derived smaller nickel particle sizes due to the higher dispersion (85% vs. 33%). Thus, the decrease in nickel particle size was instrumental in enhancing the WGS activity in 10Ni/SiO_2 (OA) catalyst. However, pure Ni catalysts exhibited lower WGS selectivity as evident from the percentage of CH_4 yield presented in **Figure 4-10(b)**. The CH_4 yield for 10Ni/SiO_2 is 4.1%, which is twice that of 10Ni/SiO_2 (OA) (1.9%). Methanation has been reported to involve hydrogenation of adsorbed carbon that is formed from dissociation of carbon monoxide [54, 55] and carbon formation is significantly is influenced by particle size significantly [56, 57]. Small metal particle size is known to yield lower carbon deposition rate due to the reduced fraction of terrace sites which have been proposed to be responsible for initiation of carbon deposition [58]. In this instance, the lower CH_4 yield observed with 10Ni/SiO_2 (OA) catalyst can be attributed to the smaller Ni particle size which increased resistance towards carbon deposition. The monometallic Cu catalysts, 10Cu/SiO_2 and 10Cu/SiO_2 (OA), registered the lowest CO conversions across all reaction temperatures with the exclusion of 250 °C, at which both catalysts

attained higher CO conversions than the other Ni-containing catalysts. This is expected since Cu-based catalysts are known to be more active at lower reaction temperatures. Comparing the activities of the monometallic Cu catalysts, it is evident that the higher Cu dispersion in $10Cu/SiO_2$ (OA) contributed to the enhanced CO conversion as compared to $10Cu/SiO_2$. Across the temperature range tested, $10Cu/SiO_2$ (OA) catalyst achieved CO conversion of at least 10% higher than that of $10Cu/SiO_2$ catalyst.

Besides, stability tests were also conducted for $5Ni5Cu/SiO_2$ and $5Ni5Cu/SiO_2$ (OA). As presented in Figure S1 (shown in **Appendix A**), the catalytic activity for $5Ni5Cu/SiO_2$ (OA) remained relatively stable throughout the runtime of 75 h whereas that of $5Ni5Cu/SiO_2$ deteriorated drastically to about 40 % after 75 h. This result proves that OA was able to anchor the bimetallic particles strongly to the support via strong metal-support interactions, preventing metal sintering and subsequent loss in catalytic activity.

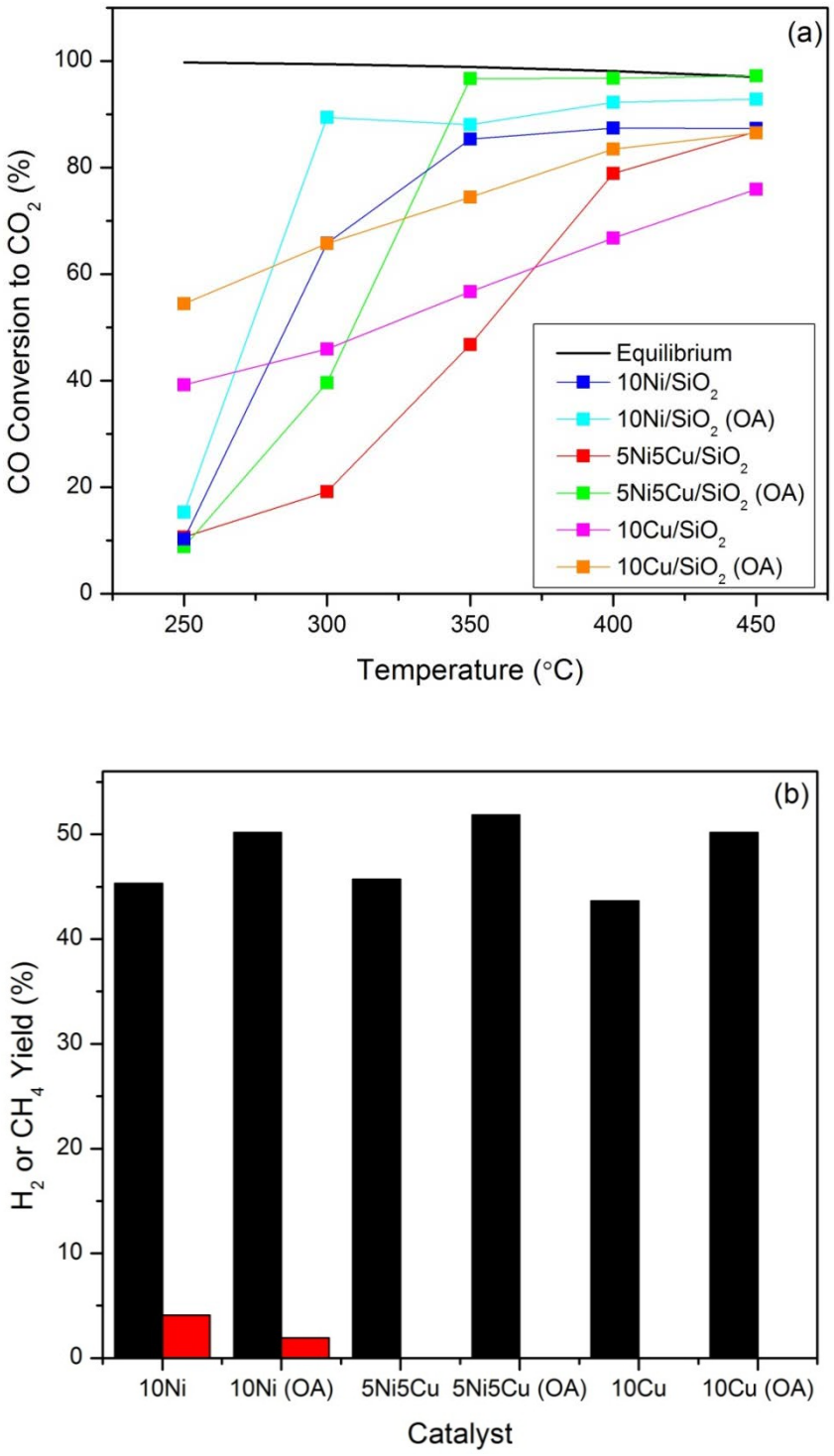

Figure 4-10 (a) Percentages of CO conversion to CO_2, and (b) H_2 and CH_4 percentage yields for xNiyCu catalysts.

4.5.7 Kinetic measurements

The WGS kinetics for 5Ni5Cu/SiO_2 and 5Ni5Cu/SiO_2 (OA) catalysts were measured with the gas composition of 6.8 % CO, 21.9 % H_2O, 8.5% CO_2, 37.4 % H_2 and balance Ar at 350 °C. The TOF values and activation energies are tabulated in **Table 4.4**, while the Arrhenius plots of 5Ni5Cu/SiO_2 and 5Ni5Cu/SiO_2 (OA) catalysts are presented in **Figure 4-11**. The TOF value and activation energy for 5Ni5Cu/SiO_2 are 0.002 s^{-1} and 107 kJ/mol while that of 5Ni5Cu/SiO_2 (OA) are 0.004 s^{-1} and 129 kJ/mol. It is evident that with the use of OA, the TOF value is doubled while the activation energy increased marginally. On a deeper analysis, it can be observed that the magnitude of enhancement in the TOF values is similar to that of the enhancement in dispersion for the 5Ni5Cu/SiO_2 (OA). The dispersion values of 5Ni5Cu/SiO_2 and 5Ni5Cu/SiO_2 (OA) are 36% and 85%, respectively. Hence, one of the attributes for the enhancement in the WGS activity can be the increase in the number of surface active sites available on the silica support. As compared to other catalysts in literature, the silica-based catalyst reported in this work is similar to that obtained by Kam et. al. for Cu/ZnO/La (weight ratio of 37:50:11) [59] and had comparatively lower TOF values than the other literature values [24, 30, 45]. This is expected since silica support, unlike other reducible oxide supports like ceria, is unable to serve as a secondary functional site for CO adsorption. Subsequent findings which will be reported later in another work reveal that the promotional effect of OA can be extended to other reducible supports like ceria and higher TOF values can be obtained with the aid of the support.

Table 4.4 Comparison of WGS rates of 5Ni5Cu/SiO_2 (with and without OA) catalysts with literature values

Catalyst	**Composition**	**T (°C)**	**Ea (kJ/mol)**	**TOF (s^{-1})**	**Reference**
5Ni5Cu/SiO_2	7% CO, 22% H_2O, 8.5% CO_2, 37% H_2, balance Ar	350	107	0.002	This work
5Ni5Cu/SiO_2 (OA)	7% CO, 22% H_2O, 8.5% CO_2, 37% H_2, balance Ar	350	129	0.004	This work
5Ni5Cu/CeO_2	7% CO, 22% H_2O, 10% CO_2, 20% H_2, balance He	350	57.6	0.013	[24]
Pd-Cu/CeO2	9,8% CO, 23.0% H_2O, 1.4% O_2, balance N_2	220-280	29.1-87.1	0.8-2.08	[46]
Cu/ZnO/La	7% CO, 22% H_2O, 8.5% CO_2, 37.5% H_2, balance N_2	230	31.6-43.1	0.004-0.018	[60]
8%CuO/Al_2O_3	7% CO, 22% H_2O, 8.5% CO_2, 37% H_2, balance Ar	300	62	0.4	[30]

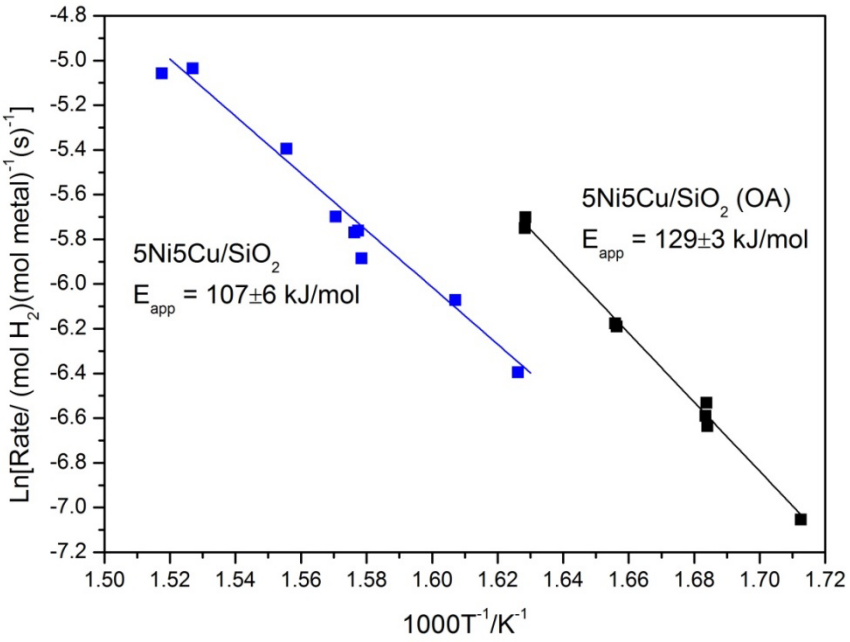

Figure 4-11 Arrhenius plots for 5Ni5Cu/SiO_2 and 5Ni5Cu/SiO_2 (OA) catalysts.

4.5.8 In-situ DRIFTS

To investigate the role of bimetallic alloy on the suppression of methane during the WGS reaction and to account for the differences in the activities observed, DRIFTS studies were conducted on identify the active surface species on the reduced catalysts. Prior to analysis, the catalysts were reduced in-situ and then subjected to continuous flow of CO and H_2 to simulate CO hydrogenation conditions. The wavenumber and mode assignments for the reduced catalysts are summarized in **Table 4.5**.

Table 4.5 Wavenumber and mode assignments for reduced xNiyCu/SiO_2 catalysts during DRIFTS

Surface species	**Wavenumber (cm^{-1})**	**Catalysts**					
	Literature value	**10Ni**	**10Ni (OA)**	**5Ni5Cu**	**5Ni5Cu (OA)**	**10Cu**	**10Cu (OA)**
Surface hydroxyl							
Terminal -OH	3747	-	3747	-	3747	3747	3747
Surface carbonyl							
Subcarbonyl	2080-2050	2075	2054	-	-	-	-
Linear	2040, 2010	2031, 2010	2033, 2013	2120, 2032,2012 (25°C), 2041 (300°C)	2120, 2030, 2005 (25°C), 2012 (300°C)	2121, 2031, 2010 (25°C)	2121, 2032, 2012 (25°C)
Bridged	2003	-	-	-	-	1938 (300°C)	1941 (300°C)
Surface carbonate							
Bidentate carbonate	1562, 1286, 1028	1578, 1259, 1101	1576, 1257, 1099	1577, 1256, 1101	1582, 1255, 1099	1582, 1259, 1097	1590, 1256, 1097

4.5.8.1 10Ni/SiO_2 and 10Ni/SiO_2 (OA) catalysts

Figure 4-12(a) presents the DRIFTS spectra of reduced 10Ni/SiO_2 catalyst. At the carbonylic region, bands at 2031 and 2010 cm^{-1} which can be assigned to CO adsorbed on hydrogen-modified Ni and linear CO can be observed at 25 °C [14, 60]. The intensities of these bands weaken and disappear as temperature increased from 25 °C to 200 °C. The disappearance of these linear carbonyls were accompanied by the appearance of a band beginning from 100 °C at 2075 cm^{-1}, which can be attributed to subcarbonyl nickel species $Ni(CO)_n$ (n=2 or 3) [61]. Upon further increment in temperature to 400 °C, the intensity of these subcarbonyl species decrease while that of CO_2 (g) and CH_4 (g) increase, suggesting that these subcarbonyl species are involved in the reaction to form the gaseous products. Furthermore, it has been reported that subcarbonyl species are precursors for CO methanation, thus explaining the strong evolution of CH_4 (g) (3015 cm^{-1}) at temperatures above 300 °C [14]. **Figure 4-12(b)** illustrates the DRIFTS spectra of reduced 10Ni/SiO_2 (OA) catalyst. Unlike the 10Ni/SiO_2 catalyst, subcarbonyl nickel species (2054 cm^{-1}) are present alongside with the linear carbonyls (2033 and 2013 cm^{-1}) at 25 °C. The subcarbonyl nickel species remained stable as temperature increased while the linear carbonyls disappeared as temperatures approached 200 °C. Similar to the 10Ni/SiO_2 catalyst, these subcarbonyl species were consumed in the reaction to form CO_2 (g) and CH_4 (g) as temperatures increased. Interestingly, with the consumption of subcarbonyls, there was also a concomitant decrease in the intensity of the band at 3747 cm^{-1}, which can be assigned to terminal hydroxyl (-OH) groups on SiO_2 surface. A

closer look at this hydroxyl region can be found in Figure S2(a) (shown in **Appendix A**). This suggests that these OH groups were consumed and participated in the reaction. It has been reported that isolated OH groups on SiO_2 can react with CO on Rh/SiO_2 catalyst to produce $Rh(CO)_2$ and H_2 [62]. In this instance, the activation of terminal OH groups on SiO_2 surface is attributed to the strong CO adsorption on nickel. Comparing the wavenumbers of subcarbonyl species on $10Ni/SiO_2$ (2075 cm^{-1}) and $10Ni/SiO_2$ (OA) (2054 cm^{-1}), it can be observed that CO was more strongly adsorbed on $10Ni/SiO_2$ (OA). The stronger adsorption of the subcarbonyl species is also one attribute for the lower CH_4 yield observed with the $10Ni/SiO_2$ (OA) catalyst. In the presence of OA, metal dispersion was promoted, thereby enhancing CO adsorption on metal surface and enabling activation of nearby terminal hydroxyl groups on SiO_2 surface.

4.5.8.2 5Ni5Cu/SiO_2 and 5Ni5Cu/SiO_2 (OA) catalysts

The DRIFTS spectra of reduced $5Ni5Cu/SiO_2$ catalyst are presented in **Figure 4-12(c)**. At 25 °C, three bands at 2120, 2032 and 2012 cm^{-1} can be observed. The band at 2120 cm^{-1} can be attributed to the ν(C=O) vibration of Cu^+-CO species which vanished at about 150 °C [63], while the bands at 2032 and 2012 cm^{-1} can be assigned to linear carbonyls adsorbed on Cu^0 [64-66]. As shown later, the bands at these wavenumbers observed in the bimetallic catalysts are similar to those observed in pure Cu catalysts, suggesting that CO is adsorbed on surface Cu. At 200 °C, these linear carbonyls disappear, followed by the appearance of a single band at 2041 cm^{-1} that can be attributed to carbonyls

formed on Ni-Cu alloy [67, 68]. The gradual decrease in the intensity of this band is accompanied by the increase in the intensities of the carbonates. At the carbonates region, three bands situated at 1577, 1256 and 1101 cm^{-1} can be discerned as temperature was increased from 100 °C and beyond. These bands can be assigned to bidentate carbonate which gradually weakened in intensity at higher temperatures of 300 to 400 °C. Concurrently, weak appearance of gaseous CO_2 was observed, indicating the conversion of carbonates to CO_2 gaseous product. **Figure 4-12(d)** illustrates the DRIFTS spectra of reduced 5Ni5Cu/SiO_2 (OA) catalyst. At 25 °C, bands at similar wavenumbers were observed at 2120, 2030 and 2005 cm^{-1}. However, as compared to 5Ni5Cu/SiO_2 (OA), it can be observed that the carbonyl formed on the Ni-Cu alloy occurs at a lower temperature of 150 °C and at a lower wavenumber of 2012 cm^{-1}. Moreover, there was a gradual consumption of terminal OH groups at 3747 cm^{-1} together with the decrease in intensity of the carbonyl band as temperature was increased. A magnified illustration of the hydroxyl region for 5Ni5Cu/SiO_2 (OA) can be found in Figure S2(b) (shown in **Appendix A**). Again, like in the case of 10Ni/SiO_2 (OA), stronger CO adsorption was observed with 5Ni5Cu/SiO_2 (OA), enabling the activation of terminal OH groups on SiO_2 surface for reaction. In contrast, depletion of terminal OH groups on SiO_2 surface was not observed in 5Ni5Cu/SiO_2 due to weaker CO adsorption. Additionally, no methane was generated for both catalysts and this can be traced back to the absence of subcarbonyl species which are known to be precursors for methanation [14].

Addition of copper to nickel is known to limit both the formation of subcarbonyl species (smoothing effect) as well as multibonding of CO (dilution effect) [69].

4.5.8.3 10Cu/SiO_2 and 10Cu/SiO_2 (OA) catalysts

Figure 4-12(e) shows the DRIFTS spectra of reduced 10Cu/SiO_2 catalyst. At the carbonylic region, three bands at 2121, 2031 and 2010 cm^{-1} can be observed at 25 °C. As mentioned earlier, the band at 2121 cm^{-1} can be ascribed to Cu^{+}-carbonyl species while the bands at 2031 and 2010 cm^{-1} can be assigned to monocarbonyls on Cu^{0} [64-66]. The disappearance of these bands at 200 °C was accompanied by the appearance of the band at 1938 cm^{-1}, which can be assigned to bridged carbonyl species, starting at 100 °C. Although bridged carbonyls are not common for copper, they are observed at high CO coverages and in the spectral region of 1835-1814 cm^{-1} [70, 71]. In addition, CO was found to interact with copper in the bridging mode in the range of 1885-1950 cm^{-1} [72]. Dandekar and Vannice have also reported appearance of a broad band at 2003 cm^{-1} on reduced CuO/Al_2O_3 catalyst, which was assigned to bridged species [64]. The intensity of this band grew as temperature was increased to 250 °C and diminished as temperature was increased further to 400 °C, suggesting the participation of these stable bridged carbonyls in the WGS reaction. Furthermore, it can be observed that beginning from 150 °C, there was a concurrent consumption of terminal hydroxyl groups, indicated by the decreasing intensity of the band at 3747 cm^{-1}. **Figure 4-12(f)** presents the DRIFTS spectra of the reduced 10Cu/SiO_2 (OA) catalyst. As with the 10Cu/SiO_2 catalyst, similar features were

observed with the exception that the bands at 2032 and 2012 cm^{-1} vanished at an earlier temperature of 100 °C as compared to that of $10Cu/SiO_2$ (OA). This disappearance coincided with the appearance of a dominant band at $1941cm^{-1}$ which is assigned to the bridged carbonyl species. The dominant presence of this band at a lower reaction temperature suggests the importance of bridged carbonyl species in the reaction, thus explaining the higher activity observed in $10Cu/SiO_2$ (OA) than $10Cu/SiO_2$.

From the DRIFTS studies, it can be seen that the terminal hydroxyl groups on silica surface were only activated in the presence of strong CO adsorption observed in the catalysts with OA as well as the pure Cu catalysts. Hence, in the presence of OA, CO adsorption was strengthened in the Ni-based catalysts, activating the otherwise unreactive surface hydroxyl groups for enhanced WGS activity.

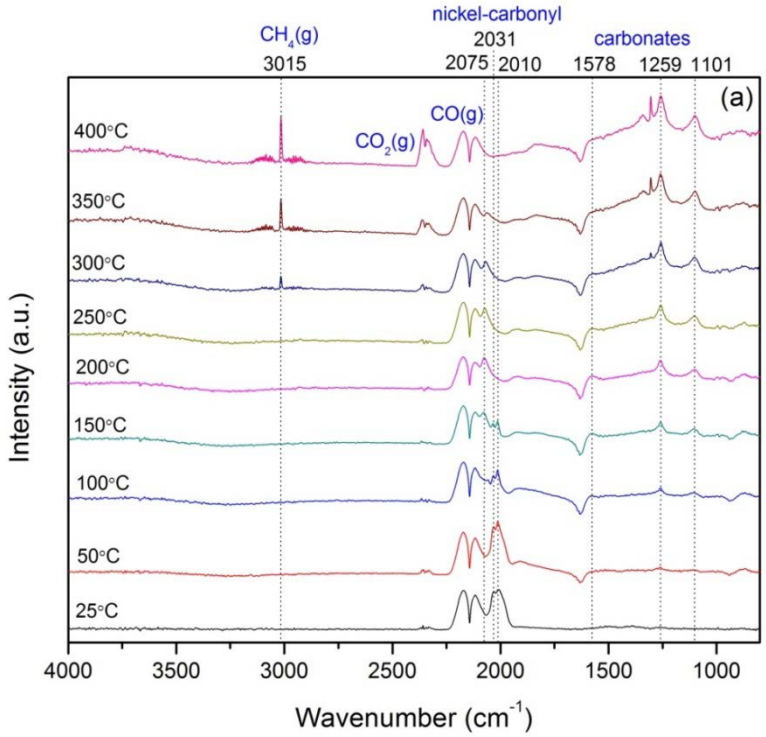
CH4(g)
3015
nickel-carbonyl
2031
2075
2010
carbonates
1578
1259
1101
(a)
CO2(g)
CO(g)
400°C
350°C
300°C
250°C
200°C
150°C
100°C
50°C
25°C
Intensity (a.u.)
4000
3500
3000
2500
2000
1500
1000
Wavenumber (cm-1)

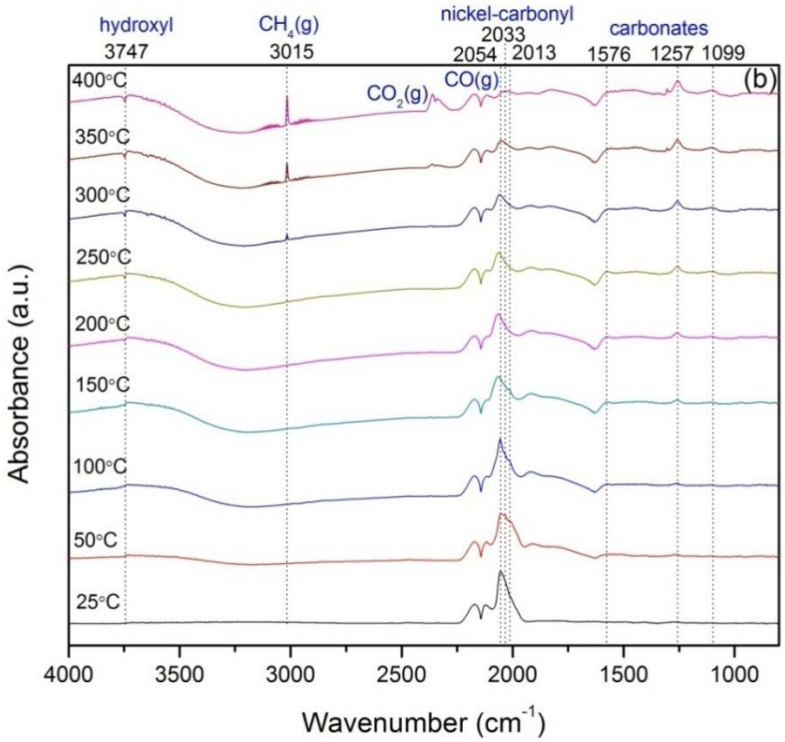
hydroxyl
3747
CH4(g)
3015
nickel-carbonyl
2033
2054
2013
carbonates
1576
1257
1099
(b)
CO2(g)
CO(g)
400°C
350°C
300°C
250°C
200°C
150°C
100°C
50°C
25°C
Absorbance (a.u.)
4000
3500
3000
2500
2000
1500
1000
Wavenumber (cm-1)

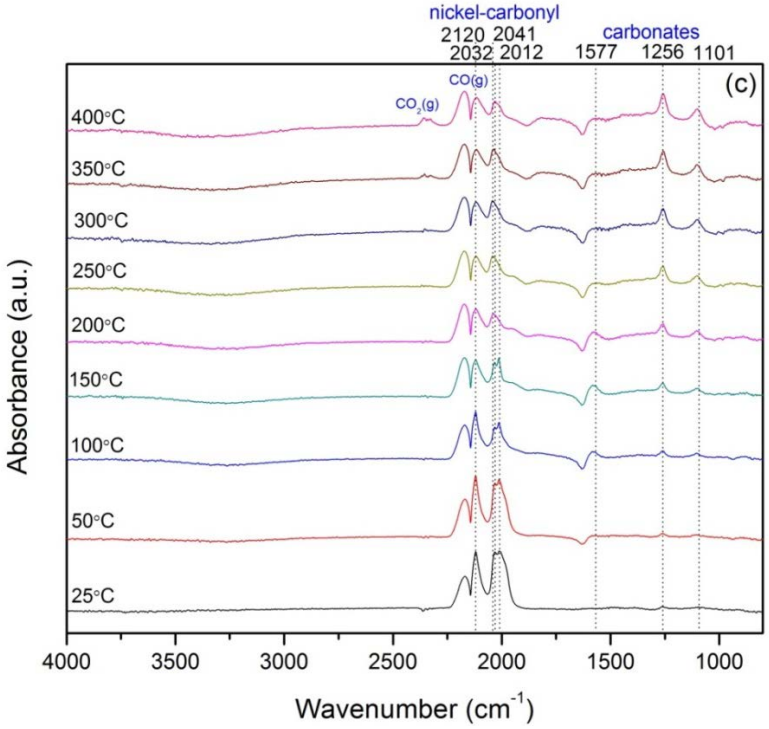
nickel-carbonyl
2120 2041
2032 2012
carbonates
1577 1256 1101
(c)
CO(g)
CO2(g)
400°C
350°C
300°C
250°C
200°C
150°C
100°C
50°C
25°C
Absorbance (a.u.)
4000 3500 3000 2500 2000 1500 1000
Wavenumber (cm-1)

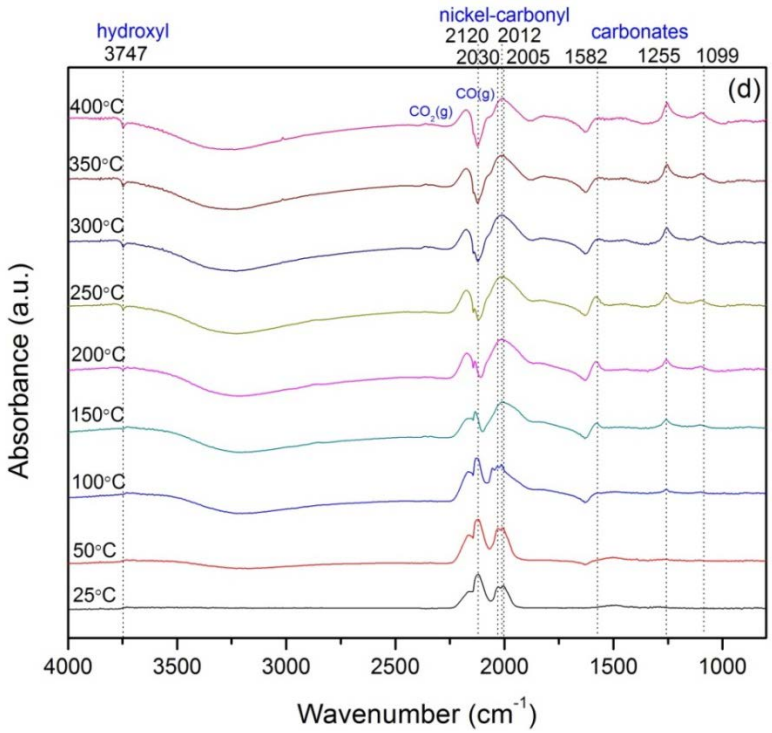
hydroxyl
3747
nickel-carbonyl
2120 2012
2030 2005
carbonates
1582 1255 1099
(d)
CO(g)
CO2(g)
400°C
350°C
300°C
250°C
200°C
150°C
100°C
50°C
25°C
Absorbance (a.u.)
4000 3500 3000 2500 2000 1500 1000
Wavenumber (cm-1)

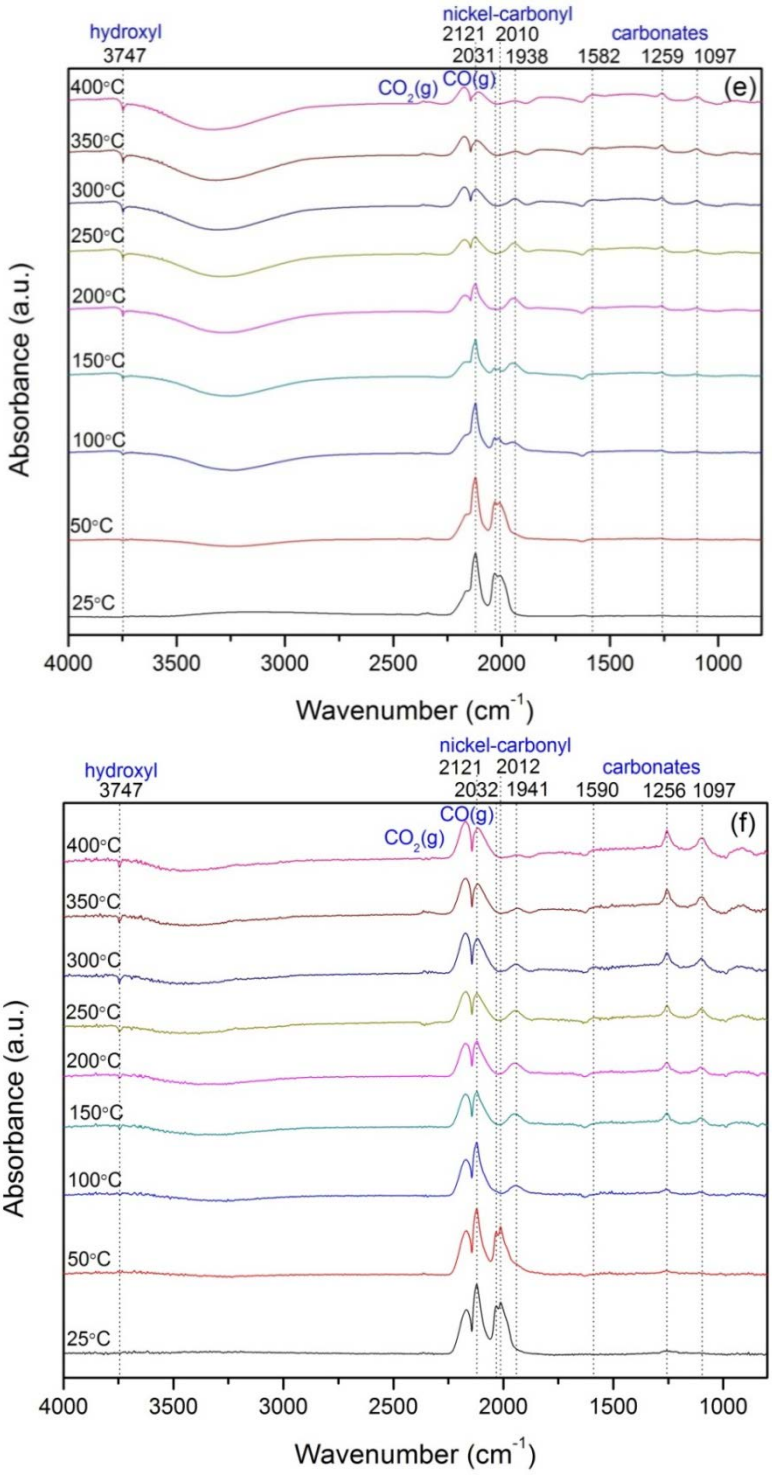

Figure 4-12 FTIR spectra of (a) 10Ni/SiO_2, (b) 10Ni/SiO_2 (OA), (c) 5Ni5Cu/SiO_2, (d) 5Ni5Cu/SiO_2 (OA), (e) 10Cu/SiO_2 and (f) 10Cu/SiO_2 (OA) catalysts under continuous flow of CO and H_2 at temperature increments of 50°C.

4.5.9 CO-temperature-programmed-reduction-mass spectroscopy (CO-TPR-MS)

In the previous section, DRIFTS studies reveal that enhanced CO adsorption enabled the activation of surface terminal hydroxyl groups on SiO_2. To further validate this proposition, CO-TPR-MS was conducted on reduced 5Ni5Cu/SiO_2 and 5Ni5Cu/SiO_2 (OA) catalysts to identify the surface reducible oxygen species. Various oxygen species, such as weakly bound oxygen species, surface capping oxygen, and lattice oxygen can be discerned based on the temperature at which CO consumption occurs [73, 74]. In particular, the activation of surface hydroxyls which are responsible for the onset of the WGS reaction can be identified [17]. The CO-TPR profiles depicting the CO consumption as well as H_2 and CO_2 production are presented in **Figure 4-13**. As shown in **Figure 4-13(a)**, the main H_2 production peak occurs at around 650 °C for 5Ni5Cu/SiO_2 catalyst. In contrast, for the 5Ni5Cu/SiO2 (OA) catalyst, two H_2 production peaks can be discerned; one at a lower temperature of about 330 °C and another at about 520 °C. Zhai et al. has reported that reducible oxygen is present on Pt-SiO_2 catalyst to react with CO to form CO_2 at temperatures above 200 °C and only insignificant amount of OH groups were activated at higher temperatures above 320 °C. On the other hand, Na-promoted Pt-SiO_2 catalyst possessed ample OH groups which were activated for WGS reaction [17]. Hence, the production of H_2 at a lower temperature on 5Ni5Cu/SiO_2 (OA) catalyst indicates that in the presence of OA, highly dispersed bimetallic Ni-Cu alloy

enabled stronger CO adsorption (as evidenced in DRIFTS) which activated surface hydroxyls in the vicinity more easily than 5Ni5Cu/SiO_2 catalyst.

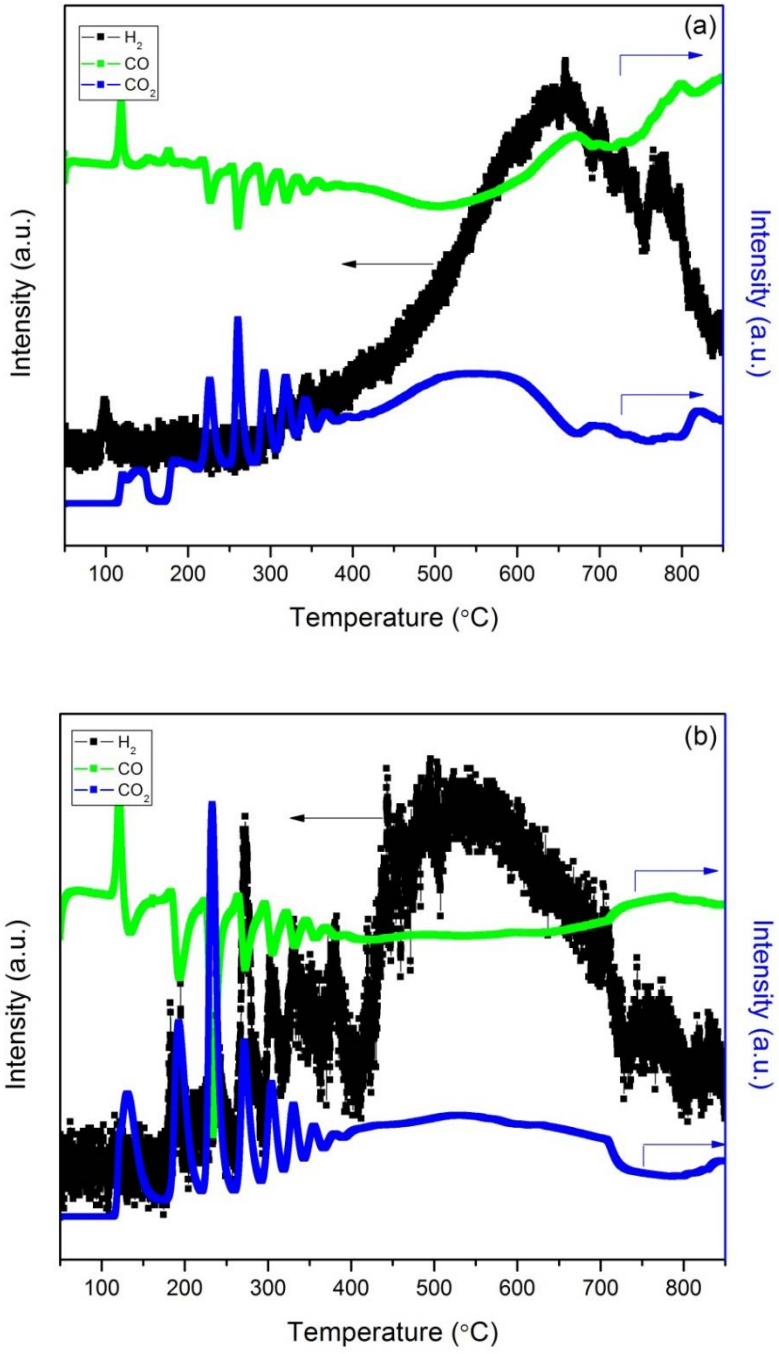

Figure 4-13 CO-TPR-MS profiles of (a) 5Ni5Cu/SiO_2, and (b) 5Ni5Cu/SiO_2 (OA) catalysts.

4.5.10 The role of Cu and OA in WGS reaction

The incorporation of Cu in the bimetallic (with and without OA) catalysts has shown significant reduction in methane formation as compared to the pure Ni/SiO_2 catalysts. From the DRIFTS studies on $5Ni5Cu/SiO_2$ (with and without OA) catalysts, CO was observed to be adsorbed Cu sites in the Ni-Cu alloy i.e. same band positions as pure Cu catalysts. As Cu is known to be less active for CO cleavage, there is lesser tendency for formation of carbon precursors which hydrogenate subsequently to form CH_4. If the role of Cu had been to break up Ni ensembles, then one would still expect to form CH_4 from the segregated Ni phases. In this instance, the absence of CH_4 production during catalytic activity testing coupled with characterizations such as XPS and XAS indicate that CO adsorption on the Cu sites of Ni-Cu alloy is responsible for the suppression of methane in the $5Ni5Cu/SiO_2$ (with and without OA) catalysts.

Comparing the activity results of $5Ni5Cu/SiO_2$ and $5Ni5Cu/SiO_2$ (OA), it is clear that in the presence of OA, $5Ni5Cu/SiO_2$ (OA) catalyst achieved a higher TOF value of 0.004 s^{-1} and maintained a much more stable performance over 75 h as compared to $5Ni5Cu/SiO_2$ during the stability test. The role of OA in enhancing WGS activity can be accounted for by two attributes i.e. enhanced dispersion and stronger metal-support interaction. As shown N_2O pulse titration, XRD and XAS, the higher dispersion in $5Ni5Cu/SiO_2$ (OA) catalysts resulted in the formation of more surface active metal sites which are smaller in size. These Ni-Cu alloy particles which are highly dispersed and small are able to enhance

CO adsorption and activate hydroxyl groups on SiO_2 surface. Furthermore, OA was also found to increase metal-support interaction which led to greater catalyst stability. From XAS results, even though only 50 % of Ni was reduced, the catalysts with OA proved to be more active. As mentioned earlier, this can be attributed to the higher dispersion of active metal sites on the surface. In contrast, for catalysts without OA, lower metal dispersion inferred that there were less available surface active metal sites for catalysis even though 100 % of Ni was reduced. In addition, the presence of NiO detected in XAS can likely be assigned to Ni that is strongly interacting with SiO_2 support. As a result of the strong metal-support interaction, only surface NiO species are reduced while NiO species which exist at the metal-support interface remains unreduced at 450 °C. These NiO species are vital in the WGS reaction since the strong metal-support interaction ensures that the small alloy particles remain anchored to the support and confers it stability throughout long term reaction.

4.6 Conclusion

From the present study, the following conclusions can be made for the xNiyCu/SiO_2 catalysts:

(a) Oleic acid was found to promote metal dispersion and stronger metal-support interaction in both monometallic and bimetallic catalysts. High dispersion of small metal particles led to provision of greater surface active sites on which CO adsorption can occur.

(b) Formation of highly dispersed and homogeneous Ni-Cu alloy was confirmed by XRD and XAS. Enhanced CO adsorption on Cu sites led to the suppression of methane and the activation of terminal hydroxyl groups on SiO_2 surface as evidenced in DRIFTS and CO-TPR-MS. The activation and provision of OH in the vicinity of bimetallic Ni-Cu alloy is vital in increasing the reactivity of CO and OH, and in the eventual enhancement of the WGS activity.

(c) Strong metal-support interaction resulted in catalytic stability as observed in the long term reaction conducted for 5Ni5Cu/SiO_2 (OA) catalyst.

Supporting information (Appendix A)

Stability tests of 5Ni5Cu/SiO_2 and 5Ni5Cu/SiO_2 (OA) catalysts for 75 h reaction, and FTIR spectra in the hydroxyl region (3500 – 4000 cm^{-1}) for (a) 10Ni/SiO_2 (OA) and (b) 5Ni5Cu/SiO_2 (OA) catalysts are presented in the supporting information in **Appendix A** (Figures S1 and S2).

4.7 References

[1] M.P. Andersson, F. Abild-Pedersen, I.N. Remediakis, T. Bligaard, G. Jones, J. Engbæk, O. Lytken, S. Horch, J.H. Nielsen, J. Sehested, J.R. Rostrup-Nielsen, J.K. Nørskov, I. Chorkendorff, J. Catal., 255 (2008) 6.
[2] I. Czekaj, F. Loviat, F. Raimondi, J. Wambach, S. Biollaz, A. Wokaun, Appl. Catal. A, 329 (2007) 68.
[3] D. Hu, J. Gao, Y. Ping, L. Jia, P. Gunawan, Z. Zhong, G. Xu, F. Gu, F. Su, Ind. Eng. Chem. Res., 51 (2012) 4875.
[4] M. Krämer, M. Duisberg, K. Stöwe, W.F. Maier, J. Catal., 251 (2007) 410.
[5] Y.S. Mok, H.C. Kang, H.J. Lee, D.J. Koh, D.N. Shin, Plasma Chem. Plasma P., 30 (2010) 437.
[6] J. Ashok, S. Kawi, Int. J. Hydrogen Energ, 38 (2013) 13938.
[7] Z. Li, L. Mo, Y. Kathiraser, S. Kawi, ACS Catal., 4 (2014) 1526.
[8] L. Mo, K.K.M. Leong, S. Kawi, Catal. Sci. Technol., 4 (2014) 2107.
[9] J. Ni, L. Chen, J. Lin, M.K. Schreyer, Z. Wang, S. Kawi, Int. J. Hydrogen Energ, 38 (2013) 13631.
[10] U. Oemar, M.L. Ang, W.F. Hee, K. Hidajat, S. Kawi, Appl. Catal. B, 148–149 (2014) 231.
[11] U. Oemar, P.S. Ang, K. Hidajat, S. Kawi, Int. J. Hydrogen Energ, 38 (2013) 5525.
[12] U. Oemar, K. Hidajat, S. Kawi, Appl. Catal. A, 402 (2011) 176.
[13] K. Sutthiumporn, T. Maneerung, Y. Kathiraser, S. Kawi, Int. J. Hydrogen Energ, 37 (2012) 11195.
[14] M.L. Ang, U. Oemar, E.T. Saw, L. Mo, Y. Kathiraser, B.H. Chia, S. Kawi, ACS Catal., 4 (2014) 3237.
[15] H. Evin, G. Jacobs, J. Ruiz-Martinez, G. Thomas, B. Davis, Catal. Lett., 120 (2008) 166.
[16] J.H. Pazmiño, M. Shekhar, W. Damion Williams, M. Cem Akatay, J.T. Miller, W. Nicholas Delgass, F.H. Ribeiro, J. Catal., 286 (2012) 279.
[17] Y. Zhai, D. Pierre, R. Si, W. Deng, P. Ferrin, A.U. Nilekar, G. Peng, J.A. Herron, D.C. Bell, H. Saltsburg, M. Mavrikakis, M. Flytzani-Stephanopoulos, Science, 329 (2010) 1633.
[18] X. Zhu, M. Shen, L.L. Lobban, R.G. Mallinson, J. Catal., 278 (2011) 123.
[19] B. Zugic, D.C. Bell, M. Flytzani-Stephanopoulos, Appl. Catal. B, 144 (2014) 243.
[20] A. Jha, D.-W. Jeong, W.-J. Jang, C.V. Rode, H.-S. Roh, RSC Advances, 5 (2015) 1430.
[21] P.B. Jiann-Horng Lin, Vadim V. Guliants, Scott Misture, Appl. Catal. A, 387 (2010) 87.
[22] T.S. Kingkaew Chayakul, Sunantha Hengrasmee, Catal. Today, 175 (2011) 420.
[23] J.-H. Lin, P. Biswas, V.V. Guliants, S. Misture, Appl. Catal. A, 387 (2010) 87.

[24] E.T. Saw, U. Oemar, X.R. Tan, Y. Du, A. Borgna, K. Hidajat, S. Kawi, J. Catal., 314 (2014) 32.
[25] T. Wang, M.D. Porosoff, J.G. Chen, Catal. Today, 233 (2014) 61.
[26] J.-H. Lin, V.V. Guliants, Appl. Catal. A, 445–446 (2012) 187.
[27] L. Barrio, A. Kubacka, G. Zhou, M. Estrella, A. Martínez-Arias, J.C. Hanson, M. Fernández-García, J.A. Rodriguez, J. Phys. Chem. C, 114 (2010) 12689.
[28] W.T. Gibbons, T.H. Liu, K.J. Gaskell, G.S. Jackson, Appl. Catal. B, 160–161 (2014) 465.
[29] R.J. Madon, D. Braden, S. Kandoi, P. Nagel, M. Mavrikakis, J.A. Dumesic, J. Catal., 281 (2011) 1.
[30] A.A.P. N.A. Koryabkina, W.F. Ruettinger, R.J. Farrauto, and F.H. Ribeiro, J. Catal., 217 (2003) 233.
[31] C.-S. Chen, J.-H. Lin, T.-W. Lai, B.-H. Li, J. Catal., 263 (2009) 155.
[32] C.-S. Chen, T.-W. Lai, C.-C. Chen, J. Catal., 273 (2010) 18.
[33] M.T. Tavares, I. Alstrup, C.A. Bernardo, J.R. Rostrup-Nielsen, J. Catal., 158 (1996) 402.
[34] A.J. Vizcaíno, A. Carrero, J.A. Calles, Int. J. Hydrogen Energ, 32 (2007) 1450.
[35] A. Hornés, P. Bera, M. Fernández-García, A. Guerrero-Ruiz, A. Martínez-Arias, Appl. Catal. B, 111–112 (2012) 96.
[36] L. De Rogatis, T. Montini, A. Cognigni, L. Olivi, P. Fornasiero, Catal. Today, 145 (2009) 176.
[37] A.R.S. Rad, M.B. Khoshgouei, S. Rezvani, A.R. Rezvani, Fuel Processing Technology, 96 (2012) 9.
[38] J.-H. Lin, V.V. Guliants, ChemCatChem, 4 (2012) 1611.
[39] L. Mo, S. Kawi, Journal of Materials Chemistry A, 2 (2014) 7837.
[40] L. Bollmann, J.L. Ratts, A.M. Joshi, W.D. Williams, J. Pazmino, Y.V. Joshi, J.T. Miller, A.J. Kropf, W.N. Delgass, F.H. Ribeiro, J. Catal., 257 (2008) 43.
[41] M. Shekhar, J. Wang, W.-S. Lee, M. Cem Akatay, E.A. Stach, W. Nicholas Delgass, F.H. Ribeiro, J. Catal., 293 (2012) 94.
[42] A. Infantes-Molina, J. Mérida-Robles, P. Braos-García, E. Rodríguez-Castellón, E. Finocchio, G. Busca, P. Maireles-Torres, A. Jiménez-López, J. Catal., 225 (2004) 479.
[43] B. Mile, D. Stirling, M.A. Zammitt, A. Lovell, M. Webb, J. Catal., 114 (1988) 217.
[44] A. Ungureanu, B. Dragoi, A. Chirieac, C. Ciotonea, S. Royer, D. Duprez, A.S. Mamede, E. Dumitriu, ACS Applied Materials & Interfaces, 5 (2013) 3010.
[45] J. Kugai, J.T. Miller, N. Guo, C. Song, J. Catal., 277 (2011) 46.
[46] L. Kundakovic, M. Flytzani-Stephanopoulos, Appl. Catal. A, 171 (1998) 13.
[47] F.S. Delk Ii, A. Vāvere, J. Catal., 85 (1984) 380.
[48] J. Kugai, J.T. Miller, N. Guo, C. Song, Appl. Catal. B, 105 (2011) 306.
[49] S.D. Robertson, B.D. McNicol, J.H. De Baas, S.C. Kloet, J.W. Jenkins, J. Catal., 37 (1975) 424.

[50] M.C. Biesinger, B.P. Payne, L.W.M. Lau, A. Gerson, R.S.C. Smart, Surf. Interface Anal., 41 (2008) 324.
[51] A.R. Naghash, T.H. Etsell, S. Xu, Chemistry of Materials, 18 (2006) 2480.
[52] Y. Shen, A.C. Lua, RSC Advances, 4 (2014) 42159.
[53] S. Velu, K. Suzuki, M. Vijayaraj, S. Barman, C.S. Gopinath, Appl. Catal. B, 55 (2005) 287.
[54] M. Araki, V. Ponec, J. Catal., 44 (1976) 439.
[55] P.R. Wentrcek, B.J. Wood, H. Wise, J. Catal., 43 (1976) 363.
[56] D. Baudouin, U. Rodemerck, F. Krumeich, A.d. Mallmann, K.C. Szeto, H. Ménard, L. Veyre, J.-P. Candy, P.B. Webb, C. Thieuleux, C. Copéret, J. Catal., 297 (2013) 27.
[57] D. Chen, K.O. Christensen, E. Ochoa-Fernández, Z. Yu, B. Tøtdal, N. Latorre, A. Monzón, A. Holmen, J. Catal., 229 (2005) 82.
[58] A.L.M. da Silva, J.P. den Breejen, L.V. Mattos, J.H. Bitter, K.P. de Jong, F.B. Noronha, J. Catal., 318 (2014) 67.
[59] R. Kam, C. Selomulya, R. Amal, J. Scott, J. Catal., 273 (2010) 73.
[60] F.B. Tatyana Tabakova, Maela Manzoli, Donka Andreeva, Appl. Catal. A, 252 (2003) 385.
[61] M. Agnelli, H.M. Swaan, C. Marquez-Alvarez, G.A. Martin, C. Mirodatos, J. Catal., 175 (1998) 117.
[62] P. Basu, D. Panayotov, J.T. Yates, J. Am. Chem. Soc., 110 (1988) 2074.
[63] D. Gamarra, C. Belver, M. Fernández-García, A. Martínez-Arias, J. Am. Chem. Soc., 129 (2007) 12064.
[64] A. Dandekar, M.A. Vannice, J. Catal., 178 (1998) 621.
[65] M.A. Kohler, N.W. Cant, M.S. Wainwright, D.L. Trimm, J. Catal., 117 (1989) 188.
[66] K. Hadjiivanov, T. Venkov, H. Knözinger, Catal. Lett., 75 (2001) 55.
[67] A. Kitla, O. Safonova, K. Föttinger, Catal. Lett., 143 (2013) 517.
[68] M.S. Kharson, A.A. Slinkin, E.A. Fedorovskaya, V.G. Pimenov, S.L. Kiperman, React. Kinet. Catal. Lett., 24 (1984) 389.
[69] M. Agnelli, C. Mirodatos, J. Catal., 192 (2000) 204.
[70] B.E. Hayden, K. Kretzschmar, A.M. Bradshaw, Surf. Sci., 155 (1985) 553.
[71] R. Raval, S.F. Parker, M.E. Pemble, P. Hollins, J. Pritchard, M.A. Chesters, Surf. Sci., 203 (1988) 353.
[72] R.M. Hernández-R, M. Kalaji, J. Electroanal. Chem., 434 (1997) 209.
[73] Q. Fu, H. Saltsburg, M. Flytzani-Stephanopoulos, Science, 301 (2003) 935.
[74] M. Yang, J. Liu, S. Lee, B. Zugic, J. Huang, L.F. Allard, M. Flytzani-Stephanopoulos, J. Am. Chem. Soc., 137 (2015) 3470.

Chapter 5 Highly Active Ni/xNa/CeO_2 Catalyst for Water-Gas Shift Reaction: Effect of Sodium on Methane Suppression

In this chapter, the effect of Na loading on the water-gas shift (WGS) activity of Ni/xNa/CeO_2 (with x=0, 0.5, 1, 2, 5 and 10 wt %) catalysts has been investigated. Ni/2Na/CeO_2 exhibited the highest performance in terms of WGS activity and methane suppression. Through H_2-TPR and XRD, the solubility limit of Na^+ in CeO_2 was found to be 2 wt%. At low loadings of Na (0.5 to 2 wt%), Na^+ was incorporated into the CeO_2 lattice, generating a lattice strain and activating the lattice O_2, thereby increasing the reducibility of the catalyst. However, beyond the solubility limit of 2 wt%, Na deposited on the CeO_2 surface, retarding the reducibility of the catalyst. XPS spectra reveal greater surface concentration of adsorbed oxygen species with the introduction of Na. This can be attributed to the generation of more oxide vacancies for oxygen adsorption due to Na substitution into the ceria lattice. By in-situ DRIFTS, methanation was found to be inhibited by the interaction between Na and Ni, leading to the absence of subcarbonyl species which are responsible for this undesirable side reaction.

5.1 Introduction

Much effort has been devoted into developing nickel-based catalysts that suppress methanation reaction during WGS reaction. For instance, Gan and Zhao [1] reported an inverse NiO_{1-x}/Cu catalyst that was able to suppress methanation. They attributed the suppression to the presence of oxidized $Ni^{\delta+}$ species which had weak interaction with CO and low activity towards CO dissociation. Next,

Lee et al. [2] investigated the effect of zinc addition into $NiFe_2O_4$ catalyst and methane suppression was found to be related to the enhanced redox property of the inverse-spinel species. Recently, a lack of CO methanation activity was also observed by Shinde and Madras for Pd-modified Ni/CeO_2 catalyst [3]. They attributed it to the creation of oxide vacancies – due to ionic substitution of Pd and Ni into CeO_2 – that induces H_2O dissociation, leading to higher activity and selectivity towards WGS reaction. From the above-mentioned works, it can be seen that oxygen plays an important role in enhancing WGS activity for nickel-based catalysts. Thus, in order to utilize nickel-based catalysts for WGS reaction, it is necessary to couple it with an oxygen-providing or partially reducible oxide support. This therefore leads us to ceria-based catalysts – a metal oxide that is well known for its high oxygen storage capacity.

Ceria has been highly effective and widely applied in catalysis applications due to its high oxygen storage capacity (OSC), enabling it to release oxygen in reducing conditions and to store oxygen in oxidizing conditions [4]. Ceria has been used in formulations of automobile three-way catalysts [5, 6], water gas shift catalysts [7-11], steam reforming catalysts [12], catalysts for hydrogenation and oxidation reactions [13-15], and electrodes of solid oxide fuel cells [16, 17]. Upon reduction, removal of an oxygen atom creates a oxygen vacancy site and results in the reduction of Ce^{4+} to Ce^{3+}, with the two remaining electrons localized into the 4f states of two adjacent Ce ions [18]. The reduction of ceria can be expressed in Kröger-Vink notation (Eq. 5.1) as [19]:

$$O_O + 2Ce_{Ce} \rightarrow \frac{1}{2}O_2(gas) + V_O^{\cdot\cdot} + 2Ce'_{Ce} \quad (5.1)$$

Where O_O and Ce_{Ce} denotes neutral O and Ce in the ceria lattice, $V_O^{\cdot\cdot}$ is a oxygen vacancy site with an effective charge of +2, and Ce'_{Ce} refers to Ce with an effective charge of -1.

Alkali promotion for WGS reaction has been studied extensively and significant enhancements has been observed when doping alkali such as Na, Li and K to Pt-based catalyst supported on oxide supports such as CeO_2 [20, 21], ZrO_2 [22, 23], TiO_2 [24, 25], Al_2O_3 [24], activated carbon [26]. Flytzani-Stephanopoulos and co-workers have proposed the promoting effect of alkali, in particular, sodium (or potassium) atoms, to be that of providing oxygen to the active Pt metal site in the form of hydroxyls that are bound to Pt with oxygen links in a Pt-Na(K)-$O_x(OH)_y$ clusters [26-28]. Water dissociation occurs on these clusters, forming –OH group which reacts with CO at low temperatures. Alternative postulation proposed by Davis and co-workers suggest that alkali promotes the WGS reaction by weakening the formate C-H bond, thereby increasing the rate of formate decomposition. This formate decomposition step has been proposed as a rate determining step for low-temperature WGS reaction [20-22]. Sodium, in particular, has been widely acclaimed to promote the WGS reaction. Incorporation of Na^+ into t-ZrO_2 supports was found to promote WGS by stabilizing ZrO_2 in the tetragonal phase [23]. The promotional role of Na was also attributed to the strong interaction between Pt and NaO_x, and the consequent formation of highly active Pt-NaO_x sites at the interface with the support that

enhance WGS [29]. The objective of this work is therefore to study the role of Na in Ni/CeO_2 catalysts in enhancing WGS activity and increasing selectivity towards WGS reaction, thereby suppressing the unwanted side reaction of methanation.

5.2 Experimental

5.2.1 Catalyst preparation

5.2.1.1 Preparation of Na-doped ceria support

Nano-sized ceria support was prepared by reverse microemulsion method according to a procedure described elsewhere [30] but with slight modifications. The typical procedure for preparing pure CeO_2 support is as follows. 12.132 g cetyltrimethylammonium bromide (CTAB) was added to 450 ml dry toluene and was stirred vigorously for 2 h. Dry toluene was obtained by storing toluene over molecular sieves for 24 h to remove moisture. Subsequently, 5.9814 ml of tetramethylammonium hydroxide (TMAH) was added dropwise to the mixture. After 2 h of stirring, the cerium precursor solution prepared by dissolving 1.8180 g $Ce(NO_3)_3.6H_2O$ (Sigma Aldrich) dissolved in 13.394 ml de-ionized water, was added dropwise to the mixture. The microemulsion was then aged for 6 days to allow complete hydrolysis and condensation of Ce^{4+} hydroxyl species to form ceria. To obtain the final product, the resultant mixture was centrifuged for 20min at 10 000 rpm. The supernatant was decanted and the residue was washed with ethanol to remove the excess sodium ions and CTAB. This washing and centrifuging process was repeated thrice. Finally, the solid product was dried in a

vacuum oven overnight and calcined at a heating rate of 2°C/min in static air for 2 h.

The calcined pure CeO_2 support was then doped with Na via wet-impregnation method. Na loading in xNa/CeO_2 supports was varied with x=0, 0.5, 1, 2, 5 and 10 wt%. The weight percentages of Na refer to the final weight percentages of Na in the respective $Ni/xNa/CeO_2$ catalysts. Typical procedure for preparing $5Na/CeO_2$ support is as follows. 0.076080 g of $NaNO_3$ (Sigma-Aldrich) was dissolved in 10.000 ml of de-ionized water and the aqueous solution was then mixed with 0.35000 g of calcined pure CeO_2 support to obtain the required Na loading. The mixture was dried under constant stirring at 80 °C and further dried at 100 °C for another 24 h before it was calcined at 650 °C with a heating rate of 2 °C/min in static air for 2 h.

5.2.1.2 Nickel impregnation on Na-doped support

Upon yielding the Na-doped CeO_2 supports, an aqueous solution containing the required $Ni(NO_3)_2.6H_2O$ (Sigma-Aldrich) was mixed with the requisite amount of Na-doped CeO_2 support to obtain the 10 wt% $Ni/xNa/CeO_2$ catalysts. The mixtures were then dried under constant stirring at 80 °C and further dried at 100 °C for another 24 h before they were calcined at 650 °C with a heating rate of 2 °C/min in static air for 2 h.

5.2.2 Catalyst characterization

BET, N_2O pulse titration, XRD, H2-TPR, XPS, TEM and DRIFTS were utilized to characterize the $Ni/xNa/CeO_2$ catalysts. The details for these

techniques are described in Section 3.4. For analyses which required catalyst reduction, the reduction condition employed for Ni/xNa/CeO_2 catalysts was 650 °C for 1 h.

5.2.3 Catalyst activity measurements

The procedures for catalyst activity testing of Ni/xNa/CeO_2 catalysts follow the description stated in Section 3.2. Stability test was conducted for Ni/2Na/CeO_2 catalyst for 100 h. To measure the amount of adsorbed carbon (CH_4 precursor) on the spent catalysts, thermogravimetric analysis (TGA) was conducted using the Shimadzu DTG-60 gravimetric analyzer. Around 10 mg of spent catalyst was used in each TGA analysis and heated in air to 800 °C with a heating rate of 10 °C/min.

5.3 Results and discussion

5.3.1 BET surface area

Table 5.1 shows the BET surface area of Ni/xNa/CeO_2 catalysts. It was observed that the surface areas of the catalysts decreased greatly with increasing loading of Na. This is primarily due to the penetration of Na into the pores of ceria support during impregnation, resulting in the blockage of pores and a subsequent decrease in the surface area. Besides, different loadings of Na can also affect the texture of ceria to variable extents.

5.3.2 N_2O pulse titration

The metal dispersion in reduced Ni/xNa/CeO_2 catalysts was measured using N_2O chemisorption. As shown in **Table 5.1**, metal dispersion decreased upon increasing Na loading. This is largely due to the reduction in surface area with higher Na loadings. However, as evident from the catalytic results, lower metal dispersion in higher Na loading Ni/CeO_2 catalysts did not decrease the activity greatly.

5.3.3 X-ray diffraction (XRD)

The catalysts were analyzed using XRD to identify the crystalline phases and the XRD patterns for the fresh, calcined catalysts are shown in **Figure 5.1(a)**. The cubic fluorite structure of CeO_2 (JCPDS No. 00-043-1002) and the face-centred cubic structure of NiO (JCPDS No. 04-0835) are apparent in all samples. **Table 5.1** displays the lattice parameters and crystallite sizes of NiO and CeO_2 derived using Bragg's law and Scherrer's equation respectively. The average crystallite sizes of NiO were determined by line broadening of (200) line of NiO at about 2θ=43.3°. Ni crystallite sizes were estimated to be 20.7, 26.7, 25.7, 27.1, 25.5, and 27.1 nm for Ni/0Na/CeO_2, Ni/0.5Na/CeO_2, Ni/1Na/CeO_2, Ni/2Na/CeO_2 Ni/5Na/CeO_2 and Ni/10Na/CeO_2 catalysts, respectively. Similarly, average crystallite sizes for CeO_2 were determined by line broadening of (111) at about 2θ=28.6° and were approximated to be 12.3, 16.9, 20.3, 22.8, 22.1, and 19.2 nm for Ni/0Na/CeO_2, Ni/0.5Na/CeO_2, Ni/1Na/CeO_2, Ni/2Na/CeO_2, Ni/5Na/CeO_2 and Ni/10Na/CeO_2 catalysts, respectively. Upon introduction of Na, NiO crystallite

size increases abruptly from 20.7 nm to 26.7 nm and remains approximately constant when Na loading was increased from 0.5 wt% to 10 wt%. However, in the case of CeO_2 crystallite size, a monotonic increase in CeO_2 crystallite size was observed with increasing Na loading from 0 wt% to 2 wt%. Beyond 2 wt%, CeO_2 crystallite size gradually decreases as Na loading was increased from 5wt% to 10 wt%. This volcanic trend can be explained by the change in grain boundary mobility brought about by different Na loadings. At low Na loading of 0.5 wt% to 2 wt%, Na^+ cations diffuse and incorporate into the CeO_2 lattice, thereby generating oxygen vacancies which enhance the grain boundary mobility [31, 32]. However, beyond the solubility limit of 2 wt%, increasing Na loading results in the suppression of grain boundary mobility due to solute drag effect [31, 33]. A steep Na concentration gradient between the bulk and intergrain interfaces is formed when excess Na is deposited on the CeO_2 surface boundaries. This Na solute gradient then generates a strong drag to the grain boundary mobility, suppressing grain growth and reducing the CeO_2 size [33]. A similar trend was also observed by Lee et al. [32], in which the grain size of gadolinia-doped ceria was found to increase with increasing Ga_2O_3 content up to 5 mol% and then decreased with further introduction of Ga_2O_3. In order to show the presence of reduced metal on the reduced Ni/xNa/CeO_2 catalysts, narrow scan was performed and the result is shown in Figure S1 (as shown in **Appendix B**). The average crystallite sizes of Ni were determined by line broadening of (111) line of Ni at about $2\theta=44.4°$. Ni crystallite sizes were estimated to be 14.7, 15.3, 13.7, 15.0, 24.7, and 27.4 nm for Ni/0Na/CeO_2, Ni/0.5Na/CeO_2, Ni/1Na/CeO_2, Ni/2Na/CeO_2

Ni/5Na/CeO_2 and Ni/10Na/CeO_2 catalysts, respectively. Likewise, a similar upward trend in the metallic Ni crystallite size is observed as Na loading was increased.

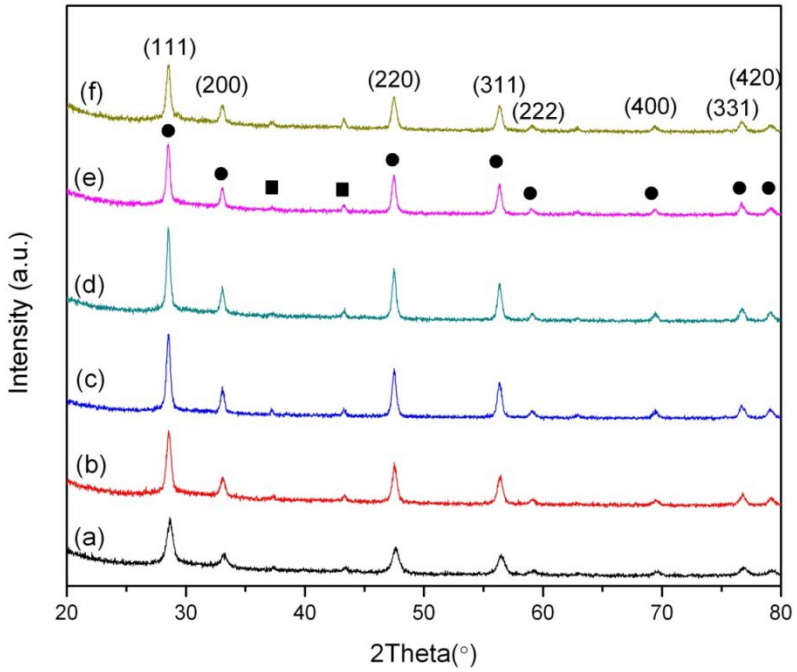

Figure 5-1 XRD patterns of freshly calcined (a) Ni/0Na/CeO_2, (b) Ni/0.5Na/CeO_2, (c) Ni/1Na/CeO_2, (d) Ni/2Na/CeO_2, (e) Ni/5Na/CeO_2, and (f) Ni/10Na/CeO_2 catalysts. Circles denote CeO_2 phase and squares denote NiO phase.

From **Table 5.1**, it is evident that the lattice parameter of Ce increased linearly from 5.394 Å (in Ni/0Na/CeO_2) to 5.418 Å (in Ni/1Na/CeO_2) and remains approximately constant. This observation is consistent with Vegard's law. This increase can be attributed to the substitution of bigger Na^+ ions (1.18 Å) for Ce^{4+} ions (0.97 Å) [34, 35] which generates a lattice expansion and forms oxygen vacancies because of charge compensation. At Na loadings close to the solubility limit of 2 wt%, lattice expansion reaches a maximum of about 5.418 Å. Therefore,

increasing Na loading beyond 2 wt% does not increase the lattice parameter further.

5.3.4 H_2-temperature-programmed-reduction (H_2-TPR)

H_2-TPR profiles for Ni/xNa/CeO_2 catalysts are reported in **Figure 5.2**. In general, two main reduction peaks can be discerned. The first reduction peak centred at about 400°C can be attributed to the reduction of Ni^{2+} to Ni^0 and probably to the reduction of surface capping oxygen of ceria [36], while the broad reduction peak started at around 850°C can be attributed to the reduction of bulk oxygen in CeO_2. As compared to other Na-doped catalysts, Ni/0Na/CeO_2 has an additional subtle low temperature peak at 320°C which can be ascribed to free NiO particles [37]. An interesting phenomenon was observed as Na loading was varied from 0 to 10 wt%. Initially, as Na loading was increased from 0 wt% to 0.5wt%, the main reduction peak shifted to higher temperature from 367°C (in Ni/0Na/CeO_2) to 430°C (in Ni/0.5Na/CeO_2). However, further increment in Na loading from 0.5 wt% to 2 wt% shifted the main reduction peak from 430°C (in Ni/0.5Na/CeO_2) to 413°C (in Ni/1Na/CeO_2) and subsequently to 403°C (in Ni/2Na/CeO_2). Interestingly, upon further increment in Na loading to 5 wt % and 10 wt%, this reduction peak shifted in the opposite direction to even higher temperatures of 458°C and 525°C respectively. At the onset, the addition of 0.5 wt% Na increased the reduction temperature due to the stronger interaction between Ni and the Na-doped CeO_2 support. However, further introduction of Na from 0.5wt% to 2 wt% increases the reducibility of the catalyst due to the

incorporation of Na^+ into the CeO_2 lattice, resulting in lattice distortion and creation of oxygen vacancies. It has been reported that Na^+ (ionic radius of 1.18 Å), due to its similar ionic radius to that of Ce^{4+} (0.97 Å), has a high possibility of incorporating into the ceria lattice [37]. Factoring in the high calcination temperature of 650°C, there is a great likelihood that a solid solution, $Na_xCe_{1-x}O_{2-y}$, was formed between Ce and Na. Thus, it is expected that at low Na loadings of 0.5 wt% to 2 wt%, Na was incorporated into the CeO_2 lattice, leading to a lattice expansion as observed from the XRD results stated above. This lattice distortion and generation of oxygen vacancies increase the oxygen mobility and in turn enhance the reducibility of the catalyst [38]. Song and Ozkan have reported enhanced oxygen mobility in Co/CeO_2 catalyst by incorporation of Ca, which in turn increased the H_2 yield and TOF over Ca-doped Co/CeO_2 catalyst in ethanol steam reforming reaction [39]. Shinde and Madras [40] have made similar observation, whereby ionic substitution of bimetallic Cu-Ni and Cu-Fe was found to activate lattice oxygen in CeO_2, increase the reducibility and oxygen storage capacity of bimetallic substituted CeO_2. With the inclusion of more sodium, the ceria lattice could no longer accommodate more sodium due to its solubility limit and the excess sodium deposited on the surface of ceria support. Despite the increased reducibility conferred by the doping of Na into CeO_2 lattice, the excess Na that formed an overlayer resulted in an overall decrease in reducibility of the catalyst at higher Na loadings of 5 wt% and 10 wt% due to stronger interactions between Ni and Na possibly through the formation of $Ni\text{-}O_x\text{-}Na$ complexes [27, 28]. The phenomenon of shifting to higher reduction temperatures had also been

observed in the case of alkali-doped Pt/CeO_2 catalyst [27], K-doped Co/SiO_2 catalyst [41], and alkali-doped Pd/Fe_2O_3 catalysts [42]. The deposition of excess Na can also be inferred from the H_2 uptake values tabulated in **Table 5.1**. From **Table 5.1**, it is evident that H_2 uptake remains relative constant for 0 wt% to 2 wt% Na loading. However, as Na loading increased from 2 wt% to 10 wt%, H_2 uptake increased from 2.83 mmol H_2/g (in $Ni/2Na/CeO_2$) to 8.25 mmol H_2/g (in $Ni/5Na/CeO_2$) and then further increased to 12.9 mmol H_2/g (in $Ni/10Na/CeO_2$). Since the Ni nominal loading is consistent at 10 wt% for all catalysts, the H_2 uptake required for reduction of Ni^{2+} to Ni^0 should be similar among all catalysts. Thus, this sharp increase in H_2 uptake observed in 5 wt% and 10 wt% Na-doped catalysts can be attributed to the reduction of excess Na_2O deposited on the surface of CeO_2 supports. As shown in **Table 5.1**, the reduction degree of NiO is approximately 100% for $Ni/xNa/CeO_2$ catalysts except for $Ni/5Na/CeO_2$ and $Ni/10Na/CeO_2$ catalysts. A possible reason for obtaining reduction degree of >150 % for $Ni/5Na/CeO_2$ and $Ni/10Na/CeO_2$ catalysts is an underestimation of the H_2 consumption of $5Na/CeO_2$ and $10Na/CeO_2$ supports due to the partial reduction of the supports in the presence of excess Na. Therefore, the H_2 uptake values also further affirms that the solubility limit of Na^+ within the CeO_2 lattice is 2 wt%. Beyond the solubility limit of 2 wt%, excess Na deposits on the surface of CeO_2 support as Na_2O.

Table 5.1 Physicochemical parameters for Ni/xNa/CeO_2 catalysts

Catalyst	BET surface area (m^2/g)	Metal dispersion[a] (%)	Metal particle[b] size (nm)	Crystallite size[d] (nm)			Lattice parameter[e] (nm)		H_2 consumption[f] (mmol/g)	Reduction degree of NiO[g] (%)
				Ni [111]	NiO [200]	CeO_2 [111]	NiO [200]	CeO_2 [111]		
0Na/CeO_2	-	-	-	-	-	14.51	-	5.400	0.40	-
0.5Na/CeO_2	-	-	-	-	-	14.73	-	5.402	0.40	-
1Na/CeO_2	-	-	-	-	-	18.46	-	5.414	0.46	-
2Na/CeO_2	-	-	-	-	-	21.67	-	5.420	0.63	-
5Na/CeO_2	-	-	-	-	-	20.80	-	5.420	2.28	-
10Na/CeO_2	-	-	-	-	-	17.30	-	5.436	8.82	-
Ni/0Na/CeO_2	25.70	20.50	4.93	14.67	20.68	12.32	4.173	5.394	2.89	100
Ni/0.5Na/CeO_2	8.75	15.18	6.66	15.32	26.71	16.87	4.176	5.411	3.16	111
Ni/1Na/CeO_2	4.79	21.03	4.80	13.70	25.74	20.25	4.181	5.418	2.79	93.6
Ni/2Na/CeO_2	7.99	9.72	10.39	15.02	27.12	22.78	4.179	5.418	2.83	88.2
Ni/5Na/CeO_2	2.50	3.36	30.04	24.73	25.51	22.08	4.181	5.420	8.25	240*
Ni/10Na/CeO_2	0.42	3.81	26.54	27.42	27.06	19.15	4.180	5.419	12.9	166*

[a] Metal dispersion was calculated by N_2O chemisorption

[b] Metal particle size was determined by the expression, d= 101/metal dispersion(%)

[c] Metal particle size determined from TEM

[d] Crystallite size was determined by XRD with the Scherrer equation

[e] Lattice parameter was determined by the formula, $\alpha = \sqrt{h^2 + k^2 + l^2}(\frac{\lambda}{2sin\theta})$

[f] H_2 consumption below 900 °C in TPR profiles shown in **Figure 5.2**

[g] Reduction degree of NiO (%) $= 100 \times \frac{H_2 \, consumed \, by \, Ni \, metal}{(H_2 \, consumed \, by \, Ni \, metal)_{Ni/0Na/CeO_2}}$

[*] Reason for anomalous percentage of reduction degree of NiO can be found in main text

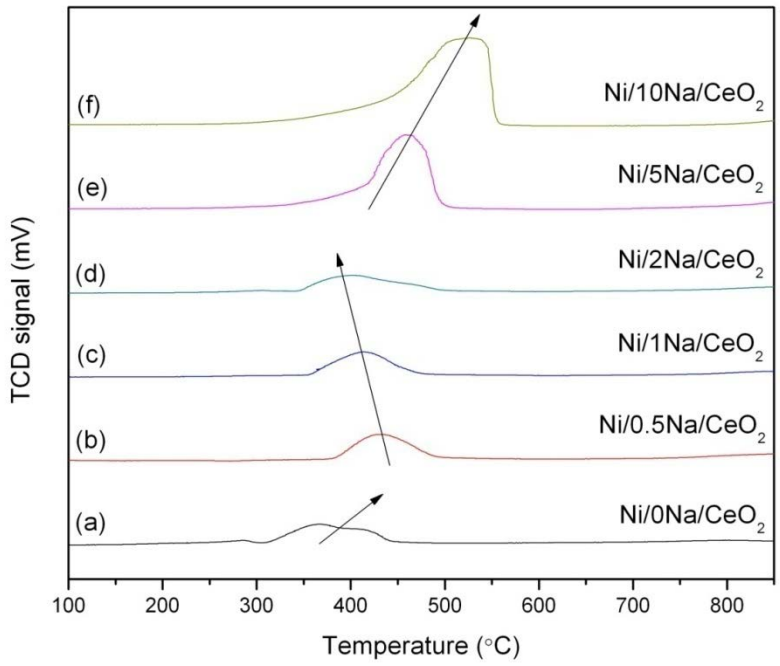

Figure 5-2 H_2-TPR profiles of (a) Ni/0Na/CeO_2, (b) Ni/0.5Na/CeO_2, (c) Ni/1Na/CeO_2, (d) Ni/2Na/CeO_2, (e) Ni/5Na/CeO_2, and (f) Ni/10Na/CeO_2 catalysts.

5.3.5 X-ray photoelectron spectroscopy (XPS)

An XPS study was conducted on the reduced Ni/xNa/CeO_2 catalysts in order to understand the oxidation states of the various surface species present during reaction. **Figure 5.3(a)** displays the Ni ($2p_{3/2}$) spectra of the reduced Ni/xNa/CeO_2 catalysts. The binding energies (BEs) of Ni metal and its satellite peak are 852.6 eV and 856.3 eV, respectively. Similarly, the BEs of Ni^{2+} in NiO and its two satellite peaks are 855.4 eV, 853.7 eV and 860.9 eV, respectively [43]. As evident from **Figure 5.3(a)**, as Na loading is increased from 0 wt% to 5 wt%, there is a clear shift in BE of Ni^0 from 852.3 eV to 852.1 eV. The downward shift of the Ni 2p BEs observed in Na-doped Ni/xNa/CeO_2 catalysts is indicative of interaction between Na and Ni and that the presence of Na^+ ions increases the

electron density on the Ni metal [44]. The Ni 2p spectra was deconvoluted corresponding to the Ni^0 and Ni^{2+} states, and the relative concentrations of the two states were calculated from the deconvoluted peaks. The relative concentration, Ni^0/Ni^{2+}, was found to be 0.649, 0.677, 0.888, 0.950, 0.419 and 0.712 for Ni/0Na/CeO_2, Ni/0.5Na/CeO_2, Ni/1Na/CeO_2, Ni/2Na/CeO_2 and Ni/5Na/CeO_2 and Ni/10Na/CeO_2 catalysts, respectively. XPS results of Ni/xNa/CeO_2 catalysts reveal that addition of Na facilitates the reduction of Ni in the Na-doped catalysts as shown by the higher relative concentration of Ni^0/Ni^{2+} for Na-doped catalysts. As shown later in DRIFTS study, nickel metal serves as the active metal sites for catalyzing the WGS reaction, thus greater ease in reduction of Ni^{2+} to Ni^0 is essential in achieving excellent WGS activity.

Figure 5.3(b) shows the core level spectrum for Ce 3d which is relatively complex due the presence of both Ce^{3+} and Ce^{4+} states. A total of 10 peaks were fitted: 3 doublets for CeO_2 and 2 doublets for Ce_2O_3. The 6 characteristic peaks for CeO_2 are labeled as v (882.4 eV), v" (888.7 eV), v''' (898.2 eV), u (900.9 eV), u" (907.3 eV) and u''' (916.5eV). On the other hand, the 4 characteristic peaks for Ce_2O_3 are labeled as v_0 (880.4 eV), v' (886.5 eV), u_0 (898.7 eV) and u' (902.9 eV) [3, 45]. As compared to Ni/0Na/CeO_2 catalyst, there is a significant shift in binding energy towards higher region. This indicates the possibility of Na^+ into CeO_2 lattice, leading to charge imbalance and lattice distortion of CeO_2. This distortion in turn generates oxygen vacancies, enabling oxygen adsorption on these vacancies [10, 45]. This finding correlates well with the H_2-TPR results,

which showed the shift towards lower reduction temperatures with the incorporation of up to 2 wt% Na.

Figure 5.3(c) shows the core level spectrum of O 1s. Three peaks are observed in the O 1s region. The first peak (O_I) at around 529 eV can be attributed to lattice oxygen (O^{2-}) in the ceria lattice, the second peak (O_{II}) at around 530 eV corresponds to adsorbed oxygen species, while the third peak (O_{III}) at around 532 eV corresponds to adsorbed water [46]. Similar to the Ce 3d spectra, with the introduction of Na, the binding energies generally shift towards higher binding energies. **Table 5.2** presents the surface composition of the reduced Ni/xNa/CeO_2 catalysts. Evidently, as Na loading increases, concentration of lattice oxygen decreases while concentration of adsorbed oxygen increases. This result is in agreement with the inference made from Ce 3d spectra as well as the H_2-TPR results that the inclusion of Na^+ into CeO_2 lattice generates oxygen vacancies which lead to higher amount of oxygen adsorption. The surface compositions of the reduced catalysts are also shown in **Table 5.2**. The surface Na concentration increases as Na loading increases, even at low Na loadings of 0 to 2 wt%. This trend may seemingly suggest that Na is deposited on the surface. However, bearing in mind that the sampling depth is generally approximately 3-10 nm depending on the mean free path of the photoelectrons in the material [47], the surface Na content detected could possibly include that contained in the ceria lattice. Moreover, it can be seen that the surface concentration of Ce remains approximately constant at about 18-20 at % with Na loading of 0 to 2 wt%. At

higher Na loadings of 5 wt% and 10 wt%, surface concentration of Ce drastically decreases to about 10 at%. This result further affirms the postulation that beyond 2 wt% Na loading, excess Na forms an overlayer on ceria particles, thereby reducing the surface Ce concentration.

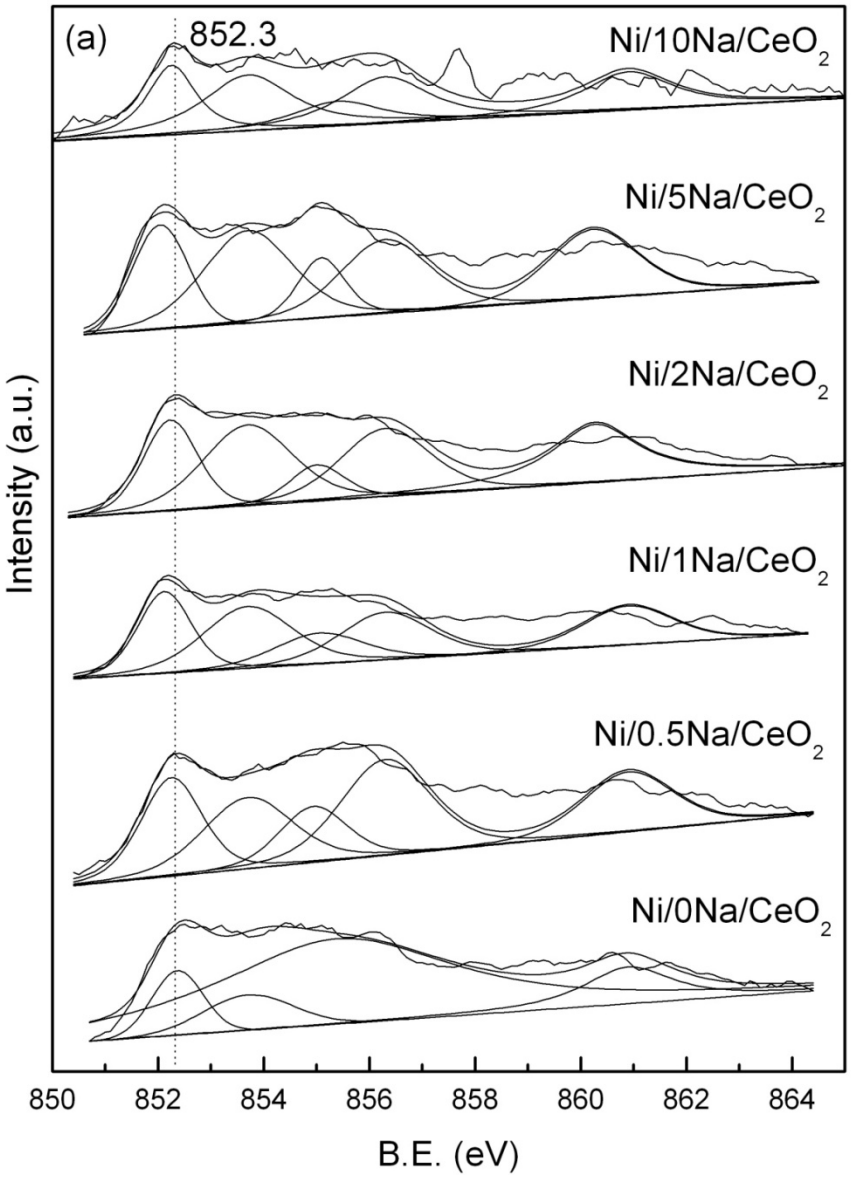

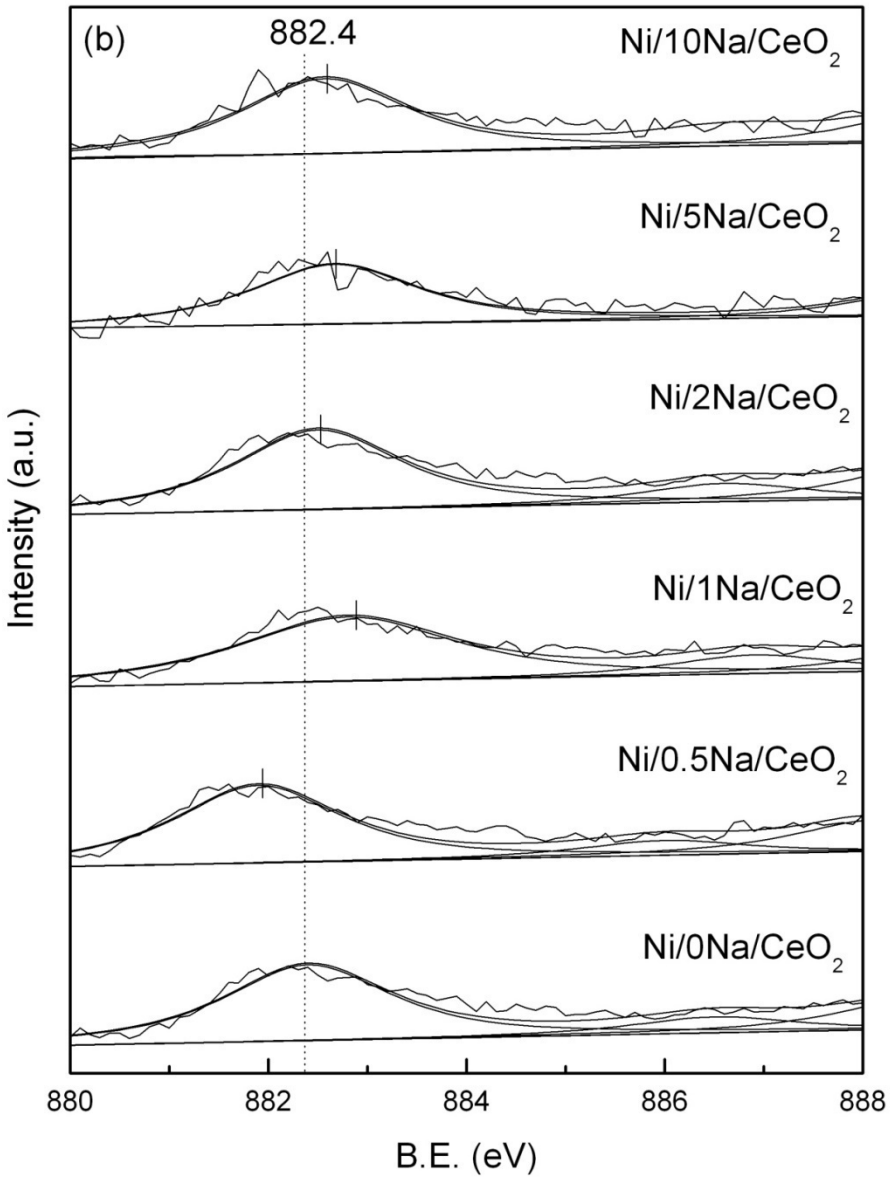
(b)
882.4
Ni/10Na/CeO2
Ni/5Na/CeO2
Ni/2Na/CeO2
Ni/1Na/CeO2
Ni/0.5Na/CeO2
Ni/0Na/CeO2
Intensity (a.u.)
880
882
884
886
888
B.E. (eV)

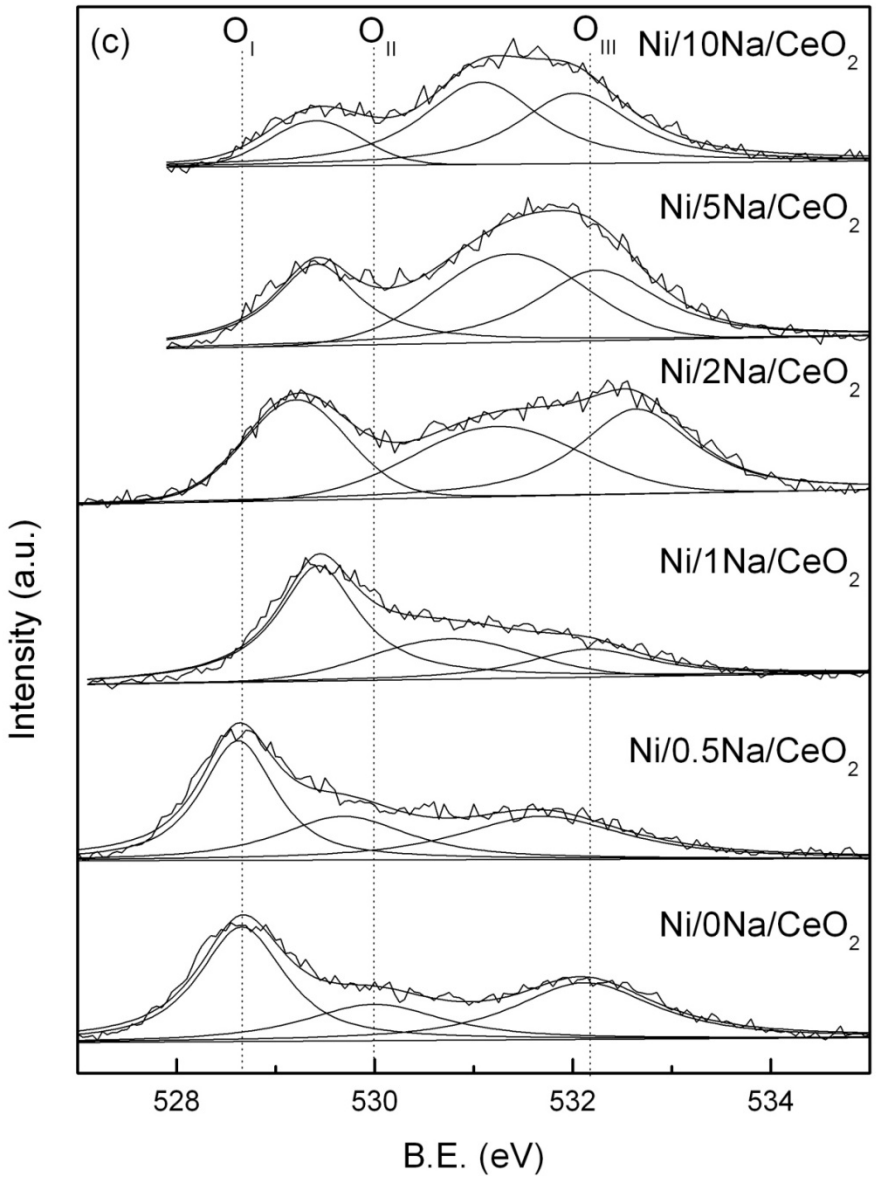

Figure 5-3 XPS spectra of Ni/xNa/CeO_2 catalysts for (a) Ni 2p, (b) Ce 3d and (c) O 1s.

Table 5.2 Surface composition derived from XPS

Catalyst	Oxygen concentration (%)			Cerium concentration (%)		Nickel ratio	Surface composition (at %)			
	Lattice oxygen	Adsorbed oxygen	Adsorbed water	$[Ce^{3+}]$	$[Ce^{4+}]$	$[Ni^0]/[Ni^{2+}]$	O	Ni	Na	Ce
$Ni/0Na/CeO_2$	43.1	22.1	34.8	13.7	86.3	0.649	76.84	2.77	0	20.39
$Ni/0.5Na/CeO_2$	40.9	26.2	32.8	12.6	87.4	0.677	72.45	2.13	3.89	21.53
$Ni/1Na/CeO_2$	56.0	25.1	18.9	10.4	89.6	0.888	68.47	3.48	6.83	21.21
$Ni/2Na/CeO_2$	30.1	32.6	37.3	10.1	89.7	0.950	70.47	1.86	9.68	18.00
$Ni/5Na/CeO_2$	29.5	36.7	33.8	9.30	90.7	0.419	72.98	2.19	13.28	11.55
$Ni/10Na/CeO_2$	14.3	46.8	38.9	9.87	90.1	0.712	67.65	1.90	20.63	9.82

5.3.6 Metal particle size of reduced catalysts

Figure 5.4 shows the HRTEM images of the reduced catalysts. From **Figure 5.4(a)**, **Figure 5.4(c)**, and **Figure 5.4(d)**, the particle size of CeO_2 are measured to be approximately 15.3 nm, 23.1 nm and 23.6 nm for Ni/0Na/CeO_2, Ni/2Na/CeO_2 and Ni/5Na/CeO_2 catalysts, respectively. The order of the ceria size is in agreement with quantitative analysis of crystal size obtained using XRD. In addition, as shown in **Figure 5.4(b)**, **Figure 5.4(d)** and **Figure 5.4(f)**, the lattice fringes are well defined, thus confirming the crystalline nature of the sample. The width of lattice fringe of 0.32 nm corresponds to (111) CeO_2. The metal particle size of Ni was unable to be clearly distinguished as they could possibly be buried underneath the ceria particles that have agglomerated partially after calcination at 650 °C. From the elemental mapping of Ni/2Na/CeO_2 catalyst as shown in **Figure 5.5**, Ni particle size can be estimated to be about 13.53 nm, which is similar to the particle size obtained via N_2O chemisorption (10.39 nm). In addition, **Figure 5.5(b)** which shows the elemental mapping of Na on the Ni/2Na/CeO_2 catalyst reveals that Na is well dispersed on the CeO_2 supports and do not agglomerate, further affirming the formation of Na-Ce-O solid solution.

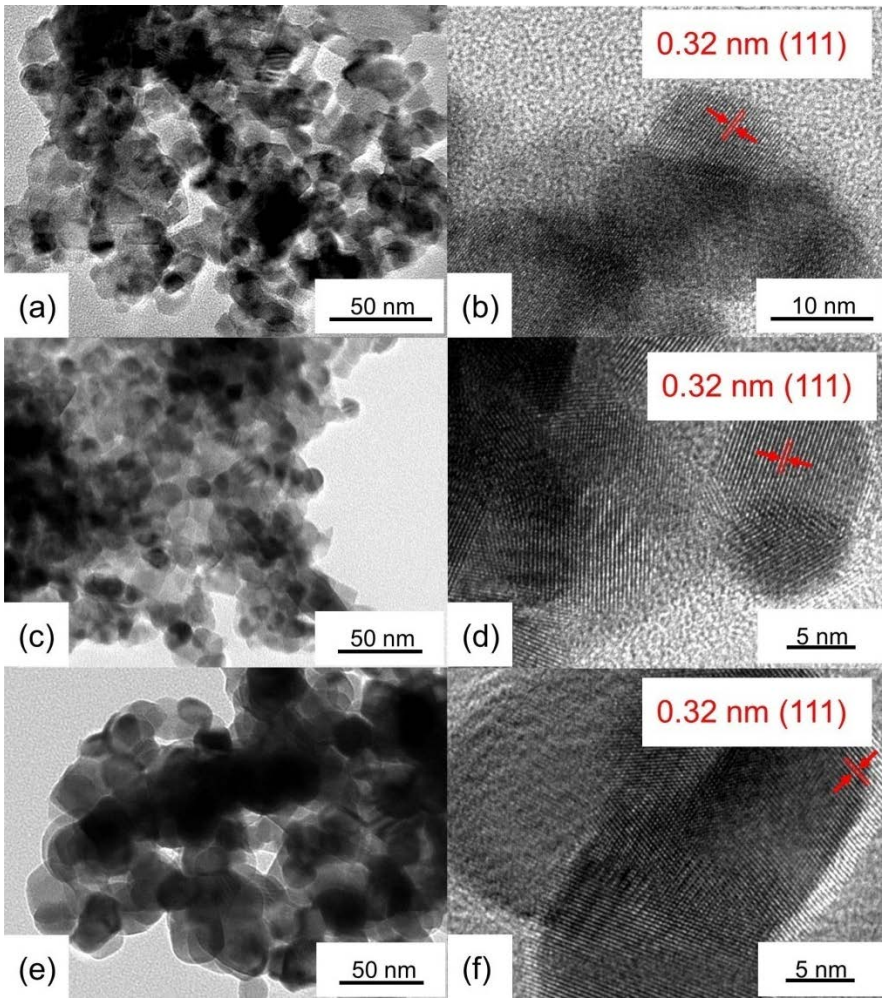

Figure 5-4 HRTEM images of reduced (a,b) Ni/0Na/CeO_2, (c,d) Ni/2Na/CeO_2, (e,f) Ni/5Na/CeO_2 catalysts.

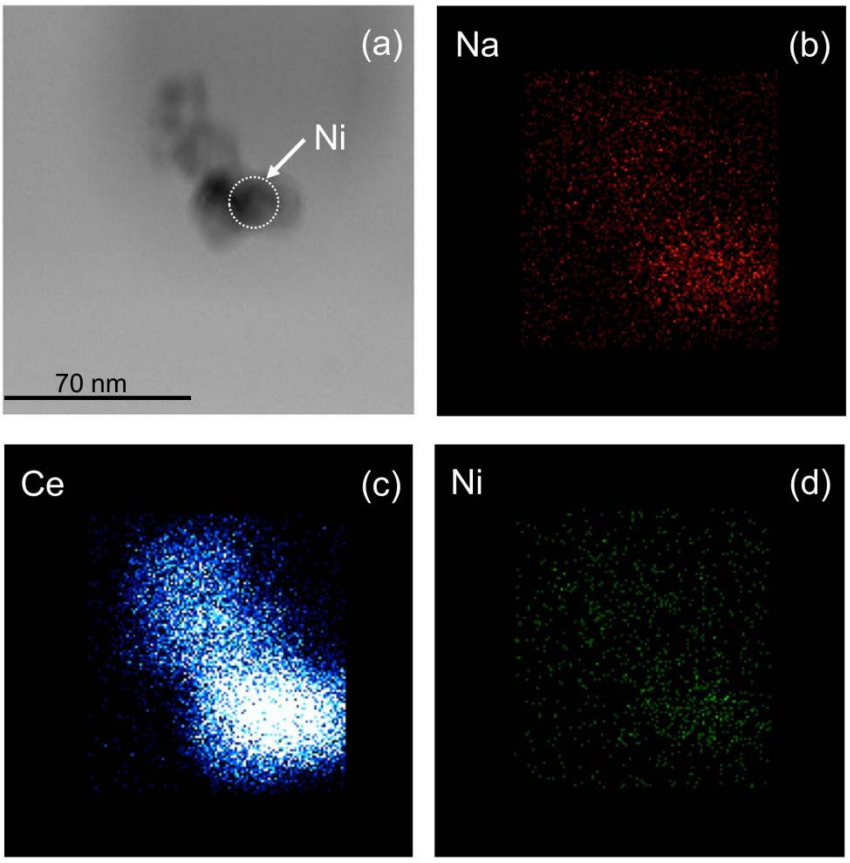

Figure 5-5 (a) HRTEM image of Ni/2Na/CeO_2 catalyst, and (b-d) corresponding EDS mapping images of (a) for Na, Ce, and Ni elements, respectively.

5.3.7 Catalytic activity and selectivity

Catalytic testing was conducted from 300°C to 600°C and **Figure 5.6(a)** displays the percentage of CO conversion to CO_2 against the reaction temperature for the Ni/xNa/CeO_2 catalysts. In general, Na-doped catalysts achieved better catalytic performance as compared to Ni/0Na/CeO_2 catalyst over the entire temperature range, with Ni/2Na/CeO_2 catalyst exhibiting the most superior performance. At 400°C, Ni/2Na/CeO_2 catalyst achieved a CO conversion of 97.5%, which is very close to that of the theoretical equilbrium level of CO conversion of 98.1%. As Na doping increases beyond 2 wt% to 5 and 10 wt%, CO

conversion decreases slightly to 97.1% and 94.4%, respectively. It has been shown that for Pt/CeO_2 catalysts, increasing alkali amount to levels that are too high will reduce the BET surface area of the catalyst, block the Pt surface sites and in turn reduce WGS activity. In contrast, at low levels of alkali, alkali promotes the WGS activity by weakening the formate C-H bond significantly [20]. Indeed, from BET analysis, the same trend of drastic reduction in surface area at high levels of Na doping was also observed. This could be the main attribute for the slight deterioration in catalytic activity observed in $Ni/5Na/CeO_2$ and $Ni/10Na/CeO_2$ catalysts. Besides displaying excellent WGS activity in terms of CO conversion to CO_2, the activity enhancement by $Ni/2Na/CeO_2$ catalyst was accompanied with an increase in selectivity towards WGS reaction. **Figure 5.6(b)** shows the percentages of CH_4 and H_2 yields at 400°C for all catalysts. As evident from **Figure 5.6(b)**, CH_4 yield is the highest at 1.93% for Na-free $Ni/0Na/CeO_2$ catalyst and abruptly decreases to a low value of 0.52% with the addition of 0.5 wt% Na before gradually decreasing to a gradual plateau as Na was increased from 0.5 to 10 wt%. Consequently, $Ni/0Na/CeO_2$ catalyst has the lowest H_2 yield of 43.5% while Na-doped catalysts generally achieved high H_2 yield of at least 46.0%. Therefore, incorporation of 2 wt% Na into Ni/CeO_2 catalyst was able to enhance the WGS activity, increase the selectivity towards WGS reaction and effectively suppress the side reaction, methanation.

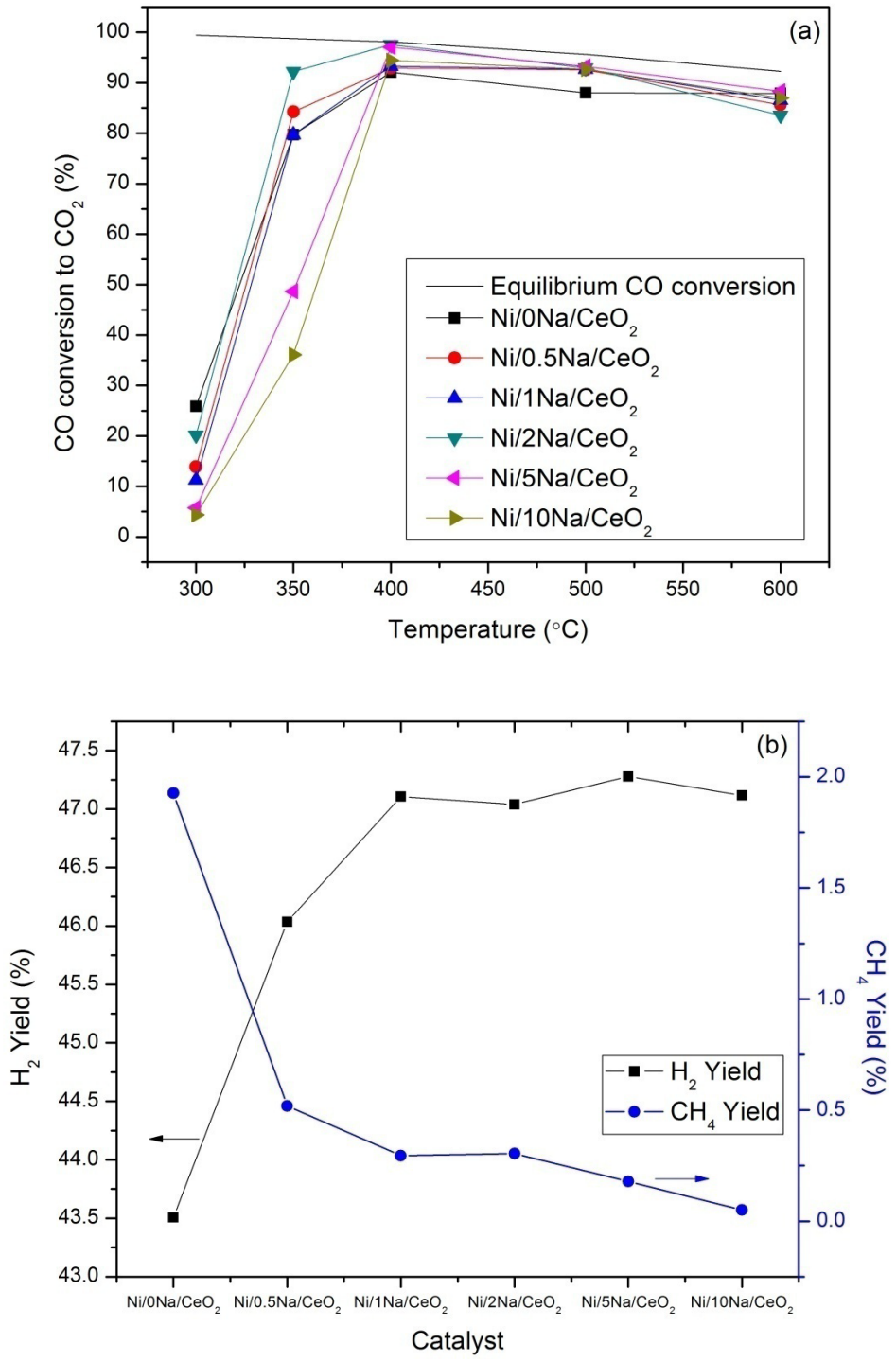

Figure 5-6 (a) Percentages of CO conversion to CO_2, and (b) H_2 and CH_4 percentage yields for Ni/xNa/CeO_2 catalysts.

Besides, stability test conducted for 100 h as shown in **Figure 5.7** reveals that Ni/2Na/CeO_2 is catalytically stable and remains selective towards WGS reaction throughout the 100 h runtime. Post-reaction characterization of the spent catalyst shows that the Ni metal crystallite size increased slightly from 15.0 to 20.4 nm (shown in Figure S2 in **Appendix B**) and TGA analysis (shown in Figure S3(b) of **Appendix B**) reveals no deposition of carbon (CH_4 precursor) on the spent catalyst. In addition, XPS analysis of the spent Ni/2Na/CeO_2 catalyst indicates no noticeable changes in the surface concentration of Na from the catalyst. The surface atomic concentrations of Na on Ni/2Na/CeO_2 catalyst are 9.7 at % and 7.7 at% before and after the reaction, respectively. Stability test for 100 h was also conducted for the Ni/0Na/CeO_2 catalyst. As compared to Ni/2Na/CeO_2 catalyst, it has a lower CO conversion and a higher CH_4 yield. Contrary to that of Ni/2Na/CeO_2 catalyst, TGA analysis of spent Ni/0Na/CeO_2 catalyst (shown in Figure S3(a) of **Appendix B**) shows deposition of adsorbed carbon (CH_4 precursor) after 100 h runtime, affirming the presence of adsorbed carbon as an intermediate for CH_4 formation.

In addition, the activity of the Ni/2Na/CeO_2 catalyst was also compared with other catalysts found in literature. The calculated TOF values, rate of hydrogen formation as well as the various operating conditions used in testing of different catalyst systems have been tabulated in **Table 5.3**. As evident from **Table 5.3**, the current Ni/2Na/CeO_2 catalyst has a lower TOF value than the Pt-based catalyst as reported by Zhu et al. [29] that was tested at 300 °C. However, it

showed more superior performance (in terms of TOF and hydrogen formation rate) as compared to conventional catalyst [48] and other Ni-based catalysts [49, 50] at higher temperature regions of >350 °C. A TOF value of 0.46 s^{-1} and hydrogen formation rate of 75.4 µmol/gcat.s was achieved with the Ni/2Na/CeO_2 catalyst. Hence, Ni/2Na/CeO_2 catalyst is a promising and highly active catalyst which can be utilized for WGS reactions conducted at higher temperatures of approximately 400 °C.

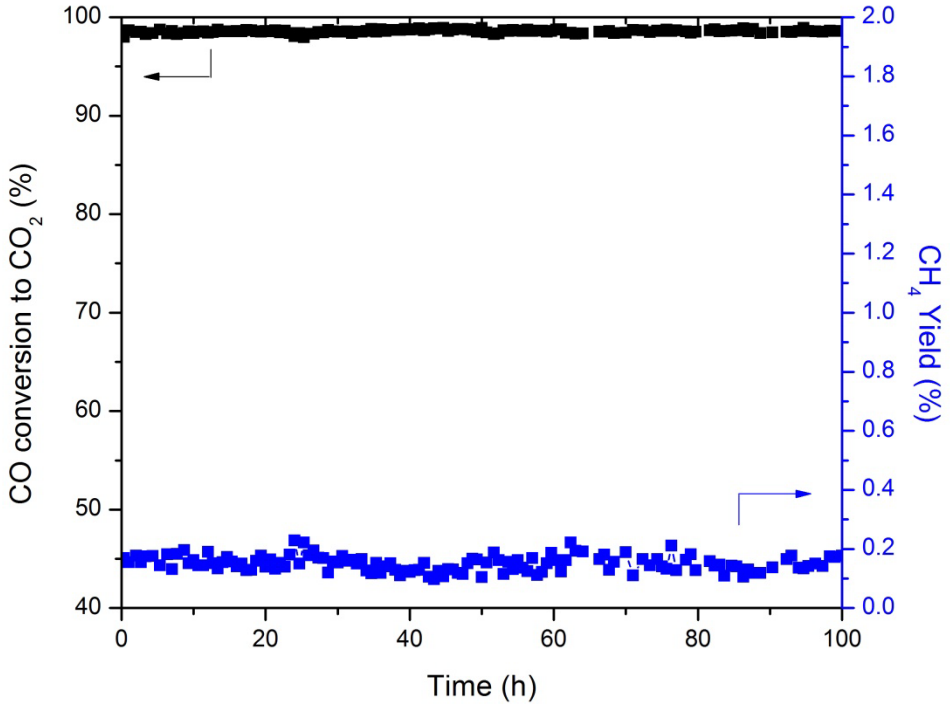

Figure 5-7 Percentages of CO conversion to CO_2 (left axis) and CH_4 yield (right axis) of Ni/2Na/CeO_2 catalyst for 100 h reaction.

Table 5.3 Comparison of water-gas shift rates of Ni/2Na/CeO_2 catalyst with other literature findings and the conventional catalyst

Catalyst	**Conditions**	**T/°C**	**TOF (s^{-1})**	**Rate (μmol H_2/gcat.s)**	**Reference**
Ni/2Na/CeO_2	7% CO, 22% H_2O, 10% CO_2, 20% H_2, balance He	400	0.46	75.4	This work
5Ni5Cu/CeO_2	7% CO, 22% H_2O, 10% CO_2, 20% H_2, balance He	350	0.013	18.5	[45]
3.9Pt/t-ZrO_2	6.8% CO, 21.9% H_2O, 8.5% CO_2, 37% H_2, balance Ar	250	0.4	40.0	[23]
1Pt-3Na-SiO_2	11% CO, 26% H_2O, 7% CO_2, 26% H_2, balance He	270	0.1-0.8	26.0	[27]
Pt/TiO_2	2.83% CO, 5.66% H_2O, 37.7% H_2, balance He	300	0.36	6.98	[29]
Pt-4Na/TiO_2	2.83% CO, 5.66% H_2O, 37.7% H_2, balance He	300	3.82	58.6	[29]
0.5Pt/0.06Na-TiO_2	3% CO, 10% H_2O, balance He	250	1.58	38.4	[25]
$Ce_{0.75}Cu_{0.1}Ni_{0.15}O_{2-\delta}$	1.3% CO, 35% H_2O, balance N_2	240	-	2.20	[40]
Ni_{20}/$CeLaO_x$	10% CO, 20% H_2O, balance He	400	-	35.6	[49]
CuO/Zn/Al_2O_3	7% CO, 22% H_2O, 8.5% CO_2, 37% H_2, balance Ar	200	-	7.60	[48]
1Re-10Ni/CeO_2	5% CO, 10% H_2O, balance He	300	-	30.0	[50]

5.3.8 In-situ DRIFTS

5.3.8.1 Interaction with CO-H_2 from 30 °C to 400 °C

To investigate the role of Na on the suppression of methane during WGS reaction, DRIFTS study was conducted by subjecting the reduced catalyst with continuous flow of CO and H_2 to simulate CO hydrogenation conditions. **Figure 5.8(a)** shows the FTIR spectra of Ni/0Na/CeO_2 catalyst reduced at 650°C and subjected to continuous flow of CO and H_2. At the carbonylic region, two bands at 2014 and 2035 cm^{-1} can be observed at 30°C. The band at 2014 cm^{-1}, assigned to CO linearly adsorbed on metallic Ni (Ni-CO), increases in intensity as temperature was raised from 30°C to 200°C. The increment in intensity of linear carbonyl suggests that CO is strongly chemisorbed on metallic nickel and there is a build-up of surface linear mono-carbonyl which eventually decomposed completely at 250°C. Below 250°C, the rate of linear CO decomposition is much slower than its adsorption, thus explaining the increase in intensity of linear mono-carbonyl band. In addition, a weak band observed at 2035 cm^{-1} can be assigned to CO on Ni modified by hydrogen atoms introduced during the reduction process. The assignment of this band is similar to that of Tabakova et al. where they have assigned 2040 cm^{-1} to be CO on $Au^{\delta-}$ modified by hydrogen atoms [51]. At 150°C, a broad shoulder band at 2086 cm^{-1}, assigned to subcarbonyl nickel species $Ni(CO)_n$ (n=2 or 3) appears and is red-shifted down to 2064 cm^{-1} as temperature was increased to 250°C [52]. This subcarbonyl band eventually disappears at 300°C. Concurrently, a significant increase of the bands

at 1370, 1565, 2843 and 2928 cm^{-1} due to the formate species adsorbed on reduced Ce^{3+} is also observed. The formation of formates is also accompanied by a gradual increase in intensity of negative band centred at 3662 cm^{-1} related to doubly bridging OH (Type II) species on Ce^{3+} [20, 53]. Subsequently, from 300°C to 400°C, a small band at 3016 cm^{-1}, assigned to gaseous CH_4 can also be observed [52, 54]. The disappearance of the subcarbonyl band at 300 °C followed by the subsequent appearance of the gaseous CH_4 band suggests that subcarbonyl species are precursors for methane formation.

The FTIR spectra of Ni/2Na/CeO_2 catalyst that is subjected to the same treatment is displayed in **Figure 5.8(b)**. Similar to Ni/0Na/CeO_2 catalyst, two carbonyl bands at 2013 and 2035 cm^{-1} assigned to linear mono-carbonyl and carbonyl adsorbed on H-modified nickel can be observed at 30°C respectively. Unlike Ni/0Na/CeO_2 catalyst, there was no increase in intensity observed for the band at 2013 cm^{-1}. Instead, the band red-shifted down from 2013 cm^{-1} to 2003 cm^{-1} as temperature was raised from 30°C to 200°C, indicating weaker C-O bond and a consequently stronger adsorption of linear mono-carbonyl on nickel. Another stark contrast between the two catalysts is the absence of subcarbonyl nickel species at 2064 cm^{-1}. In literature, it was observed in metals such as nickel and ruthenium that subcarbonyl metal species form preferentially on low coordinated nickel species at kink, corner or step positions [52, 55, 56]. The absence of this species in Ni/2Na/CeO_2 catalyst suggests that Ni does not exist as in a low coordinated state due to its interaction with Na.

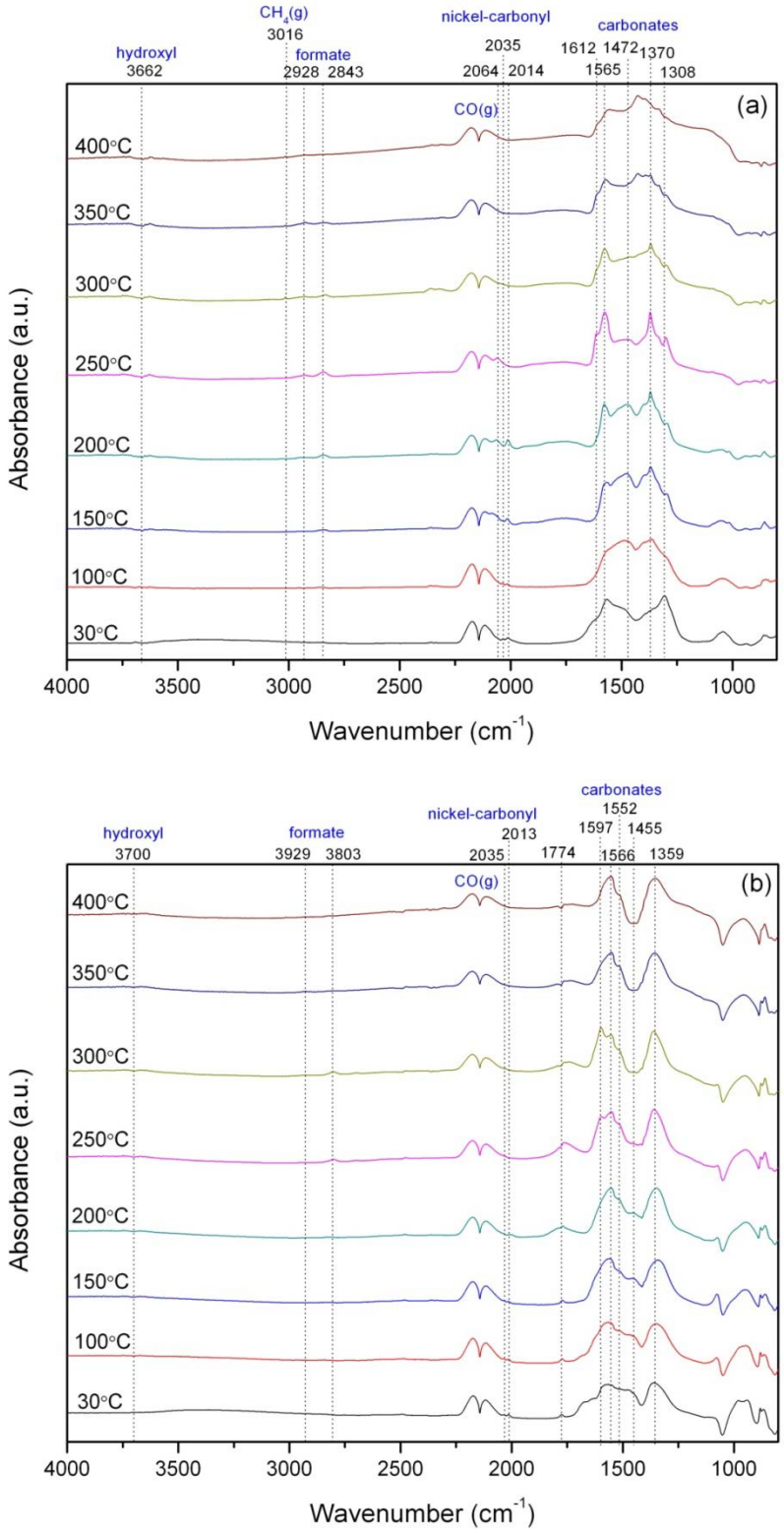

Figure 5-8 FTIR spectra of (a) Ni/0Na/CeO_2 and (b) Ni/2Na/CeO_2 catalysts under continuous flow of CO and H_2 at temperature increments of 50°C.

It has also been reported that alkali additives can migrate from the surface to the nickel surface. Additionally, DFT calculation study conducted by Bengaard et al. [57] has demonstrated that a stepped nickel surface is more active than close-packed terraces for reforming reaction and its reverse methanation process. This study has also concluded that alkali additives such as sodium preferentially adsorb to highly uncoordinated nickel atoms at step defect sites, thus blocking the active step sites that are responsible for catalyzing the methanation process. Likewise, Nakano et al. [58] investigated the carbon deposition from CO on a Ni (977) surface and found that CO dissociates at step edges. Building on these simulation works, we hypothesize that Na^+ may exist at the step/kink sites of Ni particles, blocking CO dissociation. Hence, DRIFTS studies were further conducted to study the interaction of Ni and Na, and it was found that subcarbonyl species do not form in the presence of Na.

Formate formation was also observed in the case of Ni/2Na/CeO_2 catalyst, as shown by the gradual increase in the intensity of weak bands at 1359, 1566, 2804 and 2929 cm^{-1} from 250°C to 300°C. In the main formate ν(C-H) stretching band region, Binet et al. have ascribed the band at ca. 2950 cm^{-1} to a coupling of the ν_s(OCO) mode with δ(CH) and the lower wavenumber number of ca. 2845 cm-1 to ν(C-H) to bridge-bonded formate [59]. As compared to Ni/0Na/CeO_2 catalyst, there is a clear decrease in the band position of ν(C-H) of Ni/2Na/CeO_2 catalyst, where there was insignificant change in the band assigned to ν_s(OCO) mode with δ(CH). This observation is consistent with Evin et al. where an

obvious decrease in the band position for ν(C-H) was observed for alkali-doped Pt/ceria catalysts [20]. The shift to lower wavenumber from 2843 cm^{-1} in $Ni/0Na/CeO_2$ catalyst to 2803 cm^{-1} in $Ni/2Na/CeO_2$ catalyst suggest that doping sodium had an impact on the strength of C-H bond. As summarized by Evin et al. [20], the effect of doping alkali can be due to three main reasons. The first possibility is alkali metal can exert an electronic effect on the molecule, inducing the weakening of the formate C-H bond, resulting in the shift to lower band position. The second postulation is the charge transfer from alkali to ceria, indirectly affecting the strength of formate C-H bond. The third reason proposed is alkali induces geometric or electronic changes such that the bonding of formate can transform from a bidentate mode to another mode such as monodentate. The delayed onset of formate formation on $Ni/2Na/CeO_2$ catalyst suggests that the reactivity of CO with OH groups on Ce^{3+} is lower in $Ni/2Na/CeO_2$ catalyst than that of $Ni/0Na/CeO_2$ catalyst. This can be attributed to the presence of more strongly held CO in $Ni/2Na/CeO_2$ than in $Ni/0Na/CeO_2$, inhibiting the formation of formates at lower temperatures. In addition, unlike $Ni/0Na/CeO_2$ catalyst, no gaseous CH_4 was observed at 300°C and beyond, indicating that $Ni/2Na/CeO_2$ catalyst is not selective towards CO hydrogenation to CH_4. The presence of formates in both $Ni/0Na/CeO_2$ and $Ni/2Na/CeO_2$ catalysts suggests that formate species serve as intermediates of WGS reaction or as spectators. From the above observations, it is unlikely that these formate species are the precursors for methane formation since they are also present in $Ni/2Na/CeO_2$ catalyst that has been shown to suppress methane formation during WGS reaction.

Deposition of carbon by CO dissociation and the subsequent formation of adsorbed hydrocarbon species have been reported to occur more readily on sites for weakly held CO than on sites for strongly held CO [56, 60]. Since subcarbonyl nickel species are more weakly held than linearly adsorbed CO, the subcarbonyl sites are more prone to carbon deposition than their linear counterparts. Hence, in the presence of nickel subcarbonyl species, Ni/0Na/CeO_2 catalyst has a higher tendency to form surface carbonaceous species which are precursors for methane formation as compared to Ni/2Na/CeO_2 catalyst which does not possess the subcarbonyl species.

5.3.9 The role of Na doping in Ni/xNa/CeO_2 catalysts

As proposed by Flytzani-Stephanopoulos and co-workers, alkali promotion (such as Na and K) serves to provide oxygen-containing (OH) species to the Pt atoms supported on silica that is otherwise not present, unlike on reducible ceria [26-28]. In the current system of Ni/2Na/CeO_2, similar phenomenon of oxygen-containing species was also observed. In addition to that, new insights with regards to the synergistic effect between Na and CeO_2 were also found to exist in the Ni/xNa/CeO_2 catalysts. Through H_2-TPR and XPS, it was shown that the inclusion of 2 wt% Na was able to increase the reducibility of the catalyst by generating oxygen vacancies which allows for greater adsorption of oxygen species. Hence, the use of reducible ceria as a support was able to generate more sites for oxygen adsorption as compared to non-reducible supports, such as SiO_2. Shinde and Madras has also attributed enhanced WGS rates to

higher H_2O dissociation induced by the creation of oxide vacancies due to ionic substitution of Pd and Ni ions into ceria lattice [3]. However, in the current system, the use of Na as a dopant was not only able to generate oxide vacancies, Na itself was also capable of providing oxygen species. Therefore, the synergism between Na and CeO_2 led to enhanced WGS rates observed with Ni/2Na/CeO_2 catalyst. Moreover, through DRIFTS studies, it was found that the interaction between Ni and Na resulted in less low-coordinated Ni particles which consequently hindered the formation of subcarbonyl species that are the precursors for CH_4 formation. The suppression of methane also played an important role in the enhancement of WGS rates.

5.4 Conclusion

The role of sodium in suppressing methanation during WGS activity can be summarized into two main attributes. Firstly, within the solubility limit of 2 wt%, Na^+ displaces Ce^{4+} in the CeO_2 lattice, generating oxygen vacancies and thereby increasing oxygen mobility. The enhanced oxygen mobility as evident from H_2-TPR is reflected in the highest catalytic activity achieved by Ni/2Na/CeO_2 catalyst. Secondly, methane production, which is generally agreed to undergo CO disproportionation and subsequent hydrogenation to CH_4, is largely inhibited in the presence of Na through the interaction of Na and Ni, possibly at step sites. Further DFT calculations and EXAFS studies have to be conducted to prove the hypothesis that Na^+ is located at the step sites of Ni particles. Through this work, it was found that the interaction of Na and Ni leads

to the absence of low coordinated Ni species, thereby preventing the formation of subcarbonyl nickel species which are the precursors for CO methanation reaction.

Supporting information (Appendix B)

XRD patterns of reduced Ni/xNa/CeO_2 catalysts (Figure S1), XRD pattern of spent Ni/2Na/CeO_2 catalyst after 100 h reaction (Figure S2), and TGA profiles of spent Ni/0Na/CeO_2 and Ni/2Na/CeO_2 catalysts after 100 h reaction (Figure S3) are attached in **Appendix B**.

5.5 References

[1] L.-Y. Gan, Y.-J. Zhao, J. Phys. Chem. C, 116 (2012) 16089.
[2] M.S. Lee, J.Y. Lee, D.-W. Lee, D.J. Moon, K.-Y. Lee, Int. J. Hydrogen Energ, 37 (2012) 11218.
[3] V.M. Shinde, G. Madras, Appl. Catal. B, 132-133 (2013) 28.
[4] N.V. Skorodumova, S.I. Simak, B.I. Lundqvist, I.A. Abrikosov, B. Johansson, Physical Review Letters, 89 (2002) 166601.
[5] J. Kašpar, P. Fornasiero, M. Graziani, Catal. Today, 50 (1999) 285.
[6] H.-W. Jen, G.W. Graham, W. Chun, R.W. McCabe, J.-P. Cuif, S.E. Deutsch, O. Touret, Catal. Today, 50 (1999) 309.
[7] G. Jacobs, P.M. Patterson, L. Williams, E. Chenu, D. Sparks, G. Thomas, B.H. Davis, Appl. Catal. A, 262 (2004) 177.
[8] G. Jacobs, B.H. Davis, Appl. Catal. A, 333 (2007) 192.
[9] D. Andreeva, I. Ivanov, L. Ilieva, M.V. Abrashev, Appl. Catal. A, 302 (2006) 127.
[10] Y. Li, Q. Fu, M. Flytzani-Stephanopoulos, Appl. Catal. B, 27 (2000) 179.
[11] Q. Fu, H. Saltsburg, M. Flytzani-Stephanopoulos, Science, 301 (2003) 935.
[12] D. Srinivas, C.V.V. Satyanarayana, H.S. Potdar, P. Ratnasamy, Appl. Catal. A, 246 (2003) 323.
[13] A. Martínez-Arias, M. Fernández-García, O. Gálvez, J.M. Coronado, J.A. Anderson, J.C. Conesa, J. Soria, G. Munuera, J. Catal., 195 (2000) 207.
[14] S. Zhao, R.J. Gorte, Appl. Catal. A, 277 (2004) 129.
[15] A. Guerrero-Ruiz, A. Sepúlveda-Escribano, I. Rodríguez-Ramos, Appl. Catal. A, 120 (1994) 71.
[16] S. Park, J.M. Vohs, R.J. Gorte, Nature, 404 (2000) 265.
[17] K. Eguchi, Setoguchi, T., Inoue, T., Arai, H., Solid State Ionics, 52 (1992) 165.
[18] S. Fabris, S.d. Gironcoli, S. Baroni, G. Vicario, G. Balducci, Physical Review B, 71 (2005) 041102.
[19] A.B. Kehoe, D.O. Scanlon, G.W. Watson, Chemistry of Materials, 23 (2011) 4464.
[20] H. Evin, G. Jacobs, J. Ruiz-Martinez, G. Thomas, B. Davis, Catal. Lett., 120 (2008) 166.
[21] L.Z. Linganiso, G. Jacobs, K.G. Azzam, U.M. Graham, B.H. Davis, D.C. Cronauer, A.J. Kropf, C.L. Marshall, Appl. Catal. A, 394 (2011) 105.
[22] J.M. Pigos, C.J. Brooks, G. Jacobs, B.H. Davis, Appl. Catal. A, 328 (2007) 14.
[23] H. Xie, J. Lu, M. Shekhar, J.W. Elam, W.N. Delgass, F.H. Ribeiro, E. Weitz, K.R. Poeppelmeier, ACS Catal., 3 (2013) 61.
[24] J.H. Pazmiño, M. Shekhar, W. Damion Williams, M. Cem Akatay, J.T. Miller, W. Nicholas Delgass, F.H. Ribeiro, J. Catal., 286 (2012) 279.
[25] P. Panagiotopoulou, D.I. Kondarides, J. Catal., 267 (2009) 57.
[26] B. Zugic, D.C. Bell, M. Flytzani-Stephanopoulos, Appl. Catal. B, 144 (2014) 243.

[27] Y. Zhai, D. Pierre, R. Si, W. Deng, P. Ferrin, A.U. Nilekar, G. Peng, J.A. Herron, D.C. Bell, H. Saltsburg, M. Mavrikakis, M. Flytzani-Stephanopoulos, Science, 329 (2010) 1633.
[28] Y. Wang, Y. Zhai, D. Pierre, M. Flytzani-Stephanopoulos, Appl. Catal. B, 127 (2012) 342.
[29] X. Zhu, M. Shen, L.L. Lobban, R.G. Mallinson, J. Catal., 278 (2011) 123.
[30] C.M.Y. Yeung, K.M.K. Yu, Q.J. Fu, D. Thompsett, M.I. Petch, S.C. Tsang, J. Am. Chem. Soc. Comm., 127 (2005) 18010.
[31] P.-L. Chen, I.-W. Chen, Journal of American Ceramic Society, 79 (1996) 1793.
[32] J.-S. Lee, K.-H. Choi, B.-K. Ryu, B.-C. Shin, I.-S. Kim, Materials Research Bulletin, 39 (2004) 2025.
[33] H. Inaba, T. Nakajima, H. Tagawa, Solid State Ionics, (1998) 263.
[34] S. RD, P. CT, Acta Crystallographica Section B, 25 (1969) 925.
[35] S. RD, P. CT, Acta Crystallographica Section B, 26 (1970) 1046.
[36] Y. Wang, A. Zhu, Y. Zhang, C.T. Au, X. Yang, C. Shi, Appl. Catal. B, 81 (2008) 141.
[37] I. Pashalidis, C.R. Theocharis, Stud. Surf. Sci. Catal., 128 (2000) 643.
[38] W. Shan, M. Luo, P. Ying, W. Shen, C. Li, Appl. Catal. A, 246 (2003) 1.
[39] H. Song, U.S. Ozkan, J. Phys. Chem. A, 114 (2010) 3796.
[40] V.M. Shinde, G. Madras, Appl. Catal. B, 123-124 (2012) 367.
[41] G. Jacobs, T.K. Das, Y. Zhang, J. Li, G. Racoillet, B.H. Davis, Appl. Catal. A, 233 (2002) 263.
[42] R. Watanabe, Y. Sakamoto, K. Yamamuro, S. Tamura, E. Kikuchi, Y. Sekine, Appl. Catal. A, 457 (2013) 1.
[43] M.C. Biesinger, B.P. Payne, L.W.M. Lau, A. Gerson, R.S.C. Smart, Surf. Interface Anal., 41 (2008) 324.
[44] L.F. Liotta, G.A. Martin, G. Deganello, J. Catal., 164 (1996) 322.
[45] E.T. Saw, U. Oemar, X.R. Tan, Y. Du, A. Borgna, K. Hidajat, S. Kawi, J. Catal., 314 (2014) 32.
[46] U. Oemar, M.L. Ang, W.F. Hee, K. Hidajat, S. Kawi, Appl. Catal. B, 148–149 (2014) 231.
[47] D.R. Vij, Springer US, 2006.
[48] A.A.P. N.A. Koryabkina, W.F. Ruettinger, R.J. Farrauto, and F.H. Ribeiro, J. Catal., 217 (2003) 233.
[49] J.-H. Lin, P. Biswas, V.V. Guliants, S. Misture, Appl. Catal. A, 387 (2010) 87.
[50] T.S. Kingkaew Chayakul, Sunantha Hengrasmee, Catal. Today, 175 (2011) 420.
[51] F.B. Tatyana Tabakova, Maela Manzoli, Donka Andreeva, Appl. Catal. A, 252 (2003) 385.
[52] M. Agnelli, H.M. Swaan, C. Marquez-Alvarez, G.A. Martin, C. Mirodatos, J. Catal., 175 (1998) 117.
[53] C.B.a.J.-C.L. Ahmed Badri, J. Chem. Soc., Faraday Trans., 92 (1996) 4669.

[54] L. Barrio, A. Kubacka, G. Zhou, M. Estrella, A. Martínez-Arias, J.C. Hanson, M. Fernández-García, J.A. Rodriguez, J. Phys. Chem. C, 114 (2010) 12689.
[55] R.A.D. Betta, Journal of Physical Chemistry 79 (1975) 2519.
[56] H. Yamasaki;, Y. Kobori;, S. Naito;, T. Onishi;, K. Tamaru;, Journal of the Chemical Society, Faraday Transactions 1, 77 (1981) 2913.
[57] H.S. Bengaard, J.K. Nørskov, J. Sehested, B.S. Clausen, L.P. Nielsen, A.M. Molenbroek, J.R. Rostrup-Nielsen, J. Catal., 209 (2002) 365.
[58] H. Nakano, S. Kawakami, T. Fujitani, J. Nakamura, Surf. Sci., 454-456 (2000) 295.
[59] C. Binet, M. Daturi, J.-C. Lavalley, Catal. Today, 50 (1999) 207.
[60] S. Ichikawa;, H. Poppa;, M. Boudart, J. Catal., 91 (1985) 1.

Chapter 6 High-Temperature Water-Gas Shift Reaction over Ni/xK/CeO_2 Catalysts: Suppression of Methanation via Formation of Bridging Carbonyls

As an extension to the previous chapter on the investigation of role of sodium, this chapter studies the effect of potassium (K) loading on ceria-supported nickel (Ni/xK/CeO_2) catalysts over water-gas shift reaction. An optimum loading of 5 wt% K was found to enhance the catalytic performance in terms of activity and selectivity. As evidenced by DRIFTS, the methane suppressing effect of K is attributed to the inhibition of formation of nickel subcarbonyl species through interaction of Ni and K, coupled with the strong adsorption of carbon monoxide (CO) on Ni via the formation of bridging carbonyls. Additionally, K was found to enhance reduction of CeO_2 via XANES and promote water dissociation on reduced CeO_2 to form hydroxyl (OH) groups which dissociates further into adsorbed oxygen that react with adsorbed CO on Ni to form adsorbed carbon dioxide (CO_2). A dual-site redox mechanism was proposed and a good fit of the kinetic data with $R^2 = 0.91$ was obtained with the proposed kinetic model.

6.1 Introduction

Alkali metals are well known for suppressing carbon formation in reforming reactions by either neutralizing the acidity of the support as they are electron-donating, termed the ‘electronic effect’ [1] or by physically blocking or modifying the active metal sites that are responsible for catalyzing methanation,

termed the ‘geometric effect’ and ‘ensemble effect’ respectively [2, 3]. Besides suppressing carbon deposition, the effect of addition of alkali metals can manifest in one or more aspects, such as increasing the activity and/or selectivity, acting as modifiers, or even increasing the lifespan of a catalyst. Depending on the type of metal and reaction, the role of alkali metals may differ. However, a general consensus is that alkali metal atoms, being electron-donating, enhance the electron density of the transition metal either directly or via the support (electronic effect). This in turn affects the interaction path of the metal with reactants and/or products, ultimately affecting the activity-selectivity pattern of the catalyst [4]. This role of electron-donating or withdrawing additives in modifying chemisorption properties of transition metals has been termed as the ‘electronic ligand effect’ [5].

Extensive research has been conducted to study the promotion effect of alkali metals in WGSR [6-10] and it can be generally classified into three main attributes: (1) the generation of weakly basic hydroxyl (–OH) groups, (2) enhanced decomposition rate of formate intermediate, and (3) modification of the physicochemical properties of support. Since the effect of different alkali metals and their corresponding loadings are unequivocal, it is of great interest to investigate the effect the alkali metal doping on the WGS activity. In the preceding chapter, the promotion effect of Na had been elucidated to be that of generation of more oxide vacancies for oxygen adsorption due to Na substitution into the CeO_2 lattice. In addition, the effect of Na on methane suppression was

attributed to the strong interaction between Na and Ni, leading to the absence of subcarbonyl species which are responsible for methanation [11]. Moving forward, it is the objective of this work is to elucidate the role of K on the activity and selectivity of Ni/CeO_2 catalysts in the WGSR.

6.2 Experimental

6.2.1 Catalyst preparation

6.2.1.1 Preparation of K-doped ceria support

Nanosized ceria support was prepared by the reverse microemulsion method according to a procedure described elsewhere [12]. The yellow solid product was dried in a vacuum oven overnight and calcined at a heating rate of 2°C/min in static air for 2 h. The calcined pure CeO_2 support was then doped with K via the wet-impregnation method. K loading in xK/CeO_2 supports was varied with x=0, 1, 2, 5 and 10 wt%. The weight percentages of K refer to the final weight percentages of K in the respective $Ni/xK/CeO_2$ catalysts. The typical procedure for preparing $5K/CeO_2$ support is as follows. Potassium nitrate, KNO_3 (0.041176 g) (Sigma-Aldrich) was dissolved in 10.000 ml of de-ionized water, and the aqueous solution was then mixed with 0.70000 g of calcined pure CeO_2 support to obtain the required K loading. The mixture was dried under constant stirring at 80 °C and further dried at 100 °C for another 24 h before it was calcined at 650 °C with a heating rate of 2 °C/min in static air for 2 h.

6.2.1.2 Nickel impregnation on K-doped support

Upon yielding the K-doped CeO_2 supports, an aqueous solution containing the required nickel(II) nitrate hexahydrate, $Ni(NO_3)_2.6H_2O$ (Sigma-Aldrich) was mixed with the requisite amount of K-doped CeO_2 support to obtain the 10 wt% Ni/xK/CeO_2 catalysts. The mixtures were then dried under constant stirring at 80 °C and further dried at 100 °C for another 24 h before they were calcined at 650 °C with a heating rate of 2 °C/min in static air for 2 h.

6.2.2 Catalyst characterization

BET, N_2O pulse titration, XRD, H_2-TPR, XAS, CO-TPR-MS, XPS and DRIFTS were employed to characterize the Ni/xK/CeO_2 catalysts. The details of these characterization techniques are described in Section 3.4 and in particular, the details of XAS technique follow the description covered in as Section 3.4.8.2. For analyses which required catalyst reduction, the reduction condition employed for Ni/xK/CeO_2 catalysts was 650 °C for 1 h.

6.2.3 Catalyst activity and kinetic measurements

The procedures for catalyst activity testing of Ni/xK/CeO_2 catalysts follow the description stated in Section 3.2. Kinetic measurements were conducted according the procedures described in Section 3.3. Stability test was conducted for Ni/5K/CeO_2 catalyst for 100 h.

6.3 Results and discussion

6.3.1 BET surface area

The BET surface area of Ni/xK/CeO_2 catalysts is shown in **Table 6.1**. With increased loading of K, the surface area of the catalysts decreased greatly. This can be attributed to the blockage of pores brought about by the penetration of K into the pores of ceria support during impregnation as well as the change in the textural properties of ceria due to the introduction of K.

6.3.2 N_2O pulse titration

The metal dispersion in reduced Ni/xK/CeO_2 catalysts was measured using N_2O pulse titration. As shown in **Table 6.1**, metal dispersion decreases upon increasing K loading. The reduction in metal dispersion can be attributed to the decrease in surface area. However, as shown by the catalytic results presented later, the reduction in metal dispersion did not pose a negative effect on the WGS activity for Ni/xK/CeO_2 catalysts with higher loadings.

6.3.3 X-ray diffraction (XRD)

The crystalline phases of the catalysts were analyzed using XRD and identified from the XRD patterns for the fresh, calcined catalysts are shown in **Figure 6.1**. The face-centred cubic structure of NiO (JCPDS No. 04-0835) and the cubic fluorite structure of CeO_2 (JCPDS No. 00-043-1002) are present in all samples. The lattice parameters and crystallite sizes of NiO and Ce derived using Bragg's law and Scherrer's equation respectively have been displayed in **Table 6.1**. The average crystallite sizes of NiO were determined by line broadening of

(200) line of NiO at about 2θ=43.3°. Ni crystallite sizes were approximated to be 15.6, 16.8, 16.3, 20.6, and 18.0 nm for Ni/0K/CeO_2, Ni/1K/CeO_2, Ni/2K/CeO_2, Ni/5K/CeO_2 and Ni/10K/CeO_2 catalysts, respectively. Similarly, average crystallite sizes for CeO_2 were determined by line broadening of (111) at about 2θ=28.6° and were estimated to be 11.5, 11.5, 12.6, 15.3, and 15.7 nm for Ni/0K/CeO_2, Ni/1K/CeO_2, Ni/2K/CeO_2 Ni/5K/CeO_2 and Ni/10K/CeO_2 catalysts, respectively. There is a gradual increase in ceria crystallite size as K loading increases. Since the ionic radii of K^+ (0.151 nm) is much larger than that of Ce^{4+} (0.097 nm). K^+ is likely to be deposited on the surface of CeO_2 and does not undergo ionic substitution in the CeO_2 lattice [13].

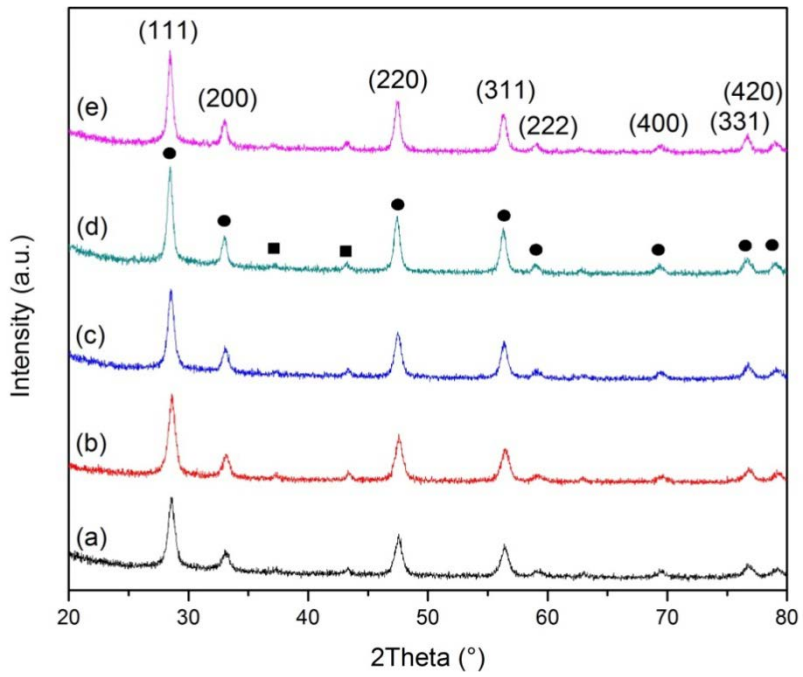

Figure 6-1 XRD patterns of freshly calcined (a) Ni/0K/CeO_2, (b) Ni/1K/CeO_2, (c) Ni/2K/CeO_2, (d) Ni/5K/CeO_2, and (e) Ni/10K/CeO_2 catalysts. Circles denote CeO_2 phase and squares denote NiO phase.

6.3.4 H_2-temperature-programmed-reduction (H_2-TPR)

H_2-TPR profiles for Ni/xK/CeO_2 catalysts are reported in **Figure 6.2**. In general, three main reduction peaks can be distinguished. The first low temperature peak at about 283 °C can be ascribed to Ni species which are weakly interacting with the CeO_2 support and this peak is more easily discerned on the un-promoted Ni/0K/CeO_2 catalyst as compared to K-doped catalysts, indicating that the introduction of K reduces the formation of weakly interacting NiO species The second reduction peak is centred at around 360 °C. On a closer observation, these major reduction peaks of Ni/xK/CeO_2 (x=0-2 wt%) catalysts are composed of two signals; a dominant peak at about 360 °C and a shoulder peak at about 400 °C. The dominant peak can be attributed to the reduction of Ni^{2+} to Ni^0 and probably to the reduction of surface capping oxygen of ceria, while the shoulder peak can be ascribed to the reduction of Ni^{2+} that is interacting with both K and CeO_2 [11, 14]. As K loading increases from 0 to 5 wt%, the dominant reduction peak shifts from 359 °C (in Ni/0K/CeO_2) to 420 °C (in Ni/5K/CeO_2), and the contribution by the shoulder peak increases, indicating stronger metal-support interaction in the presence of K. Lastly, the third reduction peak which is broad and centered at around 800 °C can be attributed to the reduction of bulk oxygen in CeO_2. Similar shifts to higher reduction temperatures upon loading of K were also observed in the case of K-doped Co/SiO_2 catalysts for the Fischer-Tropsch reaction and XANES measurements further indicated interaction of K with both Co and SiO_2 phases [15]. In addition, Weng et al. also reported that a small amount of potassium nitrate was found to enhance metal-support contact in K-

doped Cu/CeO_2 catalyst due to its low melting point, whereas excess potassium nitrate negated the promotional effect of Cu by decreasing the interfacial contact between Cu and CeO_2 [16]. In the case of $Ni/xK/CeO_2$ catalysts, further increment in K loading to 10 wt% weakens the metal-support interaction and decreases the reduction temperature to about 350°C. Furthermore, excessive amount of K at 10 wt% also resulted in inhomogeneity of Ni dispersion as evident from the sharp peak at 353 °C which can be assigned to weakly interacting Ni species in the presence of K. The detrimental effect of excessive K is also further affirmed by N_2O pulse titration calculations that are tabulated in **Table 6.1** which shows that $Ni/10K/CeO_2$ catalyst has the lowest Ni dispersion value of 4.39%.

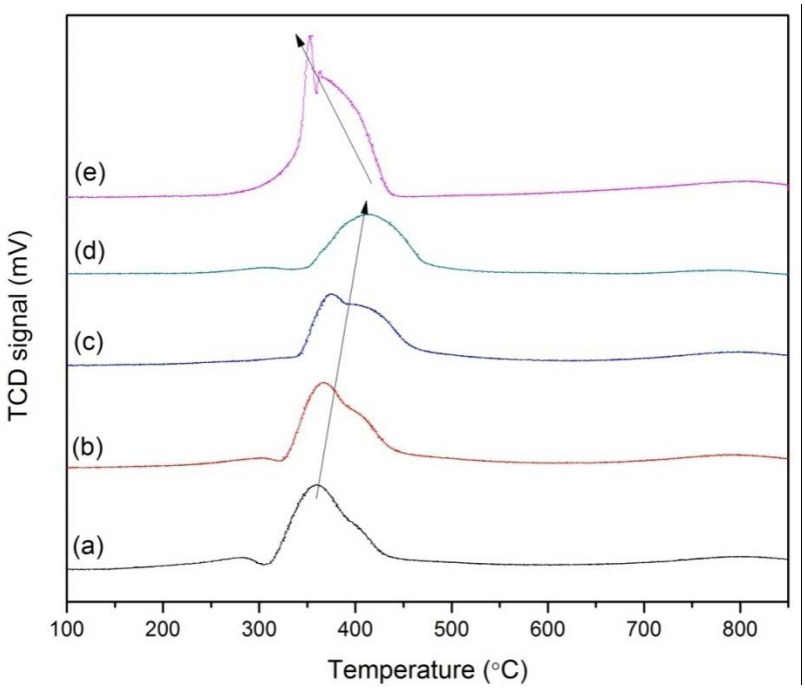

Figure 6-2 H_2-TPR profiles of (a) $Ni/0K/CeO_2$, (b) $Ni/1K/CeO_2$, (c) $Ni/2K/CeO_2$, (d) $Ni/5K/CeO_2$, and (e) $Ni/10K/CeO_2$ catalysts.

Table 6.1 Physicochemical parameters for Ni/xK/CeO_2 catalysts

Catalyst	BET surface area (m^2/g)	Metal dispersion[a] (%)	Metal particle size[b] (nm)	Crystallite size[c] (nm)			Lattice parameter[d] (nm)		H_2 consumption[e] (mmol/g)	Rate[f] (μmol/m^2.s)
				Ni [111]	NiO [200]	CeO_2 [111]	NiO [200]	CeO_2 [111]		
0K/CeO_2	-	-	-	-	-	-	-	-	15.4	-
1K/CeO_2	-	-	-	-	-	-	-	-	5.41	-
2K/CeO_2	-	-	-	-	-	-	-	-	8.64	-
5K/CeO_2	-	-	-	-	-	-	-	-	8.80	-
10K/CeO_2	-	-	-	-	-	-	-	-	37.3	-
Ni/0K/CeO_2	25.7	11.3	8.95	20.9	15.6	11.5	4.18	5.41	56.1	0.219
Ni/1K/CeO_2	10.5	6.46	15.6	21.5	16.2	11.5	4.17	5.40	55.6	0.273
Ni/2K/CeO_2	7.04	5.72	17.7	20.7	16.3	12.6	4.18	5.42	57.6	0.284
Ni/5K/CeO_2	3.07	4.54	22.2	21.9	20.6	15.3	4.19	5.43	57.9	0.333
Ni/10K/CeO_2	4.09	4.39	23.0	22.9	18.0	15.7	4.18	5.43	75.7	0.403

[a] Metal dispersion was calculated by N_2O pulse titration

[b] Metal particle size was determined by the expression, d= 101/metal dispersion(%)

[c] Crystallite size was determined by XRD with the Scherrer equation

[d] Lattice parameter was determined by the formula, $\alpha = \sqrt{h^2 + k^2 + l^2}(\frac{\lambda}{2sin\theta})$

[e] H_2 consumption below 650 °C in TPR profiles shown in Figure 6.2

[f] Catalytic rate per unit active Ni metal surface area measured at 400 °C

6.3.5 X-ray absorption spectroscopy (XAS)

The physico-chemical state of nickel and cerium after reduction has been explored by means of XAS. Specifically, the x-ray absorption near edge structure (XANES) region of XAS is used to probe the elemental oxidation states of the reduced samples. The oxidation states of Ni were studied by comparing the XANES spectra of the reduced Ni/CeO_2 and $Ni/5K/CeO_2$ catalysts with Ni foil as the reference. From **Figure 6.3(a)**, the XANES spectra of both reduced catalysts present white lines and pre-edge that is similar to that of the Ni foil, indicating that the NiO phase in both catalysts have been completely reduced to Ni^0 at 650 °C, and this result is in agreement with the H_2-TPR results presented above.

The extended x-ray absorption fine structure (EXAFS) oscillations obtained from the Ni K-edge XAS spectra and the Fourier transform (FT) functions derived for the reduced catalysts are presented in **Figure 6.3(b)** and the structural parameters derived from EXAFS analysis are presented in **Table 6.2**. The FT functions obtained from the reduced catalysts are similar to that of Ni foil, further affirming that nickel has been completely reduced to metallic state. Fitting analysis of the main peak that is ascribed to first Ni-Ni coordination shell at around 2-3 Å for Ni/CeO_2 catalyst yields a coordination number (CN) of 10.2 at a distance of 2.48 Å. On the other hand, for $Ni/5K/CeO_2$ catalyst, a CN of 10.5 at a distance of 2.48 Å was derived.

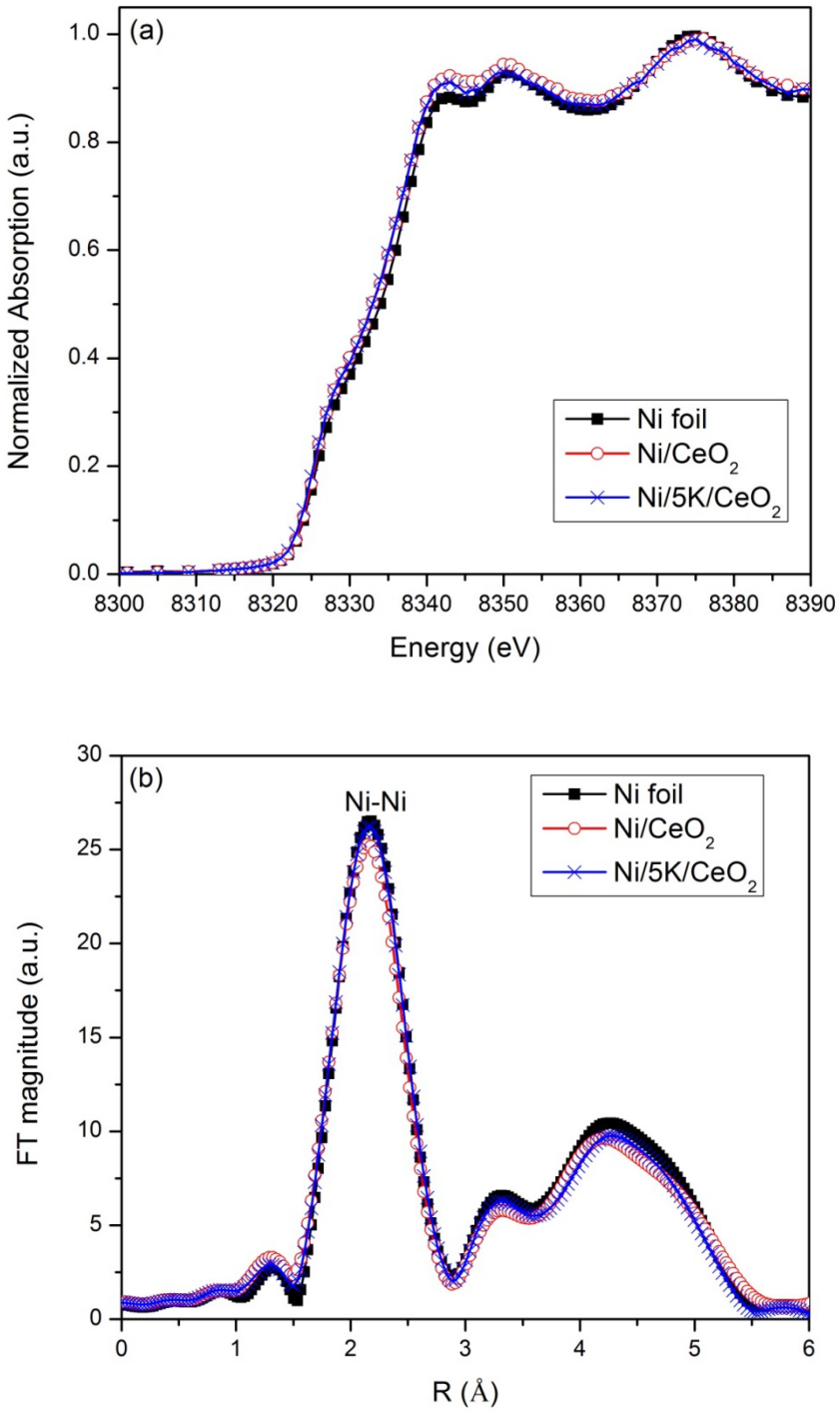

Figure 6-3 (a) Ni K-edge XANES spectra, and (b) Fourier transform functions of Ni foil and Ni/xK/CeO_2 catalysts at room temperature.

Table 6.2 Structural parameters derived from EXAFS analysis for Ni foil and reduced Ni/xK/CeO_2 catalysts

Sample	Condition	Shell	CN	R (Å)	σ^2 (Å^2)
Ni foil	-	Ni-Ni	12.0	2.49	-
Ni/CeO_2	Reduced at 650°C	Ni-Ni	10.2	2.48	0.005
Ni/5K/CeO_2	Reduced at 650°C	Ni-Ni	10.5	2.48	0.005

CN – Coordination number, R – Interatomic distance, σ^2 – Debye-Waller factor

The XANES of Ce LIII edge in the reduced Ni/CeO_2 and Ni/5K/CeO_2 are compared against the non-reduced, pure CeO_2 support in **Figure 6.4**. The absorption edges of Ce in Ni/CeO_2, Ni/5K/CeO_2 and pure CeO_2 support are observed at 5722.0 eV, 5722.0 eV and 5724.0 eV, respectively. As shown in **Figure 6.4**, the non-reduced CeO_2 support displays split peaks, B_1 and C, that are fingerprints for Ce^{4+}. In contrast, in the reduced samples, B_1 and C diminish while a new peak, B_0 develops. As reported by Jacobs et al., the development of B_0 peak, which is just below that of B_1, is ascribed to the absorption into the 5d level in the final state from the 4f occupancy in the initial state [17]. These key peaks serve as an indication of the degree of reduction of the CeO_2 component in the samples. Comparing the reduction degree of CeO_2 in Ni/0K/CeO_2 and Ni/5K/CeO_2 catalysts, it is evident that with the incorporation of 5 wt% K, the reduction degree of CeO_2 is significantly enhanced. A greater percentage of cerium atoms in Ce^{3+} state is present in Ni/5K/CeO_2 catalyst as compared to Ni/0K/CeO_2 catalyst. This indicates that even though Ni/5K/CeO_2 is harder to be reduced when compared to Ni/0K/CeO_2 as shown by H_2-TPR results, the percentage of Ce^{3+} remains higher in the prior. Consequently, the greater reduction of cerium atoms

in the surface shell from Ce^{4+} to Ce^{3+} allows for more bridging OH groups to be formed directly on the partially reduced CeO_2. The formation of these OH groups is vital in enhancing the WGS activity since they are important reaction intermediates.

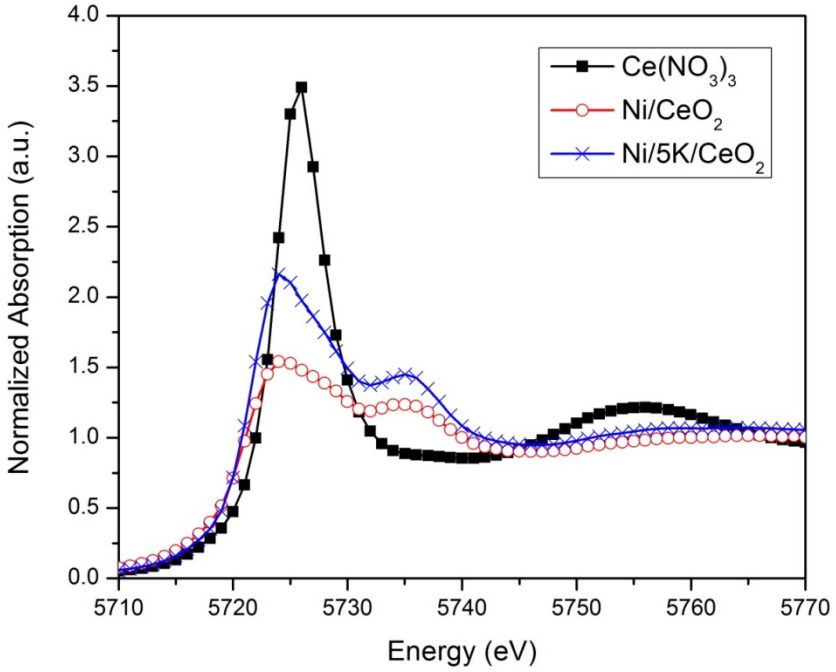

Figure 6-4 Ce L_{III}-edge XANES spectra of $Ce(NO_3)_3$ (Ce^{3+} reference) and Ni/xK/CeO_2 catalysts at room temperature.

6.3.6 CO-temperature-programmed-reduction-mass spectroscopy (CO-TPR-MS)

CO-temperature-programmed reduction (CO-TPR) is a useful technique for identifying reducible surface oxygen species, and in particular, the activation of surface hydroxyls which are required for the onset of the WGS reaction [18]. Depending on the temperature at which the CO consumption occurs, various oxygen species such as weakly bound adsorbed oxygen, surface-capping oxygen

and lattice oxygen, can be identified [19, 20]. CO-TPR results of fully reduced Ni/xK/CeO_2 catalysts are presented in **Figure 6.5**. Since the catalysts have been reduced in H_2 prior to CO-TPR, the main CO consumption peak centred at around 400 °C that is present in all catalysts tested can be assigned to surface oxygen species of ceria and of potassium. During H_2 reduction, oxygen adsorbed on metallic Ni would have been reduced and surface hydroxyls would be generated on reducible ceria and potassium. Adsorbed CO on metallic Ni can react with an OH group generated on partially reducible supports such as CeO_2 to produce CO_2 and H_2, as presented in Eq. 6.1 [21, 22].

$$CO\ (ads) + 2OH \rightarrow CO_2\ (g) + H_2\ (g) + O_L \quad (6.1)$$

As evident in the CO-TPR profiles shown in **Figure 6.5**, the CO consumption for the Ni/5K/CeO_2 catalyst occurs at the lowest temperature among all catalysts tested. This suggests that an optimum loading of 5 wt% K can generate active OH groups that can react with adsorbed CO at a lower temperature. This result is in agreement with XANES results which have shown higher degree of CeO_2 reduction in Ni/5K/CeO_2 catalyst. Besides, this result also correlates well with the markedly higher WGS activity of the Ni/5K/CeO_2 catalyst compared to other Ni/xK/CeO_2 catalysts at the reaction temperature of 350°C as shown in **Figure 6.5**. At higher loading of 10 wt% K, main temperature at which CO_2 production occurs shifts to higher temperature of about 450 °C and significant CO_2 production can be observed at higher temperature of around

610 °C. This suggests that the reducibility of surface oxygen from ceria is retarded due to an excess layer of potassium covering the surface of ceria.

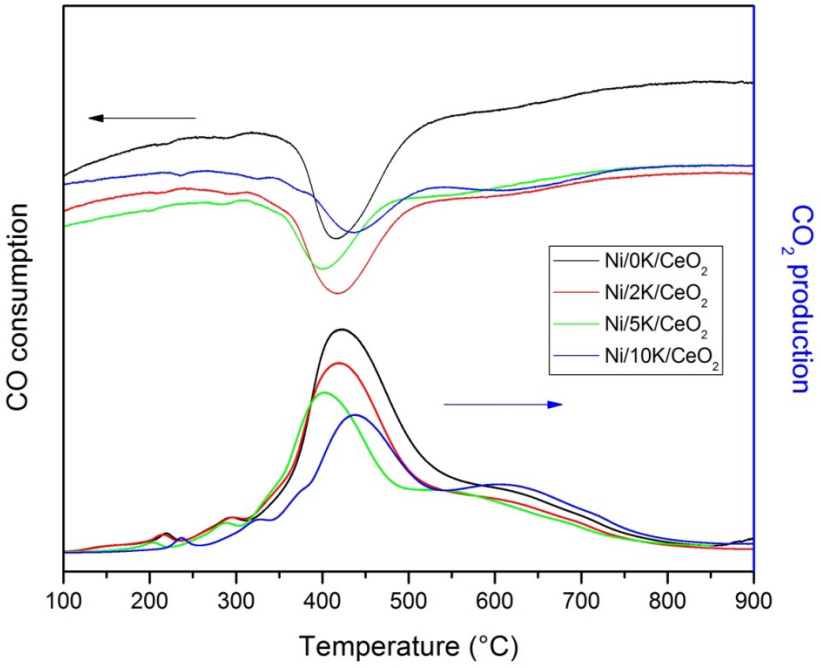

Figure 6-5 CO-TPR profiles with MS.

6.3.7 X-ray photoelectron spectroscopy (XPS)

The oxidation states of the various surface species present during the WGSR were investigated using XPS. **Figure 6.6(a)** shows the Ni 2p core level spectra of the reduced Ni/xK/CeO_2 catalysts. The binding energies (BEs) of Ni metal and its satellite peaks are approximately 852.1 eV and 856.3 eV, respectively. Likewise, the BEs of Ni^{2+} in NiO and its two satellite peaks are 855.4 eV, 853.7 eV and 860.9 eV, respectively. As observed in **Figure 6.6(a)**, BE of Ni^0 shifts to higher BEs as K loading was increased from 0 to 10 wt%. For instance, deconvolution of Ni 2p spectra of Ni/5K/CeO_2 catalyst reveals a positive

shift of 0.2 eV. This observed shift in binding energy is most likely out of the experimental uncertainty range. As reported by Biesinger et al. who have conducted XPS analysis with the same Kratos Axis Ultra, the binding energy values of nickel was allowed to vary ± 0.1 eV to allow for error associated with charge referencing to C 1s [23]. The shift to higher BEs has been reported by previous works concerning with K-doped Ni/α-alumina, bulk NiO , NiO/Fe_2O_3, and NiO/graphite [24]. According to these works, it has been proposed that K doping inhibits the nickel reduction, thereby shifting the BE of Ni 2p to higher BE, indicating a parallel increase in NiO phase. Contrary to this postulation, the upward shift in BE for Ni^0 in this instance can be attributed to the presence of K in the form of K^+ and the formation of Ni-O-K complexes [25]. The generation of these complexes resulted in an enhanced interaction between Ni metal and the K-doped CeO_2 support that eventually led to a positive shift in the BE of Ni 2p. The enhanced interaction between Ni metal and the support is further affirmed by the H_2-TPR results which showed the shift toward higher reduction temperature for K loading of up to 5 wt%. Furthermore, it can be observed from **Table 6.3** that with increasing K doping, the relative concentration of Ni^0 to Ni^{2+} was determined to be 0.71, 0.88, 0.83, 0.93, and 0.73, respectively. Hence, it is evident that K-doping did not exert an inhibitory effect on the reduction of NiO to Ni. Rather, the incorporation of K of up to 5 wt% can serve to enhance metal-support interaction.

The core level spectrum of Ce 3d is displayed in **Figure 6.6(b)** and the complex spectrum comprising of both Ce^{3+} and Ce^{4+} states can be deconvoluted

into 10 peaks: 2 doublets for Ce_2O_3 (Ce^{3+}) and 3 doublets for CeO_2 (Ce^{4+}). The 6 characteristic peaks for CeO_2 are labeled as v (882.4 eV), v" (888.7 eV), v''' (898.2 eV), u (900.9 eV), u" (907.3 eV) and u''' (916.5eV). On the other hand, the 4 characteristic peaks for Ce_2O_3 are labeled as v_0 (880.4 eV), v' (886.5 eV), u_0 (898.7 eV) and u' (902.9 eV) [21, 26]. As K loading increases, there is an upward shift in the binding energy, indicating greater charge imbalances and lattice distortions in CeO_2 which generates more oxide vacancies for water dissociation [11, 21, 27]. Areas under the respective deconvoluted peaks were summed to derive the concentrations of Ce^{3+} and Ce^{4+}, which are tabulated in **Table 6.3**. The concentration of Ce^{3+} in the catalysts does not vary significantly with different loadings of K, and ranges from 13 % to 15%. Ni/0K/CeO_2 catalyst has a Ce^{3+} concentration of 13% while the highest Ce^{3+} concentration of 15% was obtained with Ni/10K/CeO_2, indicating that high loading of K can induce greater formation of Ce^{3+}. However, for catalysts with lower K loadings, the increments in Ce^{3+} concentration are not noticeable from XPS. Hence, XANES was conducted to reveal the differences in the bulk concentrations of Ce^{3+} between Ni/0K/CeO_2 and Ni/5K/CeO_2 catalysts, and it has been shown earlier that a higher concentration of Ce^{3+} exists in the latter.

The core level spectrum of O 1s is shown in **Figure 6.6(c)** and three peaks can be distinguished in the O 1s region. The first peak (O_I) at around 529 eV can be assigned to lattice oxygen (O^{2-}) in the ceria lattice, the second peak (O_{II}) at around 530 eV can be ascribed to adsorbed oxygen species, and the third peak

(O_{III}) at around 532 eV can be attributed to adsorbed water. As compared to other catalysts, the O 1s spectrum of Ni/5K/CeO_2 catalyst displayed a significant positive shift to higher BEs. In particular, deconvolution of the spectra shows that the peak for lattice oxygen (O_I) shifted from 529.2 eV in Ni/0K/CeO_2 catalyst to 529.5 eV in Ni/5K/CeO_2, indicating a positive shift of 0.3 eV in the binding energy of the latter. More importantly, it can be observed from **Table 6.3** that the concentration of lattice oxygen in Ni/5K/CeO_2 catalyst is the highest among all catalysts. Presence of abundant surface lattice oxygen at reaction sites is governed by oxygen vacancy formation and is a result of the valence change of Ce^{4+} in CeO_2 to Ce^{3+} in CeO_{2-x} [28]. As shown above from the XANES results of Ce, there exists a higher percentage of Ce^{3+} in Ni/5K/CeO_2 catalyst as compared to that of Ni/0K/CeO_2 catalyst, thereby accounting for the higher amount of surface lattice oxygen observed in Ni/5K/CeO_2 catalyst. Since Ni/0K/CeO_2 catalyst possesses a lower percentage of Ce^{3+}, it naturally has a lower concentration of surface lattice oxygen. Li et al. has reported that free K^+ in potassium-supported oxides (MgO, CeO_2 and ZrO_2) are catalytically active sites for soot combustion and these K^+ species can activate gaseous oxygen which spills over to soot to form the reaction intermediate [29]. Similar observations were made by Janiak et al., and Lamoen and Persson who proposed based on theoretical calculations that K can enhance affinity and dissociation of gaseous O_2 [30, 31]. Likewise, in this instance, K^+ species which exist at the interface between the active Ni metal and the CeO_2 support can enhance affinity and dissociation of H_2O.

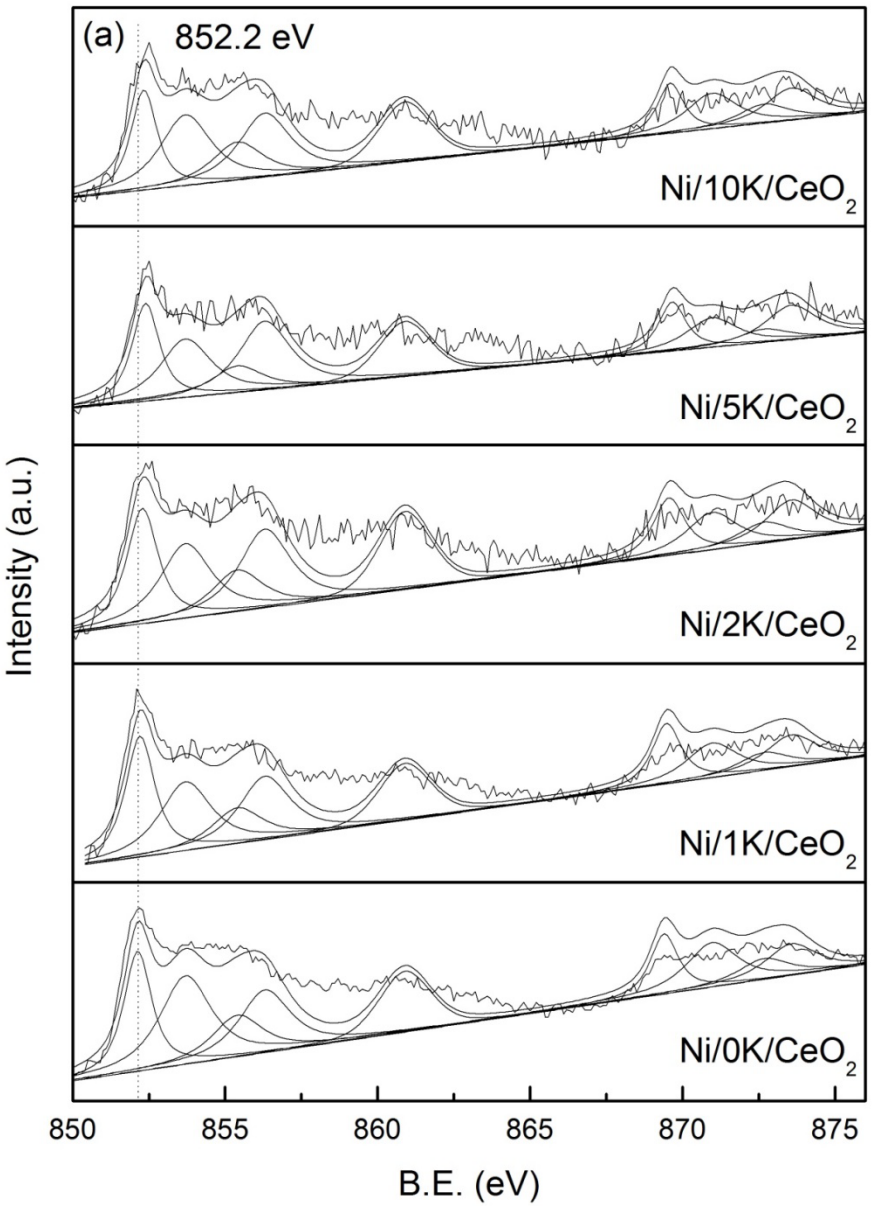
(a)
852.2 eV
Ni/10K/CeO2
Ni/5K/CeO2
Ni/2K/CeO2
Ni/1K/CeO2
Ni/0K/CeO2
Intensity (a.u.)
850
855
860
865
870
875
B.E. (eV)

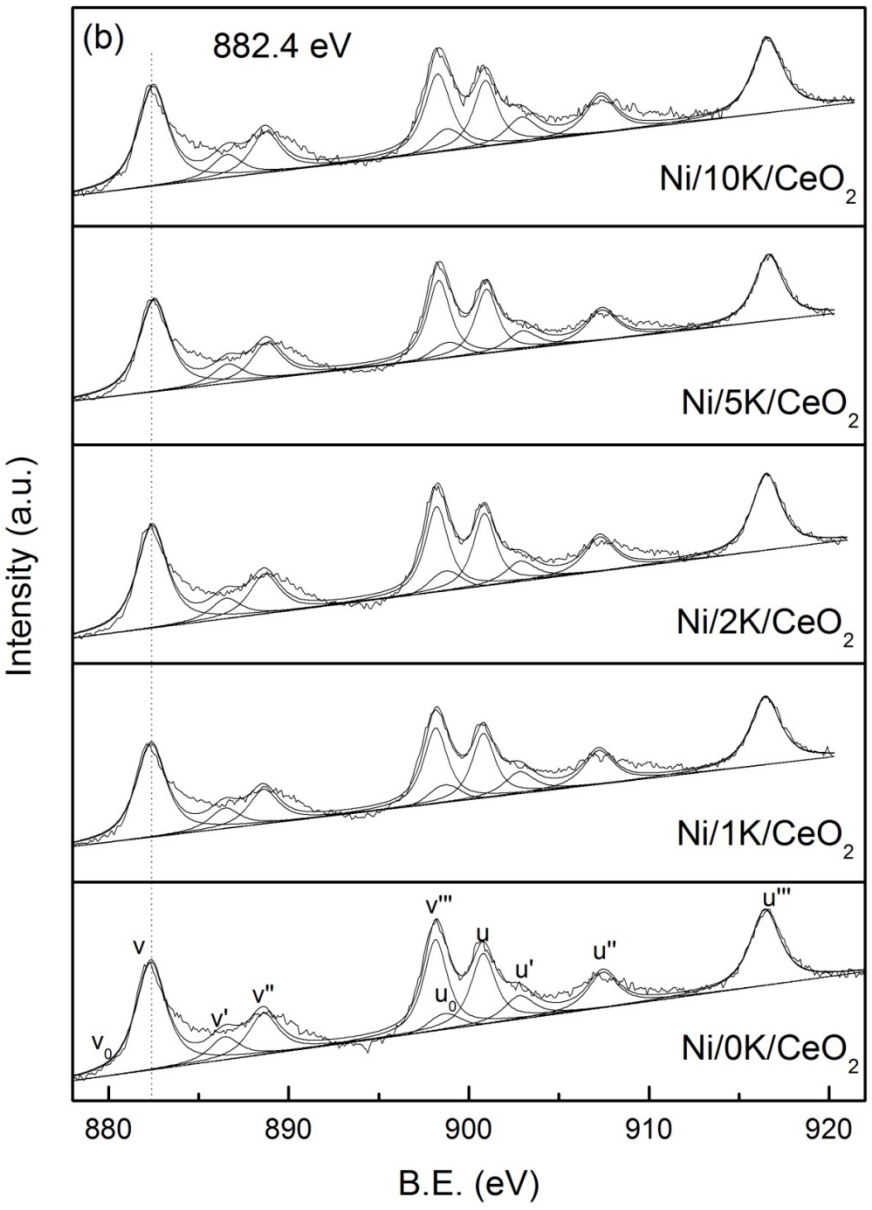
(b)
882.4 eV
Ni/10K/CeO2
Ni/5K/CeO2
Ni/2K/CeO2
Ni/1K/CeO2
Ni/0K/CeO2
v0
v
v'
v''
u0
v'''
u
u'
u''
u'''
Intensity (a.u.)
880
890
900
910
920
B.E. (eV)

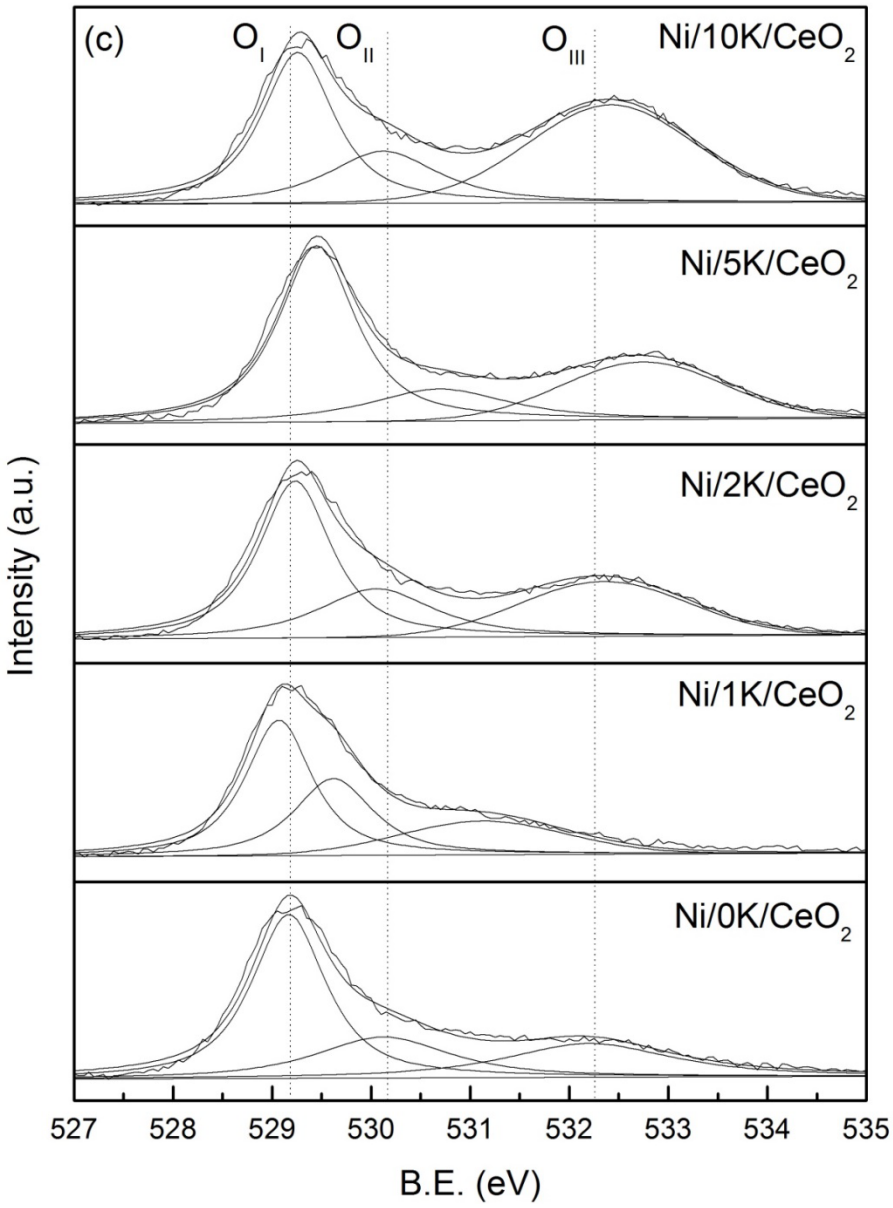

Figure 6-6 XPS spectra of Ni/xK/CeO_2 catalysts for (a) Ni 2p, (b) Ce 3d and (c) O 1s.

Table 6.3 Surface composition derived from XPS

Catalyst	Oxygen concentration (%)			Cerium concentration (%)		Nickel ratio	Surface composition (at %)			
	Lattice oxygen	Adsorbed oxygen	Adsorbed water	$[Ce^{3+}]$	$[Ce^{4+}]$	$[Ni^0]/[Ni^{2+}]$	O	Ni	K	Ce
Ni/0K/CeO_2	52	24	24	13	87	0.71	65	7.8	0.0	28
Ni/1K/CeO_2	47	31	22	14	86	0.88	64	7.6	1.0	27
Ni/2K/CeO_2	48	24	28	13	87	0.83	70	3.9	2.9	24
Ni/5K/CeO_2	55	18	27	13	87	0.93	71	4.4	1.6	23
Ni/10K/CeO_2	38	20	43	15	85	0.73	72	4.9	2.7	20

6.3.8 Catalytic activity and selectivity

The catalytic performances of the Ni/xK/CeO_2 catalysts were tested over a temperature range of 300-600 °C and the percentages of CO conversion to CO_2 are plotted against reaction temperature in **Figure 6.7(a)**. Evidently, Ni/0K/CeO_2 catalyst had the lowest CO conversion and fell short of the equilibrium CO conversion across all reaction temperatures. In contrast, equilibrium CO conversion was attained for K-doped catalysts at approximately 400 °C. Particularly, Ni/5K/CeO_2 catalyst achieved the highest CO conversion of 98.2%, which is very close to the equilibrium CO conversion of 98.9%, at the lowest temperature of 350 °C among all catalysts tested. This result is consistent with that of CO-TPR results which revealed that Ni/5K/CeO_2 catalyst has the lowest reduction temperature, indicating that surface oxygen which is essential for WGS reaction is activated at lower temperature as compared to other catalysts. However, increasing K doping to 10 wt% reduces the CO conversion slightly and equilibrium CO conversion can only be attained at 400 °C. This deterioration in catalytic activity can be attributed to the reduction in metal dispersion as shown in **Table 6.1**. With the addition of excess amount of K, in this case 10 wt%, active Ni metal is gradually covered by the excessive K, thereby decreasing its metal dispersion. Catalytic activity in terms of moles of CO converted per unit active Ni surface area was also calculated and tabulated in **Table 6.1**. The catalytic rate increases with increasing K loading despite lower Ni metal surface area at higher K loadings. However, we do wish to point out that these values may not be a true gauge of the catalyst activity since CeO_2 also acts as a secondary site for

catalyzing the dissociation of water. Moreover, since the CO conversion of Ni/10K/CeO_2 catalyst is marginally lower than Ni/5K/CeO_2 catalyst, the calculated catalytic rate is highly sensitive to the Ni surface area, which is the denominator in the formula. Hence, the overall H_2 yield achieved by the catalysts was eventually used as a gauge for catalytic activity of the catalysts. The positive effect of K on methane suppression can be clearly seen by the percentage of H_2 and CH_4 yields as shown in **Figure 6.7(b)**. With the incorporation of 1 wt% K, methane yield is greatly suppressed from 2.76% (in Ni/0K/CeO_2 catalyst) to 0.237%. Upon increasing K loading, methane yield progressively decreases from 0.377% (in Ni/2K/CeO_2 catalyst) to 0% (in Ni/5K/CeO_2 and Ni/10K/CeO_2 catalysts). On a closer scrutiny, Ni/5K/CeO_2 catalyst derives a higher H_2 yield than Ni/10K/CeO_2 catalyst despite achieving the same CH_4 yield of 0%. The higher H_2 yield achieved by the prior can be traced back to its higher CO conversion of 97.2% as compared to the CO conversion of 96.8% for Ni/10K/CeO_2 catalyst. This result indicates that Ni/5K/CeO_2 catalyst is highly selective towards WGS reaction, consequently achieving the highest H_2 yield of 48.6 %.

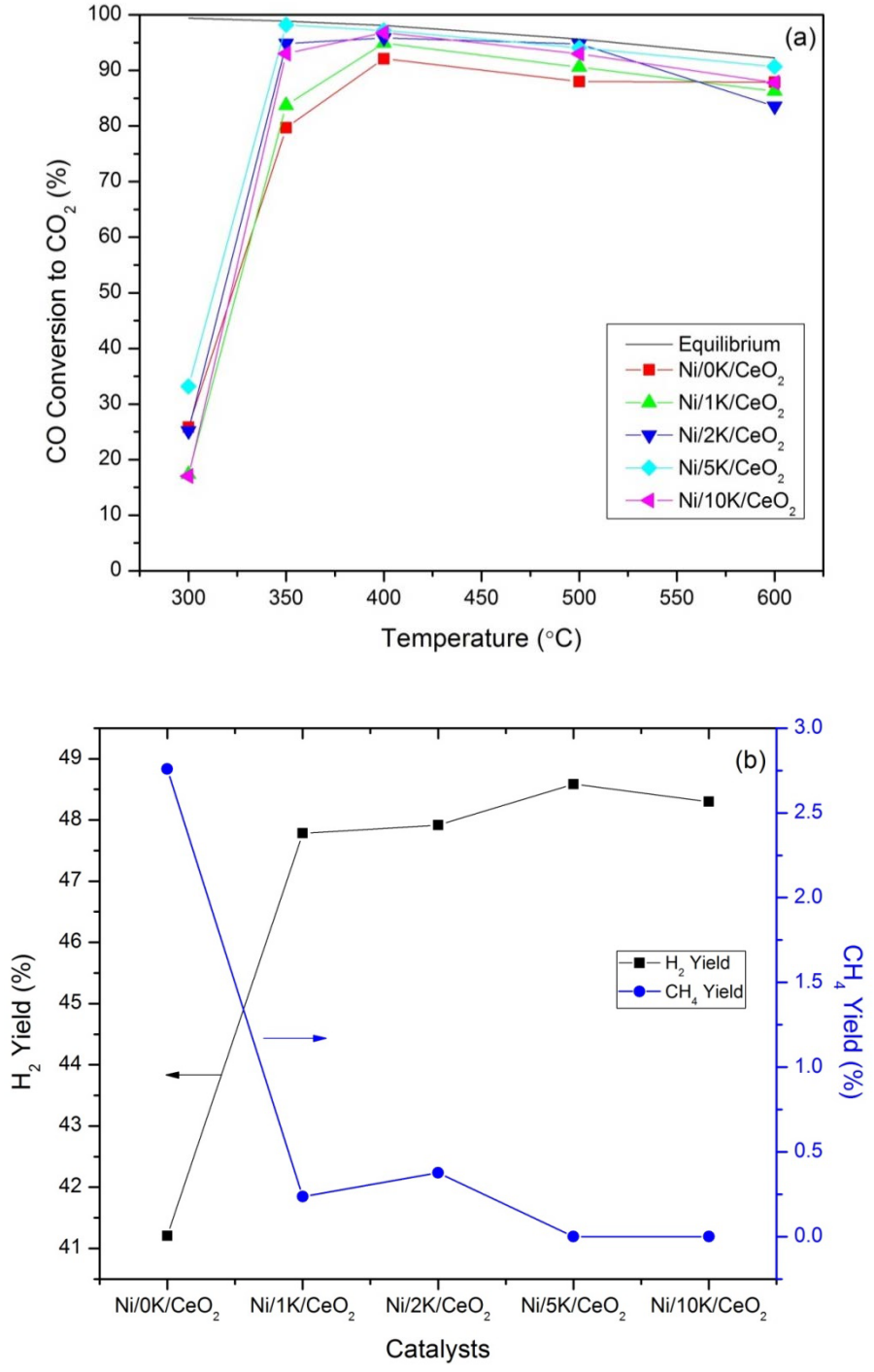

Figure 6-7 (a) Percentages of CO conversion to CO_2, and (b) H_2 and CH_4 percentage yields for Ni/xK/CeO_2 catalysts.

Long term stability test was also conducted for the Ni/5K/CeO_2 catalyst and the catalytic performance is depicted in **Figure 6.8** in terms of percentage of CO conversion to CO_2 and CH_4 yield. It can be observed that high WGS activity of approximately 97.0 % is sustained throughout the 100 h test duration. Furthermore, the observed zero CH_4 yield indicates the high selectivity of the catalyst towards WGS reaction. In addition, as revealed later by the mechanism, the interaction between K and Ni proves to be important in enhancing the WGS reaction and in the suppression of methanation. Hence, Ni-5K/CeO_2 catalyst was prepared via co-impregnation of Ni and K in a bid to further enhance the interaction between K and Ni. As presented in Figure S1 (shown in **Appendix C**) which shows the percentage of CO conversion versus temperature, Ni/5K/CeO_2 catalyst generally attained higher percentages of CO conversion at temperatures equal or greater than 350 °C, whereas Ni-5K/CeO_2 catalyst was unable to reach equilibrium CO conversion. As illustrated in Figure S2 (shown in **Appendix C**) which shows the H_2-TPR profiles of these two catalysts, this can probably be attributed to the stronger interaction between Ni and the K-doped support in the Ni/5K/CeO_2 catalyst. Moreover, sequential impregnation enabled K to be in the vicinity of both Ni and CeO_2. This is important since the presence of K at the interface of Ni and CeO_2 helps to increase the affinity of water to the support, thereby enhancing water dissociation and increasing the density of OH groups on CeO_2.

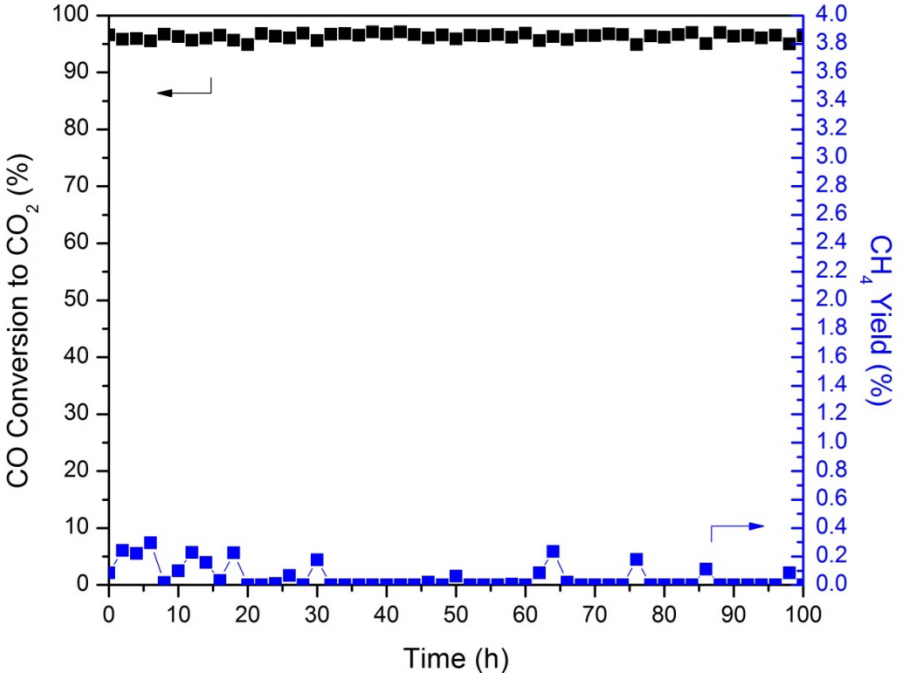

Figure 6-8 Percentages of CO conversion to CO_2 (left axis) and CH_4 yield (right axis) of Ni/5K/CeO_2 catalyst for 100 h reaction.

6.3.9 In-situ DRIFTS

In order to better understand the effect of K doping on suppression of methanation, DRIFTS studies were conducted on Ni/5K/CeO_2 catalyst. Prior to measurement of DRIFTS spectra, the Ni/5K/CeO_2 catalyst was reduced under 10 ml/min of 5% H_2/He at 650 ºC for 1 h, cooled down to room temperature and then flushed with He for 5 min to remove physisorbed hydrogen. **Figure 6.9(a)** and **Figure 6.9(b)** present the FTIR spectra for the reduced Ni/5K/CeO_2 catalyst that is subjected to continuous flow of CO and H_2.

6.3.9.1 DRIFTS spectra in the 2250 – 1700 cm^{-1} region

At the carbonylic region magnified by **Figure 6.9(a)**, four types of nickel-carbonyl species can be elucidated and they are mainly classified as follows, in

order of decreasing wavenumber. The first band at 2034 cm^{-1} can be assigned to CO adsorbed on Ni modified by hydrogen atoms which are adsorbed onto Ni during the reduction process, while the second carbonyl band at 2013 cm^{-1} can be ascribed to linear monocarbonyl. The intensities of these two bands decrease as temperature was raised from 30ºC to 150 ºC and completely disappeared at 200 ºC. The disappearance of these carbonyl species is accompanied by a subsequent increase in the intensities of the third and fourth carbonyl band at 1981 cm^{-1} and 1768 cm^{-1}, respectively. The third carbonyl band at 1981 cm^{-1} can be assigned to μ_2-bridging CO on Ni while the fourth carbonyl band at 1768 cm^{-1} can be ascribed to u_3-bridging CO adsorbed on a Ni-K site. μ_2-bridging mode correspond to a two-fold coordinated CO species on Ni sites while μ_3-bridging mode refers to a three-fold coordinated CO species on the Ni sites interacting with K [32]. The observations made in these conditions are similar to those reported by other authors at room and higher temperatures. For instance, Derrouiche et al. who studied 2.9%Pt-10%K-Al_2O_3 catalysts designated the carbonyl bands at 2050, 1950 and 1763 cm^{-1} to be that of CO adsorbed onto Pt metal in the linear and bridging modes, and of CO adsorbed on Pt-K site, respectively [32]. Other works have also assigned bridging carbonyls on Pt to be in the range of 1950-1850 cm^{-1} on both low index faces [33] and on stepped surfaces [34]. Besides Pt, bridging CO species on Pd were also observed in the regions of 1980-1880 cm^{-1} and 1960-1905 cm^{-1} [35, 36]. The intensities of the bands assigned to bridging CO and CO adsorbed on Ni-K site reached their maxima at approximately 200 ºC and gradually subsided as temperature was increased to 400ºC. The presence of

carbonyls in the low wavenumber region, namely the bridging CO and CO adsorbed on Ni-K site, suggests that there is a weaker CO bond and a consequently stronger adsorption of CO on K-modified Ni metal. In addition, the absence of subcarbonyl nickel species $Ni(CO)_n$ (n=2 or 3), which are usually present at around 2064 cm^{-1}, infers that the interaction between Ni and K prevented the formation of low-coordinated Ni states [37]. Since subcarbonyl nickel species have been shown to be the precursors for CO methanation reaction, the absence of these subcarbonyl species is one of the attributes for the low methane yield observed with $Ni/5K/CeO_2$ catalyst [11]. Moreover, it has been reported that deposition of carbon by CO disproportionation occurs less readily on the sites with more strongly held adsorbed CO [21, 38, 39]. With less deposition of carbon, less hydrogenation of deposited carbon by adsorbed hydrogen to form methane. Comparing the FTIR spectra of the $Ni/5K/CeO_2$ catalyst with that of the $Ni/2Na/CeO_2$ catalyst which our group have previously reported [11], it is evident that while both K-doped and Na-doped catalysts possessed adsorbed CO in the μ_3-bridging mode and did not have the subcarbonyl nickel species, adsorbed CO in the the μ_2-bridging mode was only present in $Ni/5K/CeO_2$ catalyst. In contrast, no presence of adsorbed CO in the bridging mode was found in the Ni/CeO_2 catalyst, where adsorbed CO was mainly in the terminal mode. The unique presence of both μ_2-bridging and μ_3-bridging carbonyls in the $Ni/5K/CeO_2$ catalyst suggests that a large proportion of adsorbed CO is present in the bridged form in this catalyst. It has been reported in literature that the linear to bridging ratio decreases with increasing alkalinity of the support. In bridging mode, there is

a greater overlap between the d-orbitals of the metal and the CO orbitals, leading to a larger back donation of electrons from the metal towards CO. Consequently, there will be a larger fraction of CO coordinated in the bridging mode. Due to the lower frequency of bridging modes, representing a weaker CO bond, it in turn implies that a large proportion of CO is strongly held by Ni, resulting in a much lower tendency for CO disproportionation. Furthermore, the disappearance of these bridging carbonyls at approximately 300 ºC, which is the temperature from which catalyst activity starts to increase, suggesting that these bridging carbonyls participate in the WGSR. Thus, the presence of large proportion of bridging CO is the second reason explaining the lower CH_4 selectivity observed in Ni/5K/CeO_2 catalyst.

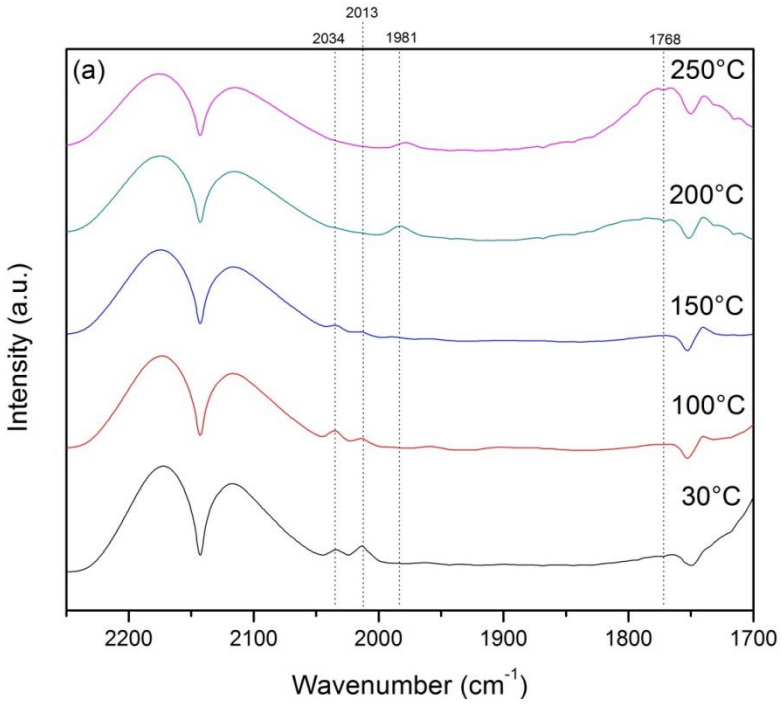

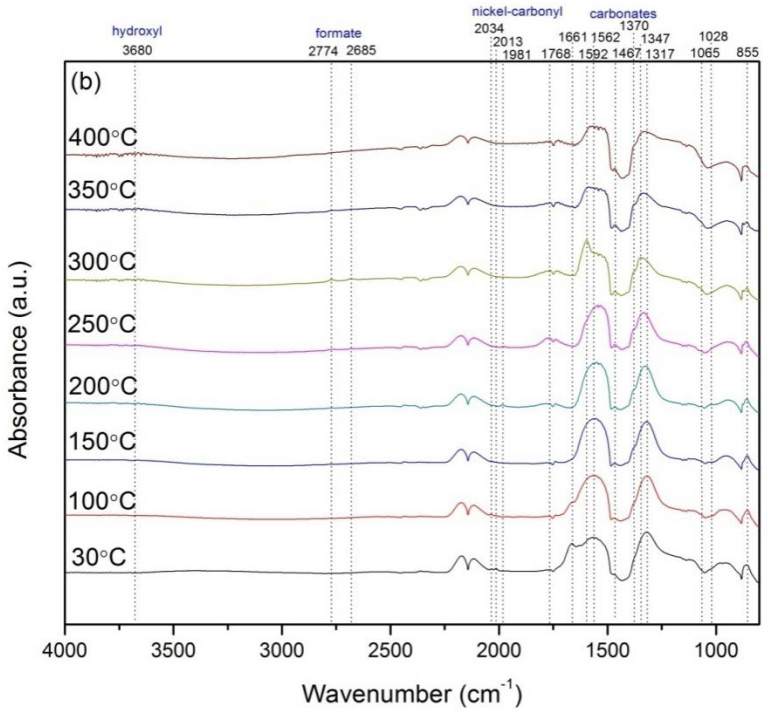

Figure 6-9 FTIR spectra of Ni/5K/CeO_2 catalyst under continuous flow of CO and H_2 at temperature increments of 50°C in the: (a) carbonylic region (2250-1700 cm^{-1}) and (b) entire region (4000-800 cm^{-1}).

6.3.9.2 DRIFTS spectra in the 3000 – 2650 cm^{-1} and 1700 – 1000 cm^{-1} regions

As shown in **Figure 6.9(b)**, the main bands observed in the 3000-2650 cm^{-1} region can be assigned to bidentate formate which has bands situated at 2774, 2685, 1592 and 1347 cm^{-1} [40]. These bidentate formate species are possibly formed as a result of reaction between adsorbed CO and geminal OH on reduced ceria support [41]. The frequencies for formate C-H stretching of Ni/5K/CeO_2 catalyst have been tabulated in **Table 6.4**. In addition, literature values of other Ni [11, 21, 42], Cu [42, 43], Au [42, 44, 45], Ru [46], Co [42], Fe [42] and Pt [6, 42, 47, 48] –based catalysts have also been included for comparison. The intensities

of these bands increase as temperature increases and reach a maximum at 300 ºC. Beyond 300 ºC, the bidentate formate species begin to decompose into carbonate and H_2 [49]. In-situ transient formate decomposition experiments were conducted to investigate the role of these formates species in the reaction mechanism and the analysis will be discussed in the later section.

At the carboxylate/carbonate region, bands situated at 1467, 1370 and 1065 cm^{-1} are observed at low CO adsorption temperatures and can be attributed to unidentate carbonate species. These species together with the band observed at 855 cm^{-1}, which corresponds to $\pi(CO_3)$ mode of carbonates, are naturally available on pure CeO_2 support. Likewise, bidentate carbonates, which have bands situated at 1562, 1289, 1028 and 855 cm^{-1}, are present at low temperatures [50, 51]. The intensities of these carbonate bands increase as temperature rises to 250 °C and decreases beyond that, indicating that these carbonates are not irreversibly adsorbed onto the ceria surface. In addition, carboxylates, which typically have bands 1560, 1510, and 1310 cm^{-1}, are not visible from the spectra, inferring that these carboxylate species do not participate in the reaction, further supporting our later findings in the kinetic study that the redox mechanism is responsible for the activity of the $Ni/5K/CeO_2$ catalyst.

Table 6.4 Formate C-H stretching band positions upon CO adsorption on CeO_2 and other metal oxides

Catalyst	Band position (cm^{-1})		Reference
	ν(CH)	δ(CH) + ν_s(OCO)	
10% Ni/5% K/CeO_2	2685	2774	This work
10% Ni/CeO_2	2843	2928	[11]
0.30% Ni/CeO_2	2840	2945	[42]
10% Ni/2% Na/CeO_2	2803	2929	[11]
5% Ni-5% Cu/CeO_2	2850	2979	[21]
5% CuO_x/CeO_2	2845	2935	[43]
$Ce_{0.8}Cu_{0.2}O_2$	2845	2935	[43]
0.33% Cu/CeO_2	2840	2945	[42]
3% Au/CeO_2	2848	2949	[44]
1% Au/CeO_2	2840	2945	[42]
4.7 at% Au/Ce(La)O_2	2830	2946	[45]
0.5% Ru/CeO_2	2840	2950	[46]
0.5% Ru-0.5% Pt/CeO_2	2840	2945	[46]
0.5% Pt/CeO_2	2840	2940	[46]
0.1% Pt/CeO_2	2847	2948	[48]
1% Pt/CeO_2	2840	2945	[42]
2% Pt/CeO_2	2844	2946	[6]

2% Pt/0.8% Li/CeO_2	2837	2947	[6]
2% Pt/0.5% Na/CeO_2	2837	2941	[6]
2% Pt/2.5% Na/CeO_2	2810	2950	[6]
2% Pt/0.9% K/CeO_2	2829	2943	[6]
2% Pt/4.3% K/CeO_2	2802	2952 - 2923	[6]
2% Pt/9.3% Rb/CeO_2	2760	2929	[6]
2% Pt/14.5% Cs/CeO_2	2809	2925	[6]
4% Pt/ZrO_2	2870	2931	[47]
0.30% Co/CeO_2	2840	2945	[42]
0.29% Fe/CeO_2	2840	2945	[42]

6.4 Kinetic study of Ni/5K/CeO_2 catalyst

In order to postulate the reaction mechanism of Ni/5K/CeO_2 catalyst, kinetic measurements were performed by changing the gas composition ranging from 2.5% to 10% CO, 5% to 25% CO_2, 10% to 55% H_2O, 5% to 20% H_2 and balance with He. Generally, there are two major schools of thoughts regarding the WGS mechanism, namely, the associative mechanism and the redox mechanism. In the associative mechanism proposed by Shido and Iwasawa, the intermediate for the reaction is a bidentate formate, produced by the reaction of adsorbed CO with terminal -OH groups from the support. The rate determining step is the decomposition of the bidentate formate to H_2 and a unidentate carbonate [52]. Formate then decomposes into the WGS products, CO_2 and H_2. Most view adsorption of CO and OH on Ce^{3+} than on Pt and this is largely backed by studies which have revealed through FTIR studies that weak formate bands do form on un-promoted ceria catalyst [17]. This indicates that in the absence of Pt, CO can adsorb on OH groups that are present on Ce^{3+} to form formates. Promotion with Pt serves to enhance the surface reduction of ceria, generation of active geminal OH groups, and also to facilitate the decomposition of surface formates [53]. However, it has also been reported that formate cannot be formed directly from CO and OH in a single elementary step due to their adsorption geometry on Pt (111). Hence, formate might not act as a reaction intermediate, but rather as a spectator species during the WGSR. Instead, carboxyl (-COOH) has been postulated as the reaction intermediate. Other studies have also reported findings of formate as a spectator species over Cu (111) and Au (111) based catalysts in

low temperature WGSR [54]. In contrast, in the redox mechanism, CO adsorbed on the metal is oxidized by CO_2 by surface oxygen from the support. The support is then re-oxidized by water, generating H_2.

Several mechanisms have been postulated for transition metal and noble metal supported on ceria for the water-gas shift reaction [48, 55]. Formate mechanism has been advocated by Davis and co-workers who have revealed that adsorbed CO react with geminal OH groups on the surface of reduced ceria to form formates, and that the decomposition of these surface formates is the rate limiting step for the mechanism [41, 42]. Another major reaction mechanism that has been widely proposed for the WGS reaction is the redox mechanism. Flytzani-Stephanopoulos and co-workers have elucidated a co-operative redox mechanism to be responsible for the WGS activity of Cu and Ni supported on ceria catalysts [27]. Besides formate and redox mechanisms, Mavrikakis and co-workers have also proposed that a carboxyl mechanism for WGS reaction on Cu and Pt metallic sites [54, 56]. Despite the extensive number of studies conducted on studying the reaction mechanisms for WGS reaction on various metal-supported catalysts, the reaction mechanism of ceria-supported catalysts remains controversial. Hence, the aim of this kinetic study is to elucidate the reaction mechanism of Ni/5K/CeO_2 catalyst.

The reaction kinetics of Ni/5K/CeO_2 catalyst was examined by studying the effect of partial pressures of reactants and products (CO, H_2O, CO_2 and H_2) on the kinetic rate of WGS reaction at 400 °C. Based on the kinetic experimental

data obtained, the apparent reaction order was calculated. **Figure 6.10(a)** shows the WGS reaction rates at different partial pressures of reactants and products and the reaction orders with respect to CO, H_2O, CO_2, and H_2 were determined to 0.19, 0.58, -0.15 and -0.51 respectively. As evident from **Table 6.5**, the apparent reaction orders of CO_2 and H_2, the inhibitory effects imposed by both products are significantly weaker than conventional Cu-based [57] catalyst but stronger than Fe-based [58] catalyst. Moreover, the apparent reaction orders derived for the Ni/5K/CeO_2 catalyst shows great similarity with that obtained for Pt/CeO_2-ZrO_2 catalyst by Radhakrishnan et al. [59] and Kugai et al. [60], respectively. This indicates that H_2 exhibits greater inhibition as compared to CO_2, and there is a larger positive order dependency for H_2O concentration than CO concentration. In contrast to Ni/5K/CeO_2 catalyst, most of the Cu and Pd-Cu catalysts reported by Kugai et al. have higher reaction order in CO, inferring their greater dependencies on CO than H_2O. The similarity observed in Ni/5K/CeO_2 and the Pt-based catalysts with respect to the higher reaction order in H_2O indicates the greater importance of H_2O on the reaction rate over Ni/5K/CeO_2 catalyst. The overall reaction rate over Ni/5K/CeO_2 catalyst is expressed in Eq. 6.2 in the form of power rate law.

$$r = Aexp\left(\frac{E_a}{RT}\right)[P_{CO}]^{0.19}\left[P_{H_2O}\right]^{0.58}\left[P_{CO_2}\right]^{-0.15}\left[P_{H_2}\right]^{-0.51}(1-\beta) \qquad (6.2)$$

where

$$\left(\beta = \frac{[CO_2][H_2]}{[CO][H_2O]K_{eq}}\right) and\ K_{eq} = exp\left(\frac{4577.8}{T} - 4.33\right)$$

In order to further elucidate the reaction mechanism, the kinetic data was fitted with the three major mechanisms, namely, redox, formate and carboxyl mechanisms. A bifunctional mechanism has been inferred in literature, in which reducible supports such as CeO_2 possessing oxygen vacancies can serve to activate water as CO is adsorbed on metallic sites [61]. Hence, a dual-site mechanism, involving Ni metal as the CO adsorbing site and CeO_2 as the water dissociation site has been proposed. Of the three kinetic models tested, the dual-site redox mechanism derived the best fit for the kinetic data, obtaining an R^2 value of 0.91 as shown in the parity plot presented in **Figure 6.10(b)**. The reaction conditions for the kinetic study and the kinetic parameters estimated from the proposed model are presented in Tables S2 and S4 (shown in the **Appendix C**). In contrast, poorer fits were obtained with the dual-site formate and carboxyl mechanisms. This implies that the formate species observed during in-situ DRIFTS are most likely spectator species. In addition, OH groups formed upon reduction of ceria do not participate in the reaction by directly reacting with CO to form COOH species as in a carboxyl mechanism. Rather, OH groups undergo further dissociation to form adsorbed O on CeO_2 and reacts with adsorbed CO on Ni to form adsorbed CO_2. This result further justifies the importance of K in enhancing the redox property of CeO_2 as shown in XANES. Furthermore, K increases the affinity of water to CeO_2, thereby promoting water dissociation and ensuring adequate oxygen supply for reaction with adsorbed CO at the Ni-Ce interface. Nonetheless, it is worth noting that K which provides OH, can exist as KOH and react with CO_2 to produce K_2CO_3. If present, K_2CO_3 will contribute to

the IR bands for unidentate carbonate species at 1467 and 1370 cm^{-1}. However, as observed from the FTIR spectra presented in **Figure 6.9(b)**, unidentate carbonate species that already existed at 30 °C increased in intensity as temperature was increased to 250 °C and decreased beyond that, indicating that these unidentate carbonate species can be decomposed. This observation may suggest that even if K_2CO_3 is present, they may be present in negligible amounts and do not affect the catalytic activity as illustrated by **Figure 6.8** which shows consistently high catalytic activity during the long term stability test. In summary, the proposed redox reaction mechanism can be written as follows in Eqs. 6.3 – 6.9:

$$CO + s_1 \overset{K_1}{\leftrightarrow} CO \cdot s_1 \tag{6.3}$$

$$H_2O + s_2 \overset{K_2}{\leftrightarrow} H_2O \cdot s_2 \tag{6.4}$$

$$H_2O \cdot s_2 \overset{K_3}{\leftrightarrow} H \cdot s_1 + OH \cdot s_2 \tag{6.5}$$

$$s_1 + OH \cdot s_2 \overset{K_4}{\leftrightarrow} H \cdot s_1 + O \cdot s_2 \tag{6.6}$$

$$CO \cdot s_1 + O \cdot s_2 \overset{K_5}{\leftrightarrow} CO_2 \cdot s_1 + s_2 \text{ (RDS)} \tag{6.7}$$

$$CO_2 \cdot s_1 \overset{K_6}{\leftrightarrow} CO_2 + s_1 \tag{6.8}$$

$$H \cdot s_1 + H \cdot s_1 \overset{K_7}{\leftrightarrow} H_2 + 2s_1 \tag{6.9}$$

First, CO is adsorbed on Ni metal site (s_1) while H_2O is adsorbed on the oxide vacancy sites of reduced K-doped CeO_2 (s_2). Water dissociation occurs near Ni-Ce interface to produce H that is preferentially adsorbed on Ni and OH that is adsorbed on reduced CeO_2 [62]. The presence of K at the interface of Ni and CeO_2 helps to increase the affinity of water to the support, thereby enhancing water dissociation and increasing the density of OH groups on CeO_2 [18, 63]. Adsorbed OH then undergoes further dissociation to form adsorbed H on Ni and

adsorbed O on CeO_2. Adsorbed CO on Ni then reacts with adsorbed O to form adsorbed CO_2 on Ni, leaving a vacant site on the support for subsequent water dissociation. The adsorbed H can then terminate each other to form H_2 gas. On the other hand, adsorbed CO_2 can also react with adsorbed H to form formate species, HCOO which are postulated to be spectator reaction intermediates observed during the in-situ DRIFTS study. Finally, adsorbed CO_2 is desorbed from the Ni metal site to produce CO_2 gas.

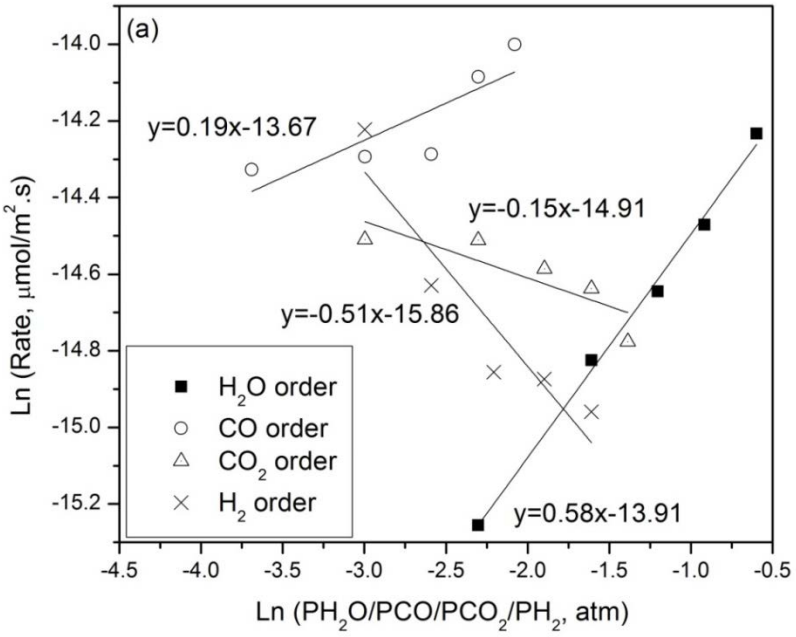

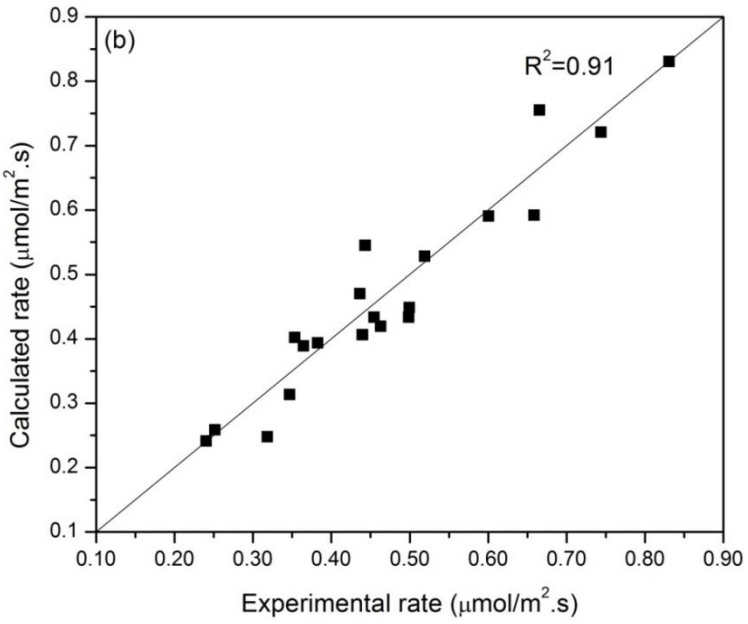

Figure 6-10 (a) Derivation of power law by varying partial pressures of H_2O, CO, CO_2 and H_2 over Ni/5K/CeO_2 catalyst, (b) parity plot of experimental and calculated reaction rate.

Table 6.5 Literature values for reaction order measurements of water-gas shift reaction

Catalyst	Temperature (°C)	Reaction orders				Reference
		CO	H_2O	CO_2	H_2	
Ni/5K/CeO_2	400	0.2	0.6	-0.2	-0.5	This work
5Ni5Cu/CeO_2	350	1.0	0.2	-0.3	-0.2	[21]
CuO/ZnO/Al_2O_3	190	0.3	0.8	-0.9	-0.9	[57]
Pt/CeO_2-ZrO_2	210-240	0.1	0.7	-0.2	-0.6	[59]
$La_{0.7}Ce_{0.2}FeO_3$	550-600	0.81	-0.01	-0.22	-0.0	[58]
Fe_2O_3-Cr_2O_3	450	0.9	0.31	-0.16	-0.05	[58]
Pt/CeO_2	260	-0.1	0.7	-	-	[60]
Pd/CeO_2	260	0.1	0.5	-	-	[60]
PtCu/CeO_2	260	0.4	0.3	-	-	[60]
PdCu/CeO_2	260	0.4	0.3	-	-	[60]
Cu/CeO_2	260	0.6	0.2	-	-	[60]
PdCu/Al_2O_3	260	0.2	-0.3	-	-	[60]

The in-situ transient formate decomposition experiments were conducted in the temperature range of 250 to 450 °C in the presence of steam for Ni/5K/CeO_2 catalyst and the spectra which is shown in **Figure 6.11(a)** and **Figure 6.11(b)** are collected upon attaining steady state condition. From Figure 11(a), upon CO adsorption, there is weak coverage of formates (2774, 2685, 1592, 1347 cm^{-1}) on the catalyst surface at 300 °C. Subsequently, steam was introduced and it was observed that the formates decompose to unidentate (1467, 1370 cm^{-1}), bidentate (1562, 1289 cm^{-1}) and tridentate (1505, 1347 cm^{-1}) carbonates [64]. No formates were observed after steam was introduced and tridentate carbonates were the predominant carbonate species upon ramping the temperature to 400°C. In order to reaffirm the participation of formate species only as intermediate species, a second cycle of in-situ transient formate decomposition experiment was conducted after the first cycle [21]. The spectra collected are illustrated in Figures 12(a) and (b). Similar to the spectra collected after first cycle of steam introduction, formates were not observed after the second cycle of CO adsorption. Upon increasing the temperature, CO was observed to be adsorbed in the bridging mode, together with the formation of unidentate, bidentate and tridentate carbonates, and the evolution of gaseous CO_2. Thereafter, a second cycle of steam was introduced and the intensities of carbonates as well as the bridging carbonyl were decreased, indicating the decomposition of these species. This possibly infers that formate species which are weakly observed in the first cycle could be an intermediate species or converted into carbonate species [64]. As proposed by Behm et al., surface formates can be formed at the interface between

the metal particles and CeO_2 and act as a storage for reaction intermediates [66]. Even though the role of formate as a reaction intermediate cannot be ruled out, it remains unclear that the main reaction intermediate leading to the formation of CO_2 is a formate [45]. Coupled with the kinetic modeling results obtained earlier, the formation of carbonates in the second cycle of CO adsorption as observed during in-situ DRIFTS probably suggests that oxygen regeneration by ceria could have occurred via redox mechanism [67, 68].

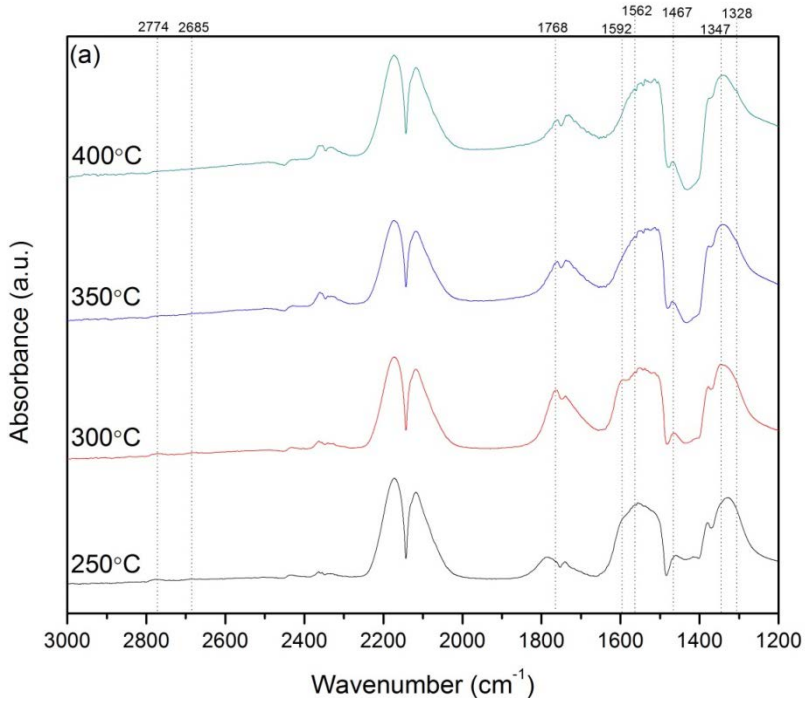

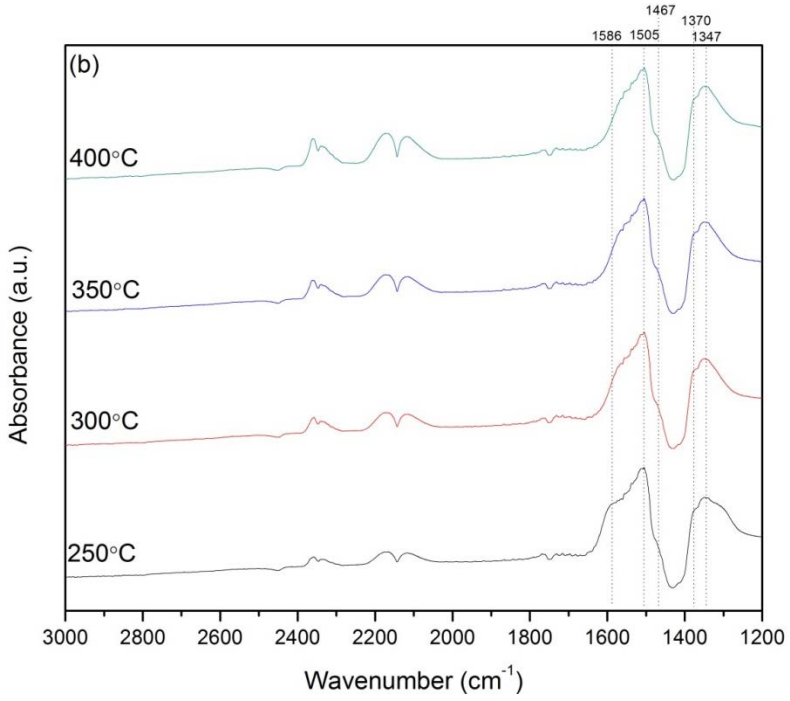

Figure 6-11 In-situ transient decomposition: FTIR spectra of Ni/5K/CeO_2 catalyst upon (a) introduction of 5%CO/He, and (b) switching to saturated steam with helium.

6.5 Conclusion

From the present study, the following concluding remarks can be made for Ni/xK/CeO_2 catalysts on the water-gas shift reaction:

(a) Effect of varying K loadings on Ni/xK/CeO_2 catalysts (x = 0-10 wt%) has been studied in detail to under the role of K in methane suppression and enhancement of WGS activity. An optimal K loading of 5 wt% was found to effectively suppress methanation during WGS reaction by enhancing CO adsorption on Ni via formation of bridging carbonyls as evidenced by in-situ DRIFTS studies. Strong adsorption of CO in the bridging modes inferred that CO disproportionation and subsequent methanation of carbon precursors were prevented. Besides the formation of bridging carbonyls,

subcarbonyl species which are precursors for methane formation were not observed in the presence of K.

(b) The role of K in enhancing WGS activity can be attributed to the provision of OH groups in the vicinity of Ni-Ce interface. As K is hygroscopic, it increases the affinity of water to the CeO_2 support, enhancing water dissociation and the subsequent formation of OH groups which are vital for forming adsorbed oxygen on the support that subsequently reacts with adsorbed CO on Ni to form the reaction products. Moreover, doping of K on CeO_2 causes charge imbalance and lattice distortion of CeO_2, thereby leading to greater concentration of surface lattice oxygen as shown by XPS. As evidenced by XANES and CO-TPR-MS, reduced CeO_2 exists predominantly in the Ce^{3+} state in the presence of K, producing oxygen species that are important for the WGS reaction.

(c) Kinetic study on Ni/5K/CeO_2 catalyst revealed that the catalyst has a large positive dependency on H_2O and a great inhibitory effect imposed by H_2. Additionally, a dual-site redox mechanism was proposed and achieved a good fit to the kinetic data obtained.

Supporting information (Appendix C)

Sample calculation for deriving Ni dispersion via N_2O pulse titration, comparison of catalytic activity and H_2-TPR profiles of Ni/5K/CeO_2 and Ni-5K/CeO_2 catalysts, reaction conditions of the kinetic study, constraints imposed

on the kinetic models, validation of kinetic model and kinetic parameters estimated from the proposed kinetic model are provided in **Appendix C**.

6.6 References

[1] W.D. Mross, Catal. Rev. Sci. Eng., 25 (1983) 591.
[2] I.G. Bajusz, D.J. Kwik, J.G. Goodwin, Jr., Catal. Lett., 48 (1997) 151.
[3] A. Parmaliana, F. Frusteri, F. Arena, N. Mondello, N. Giordano, in: A.Z. Claudio Morterra, C. Giacomo (Eds.) Stud. Surf. Sci. Catal., Elsevier, 1989, pp. 739.
[4] A. Díaz, D.R. Acosta, J.A. Odriozola, M. Montes, J. Phys. Chem. B, 101 (1997) 1782.
[5] D.W.G. C.T. Campbell, Surf. Sci., 123 (1982) 413.
[6] H. Evin, G. Jacobs, J. Ruiz-Martinez, G. Thomas, B. Davis, Catal. Lett., 120 (2008) 166.
[7] L.Z. Linganiso, G. Jacobs, K.G. Azzam, U.M. Graham, B.H. Davis, D.C. Cronauer, A.J. Kropf, C.L. Marshall, Appl. Catal. A, 394 (2011) 105.
[8] J.M. Pigos, C.J. Brooks, G. Jacobs, B.H. Davis, Appl. Catal. A, 328 (2007) 14.
[9] J.H. Pazmiño, M. Shekhar, W. Damion Williams, M. Cem Akatay, J.T. Miller, W. Nicholas Delgass, F.H. Ribeiro, J. Catal., 286 (2012) 279.
[10] H. Xie, J. Lu, M. Shekhar, J.W. Elam, W.N. Delgass, F.H. Ribeiro, E. Weitz, K.R. Poeppelmeier, ACS Catal., 3 (2013) 61.
[11] M.L. Ang, U. Oemar, E.T. Saw, L. Mo, Y. Kathiraser, B.H. Chia, S. Kawi, ACS Catal., 4 (2014) 3237.
[12] C.M.Y. Yeung, K.M.K. Yu, Q.J. Fu, D. Thompsett, M.I. Petch, S.C. Tsang, J. Am. Chem. Soc. Comm., 127 (2005) 18010.
[13] L. Liu, Y. Wang, Y. Bai, X. Zhang, K. Yang, Y. Song, Appl. Phys. B, 110 (2013) 111.
[14] Y. Wang, A. Zhu, Y. Zhang, C.T. Au, X. Yang, C. Shi, Appl. Catal. B, 81 (2008) 141.
[15] G.P. Huffman, N. Shah, J.M. Zhao, F.E. Huggins, T.E. Hoost, S. Halvorsen, J.G. Goodwin, J. Catal., 151 (1995) 17.
[16] D. Weng, J. Li, X. Wu, F. Lin, Catal. Commun., 9 (2008) 1898.
[17] G. Jacobs, U.M. Graham, E. Chenu, P.M. Patterson, A. Dozier, B.H. Davis, J. Catal., 229 (2005) 499.
[18] Y. Zhai, D. Pierre, R. Si, W. Deng, P. Ferrin, A.U. Nilekar, G. Peng, J.A. Herron, D.C. Bell, H. Saltsburg, M. Mavrikakis, M. Flytzani-Stephanopoulos, Science, 329 (2010) 1633.
[19] Q. Fu, H. Saltsburg, M. Flytzani-Stephanopoulos, Science, 301 (2003) 935.
[20] C. Li, K. Domen, K.-I. Maruya, T. Onishi, J. Catal., 123 (1990) 436.
[21] E.T. Saw, U. Oemar, X.R. Tan, Y. Du, A. Borgna, K. Hidajat, S. Kawi, J. Catal., 314 (2014) 32.
[22] H. Zhu, Z. Qin, W. Shan, W. Shen, J. Wang, J. Catal., 225 (2004) 267.
[23] M.C. Biesinger, B.P. Payne, L.W.M. Lau, A. Gerson, R.S.C. Smart, Surf. Interface Anal., 41 (2008) 324.
[24] F. Medina, P. Salagre, J.E. Sueiras, J.L.G. Fierro, J. Chem. Soc., Faraday Trans., 89 (1993) 3981.

[25] H. Praliaud, M. Primet, G.-A. Martin, Appl. Surf. Sci., 17 (1983) 107.
[26] V.M. Shinde, G. Madras, Appl. Catal. B, 132-133 (2013) 28.
[27] Y. Li, Q. Fu, M. Flytzani-Stephanopoulos, Appl. Catal. B, 27 (2000) 179.
[28] S.F. Friedrich Esch, Ling Zhou, Tiziano Montini, Cristina Africh, Paolo Fornasiero, Giovanni Comelli, and Renzo Rosei, Science, 309 (2005) 752.
[29] Q. Li, X. Wang, Y. Xin, Z. Zhang, Y. Zhang, C. Hao, M. Meng, L. Zheng, L. Zheng, Sci. Rep., 4 (2014).
[30] C. Janiak, R. Hoffmann, P. Sjovall, B. Kasemo, Langmuir, 9 (1993) 3427.
[31] D. Lamoen, B.N.J. Persson, J. Chem. Phys., 108 (1998) 3332.
[32] S. Derrouiche, P. Gravejat, B. Bassou, D. Bianchi, Appl. Surf. Sci., 253 (2007) 5894.
[33] D. Curulla, A. Clotet, J.M. Ricart, F. Illas, J. Phys. Chem. B, 103 (1999) 5246.
[34] J. Xu, J.T. Yates Jr, Surf. Sci., 327 (1995) 193.
[35] L. Bollmann, J.L. Ratts, A.M. Joshi, W.D. Williams, J. Pazmino, Y.V. Joshi, J.T. Miller, A.J. Kropf, W.N. Delgass, F.H. Ribeiro, J. Catal., 257 (2008) 43.
[36] K.I. Choi, M.A. Vannice, J. Catal., 131 (1991) 1.
[37] M. Agnelli, H.M. Swaan, C. Marquez-Alvarez, G.A. Martin, C. Mirodatos, J. Catal., 175 (1998) 117.
[38] M. Araki, V. Ponec, J. Catal., 44 (1976) 439.
[39] S. Ichikawa;, H. Poppa;, M. Boudart, J. Catal., 91 (1985) 1.
[40] A. Holmgren, B. Andersson, D. Duprez, Appl. Catal. B, 22 (1999) 215.
[41] G. Jacobs, B.H. Davis, Appl. Catal. A, 333 (2007) 192.
[42] G. Jacobs, E. Chenu, P.M. Patterson, L. Williams, D.E. Sparks, G.A. Thomas, B.H. Davis, Appl. Catal. A, 258 (2004) 203.
[43] X. Wang, J.A. Rodriguez, J.C. Hanson, D. Gamarra, A. Martínez-Arias, M. Fernández-García, J. Phys. Chem. B, 110 (2006) 428.
[44] F.B. Tatyana Tabakova, Maela Manzoli, Donka Andreeva, Appl. Catal. A, 252 (2003) 385.
[45] F.C. Meunier, D. Reid, A. Goguet, S. Shekhtman, C. Hardacre, R. Burch, W. Deng, M. Flytzani-Stephanopoulos, J. Catal., 247 (2007) 277.
[46] W. Xu, R. Si, S.D. Senanayake, J. Llorca, H. Idriss, D. Stacchiola, J.C. Hanson, J.A. Rodriguez, J. Catal., 291 (2012) 117.
[47] D. Tibiletti, F.C. Meunier, A. Goguet, D. Reid, R. Burch, M. Boaro, M. Vicario, A. Trovarelli, J. Catal., 244 (2006) 183.
[48] C.M. Kalamaras, S. Americanou, A.M. Efstathiou, J. Catal., 279 (2011) 287.
[49] O. Pozdnyakova, D. Teschner, A. Wootsch, J. Kröhnert, B. Steinhauer, H. Sauer, L. Toth, F.C. Jentoft, A. Knop-Gericke, Z. Paál, R. Schlögl, J. Catal., 237 (2006) 1.
[50] C. Li, Y. Sakata, T. Arai, K. Domen, K.-i. Maruya, T. Onishi, J. Chem. Soc., Faraday Trans., 85 (1989) 929.
[51] C. Li, Y. Sakata, T. Arai, K. Domen, K.-i. Maruya, T. Onishi, J. Chem. Soc., Faraday Trans., 85 (1989) 1451.
[52] T. Shido, Y. Iwasawa, J. Catal., 141 (1993) 71.

[53] G. Jacobs, L. Williams, U. Graham, G.A. Thomas, D.E. Sparks, B.H. Davis, Appl. Catal. A, 252 (2003) 107.
[54] L.C. Grabow, A.A. Gokhale, S.T. Evans, J.A. Dumesic, M. Mavrikakis, J. Phys. Chem. C, 112 (2008) 4608.
[55] A. Karpenko, R. Leppelt, V. Plzak, R.J. Behm, J. Catal., 252 (2007) 231.
[56] A.A. Gokhale, J.A. Dumesic, M. Mavrikakis, J. Am. Chem. Soc., 130 (2008) 1402.
[57] A.A.P. N.A. Koryabkina, W.F. Ruettinger, R.J. Farrauto, and F.H. Ribeiro, J. Catal., 217 (2003) 233.
[58] S.S. Hla, Y. Sun, G.J. Duffy, L.D. Morpeth, A. Ilyushechkin, A. Cousins, D.G. Roberts, J.H. Edwards, Int. J. Hydrogen Energ, 36 (2011) 518.
[59] R. Radhakrishnan, R.R. Willigan, Z. Dardas, T.H. Vanderspurt, Appl. Catal. B, 66 (2006) 23.
[60] J. Kugai, E.B. Fox, C. Song, Applied Catalysis A: General, 497 (2015) 31.
[61] B. Zugic, S. Zhang, D.C. Bell, F. Tao, M. Flytzani-Stephanopoulos, J. Am. Chem. Soc., 136 (2014) 3238.
[62] Y. Chen, H. Wang, R. Burch, C. Hardacre, P. Hu, Faraday Discuss., 152 (2011) 121.
[63] K.-R. Hwang, C.-B. Lee, J.-S. Park, J. Power Sources, 196 (2011) 1349.
[64] G.N. Vayssilov, M. Mihaylov, P.S. Petkov, K.I. Hadjiivanov, K.M. Neyman, J. Phys. Chem. C, 115 (2011) 23435.
[65] G. Jacobs, P.M. Patterson, U.M. Graham, D.E. Sparks, B.H. Davis, Appl. Catal. A, 269 (2004) 63.
[66] B.S. R. Leppelt, V. Plzak, M. Kinne, R. Behm, J. Catal., 244 (2006) 137.
[67] K.G. Azzam, I.V. Babich, K. Seshan, L. Lefferts, J. Catal., 251 (2007) 153.
[68] K.G. Azzam, I.V. Babich, K. Seshan, L. Lefferts, J. Catal., 251 (2007) 163.

Chapter 7 Cubic CeO_2@Nickel Phyllosilicate@CeO_2 Core-Shell Nano-Composite for Water-Gas Shift Reaction

Nano-catalysts are known to possess superb catalytic activity due to size effect. However, sintering of both its active metal and support are usually inevitable under high temperatures, thereby leading to deterioration of catalytic activity and selectivity. It is hence highly desirable to devise methods to prevent sintering of these nano-catalysts. In this chapter, a facile method is demonstrated to simultaneously preserve active metal dispersion and support morphology by synthesizing cubic CeO_2@Ni phyllosilicate@CeO_2 (CeO_2@Ni-Phy@CeO_2) core-shell catalysts, which exhibited excellent catalytic performance for water-gas shift (WGS) reaction. Sintering of active Ni was prevented by formation of Ni phyllosilicate which has strong interaction with metal Ni while agglomeration of CeO_2 was eliminated by the encapsulation with Ni-Phy which isolated cubic CeO_2 as separate entities. Secondary CeO_2 shell in dual-coated core-shell catalysts conferred enhanced metal-support interaction and reducibility which was reflected through higher WGS activity and selectivity than single-coated CeO_2@Ni-Phy catalyst.

7.1 Introduction

As one of the most reactive rare earth oxides, ceria (CeO_2) has garnered tremendous attention due to its widespread use in a variety of applications such as three-way catalysts (TWCs) for conversion of toxic pollutants into harmless emissions, water-gas shift reaction [1-6], CO oxidation [7], fuel cells and solar

cells. These applications capitalize on its high oxygen mobility and excellent oxygen storage capacity (OSC) which is associated with its redox potential to shuffle between Ce^{3+} and Ce^{4+} and its rich oxygen vacancies. Over the past decade, significant advancements have been made in the field of nanotechnology. Nanocrystalline ceria has been shown to exhibit more superior physical and chemical properties than their counterparts which are micro-sized. With nano-sized structures, the energies required for defect formation may be significantly decreased, leading to greater formation of non-stoichiometry and electronic carrier generation [8]. Besides crystal size, crystal shape also has substantial impact on the physicochemical properties of these nanocrystalline structures. Recently, much effort has been devoted on the development of robust synthetic approaches for size/shape-controlled CeO_2 nanostructures (plates [9-11], polyhedra [12, 13], disks [14], dots [15-17], rods [18, 19], tubes [20, 21], wires [22, 23] and cubes [24, 25]). Different crystal facets exposed on CeO_2 nanocrystals with different shapes have been correlated with shape-dependent catalytic properties which lead to different catalytic reactivities [8, 24, 26]. In particular, anisotropic CeO_2 nanorods and nanocubes have been shown to possess higher oxygen storage capacity as well as exhibit higher CO conversion at lower temperature than nanospheres due to the greater concentration of {100} and {110} surfaces [27-29]. Furthermore, it has been shown that the {100} plane, which is dominant in nanocubes, is more active catalytically due to its high energetic instability as compared to the other two planes (i.e. {111} and {100}) [25, 29].

However, the {100} facet is also prone to transformation to the less reactive {111} upon heating to high temperatures since it is energetically unstable [25].

Numerous efforts have been devoted to enhance the active metal dispersion including the formation of core-shell structures [30-32], perovskite structures [33-37], spinel structure [38] and bimetallic alloy [39-41]. In particular, exploration of core-shell nanostructures has been gaining momentum in recent years with the aim of capitalizing on the advantage of its unique structure that confers enhanced activity and selectivity [42]. Core-shell structures have been found to exhibit strong-metal support interaction, leading to superb catalytic properties as compared to conventional supported catalysts for water-gas shift (WGS) reaction [43-48]. However, these core-shell catalysts were often utilized in low-temperature WGS and their application in high-temperature WGS is scarce or obsolete. Despite the importance of ceria in the reaction, little has been done to prevent the sintering of oxide support. Recently, coating a second layer on nano-materials which are prone to sintering to form core/yolk shell or embedded structure has been shown to be an effective method to enhance their sintering resistance property [49-56]. SiO_2 is widely selected as the shell material since it is stable at high temperatures and can be easily modified to meet certain applications. Metal silicates have also attracted extensive attention since they have a large surface area, good thermal stability, and chemical reactivity. They are widely employed as adsorbents in waste water treatment [57] and catalyst supports [58]. Ni phyllosilicate (Ni-Phy) has a promising application as a catalyst with Ni as the

active metal. Recently, it was used as a precursor to form the catalyst Ni/SiO_2 and exhibited good catalytic performance for the ethanol steam reforming reaction [59]. The improved catalytic performance was attributed to the increased interactions between Ni and SiO_2 support. Strong metal support interaction has been reported to prevent sintering of the active metal during both the preparation process and the reaction process.[54, 60-62] Therefore, it is speculated that when Ni-Phy is employed for high temperature reactions, sintering of Ni can be prevented due to its strong interaction with the Ni-Phy matrix. Furthermore, by encapsulating cubic CeO_2 with Ni-Phy, the morphology of cubic CeO_2 and its advantageous inherent properties can be preserved.

As discussed above, in order to simultaneously maintain the morphology of oxide support and active metal dispersion, catalysts with oxides which are more prone to sintering were designed as the core and metal silicates as the shell. To further enhance the metal-support (i.e. Ni-Ce) interaction, a second layer of CeO_2 was coated around the Ni-Phy layer. Oxides confined within the shell of metal silicate can be prevented from high temperature sintering. Similarly, active metals are unable to sinter by confining them within the crystal structure of metal silicates. Herein, cubic CeO_2 is used as the core material to take advantage of the high reactivity of the {100} facet, and Ni-Phy is selected as the primary shell material with another CeO_2 layer as a secondary layer to further improve the metal-support interaction. The catalysts were then tested for WGS reaction which was chosen as a probe reaction to characterize the catalyst reactivity since Ni-

CeO_2 catalysts have been shown to be bi-functional catalysts for the WGS reaction [1-3]. The cubic CeO_2@Ni-Phy@CeO_2 core-shell nano-composite exhibited superb catalytic activity and stability for the WGS reaction. The objective of this work is therefore to investigate the role of metal-support interaction while simultaneously preserve the catalyst support morphology and the active metal via the formation of dual-coated core-shell structure.

7.2 Experimental

7.2.1 Catalyst preparation

7.2.1.1 Synthesis of cubic CeO_2

Cubic CeO_2 was synthesized by the reported hydrothermal method with some modifications [63]. Specifically, 0.545 g ceric ammonium nitrate was mixed with 8.02 g oleylamine (70%, Sigma-Aldrich) and preheated at 100 ^oC for 20 min under magnetic stirring. After that, 2.82 g Oleic acid (90%, Sigma-Aldrich) was injected into the above mixture at room temperature. This mixture was magnetically stirred while adding a second mixture of 50 mL of DI water and 0.0144 g of sodium laurylsulfonate, forming an orange coloured slurry. Then, the orange coloured slurry was transferred into the autoclave. After heating the autoclave at 220 °C for 24 h, the yellow organic part was separated by centrifuge to obtain cubic CeO_2. The newly obtained cubic CeO_2 was dispersed into cyclohexane for further use.

7.2.1.2 Synthesis of cubic CeO_2@SiO_2 core-shell nanoparticles with different shell thickness

Cubic CeO_2@SiO_2 core shell nanoparticles were synthesized by the micro emulsion method. In detail, 175 mL of cyclohexane containing the above synthesized CeO_2 was mixed with Igepal CO-630 and 1 mL ammonia (28%). After stirring at room temperature for 30 min, 0.3 mL or 1.5 mL ethyl silicate was added drop wise into the above micro emulsion with a speed of 1 $mL \cdot h^{-1}$ to obtain CeO_2@SiO_2 with the shell thickness of 3.7 nm or 15 nm. After stirring for 24 h, CeO_2@SiO_2 was separated and dispersed into ethanol for further use.

7.2.1.3 Synthesis of cubic CeO_2@Ni-phy core-shell nanocomposite

Thirty (30) mL of ethanol containing CeO_2@SiO_2 with a shell thickness of 15 nm was mixed with 40 mL of DI water, 2.60 g of urea, and 0.280 g of $Ni(NO_3)_2 \cdot 6H_2O$ in the autoclave. After stirring for 10 min at room temperature, the autoclave was heated at 200 °C for 15 h. After cooling down to room temperature, the sample was separated by centrifuge and dried at room temperature. The powder was calcined at 700 °C for 4 h at the ramping rate of 2 $°C \cdot min^{-1}$.

7.2.1.4 Synthesis of cubic CeO_2@SiO_2@CeO_2

0.500 g cubic CeO_2@SiO_2 nanoparticles and 2.66 g $Ce(NO_3)_3$ were dispersed into 80 ml ethanol by stirring to ensure that the nanoparticles are well dissolved. This beaker was denoted as beaker 1. In another beaker (denoted as beaker 2), 10 g hexamethylenetetramine was dispersed into 20 ml DI water under

stirring. The mixture in beaker 2 was then introduced into beaker 1. The combined mixtures were stirred, heated at 70 °C for 7 h. Subsequently, the mixture was centrifuged and the precipitate was dried and denoted as c-CeO_2@SiO_2@CeO_2. The thickness of CeO_2 can be varied by adjusting the amount of $Ce(NO_3)_3$ and the reaction time.

7.2.1.5 Synthesis of CeO_2@Nickel Phyllosilicate@CeO_2 core-shell nanocomposite

0.500 g c-CeO_2@SiO_2@CeO_2 nanoparticles (with thickness of 3 nm or 15 nm) were dispersed into 100 ml DI water under stirring. The pH was adjusted to around 11 using ammonia solution and 0.500 g $Ni(NO_3)_2$ was added. The solution was then heated to 60 °C and kept at the temperature for 12 h. The thickness of Ni-phy can be varied by adjusting the amount of $Ni(NO_3)_2$ and the reaction time.

7.2.2 Catalyst characterization

TEM, BET, XRD, ICP-MS, H_2-TPR and DRIFTS were utilized to characterize the core-shell catalysts. The details of these characterization techniques are described in Section 3.4.

7.2.3 Catalyst activity measurement

The procedures for catalyst activity testing of CeO_2@Ni-Phy and CeO_2@Ni-Phy@CeO_2 catalysts follow the description stated in Section 3.2.

7.3 Results and discussion

7.3.1 Synthesis and morphology of core-shell nanocomposites

The schematic procedure to prepare cubic CeO_2@Ni-Phy@CeO_2 core-shell nano-composite is illustrated in **Figure 7.1**.

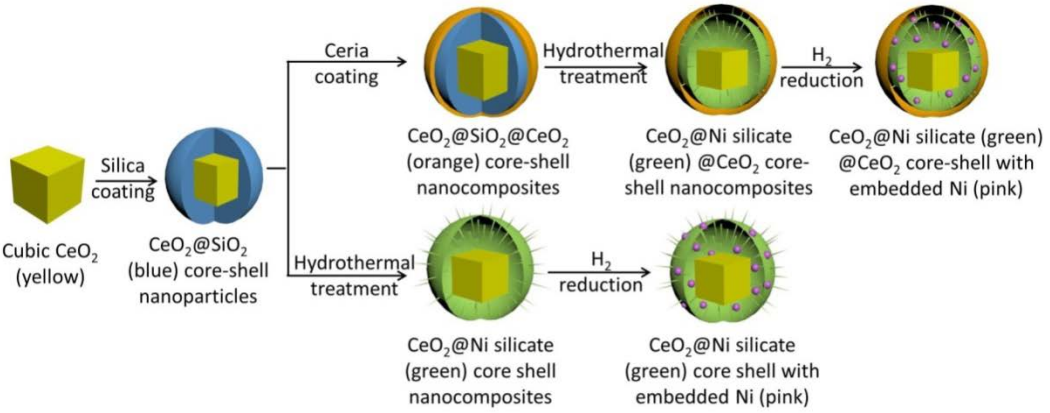

Figure 7-1 Schematic illustration of formation process of cubic CeO_2@Ni phyllosilicate@CeO_2 core-shell nanocomposite.

Firstly, cubic CeO_2 was synthesized via a modified hydrothermal method [63]. As can be seen from **Figure 7.2(a)**, CeO_2 nano-cubes mainly enclosed with {100} crystal planes have been successfully synthesized and their crystalline structure have been confirmed from XRD (JCPDS 04-0593) (**Figure 7.3(a)**). Subsequently, CeO_2@SiO_2 core shell nanoparticles with shell thickness of around 3 nm and 15 nm were synthesized (**Figure 7.2(b)** and **Figure 7.2(c)**). The appearance of silica peak centred at around 23.5^o (**Figure 7.3 (b)**) verified the successful coating of SiO_2 on CeO_2. Thirdly, Ni-Phy was formed as the shell via hydrothermal treatment using SiO_2 shell as the silica source. **Figure 7.2(d)** demonstrates the formation of the core-shell structure with CeO_2 uniformly

isolated and trapped within the Ni-Phy shell. X-ray diffraction (**Figure 7.3(c)**) peaks centred at 24.3°, 34.2°, 36.7° and 60.5° corresponding to (004), (200), (202) and (208) planes confirmed the formation of 1:1 Ni-Phy ($Ni_3Si_2O_5(OH)_4$) (JCPDS 22-0754). Finally, upon reduction at 700 °C, active Ni metal was reduced within Ni-Phy crystal structure. Due to the low concentration of Ni-Phy in CeO_2@Ni-Phy-thin@CeO_2 (**Figure 7.3(d)**) and CeO_2@Ni-Phy-thick@CeO_2 (**Figure 7.3(e)**) as revealed by ICP-MS measurements (**Table 7.1**), the characteristic peaks are hard to discern. The formation of Ni-Phy phase were reaffirmed using FTIR analysis and discussed later in the below Section 7.3.5.

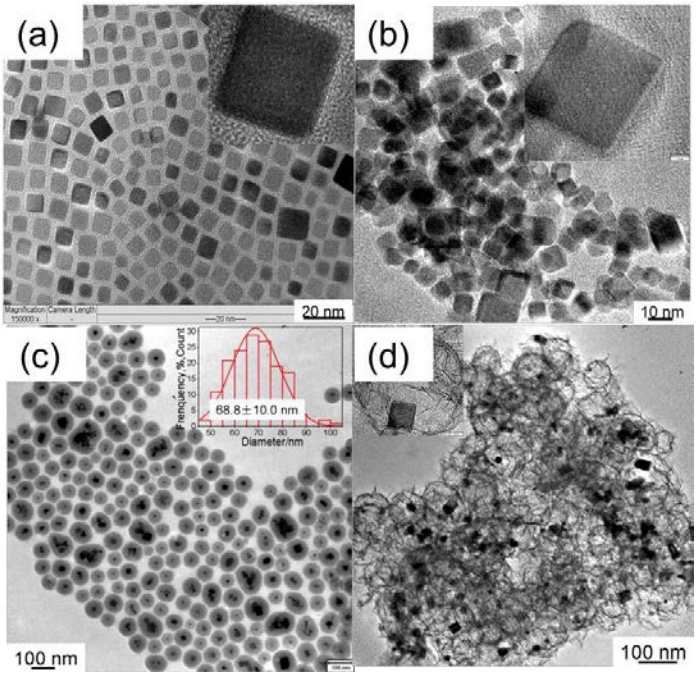

Figure 7-2 TEM images of (a) cubic CeO_2, (b) cubic CeO_2@SiO_2-thin, (c) cubic CeO_2@SiO_2-thick and (d) cubic CeO_2@Ni-Phy nanocomposite.

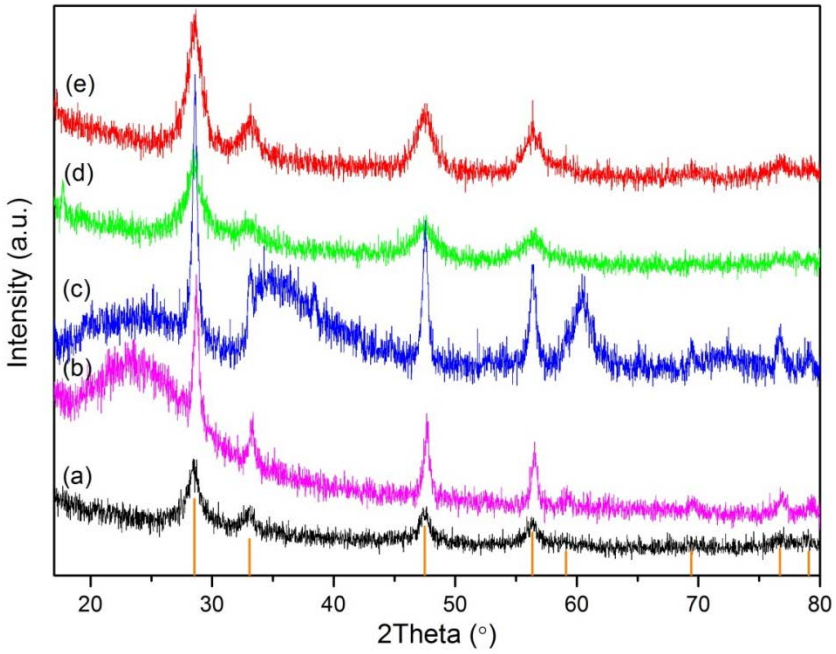

Figure 7-3 XRD patterns of (a) cubic CeO_2, (b) cubic CeO_2@SiO_2, (c) cubic CeO_2@Ni-Phy nanocomposite, (d) cubic CeO_2@Ni-Phy-thin@CeO_2 and (e) cubic CeO_2@Ni-Phy-thick@CeO_2.

In order to further enhance the metal-support (i.e. Ni-Ce) interaction, a secondary layer of CeO_2 was coated onto the primary layer of SiO_2 before introducing nickel to produce cubic CeO_2@Ni-Phy@CeO_2 core-shell catalysts (as illustrated in **Figure 7.4**). Briefly, the thickness of the Ni-Phy layer in the CeO_2@Ni-Phy@CeO_2 catalysts were varied by using CeO_2@SiO_2@CeO_2 with 3 nm **Figure 7.4(a)** and **Figure 7.4(b)**) and 15 nm (**Figure 7.4(d)** and **Figure 7.4(e)**) as templates to derive CeO_2@Ni-Phy-thin@CeO_2 (**Figure 7.4(c)**) and CeO_2@Ni-Phy-thick@CeO_2 (**Figure 7.4(f)**).

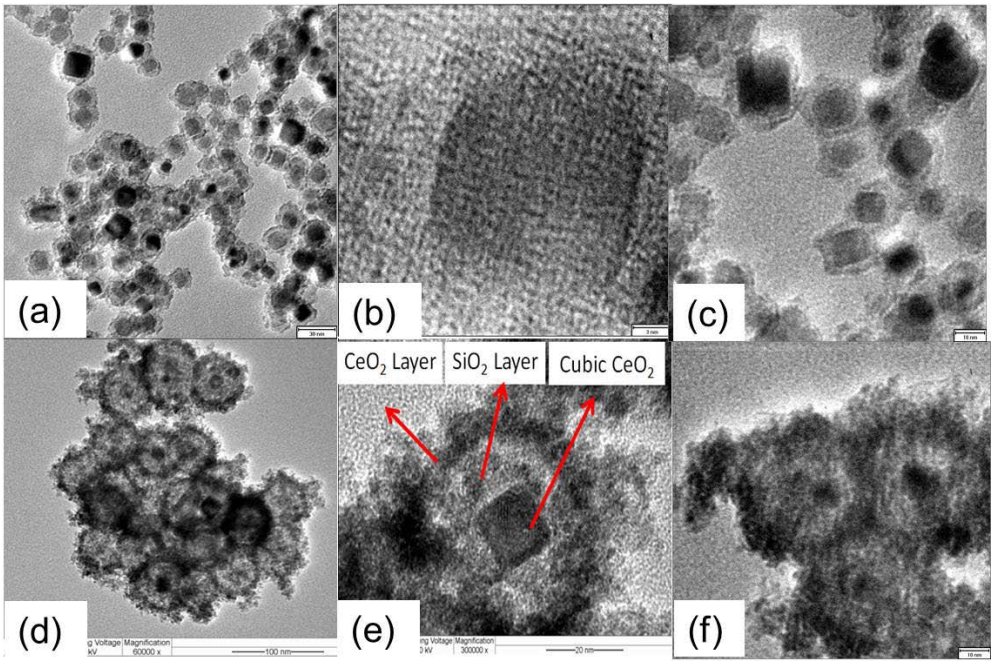

Figure 7-4 TEM and HRTEM images of (a-b) CeO_2@SiO_2@CeO_2 with SiO_2 thickness around 3 nm, (c) CeO_2@Ni phyllosilicate@CeO_2 using (a) as the template, (d-e) CeO_2@SiO_2@CeO_2 with SiO_2 thickness around 15 nm, and (f) CeO_2@Ni phyllosilicate@CeO_2 using (d) as the template.

7.3.2 Textural properties

The textural properties of the catalysts were characterized by N_2 adsorption-desorption method. The calculated values from the BET isotherms are tabulated in **Table 7.1**. CeO_2@Ni-Phy catalyst showed the largest pore volume and BET surface area of 0.690 cm^3/g and 241 m^2/g, respectively. In contrast, CeO_2@Ni-Phy-thin@CeO_2 and CeO_2@Ni-Phy-thick@CeO_2 catalysts showed lower surface areas and pore volumes, with the prior having marginally higher surface area (149 m^2/g) and pore volume (0.310 cm^3/g) than the latter (125 m^2/g and 0.290 cm^3/g). The decrease in surface area in the dual-coated core-shell catalysts can be attributed to the penetration of Ce into the pores of the Ni-phy shell, resulting in the blockage of pores and a consequent decrease in the surface

area. The elemental composition of the catalysts were measured by ICP-MS and as shown in **Table 7.1**, the Ni composition in the dual-coated core-shell catalysts is similar while that of CeO_2@Ni-Phy is about 5 times greater.

Table 7.1 Textural properties and element ratio of catalysts with different structures

Catalyst	**Surface area (m^2/g)[a]**	**Pore volume (cm^3/g)**	**Elemental ratio (%)[b]**		
			Ni	**Ce**	**Si**
CeO_2@Ni-Phy-thin@CeO_2	149	0.310	3.62	56.0	9.58
CeO_2@Ni-Phy-thick@CeO_2	125	0.290	5.37	41.8	10.1
CeO_2@Ni-Phy	241	0.690	25.9	7.43	26.5

[a] Measured by BET method. [b] Determined from Inductively Coupled Plasma-Mass Spectrometry (ICP-MS) analysis.

7.3.3 Metal-support interaction (H_2-TPR)

H_2-TPR was performed to examine the extent of metal support interaction of Ni with Ni-Phy and CeO_2, and the profiles are shown in **Figure 7.5**. Three main reduction peaks can be discerned. The low temperature reduction peak centred at around 330 °C can be attributed to the reduction of surface capping oxygen of ceria and to the reduction of weakly interacting Ni with CeO_2 [64]. The moderate temperature reduction peak centred at around 530 °C can be ascribed to the reduction of Ni^{2+} to Ni^0. As compared to the Ni species reduced at lower reduction temperature of 330 °C, these species which require high reduction temperature have stronger interaction with CeO_2. Lastly, the high temperature reduction peak positioned at around 700-800°C can be attributed to the reduction

of nickel phyllosilicate species. It has been reported that the reduction peaks for 1:1 and 2:1 Ni phyllosilicate species ranged between 450-650 °C and 690-760 °C, respectively [65, 66]. Ni phyllosilicates with greater crystallinity have higher reduction peaks [66]. It is noteworthy to highlight that both the dual-coated core-shell catalysts (i.e. CeO_2@Ni-Phy-thin@CeO_2 and CeO_2@Ni-Phy-thick@CeO_2) required lower temperature for the reduction of Ni phyllosilicate species. The reduction temperature for Ni phyllosilicate species in CeO_2@Ni-Phy-thin@CeO_2 and CeO_2@Ni-Phy-thick@CeO_2 is around 700 °C while that of CeO_2@Ni-Phy is about 800 °C. The lower reduction temperatures for the former can be attributed to the interaction between Ni phyllosilicates with both the cubic CeO_2 core and the secondary CeO_2 shell. Enhanced interaction between metal species and CeO_2 had been shown to increase the reducibility of metal species [67]. In addition, CeO_2@Ni-Phy also requires higher reduction temperature for the reduction of Ni^{2+} species than the dual-coated core-shell catalysts. This observation affirms the importance of the secondary CeO_2 shell in promoting the reducibility of the Ni species within the catalysts. In the presence of a secondary CeO_2 shell, greater metal-support interaction is derived due to the increase in total metal-support interfacial area. This leads to greater reducibility and shifting of reduction temperatures towards lower regions. As revealed in the catalytic tests later, the strong metal-support interaction and the consequent increase in catalyst reducibility play an important role in catalyzing the WGS reaction at lower temperatures. Moreover, based on the reduction profiles of CeO_2@Ni-Phy-thin@CeO_2 and CeO_2@Ni-Phy-thick@CeO_2 catalysts, it can be observed that

CeO_2@Ni-Phy-thin@CeO_2 catalyst possesses greater dominance of Ni-Ce species as compared to CeO_2@Ni-Phy-thick@CeO_2 catalyst which has a major reduction peak for the reduction of Ni phyllosilicate species at 670 °C. With a thinner layer of Ni phyllosilicate sandwiched between the CeO_2 nanocube and secondary CeO_2 shell, enhanced metal-support interaction is conferred in CeO_2@Ni-Phy-thin@CeO_2 catalyst, resulting in the greater prominence of Ni-Ce species as compared to CeO_2@Ni-Phy-thick@CeO_2 catalyst.

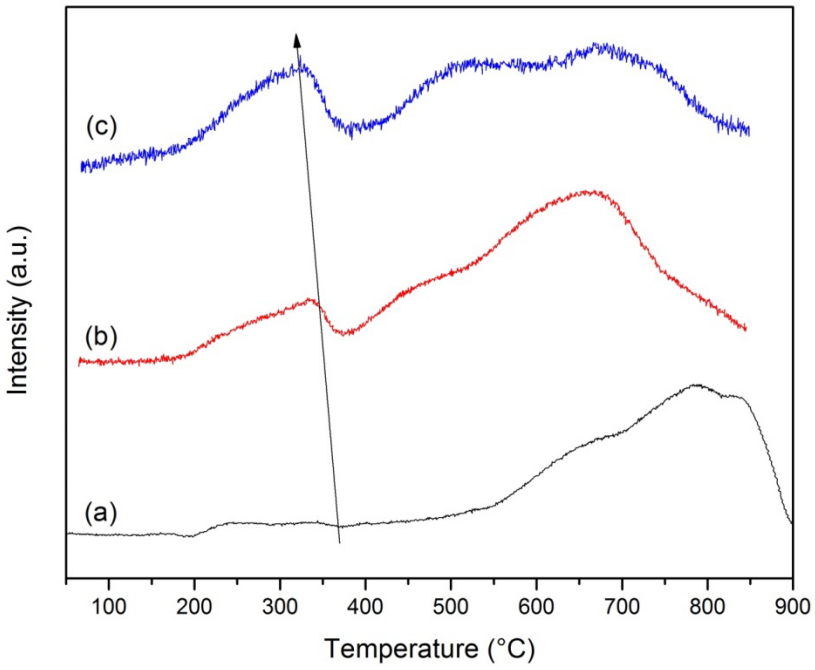

Figure 7-5 H_2-TPR profiles of (a) CeO_2@Ni-Phy, (b) CeO_2@Ni-Phy-thick@CeO_2, and (c) CeO_2@Ni-Phy-thin@CeO_2 catalysts.

7.3.4 Catalyst activity and selectivity

Water-gas shift (WGS) reaction was used as a probe reaction to test the activity of the catalysts. The plots of percentage of CO conversion to CO_2 versus reaction temperature for the CeO_2 nanocube support and the catalysts are

presented in **Figure 7.6(a)**. With solely the cubic CeO_2 support, the onset of CO conversion is observed to occur gradually at 400 °C and then more significantly at 500 °C. It is known that in the absence of a transition metal (e.g. Ni or Cu), CeO_2 is capable of functioning as an active site for water dissociation and subsequent reaction with CO to produce CO_2 and H_2. The onset temperature of 400 °C observed with the CeO_2 nanocube support is consistent with the temperature required for the reduction of surface oxygen species of CeO_2. As temperature increases, bulk oxygen in CeO_2 is increasingly reduced, leading to the observed enhancement in activity at higher temperatures of 500 °C and beyond. Comparing the activity of the core-shell catalysts, it is evident that CeO_2@Ni-Phy-thin@CeO_2 catalyst achieved the highest CO conversion of 94.5% at 400 °C as compared to CeO_2@Ni-Phy-thick@CeO_2 (80.3%) and CeO_2@Ni-Phy (84.2%) catalysts. Moreover, CeO_2@Ni-Phy-thin@CeO_2 exhibits the highest selectivity towards WGS reaction as compared to other catalysts.

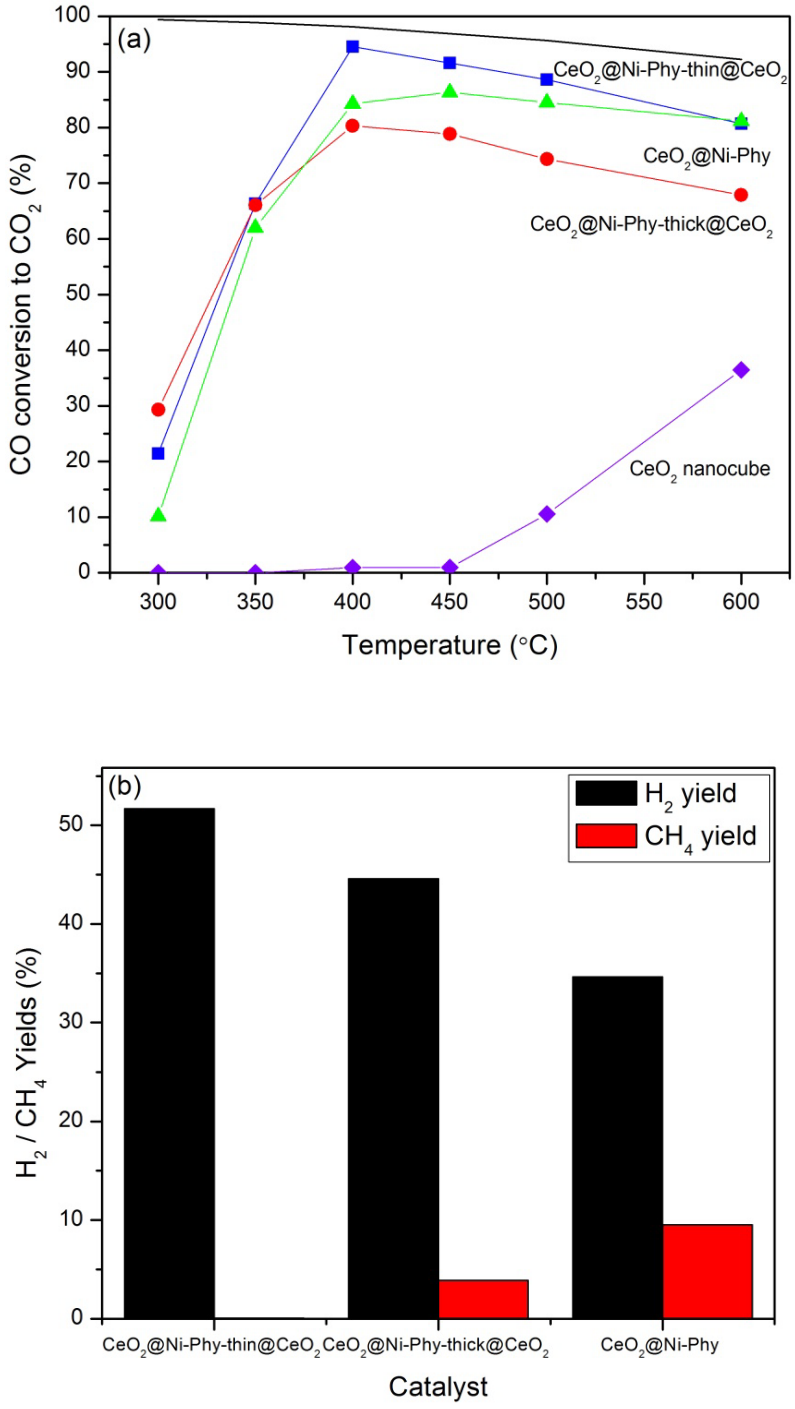

Figure 7-6 (a) Percentages of CO conversion to CO_2, and (b) H_2 and CH_4 percentage yields for core-shell catalysts and CeO_2 nanocube support.

As shown by **Figure 7.6(b)**, which displays the hydrogen and methane yield of the catalysts at 400 °C, CeO_2@Ni-Phy-thin@CeO_2 generates the highest hydrogen yield (51.7%) due to almost zero methane formation (0.046%). Contrastingly, CeO_2@Ni-Phy-thick@CeO_2 and CeO_2@Ni-Phy generated high methane yields of 3.89% and 9.52%, respectively. As a result of their lower selectivities towards WGS reaction, reduced hydrogen yields of 44.6% and 34.6% were attained for CeO_2@Ni-Phy-thick@CeO_2 and CeO_2@Ni-Phy, respectively. The high methane yield observed with CeO_2@Ni-Phy can be attributed to excessively high nickel coverage as well as the lower metal-support interaction as compared to the dual-coated core-shell catalysts [68].

Figure 7.7 depicts the Arrhenius plots for the water-gas shift reaction over CeO_2@Ni-Phy-thin@CeO_2 and CeO_2@Ni-Phy-thick@CeO_2 catalysts in the temperature range of 375 to 450 °C. The apparent activation energies (E_a) were obtained based on intrinsic CO conversions which were far below the corresponding equilibrium conversions to ensure elimination of internal and external mass transfer limitation. Considering that Ni loading of the catalysts were different (**Table 7.1**), same Ni content was achieved by diluting the catalysts with quartz SiO_2. Consistent with the catalytic activity results presented in **Figure 7.6(a)**, CeO_2@NiPhy-thin@CeO_2 catalyst exhibited higher activity with TOF of 0.016 s^{-1} at 400 °C with a lower E_a value of 31 kJ/mol as compared to CeO_2@Ni-Phy-thick@CeO_2 which has a lower activity with TOF of 0.006 s^{-1} at 400 °C with a higher E_a value of 36 kJ/mol.

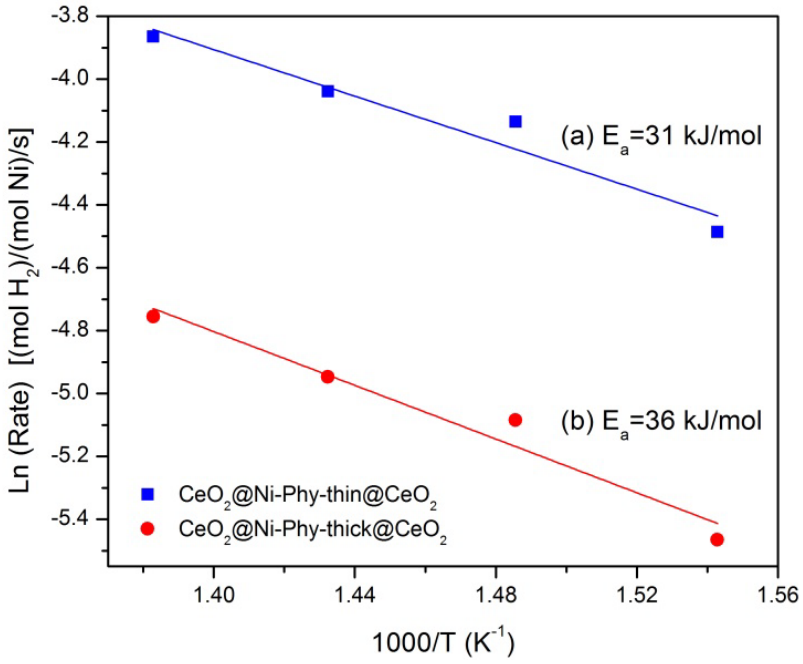

Figure 7-7 Arrhenius plots for the water-gas shift reaction over (a) CeO_2@Ni-Phy-thin@CeO_2, and (b) CeO_2@Ni-Phy-thick@CeO_2 catalysts in 5% CO, 25% H_2O and balance He.

As evident, the TOF of CeO_2@Ni-Phy-thin@CeO_2 is almost thrice that of CeO_2@Ni-Phy-thick@CeO_2, the higher catalytic activity can be attributed to the enhanced metal-support interfacial area which serves as active sites for catalyzing WGS reaction. In CeO_2@Ni-Phy-thick@CeO_2 catalyst, nickel species embedded within Ni-Phy phase has less interaction with CeO_2, resulting in lower metal-support interaction. In addition, the enhanced metal-support interaction in CeO_2@Ni-Phy-thin@CeO_2 catalyst results in lower activation energy since strong metal-support interaction has been shown to decrease the activation energy barriers for water dissociation which is commonly known to be the rate determining step in WGS reaction [69]. This result is consistent with the findings from H_2-TPR results (**Figure 7.5**) which revealed that CeO_2@Ni-Phy-thin@CeO_2

catalyst has greater reducibility which can result in higher generation of oxide vacancies and increased ease in water dissociation.

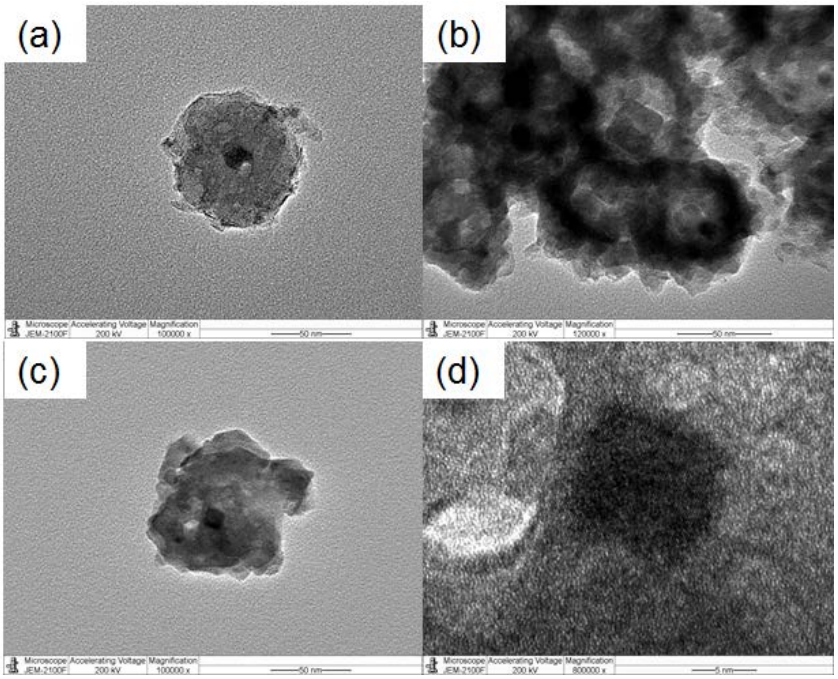

Figure 7-8 TEM images of spent catalysts after catalytic test (a)CeO_2@Ni-Phy, (b) CeO_2@Ni-Phy-thick@CeO_2, (c) and (d) CeO_2@Ni-Phy-thin@CeO_2.

TEM analysis was conducted on the spent catalysts and the images are presented in **Figure 7.8**. As evident from the TEM images of the spent catalysts, the morphology of cubic CeO_2 is preserved in all three core-shell catalysts, indicating that the structural stability of cubic CeO_2 was maintained by the surrounding Ni phyllosilicate layer which is thermally stable. This is of importance since the [100] plane, which is dominant in nanocubes, is catalytically active and plays a vital role in enhancing the WGS reaction. Moreover, it can be observed from **Figure 7.8(c)** and **Figure 7.8(d)** that both the morphology of cubic CeO_2 and small Ni particle sizes are maintained, inferring that the thin Ni-Phy

phase surrounding the cubic CeO_2 core was sufficient and effective in preventing the sintering of both the metal oxide and active Ni metal. The preservation of both the morphology of CeO_2 and small Ni metal particles are the main attributes for the excellent WGS activity and selectivity observed in the CeO_2@Ni-Phy-thin@CeO_2 catalyst.

7.3.5 In-situ DRIFTS

DRIFTS analysis was conducted to further confirm the formation of Ni phyllosilicate phase for these catalysts and to identify the reaction intermediates formed during CO adsorption. **Figure 7.9** presents the hydroxyl region of the spectra taken at 300 °C. The absorption band at 3746 cm^{-1} corresponds to the isolated silanol (-OH) groups on silica surface [70]. In general, two bands at 3629 cm^{-1} and 3649 cm^{-1} are attributed to the stretching of γ_{OH} band in 2:1 nickel phyllosilicate and 1:1 nickel phyllosilicate respectively [65]. As observed in **Figure 7.9**, both bands are evident in the spectra of CeO_2@Ni-Phy-thick@CeO_2 and CeO_2@Ni-Phy but in the case of CeO_2@Ni-Phy-thin@CeO_2, only a weak band at 3629 cm^{-1} is present. The absence of the band at 3649 cm^{-1} and the weak intensity of the band at 3629 cm^{-1} might be due to the low concentration of nickel phyllosilicate in the thin shell that is encapsulating cubic ceria. The presence of these bands affirms the formation of nickel phyllosilicate in these catalysts.

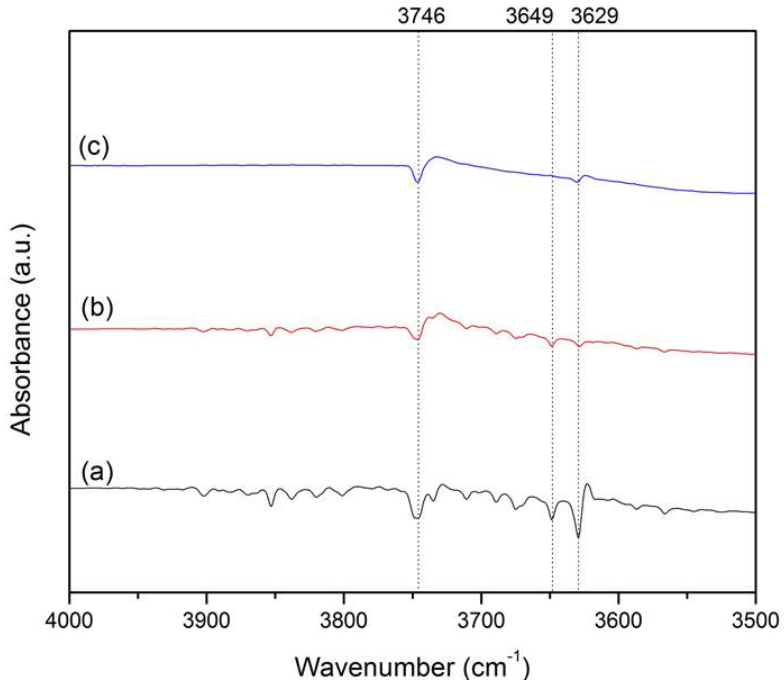

Figure 7-9 DRIFTS spectra (hydroxyl region) taken at 300 °C for (a) CeO_2-Ni-Phy, (b) CeO_2@Ni-Phy-thick@CeO_2, and (c) CeO_2@Ni-Phy-thin@CeO_2 catalysts.

The carbonylic and carbonates regions of the spectra measured at 300 °C are displayed in **Figure 7.10**. The doublet band at 2173 cm^{-1} is attributed to gaseous carbon monoxide while the doublet band at 2344 cm^{-1} is assigned to gaseous carbon dioxide [71]. In the carbonates region, both monodentate carbonate (1566, 1305, 1257 and 858 cm^{-1}) and bidentate carbonate (1449, 1390, 1075 cm^{-1}) are observed. The strong presence of the carbonates suggests the involvement of these species as intermediates in the reaction. Different modes of CO adsorption can be discerned from the spectra of all three catalysts. The vibrational bands of Ni-CO species marked in the figure are 2070 cm^{-1} (subcarbonyl), 2020 cm^{-1} (linear carbonyl), 1957 and 1925 cm^{-1} (bridged carbonyls), and 1844 cm^{-1}(multi-bonded carbonyl) [71]. As compared to the other

two catalysts, CeO_2@Ni-Phy-thin@CeO_2 possesses a distinct band at 2070 cm^{-1} and greater prominence of the doublet band assigned to gaseous carbon dioxide. The sharp band at 2070 cm-1 indicates the homogenous formation of Ni species strongly interacting with CeO_2 (i.e. Ni-O-Ce species). In contrast, more heterogeneity of Ni species can be inferred from the broad bands observed with CeO_2@Ni-Phy and CeO_2@Ni-Phy-thick@CeO_2.

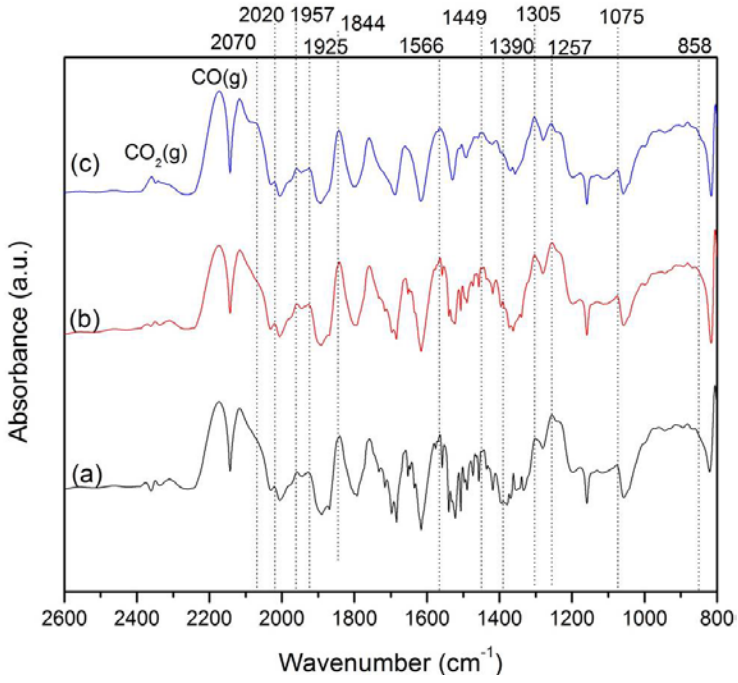

Figure 7-10 DRIFTS spectra (carbonylic and carbonate regions) taken at 300 °C for (a) CeO_2-Ni-Phy, (b) CeO_2@Ni-Phy-thick@CeO_2, and (c) CeO_2@Ni-Phy-thin@CeO_2 catalysts.

7.4 Conclusion

In conclusion, a facile method to simultaneously preserve active metal and morphology of support while attaining strong metal-support interaction was demonstrated via synthesis of CeO_2@Ni-Phy@CeO_2 core-shell catalyst and its

application for WGS reaction. Compared to single-coated CeO_2@Ni-Phy core-shell catalyst, dual-coated CeO_2@Ni-Phy@CeO_2 catalysts exhibited superb catalytic activity and selectivity. The secondary CeO2 shell plays the role of increasing metal-support (i.e. Ni-Ce) interaction, thereby leading to greater catalyst reducibility and higher WGS activity. Strong interaction between Ni and Ni-Phy prevents sintering of active Ni metal while Ni-Phy shell prohibits the sintering of cubic CeO_2 core. Upon reduction of CeO_2@Ni-Phy@CeO_2 catalysts, small Ni particles are derived. These small Ni particles create strong metal-support interaction with both cubic CeO_2 core and secondary CeO_2 shell. In particular, thin layer of Ni-Phy phase sandwiched between cubic CeO_2 core and secondary CeO_2 shell was found to further enhance Ni-Ce interaction by increasing the interfacial area between Ni metal and surrounding CeO_2, leading to lowering of activation energy barrier and increment in WGS activity and selectivity.

7.5 References

[1] M.L. Ang, U. Oemar, Y. Kathiraser, E.T. Saw, C.H.K. Lew, Y. Du, A. Borgna, S. Kawi, J. Catal., 329 (2015) 130.
[2] M.L. Ang, U. Oemar, E.T. Saw, L. Mo, Y. Kathiraser, B.H. Chia, S. Kawi, ACS Catal., 4 (2014) 3237.
[3] E.T. Saw, U. Oemar, X.R. Tan, Y. Du, A. Borgna, K. Hidajat, S. Kawi, J. Catal., 314 (2014) 32.
[4] C. Wen, Y. Zhu, Yingchun Ye, S. Zhang, F. Cheng, Y. Liu, P. Wang, F.F. Tao, ACS Nano, 6 (2012) 9305.
[5] S. Agarwal, L. Lefferts, B.L. Mojet, D.A.J.M. Ligthart, E.J.M. Hensen, D.R.G. Mitchell, W.J. Erasmus, B.G. Anderson, E.J. Olivier, J.H. Neethling, A.K. Datye, ChemSusChem, 6 (2013) 1898.
[6] R. Si, M. Flytzani-Stephanopoulos, Angew. Chem. Int. Ed., 47 (2008) 2884.
[7] G. Vilé, S. Colussi, F. Krumeich, A. Trovarelli, J. Pérez-Ramírez, Angew. Chem. Int. Ed., 53 (2014) 12069.
[8] F. Zaera, ChemSusChem, 6 (2013) 1797.
[9] D. Wang, Y. Kang, V. Doan-Nguyen, J. Chen, R. Küngas, N.L. Wieder, K. Bakhmutsky, R.J. Gorte, C.B. Murray, Angew. Chem. Int. Ed., 50 (2011) 4378.
[10] Y. Minamidate, S. Yin, T. Sato, Mater. Chem. Phys., 123 (2010) 516.
[11] Y. Zhang, F. Hou, Y. Tan, Chemical Communications, 48 (2012) 2391.
[12] R. Si, Y.-W. Zhang, L.-P. You, C.-H. Yan, Angew. Chem. Int. Ed., 44 (2005) 3256.
[13] X. Feng, D.C. Sayle, Z.L. Wang, M.S. Paras, B. Santora, A.C. Sutorik, T.X.T. Sayle, Y. Yang, Y. Ding, X. Wang, Y.-S. Her, Science, 312 (2006) 1504.
[14] X.-H. Guo, C.-C. Mao, J. Zhang, J. Huang, W.-N. Wang, Y.-H. Deng, Y.-Y. Wang, Y. Cao, W.-X. Huang, S.-H. Yu, Small, 8 (2012) 1515.
[15] T. Ghoshal, P.G. Fleming, J.D. Holmes, M.A. Morris, Journal of Materials Chemistry, 22 (2012) 22949.
[16] T. Masui, K. Fujiwara, K.-i. Machida, G.-y. Adachi, T. Sakata, H. Mori, Chemistry of Materials, 9 (1997) 2197.
[17] Y.-W. Zhang, R. Si, C.-S. Liao, C.-H. Yan, C.-X. Xiao, Y. Kou, J. Phys. Chem. B, 107 (2003) 10159.
[18] N. Yi, R. Si, H. Saltsburg, M. Flytzani-Stephanopoulos, Energy Environ. Sci., 3 (2010) 831.
[19] Y. Zhou, N.J. Lawrence, T.-S. Wu, J. Liu, P. Kent, Y.-L. Soo, C.L. Cheung, ChemCatChem, 6 (2014) 2937.
[20] F. Zhu, G. Chen, S. Sun, X. Sun, Journal of Materials Chemistry A, 1 (2013) 288.
[21] S. Agarwal, X. Zhu, E.J.M. Hensen, L. Lefferts, B.L. Mojet, J. Phys. Chem. C, 118 (2014) 4131.
[22] S. Agarwal, L. Lefferts, B.L. Mojet, ChemCatChem, 5 (2013) 479.

[23] B. Tang, L. Zhuo, J. Ge, G. Wang, Z. Shi, J. Niu, Chemical Communications, (2005) 3565.
[24] E. Aneggi, D. Wiater, C. de Leitenburg, J. Llorca, A. Trovarelli, ACS Catal., 4 (2014) 172.
[25] S. Yang, L. Gao, J. Am. Chem. Soc., 128 (2006) 9330.
[26] Z.-A. Qiao, Z. Wu, S. Dai, ChemSusChem, 6 (2013) 1821.
[27] S. Chang, M. Li, Q. Hua, L. Zhang, Y. Ma, B. Ye, W. Huang, J. Catal., 293 (2012) 195.
[28] K. Zhou, X. Wang, X. Sun, Q. Peng, Y. Li, J. Catal., 229 (2005) 206.
[29] H.-X. Mai, L.-D. Sun, Y.-W. Zhang, R. Si, W. Feng, H.-P. Zhang, H.-C. Liu, C.-H. Yan, J. Phys. Chem. B, 109 (2005) 24380.
[30] Z. Li, L. Mo, Y. Kathiraser, S. Kawi, ACS Catal., 4 (2014) 1526.
[31] Z. Li, Y. Kathiraser, J. Ashok, U. Oemar, S. Kawi, Langmuir, 30 (2014) 14694.
[32] Z. Li, Y. Kathiraser, S. Kawi, ChemCatChem, 7 (2015) 160.
[33] U. Oemar, P.S. Ang, K. Hidajat, S. Kawi, Int. J. Hydrogen Energ, 38 (2013) 5525.
[34] U. Oemar, M.L. Ang, W.F. Hee, K. Hidajat, S. Kawi, Appl. Catal. B, 148–149 (2014) 231.
[35] U. Oemar, A. Ming Li, K. Hidajat, S. Kawi, AIChE Journal, 60 (2014) 4190.
[36] D.H. Kim, J.L. Park, E.J. Park, Y.D. Kim, S. Uhm, ACS Catal., 4 (2014) 3117.
[37] K. Sutthiumporn, T. Maneerung, Y. Kathiraser, S. Kawi, Int. J. Hydrogen Energ, 37 (2012) 11195.
[38] Y. Kathiraser, W. Thitsartarn, K. Sutthiumporn, S. Kawi, J. Phys. Chem. C, 117 (2013) 8120.
[39] M. Koike, D. Li, Y. Nakagawa, K. Tomishige, ChemSusChem, 5 (2012) 2312.
[40] J. Ashok, S. Kawi, Appl. Catal. A, 490 (2015) 24.
[41] J. Ashok, S. Kawi, ACS Catal., 4 (2014) 289.
[42] S. Alayoglu, A.U. Nilekar, M. Mavrikakis, B. Eichhorn, Nat Mater, 7 (2008) 333.
[43] C.M.Y. Yeung, S.C. Tsang, Journal of Molecular Catalysis A: Chemical, 322 (2010) 17.
[44] C.M.Y. Yeung, S.C. Tsang, J. Phys. Chem. C, 113 (2009) 6074.
[45] C.M.Y. Yeung, K.M.K. Yu, Q.J. Fu, D. Thompsett, M.I. Petch, S.C. Tsang, J. Am. Chem. Soc. Comm., 127 (2005) 18010.
[46] N.L. Wieder, M. Cargnello, K. Bakhmutsky, T. Montini, P. Fornasiero, R.J. Gorte, J. Phys. Chem. C, 115 (2011) 915.
[47] B. Liu, H. Xu, Z. Zhang, Catal. Commun., 26 (2012) 159.
[48] E.T. Saw, U. Oemar, M.L. Ang, K. Hidajat, S. Kawi, ChemCatChem, (2015) n/a.
[49] X. Du, D. Zhang, R. Gao, L. Huang, L. Shi, J. Zhang, Chem Commun (Camb), 49 (2013) 6770.

[50] L. Adijanto, D.A. Bennett, C. Chen, A.S. Yu, M. Cargnello, P. Fornasiero, R.J. Gorte, J.M. Vohs, Nano Letters, 13 (2013) 2252.
[51] L. Li, S. He, Y. Song, J. Zhao, W. Ji, C.-T. Au, J Catal, 288 (2012) 54.
[52] J.W. Han, C. Kim, J.S. Park, H. Lee, ChemSusChem, 7 (2014) 451.
[53] L. Li, Y. Yao, B. Sun, Z. Fei, H. Xia, J. Zhao, W. Ji, C.T. Au, ChemCatChem, 5 (2013) 3781.
[54] S. Zhang, J. Wang, H. Liu, X. Wang, Catalysis Communications, 9 (2008) 995.
[55] M. Pérez-Lorenzo, B. Vaz, V. Salgueiriño, M.A. Correa-Duarte, Chemistry - A European Journal, 19 (2013) 12196.
[56] A. Cao, R. Lu, G. Veser, Phys Chem Chem Phys, 12 (2010) 13499.
[57] Y. Yang, Y. Zhuang, Y. He, B. Bai, X. Wang, Nano Research, 3 (2010) 581.
[58] R. Jin, S. Sun, Y. Yang, Y. Xing, D. Yu, X. Yu, S. Song, Dalton Transactions, 42 (2013) 7888.
[59] C. Zhang, H. Yue, Z. Huang, S. Li, G. Wu, X. Ma, J. Gong, ACS Sustainable Chemistry and Engineering, 1 (2013) 161.
[60] S. Corthals, J. Van Nederkassel, J. Geboers, H. De Winne, J. Van Noyen, B. Moens, B. Sels, P. Jacobs, Catal Today, 138 (2008) 28.
[61] B.K. Min, A.K. Santra, D.W. Goodman, Catal Today, 85 (2003) 113.
[62] R.P. Mogorosi, N. Fischer, M. Claeys, E. van Steen, J Catal, 289 (2012) 140.
[63] H.-P. Zhou, H.-S. Wu, J. Shen, A.-X. Yin, L.-D. Sun, C.-H. Yan, J Am Chem Soc, 132 (2010) 4998.
[64] Y. Wang, A. Zhu, Y. Zhang, C.T. Au, X. Yang, C. Shi, Appl. Catal. B, 81 (2008) 141.
[65] T. Lehmann, T. Wolff, C. Hamel, P. Veit, B. Garke, A. Seidel-Morgenstern, Microporous and Mesoporous Materials, 151 (2012) 113.
[66] P. Burattin, M. Che, C. Louis, Journal of Physical Chemistry B, 101 (1997) 7060.
[67] S. Zhang, S. Muratsugu, N. Ishiguro, M. Tada, ACS Catal., 3 (2013) 1855.
[68] S.D. Senanayake, J. Evans, S. Agnoli, L. Barrio, T.-L. Chen, J. Hrbek, J.A. Rodriguez, Topics in Catalysis, 54 (2011) 34.
[69] J. Carrasco, D. Lõpez-Durán, Z. Liu, T. Duchoň, J. Evans, S.D. Senanayake, E.J. Crumlin, V. Matolín, J.A. Rodríguez, M.V. Ganduglia-Pirovano, Angewandte Chemie - International Edition, 54 (2015) 3917.
[70] I. Braschi, G. Gatti, C. Bisio, G. Berlier, V. Sacchetto, M. Cossi, L. Marchese, J. Phys. Chem. C, 116 (2012) 6943.
[71] M. Agnelli, H.M. Swaan, C. Marquez-Alvarez, G.A. Martin, C. Mirodatos, J. Catal., 175 (1998) 117.

Chapter 8 Conclusions and Recommendations

8.1 Conclusions

With fast-rising energy demand and increasingly volatile energy prices, there is a need for the development of low cost energy options such as production of syngas/hydrogen via high-temperature reactions. Since the WGS reaction serves a vital role to increase the hydrogen yield of the syngas, there is a pressing requirement to develop high performance, low cost and robust WGS catalyst. In a nutshell, the achievements of this thesis are therefore focused on developing highly active and selective WGS catalyst that suppresses methanation through the application of unique catalyst formulations and rational catalyst structural design. The first milestone is the development of highly dispersed bimetallic Ni-Cu alloy nanoparticles supported on SiO_2 ($NiCu/SiO_2$) for the water-gas shift reaction (Chapter 4). The second and third milestones are the development of alkali (Na and K) doped Ni supported on ceria ($Ni/xNa(K)/CeO_2$ catalysts which were found to display superb activity and selectivity due to enhanced CO adsorption (Chapters 5-6). Finally, novel cubic CeO_2@nickel phyllosilicate@CeO_2 core-shell nanocomposite with strong metal-support interaction was synthesized via a facile method and these dual-coated core-shell catalysts achieved excellent activity and selectivity for WGS reaction (Chapter 7). The specific contributions of this research study are summarized below.

Chapter 4 investigates the role of Ni-Cu alloy and its dispersion on the activity and selectivity in WGS reaction via the development of oleic acid-

promoted xNiyCu/SiO_2 catalysts. 5Ni5Cu/SiO_2 (OA) catalyst was found to exhibit the best catalytic performance; no methane formation was observed and TOF value was double that of 5Ni5Cu/SiO_2 catalyst. Oleic acid (OA) promoted metal dispersion and stronger-metal support interaction in both monometallic and bimetallic catalysts. Formation of highly dispersed and homogeneous Ni-Cu alloy enhanced CO adsorption on Cu sites which led to the suppression of methane and the activation of terminal hydroxyl groups on SiO_2 surface. The activation and provision of OH in the vicinity of bimetallic Ni-Cu alloy is vital in increasing the reactivity of CO and OH, and in the eventual enhancement of the WGS activity. Catalytic stability observed in the long-term reaction test is attributed to the strong metal support interaction induced by OA addition.

Chapter 5 illustrates the effect of sodium doping on Ni/CeO_2 catalysts by varying the Na loading in the Ni/xNa/CeO_2 catalysts. The solubility limit of Na^+ in CeO_2 was found to be 2 wt% which was also the optimal Na loading for achieving superb WGS activity and methane suppression. At low loadings of Na of 0.5 to 2 wt%, Na^+ incorporated into CeO_2 lattice can generate lattice strain, activate lattice O_2 and increase the catalyst reducibility. Beyond the optimal loading of 2 wt%, excess deposition of Na on CeO_2 decreases catalyst reducibility, leading to subpar performance. Interaction between Na and Ni led to the absence of subcarbonyl species which are responsible for methanation was revealed to be the main attribute behind methane suppression.

Chapter 6 presents the effect of potassium doping on Ni/CeO_2 catalysts by varying the K loading in the Ni/xK/CeO_2 catalysts. 5 wt% K was discovered to be

the optimum loading in enhancing the catalytic performance in WGS reaction. The role of K in suppressing methanation was attributed to the inhibition of formation of nickel subcarbonyl species through interaction of Ni and K, synergized by the strong adsorption of CO on Ni via the formation of bridging carbonyls. In terms of activity enhancement, K promoted the reduction of CeO_2 and dissociation of water on reduced CeO_2 to form hydroxyl groups which reactions with adsorbed CO on Ni to form CO_2. A dual-site redox mechanism was proposed to be the dominant pathway for Ni/5K/CeO_2 catalyst.

Chapter 7 illustrates the importance of strong metal-support interaction in enhancing WGS activity through the development of a facile method to synthesize cubic CeO_2@nickel phyllosilicate@CeO_2 core-shell catalysts. CeO_2@Ni-Phy-thin@CeO_2 catalyst attained the best catalytic performance. Nickel phyllosilicate layer sandwiched between cubic CeO_2 core and secondary CeO_2 shell prevented the sintering of active Ni metal while preserving the morphology of cubic CeO_2 support. Thin layer of nickel phyllosilicate was found to be essential in ensuring intimate and strong contact between Ni and CeO_2, thereby conferring enhanced metal-support interaction and reducibility which was reflected by the higher WGS activity and selectivity than single-coated CeO_2@Ni-Phy catalyst.

In summary, the underlying attributes for high WGS activity and selectivity unraveled from the above studies are: (a) optimal strength of CO adsorption on active metal, (b) high density of hydroxyl groups, and (c) enhanced metal-support interaction.

8.2 Recommendations

Based on the research outcomes derived in the process of preparing this thesis, several recommendations are proposed herein for future work in order to translate this research work into viable commercialization. In the present study, experimental studies have been conducted in a bid to acquire fundamental understanding behind the working mechanisms of the developed catalysts. To gain a more comprehensive understanding, it would be commendable to build upon this fundamental knowledge by further probing the reaction mechanism of these catalysts at the atomic scale by coupling micro-kinetic studies with computational modeling such as density functional theory (DFT) calculations. Detailed kinetic models derived through these thorough studies can allow for accurate designs for reactor scale-up in industrial applications.

Furthermore, with the use of harsher temperatures and complicated feedstocks, the issues of thermal deactivation and poisoning (e.g. sulfur, nitrogen, chlorine and etc.) will have to be tackled through development of thermally-stable and sulfur-tolerant catalysts for industrial applications. Despite the success in identification of exclusive active metallic sites for WGS at the atomic scale, it remains a daunting task to retain these single-site species in its active forms at higher temperatures. Moving forward, catalyst development should be geared towards the development of encapsulating these single-site species as metallic cores within a protective shell in core-shell structures in a bid to solve the issues of thermal stability and poisoning while maintaining the high activity that these species confer.

Core-shell catalysts developed in this thesis have been shown to offer excellent WGS activity and selectivity. Organized compartmentalization of individual cores within the protective shells obtained through nanoparticle synthesis has been proven to be effective in preventing metal sintering and in preserving support morphology. However, these nano-catalysts are usually obtained in small quantities. In order to increase the commercial viability of core-shell catalysts, facile methods should be developed to enhance the dispersion of these core-shell catalysts onto commercial supports such as γ-Al_2O_3 and SiO_2 for overall cost reduction while maintaining its excellent catalytic properties. These methods may encompass conventional impregnation or embedment of core-shell catalysts onto the supports. For the former instance, surface functionalization of the core-shell catalysts can be explored to allow easy deposition onto the supports. For the latter instance, self-induced embedment of core-shell catalysts of these supports can possibly be induced by the use of optimal usage of organic acid as suggested by preliminary studies conducted in our group. Therefore, future efforts can be devoted on unraveling the genesis and mechanism of these novel catalysts as it is anticipated that they possess tremendous potential for further application in important potential processes related to global energy, water and environment securities.

Appendix A

Supporting Information for Chapter 4

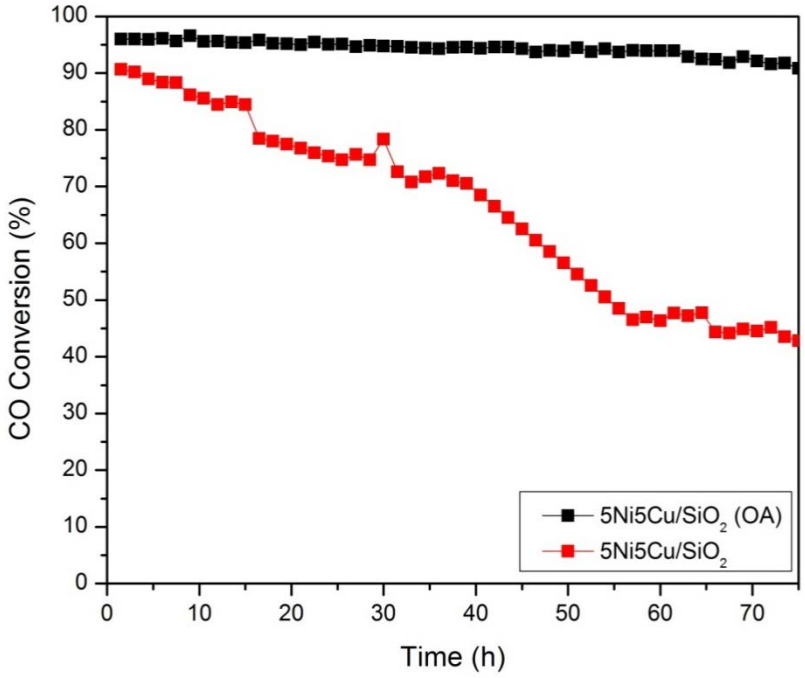

Figure S1 Percentages of CO conversion to CO_2 of $5Ni5Cu/SiO_2$ and $5Ni5Cu/SiO_2$ (OA) catalysts for 75 h reaction.

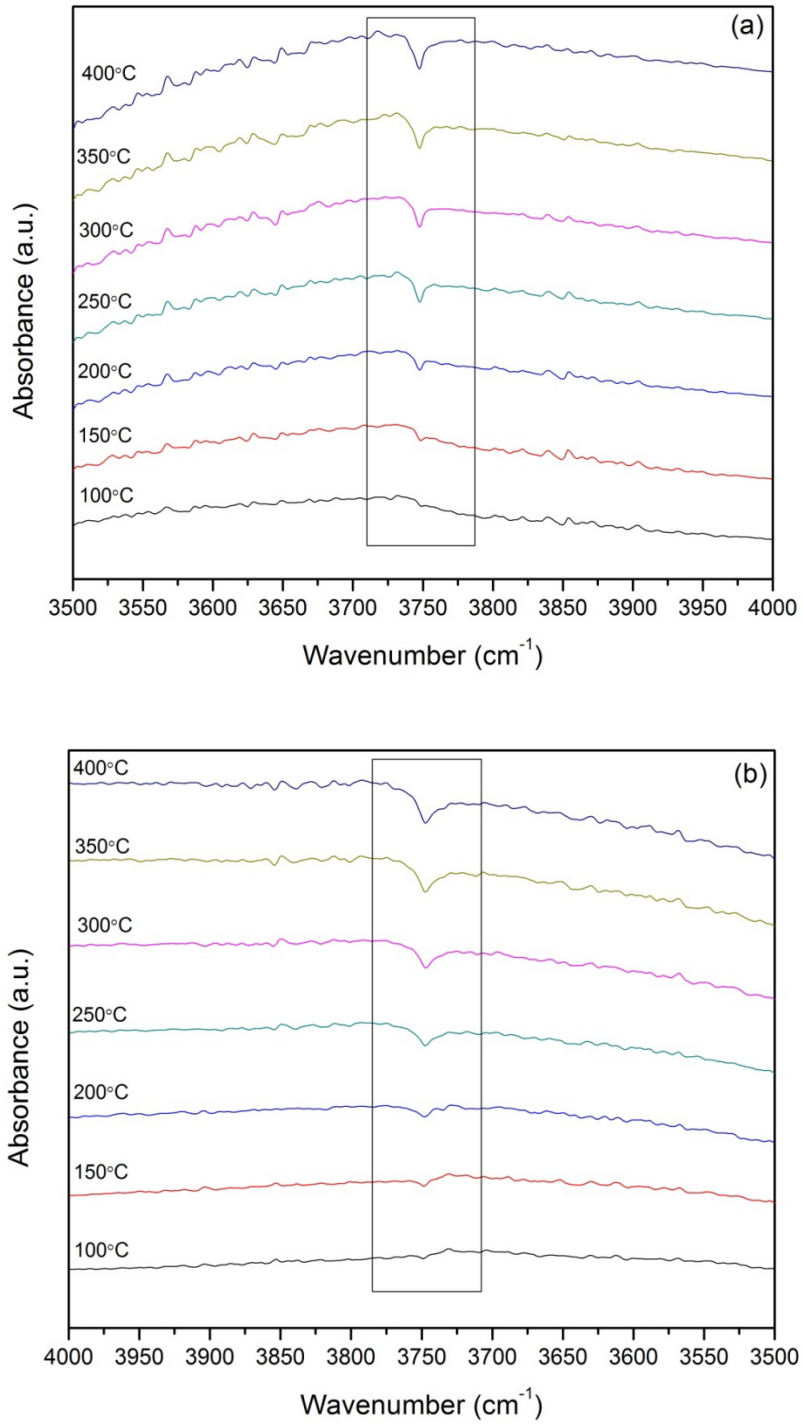

Figure S2 FTIR spectra in the hydroxyl region (3500 – 4000 cm^{-1}) for (a) 10Ni/SiO_2 (OA) and (b) 5Ni5Cu/SiO_2 (OA) catalysts.

Appendix B

Supporting Information for Chapter 5

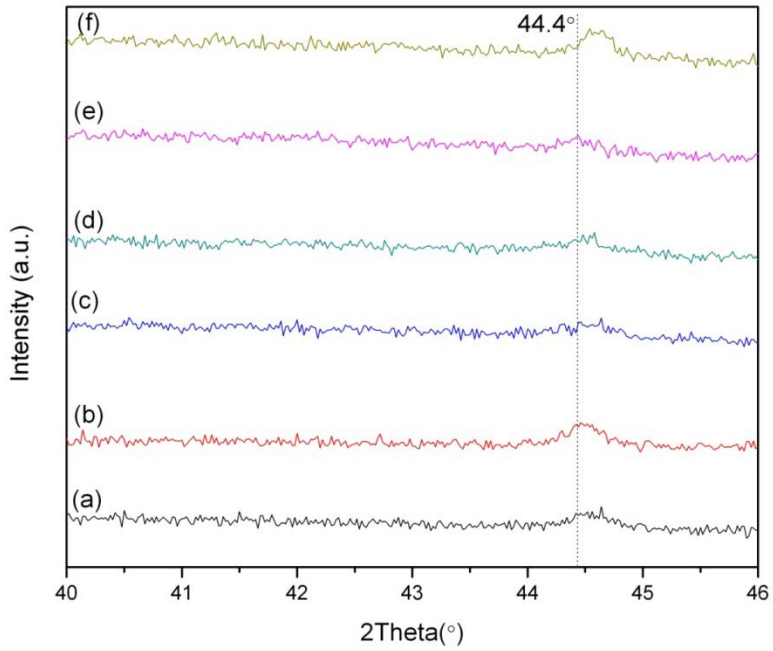

Figure S1 XRD patterns of reduced (a) Ni/0Na/CeO_2, (b) Ni/0.5Na/CeO_2, (c) Ni/1Na/CeO_2, (d) Ni/2Na/CeO_2, (e) Ni/5Na/CeO_2, and (f) Ni/10Na/CeO_2 catalysts.

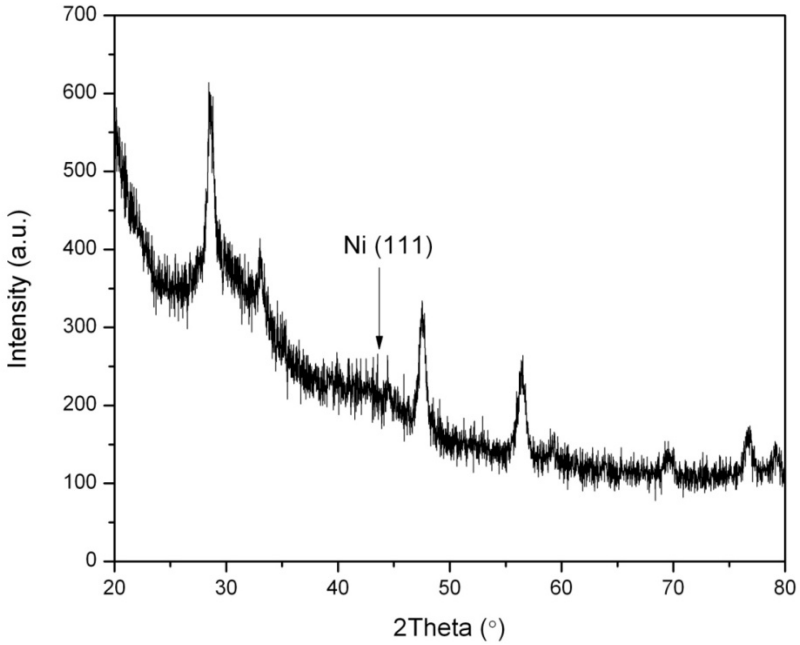

Figure S2 XRD pattern of spent Ni/2Na/CeO_2 catalyst after 100 h of reaction.

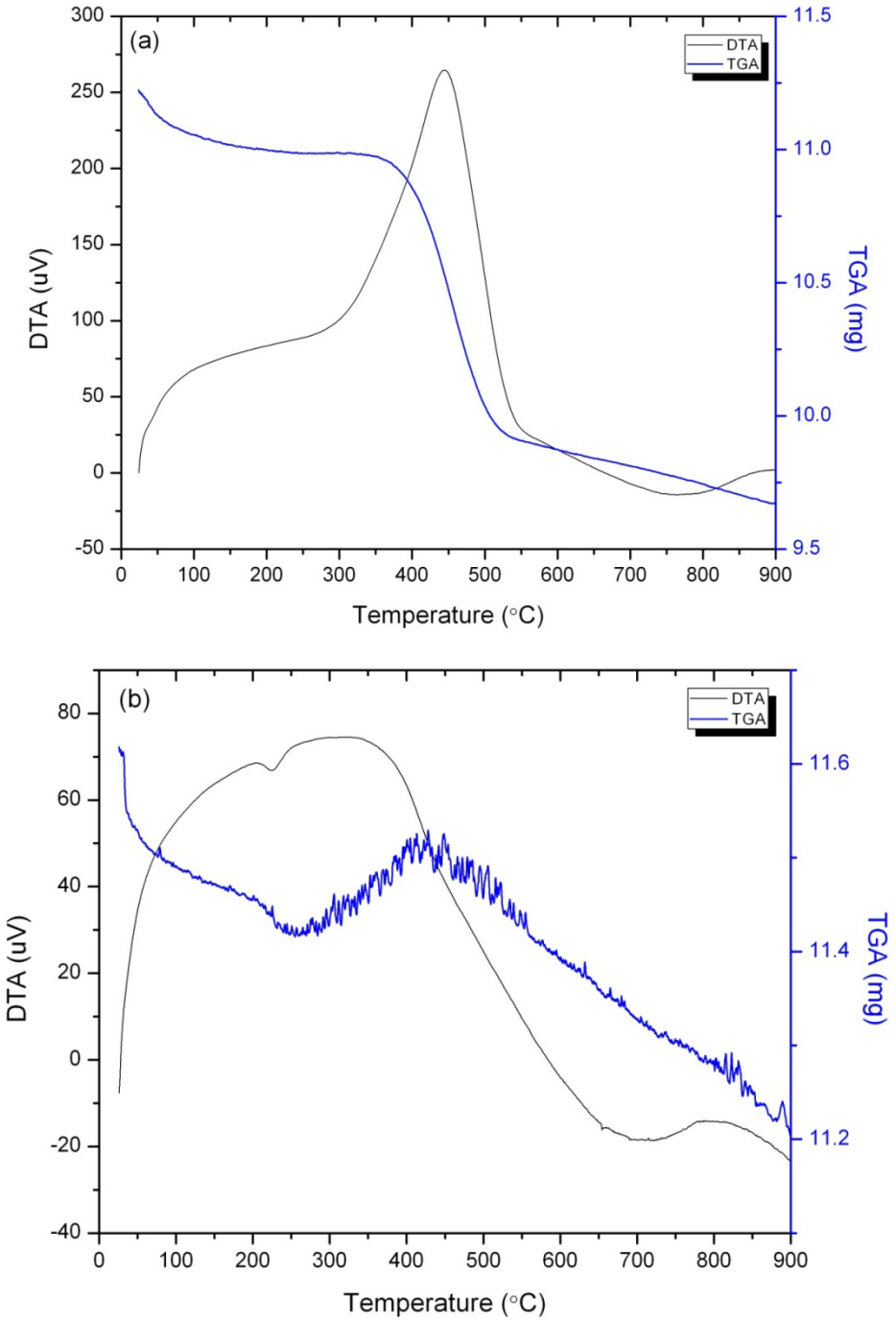

Figure S3 TGA profiles of (a) Ni/0Na/CeO_2 and (b) Ni/2Na/CeO_2 catalysts after 100 h reaction.

Appendix C

Supporting Information for Chapter 6

1. Sample calculation for deriving Ni dispersion via N_2O titration

Table S1. H_2 consumptions of samples in each stage of H_2-TPR.

Stage	H_2 Consumption (mmol)		
	Ni/5K/CeO_2	5K/CeO_2	NiO
1st H_2-TPR	2.89	0.44	2.45
2nd H_2-TPR	0.53	0.42	0.11

$$Ni\ dispersion(\%) = 100 \times \frac{H_2\ consumed\ in\ 2nd\ H_2 - TPR}{H_2\ consumed\ in\ 1st\ H_2 - TPR}$$

$$= 100 \times \frac{0.11}{2.45} = 4.54\ \%$$

2. Comparison of catalytic activity and H_2-TPR between Ni/5K/CeO_2 catalyst and Ni-5K/CeO_2 catalyst

2.1. Preparation of Ni-5K/CeO_2 catalyst

Ni-5K/CeO_2 catalyst was prepared via co-impregnation of the solution with required amounts of $Ni(NO_3)_2.6H_2O$ and KNO_3 onto the calcined CeO_2 supports to yield 10 wt% Ni-5 wt% K/CeO_2 catalyst. The mixture was then dried under constant stirring at 80°C and further dried at 100 °C for another 24 h before they were calcined at 650 °C with a heating rate of 2 °C/min in static air for 2 h.

2.2. Catalytic Activity

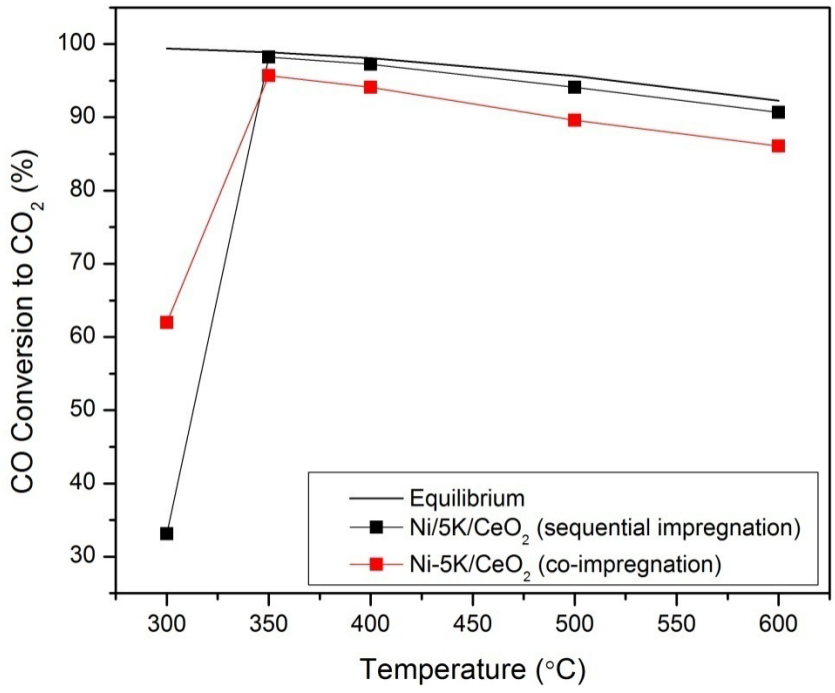

Figure S1 Percentages of CO conversion to CO_2 for Ni/5K/CeO_2 and Ni-5K/CeO_2 catalysts.

2.3.H_2-Temperature-Programmed Reduction (H_2-TPR)

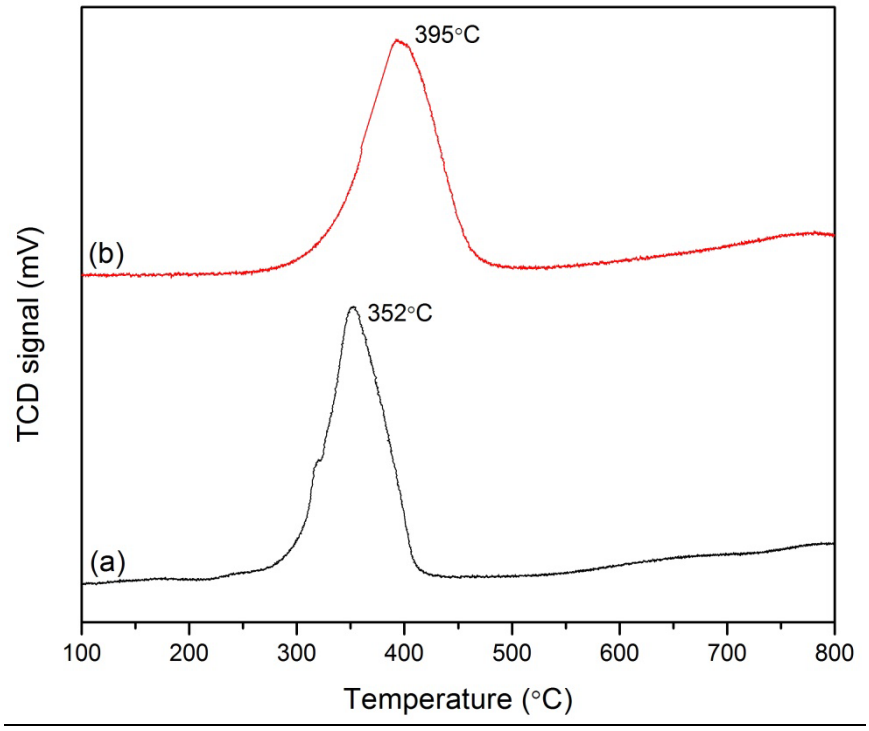

Figure S2 H_2-TPR profiles of (a) Ni-5K/CeO_2, and (b) Ni/5K/CeO_2 catalysts

3. Experimental conditions and results for kinetic study

Table S2. Experimental conditions and results for kinetic study at 400°C

Run	Gas Flow Rate (ml/min)					Rate (μmol/m^2.s)
	H_2O	CO	CO_2	H_2	He	
1	10	5	10	10	65	0.2369
2	20	5	10	10	55	0.3645
3	30	5	10	10	45	0.4364
4	40	5	10	10	35	0.5191
5	55	5	10	10	20	0.6588
6	25	2.5	10	10	52.5	0.5996
7	25	5	10	10	50	0.6202
8	25	7.5	10	10	47.5	0.6243
9	25	10	10	10	45	0.7638
10	25	12.5	10	10	42.5	0.8309
11	25	5	5	10	55	0.4993
12	25	5	10	10	50	0.4987
13	25	5	15	10	45	0.4629
14	25	5	20	10	40	0.4397
15	25	5	25	10	35	0.3828
16	25	5	10	5	55	0.6655
17	25	5	10	7.5	52.5	0.4431
18	25	5	10	11	49	0.3534
19	25	5	10	15	45	0.3470
20	25	5	10	20	40	0.3185

4. Kinetic Modeling

Three kinetic models, namely, redox, formate and carboxyl models were used to fit the kinetic data obtained. Based on the minimization of errors between the experimental data and the calculated data from the model, the kinetic parameters were estimated using a combination of Gauss-Newton and Levensberg-Marquardt methods. Using fmincon function in MATLAB software, the experimental data were fitted to the reaction rate equations by minimizing the stated objective function which was initiated using initial estimates of kinetic parameters which were randomly generated using the genetic algorithm (GA) method. In order to improve the efficiency of the GA method, constraints for the kinetic parameters estimated were imposed and are listed in Table S2.

Table S3. Constraints imposed on kinetic models

Parameter Type	**Constraints**
Adsorption Equilibrium Constant	$-200 < \Delta S_{ad} < 0$
	$-1e6 < \Delta H_{ad} < 0$
Desorption Equilibrium Constant	$1 < \Delta S_{de} < 1e3$
	$0 < \Delta H_{de} < 1e6$
General Equilibrium Constant	$-1e3 < \Delta S < 1e3$
	$-1e6 < \Delta H < 1e6$
Rate Constant	$A > 0$
	$E_a > 0$

5. Validation of Proposed Redox Kinetic Model

$$CO + s_1 \overset{K1}{\leftrightarrow} CO.s_1 \quad (1)$$

$$H_2O + s_2 \overset{K2}{\leftrightarrow} H_2O.s_2 \quad (2)$$

$$H_2O.s_2 + s_1 \overset{K3}{\leftrightarrow} H.s_1 + OH.s_2 \quad (3)$$

$$s_1 + OH.s_2 \overset{K4}{\leftrightarrow} H.s_1 + O.s_2 \quad (4)$$

$$CO.s_1 + O.s_2 \overset{K5}{\leftrightarrow} CO_2.s_1 + s_2 \text{ (rate-determining step)} \quad (5)$$

$$CO_2.s_1 \overset{K6}{\leftrightarrow} CO_2 + s_1 \quad (6)$$

$$H.s_1 + H.s_1 \overset{K7}{\leftrightarrow} H_2 + 2s_1 \quad (7)$$

Derivation

Assume step (5) is RDS, then $r = k[CO.s_1][O.s_2]$

s1 material balance

$$1 = s_1 + CO.s_1 + H.s_1 + CO_2.s_1$$

s2 material balance

$$1 = s_2 + H_2O.s_2 + OH.s_2 + O.s_2$$

Expressing the respective intermediates in terms of stable species,

$$CO.s_1 = K1P_{CO}s_1$$

$$H.s_1 = \sqrt{\left(\frac{P_{H2}}{K7}\right)}s_1$$

$$CO_2.s_1 = \frac{P_{CO2}s_1}{K6}$$

$$O.s_2 = \frac{K2K3K4K7P_{H2O}s_2}{P_{H2}}$$

$$H_2O.s_2 = K2P_{H2O}s_2$$

$$OH.s_2 = \frac{K2K3\sqrt{(K7)}P_{H2O}s_2}{\sqrt{(P_{H2})}}$$

Substituting the expressions of the intermediates into the site balance equations to make s1 and s2 the subject:

$$s_1 = \frac{1}{1 + K1P_{CO} + \sqrt{\left(\frac{P_{H2}}{K7}\right)} + \frac{P_{CO2}}{K6}}$$

$$s_2 = \frac{1}{1 + K2P_{H2O} + \frac{K2K3\sqrt{(K7)}P_{H2O}}{\sqrt{(P_{H2})}} + \frac{K2K3K4K7P_{H2O}}{P_{H2}}}$$

Therefore the overall rate equation can be determined:

$$r = k[CO.s_1][O.s_2]$$

$$r = \frac{k_f \frac{K1K2K3K4K7P_{CO}P_{H2O}}{P_{H2}} - k_b \frac{P_{CO2}}{K6}}{\left(1 + K1P_{CO} + \sqrt{\left(\frac{P_{H2}}{K7}\right)} + \frac{P_{CO2}}{K6}\right)\left(1 + K2P_{H2O} + \frac{K2K3\sqrt{(K7)}P_{H2O}}{\sqrt{(P_{H2})}} + \frac{K2K3K4K7P_{H2O}}{P_{H2}}\right)}$$

The parameters estimated from the above redox mechanism are presented in Table S3. The redox model achieved the best fit with R^2=0.91, suggesting that within the stated boundaries, this model presents the most accurate parameters to fit the experimental data obtained.

Table S4. Estimated Kinetic Parameters for Proposed Redox Model

Rate Constant	**A_i**	**$-E_i$ (J/mol)**
k_5	1.00E+3	-4.85E+2
k_{-5}	1.18E+2	-1.99E+5
	ΔS_i (J/mol.K)	**$-\Delta H_i$ (J/mol)**
K_1	-8.06E+1	7.88
K_2	-1.88E+2	2.02E+1
K_3	8.83E+1	1.22E+1
K_4	-6.34E+2	1.13E+1
K_6	9.55E+1	-4.75
K_7	1.38E+2	-1.79E+4

Appendix D

List of publications based on results obtained in this thesis

[1] **M.L. Ang**, J.T. Miller, Y. Cui, L. Mo and S. Kawi, "Bimetallic Ni-Cu Alloy Nanoparticles Supported on Silica for Water-Gas Shift Reaction: Activating Surface Hydroxyls via Enhanced CO Adsorption", *Catalysis Science & Technology* (2016) DOI: 10.1039/C5CY01885D. [Chapter 4]

[2] **M.L. Ang**, U. Oemar, E.T. Saw, L. Mo, Y. Kathiraser, B.H. Chia, and S. Kawi, "Highly Active Ni/xNa/CeO_2 Catalyst for Water-Gas Shift Reaction: effect of sodium on methane suppression", *ACS Catalysis* 4 (2014) 3237-3248. [Chapter 5]

[3] **M.L. Ang**, U. Oemar, Y. Kathiraser, E.T. Saw, C.H.K. Lew, Y. Du, A. Borgna and S. Kawi, "High-Temperature Water-Gas Shift Reaction over Ni/xK/CeO_2 Catalysts: Suppression of Methanation via Formation of Bridging Carbonyls", *Journal of Catalysis* 329 (2015) 130-143. [Chapter 6]

[4] **M.L. Ang**, Z. Li, Z. Bian, K.Y. Chong, E. Gunawan and S. Kawi, "Cubic CeO_2@Ni Phyllosilicate@CeO_2 Core-Shell Catalyst for Water-Gas Shift Reaction", *in preparation for submission to Chemical Communications*. [Chapter 7]